CRS-stack-based seismic reflection imaging for land data in time and depth domains

---

CRS-Stapelungsbasierte Zeit- und Tiefenbereichsabbildung reflexionsseismischer Landdaten

Zur Erlangung des akademischen Grades eines

DOKTORS DER NATURWISSENSCHAFTEN

von der Fakultät für Physik der

Universität (TH) Karlsruhe

genehmigte

DISSERTATION

von

Dipl.-Geophys. Zeno Heilmann

aus

Pforzheim

Abstract

Land data acquisition often suffers from rough top-surface topography and complicated near-surface conditions. The resulting poor data quality makes conventional data processing very difficult. Under such circumstances, where simple model assumptions may fail, it is of particular importance to extract as much information as possible directly from the measured data. Fortunately, the ongoing increase in available computing power makes advanced data-driven imaging approaches feasible; thus, these have increasingly gained in relevance during the past few years. The common-reflection-surface (CRS) stack, a generalized high-density velocity analysis and stacking process, is one of these promising methods. It is applied in a non-interactive manner and provides, besides an improved zero-offset simulation, an entire set of physically interpretable stacking parameters that include and complement the conventional stacking velocity. For every zero-offset sample, these so-called kinematic wavefield attributes are obtained as a by-product of the data-driven stacking process. As will be shown, they can be applied both to improve the stack itself and to support subsequent processing steps.

Using these CRS attributes, an advanced data-processing workflow can be established, leading from the time domain to the depth domain, and covering a broad range of seismic reflection imaging issues in a consistent manner. The major steps of this workflow are, besides stacking and attribute determination itself, residual static correction, redatuming, tomographic inversion, and pre- and poststack depth migration. So far, this workflow has been limited to data acquired on a planar measurement surface or at least to data for which a planar measurement surface had been simulated by elevation statics. However, conventional elevation statics may introduce a certain error into the stack and—even worse—to the attribute sections, as vertical emergence of all rays has to be assumed. In the case of rough top-surface topography, this error might cause a significant deterioration of the results of the stack, and of all the processing steps based on it. Therefore, I extended the existing implementations of CRS stack and residual static correction to consider the source and receiver elevations directly.

The presented implementation of the CRS stack for topography combines two different approaches of topography handling to minimize the computational effort: after initial values of the stacking parameters are determined for a smoothly curved floating datum using conventional elevation statics, the final stack and also the related residual static correction are applied to the original prestack data, considering the true source and receiver elevations without the assumption of nearly vertical rays. Finally, all results are extrapolated to a chosen planar reference level using the stacking parameters. This redatuming procedure removes the influence of the rough measurement surface and provides standardized input for interpretation, tomographic velocity model determination, and poststack depth migration.

Results achieved for two realistic synthetic data sets and two quite challenging real data sets are discussed. The synthetic data sets were created by the oil industry using finite difference methods. Both of them are well suited to test and further develop the implementation of a CRS-stack-based imaging workflow for land data since they include typical problems of land data processing in a realistic man-

ner. The first data set is based on a complicated velocity model resembling a true subsurface structure common to Saudi Arabia. The very shallow part directly below the rough top-surface topography is homogeneous, hence residual static corrections were omitted in this case. Besides this, a complete time-to-depth imaging workflow was conducted including CRS stack for topography, redatuming, tomographic inversion, and depth migration. The second synthetic data set aims at simulating a situation typical for the overthrust front of the Canadian Foothills. However, similar geological settings can also be found in other foothill areas. The data includes the full spectrum of difficulties that can be encountered in such a case: strongly variable top-surface topography, complex near-surface conditions and a very difficult subsurface structure. For this very complex data set the discussion will be limited on applying stack and residual static corrections rather than considering the entire workflow including tomographic inversion and depth migration.

Finally, two case studies based on real data sets from North Brazil and the Arabian Peninsula are presented. In both cases a complete CRS-stack-based imaging workflow was conducted including CRS stack for topography, residual static corrections, tomographic inversion, and pre- and poststack depth migration. The first case study resulted from an ongoing research project conducted in collaboration with the Federal University of Pará, Bélem, Brazil. The main issue of this project is to develop a new seismic reflection imaging workflow well suited for the reprocessing of existing seismic data with the aim to reevaluate exploration prospects. In this specific case, the seismic data was acquired under difficult conditions many years ago. The main problem encountered was the poor quality of the data, especially with respect to coverage and signal-to-noise-ratio. The second case study is concerned with a challenging land data set from Saudi Arabia. This data set was selected and distributed to international research teams and contractors by the national Saudi Arabian oil-company, Saudi Aramco, with the purpose to test and further develop new methods to solve specific problems of data processing in the Middle East. These problems are mainly related to the rough top-surface topography of this region and to its complex near-surface geology which often includes complexities such as sand dunes, outcropping carbonates, caves, collapses, and a very deep water table. Below these structures, the rock strata becomes more uniform and regular.

From these data examples it can be concluded that the data-driven CRS stack approach is particularly suitable for land data processing. The three parameter traveltime approximation allows for a large stacking aperture in midpoint and offset directions. Particularly for sparse or very noisy data, this highly increased fold results in an enhanced signal-to-noise ratio and event continuity of the stack section and, last but not least, in a more reliable and stable residual static correction. As will be shown, another very important advantage of CRS processing, i.e. the physical meaning of the extracted stacking parameters, is maintained by directly considering the original source and receiver elevations during stack and residual static correction. The reliability of this information is crucial to the success of CRS-stack-based time-to-depth imaging.

Zusammenfassung

Die vorliegende Dissertation wurde mit Ausnahme dieser Zusammenfassung in englischer Sprache verfasst. Hierbei wurde auf eine deutsche Übersetzung englischsprachiger Fachbegriffe verzichtet die bereits in den deutschen Sprachgebrauch eingegangen sind oder keine adäquate deutsche Entsprechung besitzen. Zur leichteren Erkennbarkeit sind solche Begriffe, mit Ausnahme ihrer groß geschriebenen Abkürzungen, im Folgenden kursiv gesetzt.

Die Auswertung reflexionsseismischer Landdaten wird oftmals erheblich erschwert durch den Einfluss rauer Oberflächentopographie und komplizierter geologischer Verhältnisse innerhalb der oberflächennahen Schichten. Da unter solchen Bedingungen einfache Modellannahmen bezüglich des sich im Untergrund ausbreitenden Wellenfeldes weitgehend ihre Gültigkeit verlieren, liefert die Anwendung konventioneller Abbildungsverfahren hier nur selten zufriedenstellende Ergebnisse. Um den oben genannten Einflüssen in geeigneter Weise Rechnung zu tragen ist neben der direkten Bestimmung der oberflächennahen Geschwindigkeiten beispielsweise anhand von Bohrlochdaten die Gewinnung von zusätzlichen Informationen aus den reflexionsseismischen Messdaten selbst von besonderer Bedeutung. Glücklicher Weise ermöglicht die kontinuierliche Zunahme der zur Verfügung stehenden Rechenleistung heute den Einsatz von hoch entwickelten daten-orientierten Abbildungsverfahren denen sehr allgemeine Modellvorstellungen zugrunde liegen. Die *Common Reflection Surface* (CRS) Stapelung, mit welcher sich die vorliegende Dissertation hauptsächlich befasst, ist eine dieser viel versprechenden Methoden.

Generell werden bei Stapelverfahren die gemessenen Daten zwecks Erhöhung des Signal-zu-Rauschen Verhältnisses aufsummiert, wobei über die bloße Struktur des Untergrundes hinausgehende Informationen aus der Parametrisierung des Summationsoperators abgeleitet werden können. In den meisten Fällen stellt die resultierende Zeitbereichsabbildung eine simulierte *Zero-Offset* Sektion dar, eine zeilenweise Aneinanderreihung von Zeitreihen, sogenannter Spuren, die hypothetischen Messungen mit koinzidenten Quell- und Empfängerlokation entsprechen. Letztere weisen jedoch aufgrund der Stapelung ein mit Einzelmessungen nicht vergleichbares Signal-zu-Rauschen Verhältnis auf.

Bei dem hier vorgestellten Verfahren geht dem eigentlichen Stapelprozess eine verallgemeinerte hochauflösende Geschwindigkeitsanalyse voraus, die im Vergleich zu konventionellen Methoden statt eines einzelnen Stapelparameters (z. B. Stapelgeschwindigkeit), mehrere physikalisch interpretierbare Stapelparameter liefert. Diese ermöglichen eine großräumige flächenhafte Approximation zusammengehörender Reflexionsereignisse, was besonders bei schwierigen Daten zu einer deutlichen Verbesserung des Stapelergebnisses führt. Wie gezeigt werden wird, profitiert jedoch nicht nur die Stapelung selbst von diesen so bestimmten kinematischen Wellenfeldattributen – auch nachfolgenden Verarbeitungsschritten dienen diese als wertvolle, über eine bloße Stapelgeschwindigkeit hinausgehende Information.

Die als Nebenprodukt der CRS Stapelung anfallenden kinematischen Wellenfeldattribute ermöglichen

die Erstellung einer neuartigen CRS-Stapelungsbasierten Datenverarbeitungsabfolge für seismische Landdaten. Diese umfasst, neben CRS Stapelung und Geschwindigkeitsanalyse, die Bestimmung reststatischer Korrekturen, die Ableitung eines glatten Geschwindigkeitsmodells mittels tomographischer Inversion sowie *Pre-* und *Poststack* Tiefenmigration. Bisher beschränkte sich die Anwendung dieses *Workflows* auf Daten, die auf einer ebenen Oberfläche gemessen wurden, wobei die oberflächennahe Geschwindigkeit als für die gesamte Messoberfläche konstant angenommen wurde. Diese Annahmen treffen für marine Daten die auf der Meeresoberfläche gemessen wurden in der Regel annähernd exakt zu.

Im Gegensatz hierzu, ist es im Falle von Landdaten meist notwendig, durch mehr oder weniger große Korrekturen den Einfluss oberflächennaher Geschwindigkeitsvariationen und rauer Oberflächentopographie zu kompensieren. Für gewöhnlich handelt es sich hierbei um sogenannte statische Korrekturen, das heißt um Korrekturen, welche nur die Quell- und Empfängerlokation selbst berücksichtigen, nicht aber die jeweiligen Auf- bzw. Abtauchwinkel der gemessenen Reflexionsereignisse. Diese werden als an der Quelle vertikal abtauchend und am Empfänger vertikal auftauchend angenommen, was durch die Brechung zur Vertikalen hin begründet wird, welche sich aus der üblicherweise zur Oberfläche hin stark abnehmenden Wellenausbreitungsgeschwindigkeit ergibt. Leider trifft diese Annahme nicht immer zu, wie zum Beispiel in dem besonders in ariden Zonen nicht seltenen Fall von direkt an der Oberfläche anstehendem nahezu unverwittertem Gestein. Zudem nimmt in den allermeisten Fällen der sich aus der Vernachlässigung des Auftauchwinkels ergebende Laufzeitfehler für ein bestimmtes Reflexionsereignis mit wachsendem Quell/Empfängerabstand (*Offset*) zu. Aus diesen Gründen kann die Verwendung statischer Korrekturen zu verfälschten Ergebnissen bei der Geschwindigkeitsanalyse führen, was sowohl bei konventionellen Verfahren als auch im Falle der CRS Stapelung sehr negativen Einfluss auf nachfolgende stapelparameternutzende Verarbeitungsschritte haben kann. Die im Zuge dieser Arbeit entwickelte und implementierte Verallgemeinerung der CRS Stapelung auf beliebige Messoberflächen führt zu einer beträchtlichen Reduzierung dieses Problems, welche sich, wie gezeigt werden wird, auch auf die Anwendung der Reststatik übertragen lässt.

Im Hinblick auf die praktische Implementierung kam folgender Problemstellung besondere Bedeutung zu: Zur Bestimmung der optimalen CRS Stapelfläche wäre, im Falle von 2D Daten[1], prinzipiell für jeden Punkt der zu erzeugenden *Zero-Offset* Sektion eine globale drei-parametrige Suche notwendig. Leider steigt der erforderliche Rechenaufwand exponentiell mit der Zahl der gleichzeitig zu bestimmenden Parameter an so dass eine solche Vorgehensweise in der Praxis kaum anwendbar ist. Aus diesem Grunde wurde schon bei der Implementierung der CRS Stapelung für ebene Messoberflächen, die der hier vorgestellten Arbeit zugrunde liegt, eine pragmatische Suchstrategie verwendet, bei welcher zuerst mittels dreier globaler Einparametersuchen in geeigneten Untermengen des Datenraumes Initialwerte der Stapelparameter bestimmt werden, die anschließend mittels einer lokalen Dreiparametersuche optimiert werden.

Diese Vorgehensweise konnte für beliebige Oberflächentopographie nicht direkt übernommen werden, da sich für den entsprechenden CRS Stapeloperator keine geeignete Zerlegung der Initialsuche in Einparametersuchen durchführen lässt. Die hier vorgestellte Implementierung nutzt daher folgende Strategie: Im Fall einer glatt gekrümmten Messoberfläche ist es möglich den Stapeloperator so zu vereinfachen, dass eine pragmatische Initialsuche nach Vorbild der CRS Stapelung für ebene Topographie möglich ist. Da aber nur in den seltensten Fällen a priori eine glatt gekrümmte Messoberfläche vor-

---

[1]Die linienhafte Aufnahme seismischer Daten wird als 2D Akquisition bezeichnet. Die hier vorgestellte Arbeit behandelt ausschließlich diese Messkonfiguration. Eine Erweiterung auf flächenhaft gemessene Daten (sog. 3D Daten), wie sie heute in der Industrie häufig verwendet werden, ist prinzipiell möglich. Für ebene Messoberflächen existieren bereits 3D CRS Stapelungsimplementationen.

liegt, werden kleine statische Korrekturen verwendet um die gemessenen Daten auf solch ein glattes *Floating Datum* zu beziehen. Anschließend wird diese Hilfsoberfläche als das frei wählbare Bezugsdatum der Stapelparameter des allgemeineren Operators für beliebige Topographie verwendet. Auf diese Weise bilden die zuvor unter Verwendung statischer Korrekturen bestimmten Stapelparameter ideale Startwerte für eine lokale Dreiparameteroptimierung, die nun wiederum auf die Originaldaten unter Berücksichtigung der wahren Quell- und Empfängerelevationen angewendet werden kann. Abschließend werden die Ergebnisse mit Hilfe einer *Redatuming*-Prozedur unter Verwendung der optimierten Stapelparameter auf ein horizontales Referenzniveau bezogen, wodurch der Einfluss der Topographie (*Acquisition Footprint*) weitestgehend eliminiert wird und ein standardisiertes Ergebnis für Interpretation und nachfolgende Verarbeitungsschritte zur Verfügung steht.

Da viele Probleme erst bei der praktischen Anwendung zu Tage treten und zudem in Charakter und Ausprägung stark vom verwendeten Datensatz abhängig sind, wurde großer Wert auf die fortlaufende Überprüfung und Weiterentwicklung der vorgestellten Implementierung mittels geeigneter Testdatensätze gelegt. Im recht umfangreichen Anwendungsteil der vorliegenden Arbeit werden Ergebnisse, gewonnen anhand zweier synthetischer und zweier realer Datensätze, vorgestellt und diskutiert. Beide synthetischen Datensätze stammen aus der Erdölindustrie und wurden mittels Finiter-Differenzen Methoden unter Berücksichtigung von für Landdaten typischen Problemstellungen modelliert. Im ersten Fall wird eine Situation nachgebildet, die recht häufig in ariden Gebieten des Mittleren Ostens anzutreffen ist und hohe Ansprüche an die verwendeten Datenverarbeitungsmethoden stellt. Das den Daten zugrunde liegende Modell ist gekennzeichnet durch Sanddünen, raue Oberflächentopographie und starke laterale Variationen der oberflächennahen Geschwindigkeiten, wie sie beispielsweise durch ausgetrocknete, mit unverfestigten Sedimenten angefüllte, Flusstäler, direkt an der Oberfläche bzw. in sehr geringen Tiefen anliegende Gesteinsformationen oder der teilweisen Auflösung von Anhydrit in oberflächennahen Schichten erzeugt werden. Für das zweite synthetische Datenbeispiel wurde eine Situation nachgebildet, wie sie an der Überschiebungsfrontlinie der *Canadian Foothills*, aber auch in anderen Vorgebirgsregionen anzutreffen ist. Dieser Datensatz ist geprägt von einer stark variierenden Oberflächentopographie und komplizierten geologischen Verhältnissen sowohl in den oberflächennahen als auch in den tieferliegenden Schichten.

An die synthetischen Datenbeispiele anschließend werden zwei Fallstudien basierend auf Realdatensätzen aus Brasilien und Saudi-Arabien präsentiert. Die erste Fallstudie wurde im Rahmen eines bestehenden Forschungsprojekts in Zusammenarbeit mit der Federal University of Pará, Bélem (Brasilien), erarbeitet. Eines der Hauptziele dieses Projekts ist die Entwicklung einer für die Neuprozessierung bestehender Daten besonders geeigneten Abfolge von Datenverarbeitungsschritten. In dem gezeigten Fall wurden die seismischen Messdaten schon vor geraumer Zeit und unter schwierigen Bedingungen akquiriert, weshalb heute die relativ geringe Qualität der Daten hinsichtlich Signalgehalt und Überdeckung die größte Herausforderung bei der Datenverarbeitung darstellt. Das letzte der behandelten Datenbeispiele wurde von der staatlichen Ölfirma Saudi-Arabiens (Saudi Aramco) ausgewählt und an verschiedene Forschungsteams und Kontraktoren verteilt, um eine gemeinsame Basis zu schaffen, mit deren Hilfe neuartige Methoden zur Behandlung oberflächennaher Einflüsse auf seismische Messdaten getestet, weiterentwickelt und verglichen werden können. Neben einer stark variierenden Topographie treten bei diesen Daten weitere für den Mittleren Osten typische Probleme wie Sanddünen, an der Oberfläche anstehende Karbonatgesteine, Karsterscheinungen und ein sehr tief liegender Wasserspiegel auf.

Mit Ausnahme des zweiten synthetischen Datenbeispiels, wurde in allen Fällen neben der CRS Stapelung selbst und der Bestimmung reststatischer Korrekturen auch die Abschätzung eines glatten Makrogeschwindigkeitsmodells mittels tomographischer Inversion der Stapelparameter sowie eine anschlie-

ßende Tiefenmigration durchgeführt. Auf diese Weise konnte sowohl die Korrektheit der strukturellen Informationen als auch die der extrahierten kinematischen Wellenfeldattribute überprüft werden.

Wie die hier gezeigten Ergebnisse belegen ist die verwendete pragmatische Suchstrategie im allgemeinen ausreichend um verlässliche Attributwerte zu bestimmen. Allerdings wird die fortlaufende Steigerung der zur Verfügung stehenden Rechenleistung bald auch die direkte Anwendung einer globalen drei-parametrigen Suche ermöglichen, was besonders im Falle geringer Überdeckung zu einer weiteren Verbesserung der Ergebnisse führen sollte. Hinsichtlich der Berücksichtigung komplexer oberfächennaher Strukturen möchte ich abschließsend noch betonen, dass die vorgestellte Implementation eine lateral variable Oberflähengeschwindigkeit nur in soweit berücksichtigt, als diese innerhalb der jeweiligen Stapelapertur als konstant angenommen werden kann. Im Falle der vorgestellten Realdatenbeispiele wurde dies durch die Anwendung von Refraktorstatik und inverser Elevationsstatik erreicht. Zudem trägt die Reststatik dazu bei etwaige Abweichungen von dieser Annahme auszugleichen. Nichtsdestotrotz bietet die direkte Berücksichtigung der lokalen *Near-Surface*-Geschwindigkeit an Quelle und Empfänger eine interessante Perspektive für zukünftige Implementierungen der noch immer jungen CRS Technologie.

Contents

Contents

Chapter 1

Introduction

> The main difference between a theologian and a geologist is that the first was never *up there* and the second never *down there* ...

The earth's interior can only be scratched by boreholes or mining and most areas inside this planet remain unreachable for any kind of direct investigation. Knowledge, e.g., concerning structures, material properties, and dynamic processes can be obtained only by geophysical methods that indirectly investigate the subsurface. We record amplitudes and traveltimes of waves that passed through the earth or measure physical properties like gravity and magnetic field that carry information regarding the interior of our planet. There are various kinds of methods depending on the size of the target region and the intended purpose of the conducted survey. Those related to wave propagation build the framework of this thesis. Seismology for instance is a powerful tool to investigate the global structure of the earth's interior using elastic body waves induced by earthquakes with dominant frequencies from 0.5-15 Hz. On the other side of the scale ground penetrating radar employs electromagnetic waves with frequencies from 10-1000 MHz emitted and recorded by a pair of closely spaced antennas at the surface to conduct very shallow surveys (penetration depth $\approx 10^{-1}$ to 10^2 m) with high resolution.

This work is concerned with exploration seismology: besides rather new applications like CO_2-storage or geothermal energy exploration, oil and gas reservoirs are the main targets to be sought for. The latter are usually found in sedimentary rocks at depths in the order of a few km. For this depth regime, reflection seismic surveys are capable of detecting and spatially resolving features at scales as small as tens of meters or less. They employ artificial sources located at the surface that emit seismic waves with an average frequency of 25 to 75 Hz into the subsurface, usually described as elastodynamic waves. Whenever these waves impinge onto changes in the earth's elastic medium parameters, they are partly transmitted and partly reflected. The reflected waves are recorded by a large number of receivers on the earth's surface. The kinematics of the wavefield allow us to obtain detailed information on the spatial distribution of the discontinuities and, thus, on geological structures, like stratigraphic traps in which oil and gas accumulates. In addition, an interpretation of the amplitudes of the measured wavefield may lead to quantitative estimates of the elastic medium parameters themselves. For instance rock density, porosity, or fluid saturation can be analyzed in order to characterize and monitor hydrocarbonate reservoirs or geothermal energy production sites.

1.1 Seismic data acquisition

The first seismic reflection exploration in history was carried through near Oklahoma City, U.S.A., on the fourth of June in the year 1921 (Brown, 2002). Since that time seismic exploration methods have been highly evolved and seismic data acquisition is carried out all over the world—on land as well as at sea. First seismic experiments at sea were made on the New Jersey continental shelf in the late 1930's. After the Second World War, offshore drilling expanded quickly, first in shallow waters adjacent to known land-based production areas, and then to other shallow and deep water areas around the world. Today, hydrocarbons are being produced in water depths down to 3 km and more and petroleum reconnaissance extends into water depths greater than 5 km. During the last decade 3D data acquisition, i. e. acquisition with sources and receivers having a spatial distribution, became standard in offshore exploration and modern exploration vessels currently conduct 3D surveys of areas of up to 10,000 km^2. On land it is expected that the greatest discoveries like, e. g. the giant Ghawar field in Saudi Arabia (4.5 million barrels per day) or the Cantarell field in Mexico (2 million barrels per day), are already made. Nevertheless, the current situation of rapidly growing demand in oil and gas made on-shore exploration, even in difficult terrains, again more and more attractive. Additional applications, e. g. in geothermal energy exploration, might increasingly gain in relevance in the future. For onshore surveys, 2D acquisition, i. e. acquisition with sources and receivers disposed along a (usually straight) line, are still common since 3D acquisition on land is quite expensive and some times hardly possible due to the infrastructure or the topographic features of the area under consideration. The work presented in this thesis is confined to the 2D case, a future extension to 3D is possible.

The fundamental principles of land and marine surveys are the same. However, the acquisition equipment and procedures differ by necessity. Moving-coil electromagnetic geophones that sense vertical velocity are usually employed as receivers in land acquisition. The seismic source on land is usually either dynamite planted in a borehole or Vibroseis, a vibrating mechanism mounted on large trucks. Unlike dynamite, the Vibroseis signal is not impulsive, but rather lasts from 7 to 40 seconds. To emit its signal, the Vibroseis source sweeps through a range of frequencies from about 10 to 80 Hz. Because seismic reflectors in the earth are more closely spaced than the length of the Vibroseis wavetrain, the reflections in raw Vibroseis records overlap, making raw Vibroseis data uninterpretable. A Vibroseis trace must be processed to produce a replacement trace with a signal equivalent to that of an impulsive source. This is accomplished by cross-correlating the raw seismogram with the Vibroseis sweep.
A reflection seismic survey typically involves generating hundreds (2D) to tens of thousands (3D) of seismic source events, so-called shots. The seismic energy generated by each shot is detected and recorded at a variety of distances from the source location. The receivers that transform ground movement or pressure into an electrical voltage that can be recorded are referred to as geophones or hydrophones, respectively. For every source event, each receiver generates a seismogram called *trace*, which is a time series representing the subsurface response at the receiver location. Each trace has a reference time zero corresponding to the time of the source event. For 2D acquisition the data can be represented by a 3D data cube, e. g. with the axes: shot-coordinate, shot-receiver distance, and time. For practical purposes it is often preferable to use another coordinate system (see Figure 1.1) where the traces are sorted with respect to the midpoint position x_m of shot and receiver and half-offset h, i.e., half the distance between shot and receiver. The 3D data cube can be subdivided in several 2D subsets, so called *gathers* that are related to (hypothetical) experiments with specific source and receiver geometries. These subsets, explained in Figure 1.1, play an important role in data processing.

1.2   Preprocessing

Before an acquired data set can be interpreted it is subject to many processing steps. Initially, it contains a multitude of different wave types. For seismic reflection imaging, only primary body-waves of a specified wave mode, usually compressional waves are considered as signal. All other wave types including multiply reflected waves (multiples), surface waves, refracted waves, and often also primary reflections of other wave modes are treated as coherent noise. In addition, the data contains also incoherent noise, i. e. random noise, caused, for instance, by traffic, industry, or wind shaking of trees. Examples for some of the different kinds of coherent and incoherent noise can be seen in the shot seismogram depicted in Figure 1.2. Generally speaking, the main issue of every seismic imaging workflow is, besides the imaging itself, the removal of all components of the data which are not intended to be imaged.

The first step in this direction is the so-called preprocessing. It usually involves the following tasks:

- geometry information is assigned to the traces and bad traces, e. g., resulting from a corrupted receiver, are zeroed out.

- small traveltimes which are not expected to be related to reflection events are muted.

- deconvolution (e. g., Robinson and Treitel, 1980) is applied to increase the temporal resolution. The underlying assumption is that a recorded seismic trace can be seen as the convolution of a series of spikes, representing reflectors, with a wavelet, i. e., the source signal (assumed to be stationary). During a so-called predictive deconvolution, reverberations or short period multiple reflections are removed from seismic traces by applying a prediction-error filter.

- band-pass filtering is used to suppress noise that lies outside the expected signal bandwidth.

- coherent noise is removed by filtering in the f-k domain, since such events can often be distinguished by their much steeper traveltime-versus-offset dip (dip-filtering).

- trace balancing is applied to correct for amplitude variations along the line caused, e. g. by varying near-surface conditions.

- the influence of the topography and the weathering layer is compensated as far as possible by so-called field static corrections which will be discussed more closely in the following section. For marine data this step is usually not required, but might be necessary in case of ocean bottom seismics (OBS), where the receivers are placed at the sea floor. In case of land data processing static corrections can be a very important issue (see, e. g., Vesnaver, 2004).

In practice seismic preprocessing is cumbersome and detail-laden. The corrections applied by each processing operation typically vary with respect to location within the survey area, source event, source-receiver offset, and time within the seismic trace. As a result, the seismic processor must usually perform a tedious analysis of the data set to select appropriate parameter values for every processing operation.
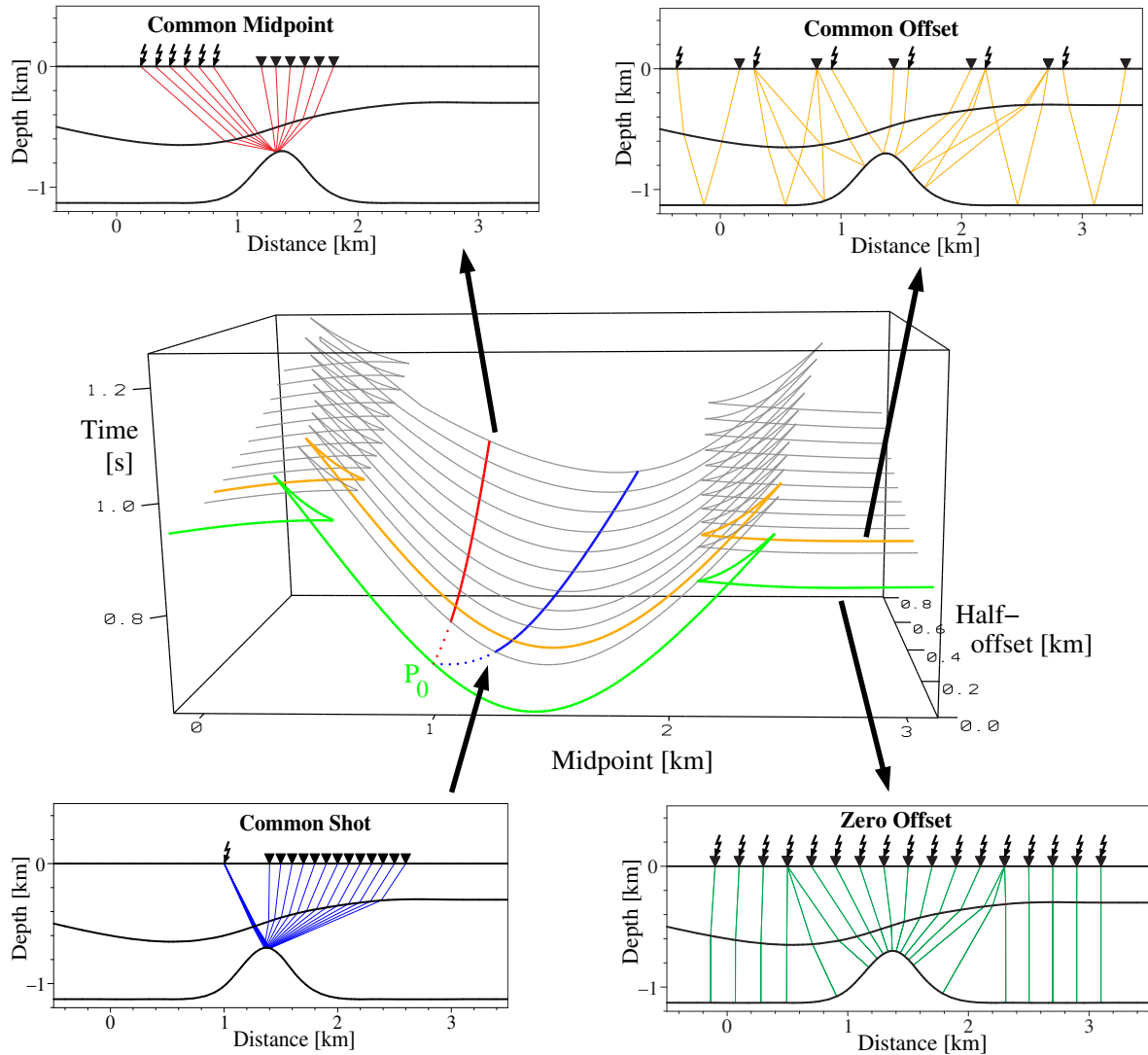
Figure 1.1: In the center, a 3D data volume typically used to visualize multi-coverage prestack data acquired by 2D acquisition is displayed. Only the traveltimes corresponding to one reflector are considered and the temporal extend of the recorded pulse is omitted. The volume can be divided into several subvolumes corresponding to specific source and receiver arrangements: A common shot (CS) gather contains all traces that have one and the same shot coordinate in common (blue). Similarly, the common-midpoint (CMP) gather (red) and the common-offset (CO) gather (yellow) contain all traces that have a certain midpoint position or a certain offset in common. The zero-offset (ZO) section (green) is a special kind of common-offset gather which cannot be directly acquired, but is usually simulated from the prestack data. Figure according to Höcht (2002).

Offset [m]

Shot seismogram
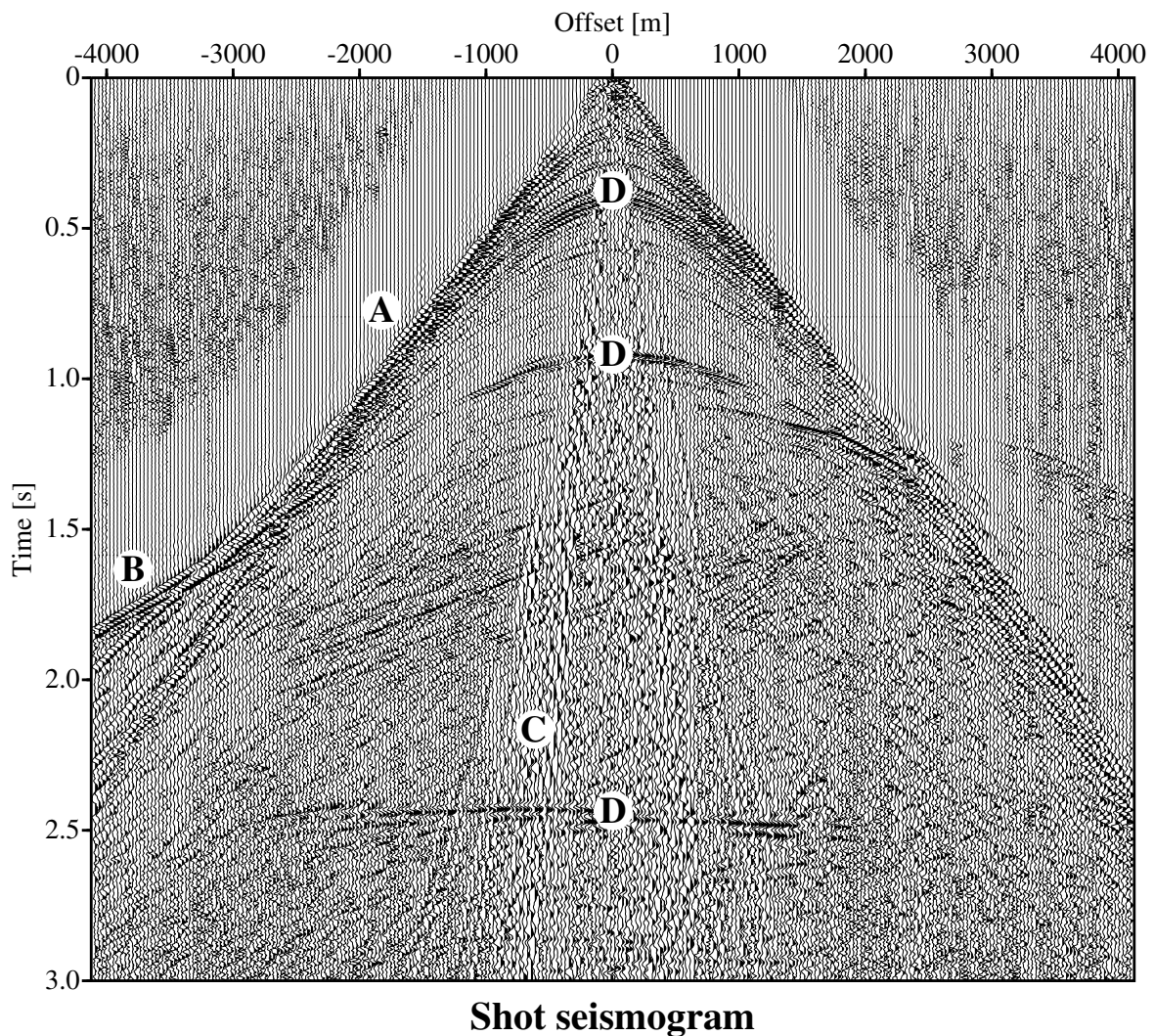
Figure 1.2: Shot gather extracted from a land seismic data set. In addition to the reflection events (some of them marked by the letter D), various other kinds of events can be observed, e. g., the direct wave (A), head wave (B), and ground roll (surface waves) (C). Figure taken from Mann et al. (2004)

1.3 Static corrections

For exploration seismics, the interpretation of a seismogram is primarily directed to structural or stratigraphic features of the subsurface at a target depth ranging from a few hundred meters up to a few kilometers. However, since most seismic data is acquired at or close to the earth's surface, the interpreter must be aware of the influence of both the top-surface topography and of the near-surface geology. This is especially important when these conditions rapidly change within a given survey. For seismic land data it is quite typical that,

- the near-surface geology, particularly the weathering layer, is characterized by high attenuation levels and low and strongly fluctuating wave propagation velocities (Cox, 1999),

- the coupling of neighboring seismic sources or receivers can vary greatly even across similar ground or near-surface conditions, and

- the influence of the measurement surface topography results in a so-called *acquisition footprint* which makes processing and time-domain interpretation more difficult.

The surface and near-surface effects on the traveltimes often bias the information which is obtained from the target area. They can corrupt the stack and possibly introduce false structure into deep reflectors. For this purpose, static corrections that aim at compensating these effects are a very important issue for land-data processing. In addition, most conventional imaging tools assume a planar measurement surface to simplify data handling and processing and, thus, rely on static corrections that simulate such an acquisition geometry.

Analyzing the problems mentioned above reveals a major difference between topographic features and features of the near-surface geology: the elevations of the source and receiver locations can easily be measured during the data acquisition but information concerning the often complex near-surface geology is much more difficult to obtain (see, e. g., Vesnaver et al., 2006). Mostly static correction methods rely exclusively on the near-surface velocity information extracted from conventional seismic data. In cases where this information is inadequate to resolve the near-surface structure, borehole data from so called *uphole measurements* and specific refraction seismic surveys (see, e. g., Cox, 1999; Bridle et al., 2006) with dense source and receiver spacing are conducted to obtain ancillary information. E. g., in Saudi Arabia, where near-surface features like sand dunes, carbonate outcrops, or wadis (dry flash flood valleys) have often a large influence on the measured wavefield, it is standard for the national Saudi Arabian oil company, Saudi Aramco, to acquire uphole information from boreholes of about 100 m depth every 4 km along the seismic line. Unfortunately, the influence of the topography and of the near-surface structure are closely interrelated and cannot be treated separately. In this thesis, I will present a solution of the topography problem assuming the near-surface velocities to be known. However, it will also be demonstrated how unwanted time-shifts caused by inaccuracies of the utilized near-surface model can be compensated by CRS-stack-based residual static corrections.

The seismic weathering layer is highly important for understanding the concept of static corrections. It is defined as a near-surface low velocity layer in which the portion of the air filled pore space of rocks is larger than the portion of water filled (Cox, 1999). Within this layer the effective or average velocity is typically about 500 - 800 m/s[1] and, thus, much lower than the sub weathering velocities (>1500 m/s). As this *low velocity layer* (LVL) usually consists of unconsolidated materials, its velocity strongly depends on water saturation and is related to compaction and thickness. The latter may vary along the survey from a few centimeters up to 50 meters or even more. For example, an error of only one meter in calculating the thickness of near-surface materials with a velocity of 500 m/s, results in a static-correction error of 1.5 ms.

The terms static correction and redatuming should not be confused. There are different methods of redatuming prestack data "downwards" to the base of weathering, e. g., wave equation datuming (Yang et al., 1999, and references given therein), CFP-based redatuming (Kelamis et al., 2000), or straight

---

[1]It is a widely-spread misbelief that P-wave velocity in earth materials is never less than about 330 m/s (the velocity of sound in air) since according to the well-known Wyllie-equation (Wyllie et al., 1956) the seismic P-wave velocity in a material is an average of the velocity in the pore fluid (air) and the mineral grains through which the seismic wave passes. This argument works quite well in case of water-saturated solid rocks but does not apply to the P-wave velocity in unconsolidated materials where the velocity depends on the shear modulus, the bulk modulus, and the density of the total material, not on the average of these properties for the constituent materials.
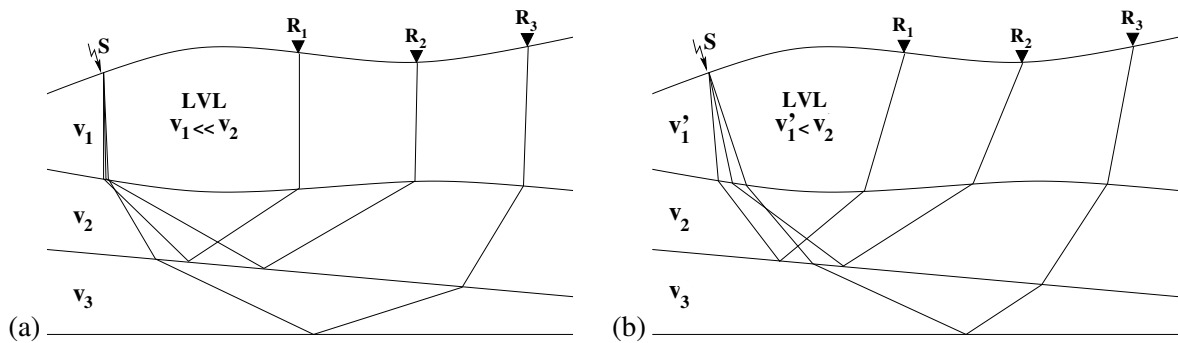
Figure 1.3: Basic assumptions of static corrections: For a simple subsurface model the ray paths connecting a source S and three receivers R_1, R_2, R_3 are shown. In (a) the assumptions of *surface consistency* and *time invariance* are well met, due to the high velocity contrast between the weathering layer and the layer below the base of weathering ($v_1 \ll v_2$). For (b) this is not the case. Here v'_1 is too high compared to v_2 to generate nearly vertical ray paths within the weathering layer by refraction at the base of weathering. Figure modified after Koglin (2005).

rays redatuming (Alkhalifah and Bagaini, 2006). These methods usually involve a different time-shift for each sample of a trace which depends besides the source and receiver position also on the associated traveltime. In contrast to this dynamic correction, static corrections assume the correction time to depend on the respective source and receiver positions only (time invariance), and furthermore to be composed of mutually independent source and receiver parts that are fixed for arbitrary rays (surface consistency). These two assumptions are justified if a weathering layer of sufficiently low velocity is present so that the up-coming waves propagate along virtually vertical ray paths after they have been refracted at the base of weathering (see Figure 1.3). Static correction methods can be subdivided into *field static corrections* (see also Chapter 3) which are applied before the processing and *residual static corrections* which are part of the processing itself. The latter will be discussed in Chapter 5.

1.4 Data-driven seismic imaging

With few exceptions, one can state that the final aim of seismic reflection imaging is to obtain a depth domain image of the subsurface from the time domain multi-coverage prestack data. This process can be roughly divided into two main tasks:

- **Stacking**, i.e., suitable summation of the recorded prestack data with the purpose to reduce its amount for further processing and to use its inherent redundancy to attenuate incoherent noise. Assuming a perfect summation of all seismic energy that stems from the same reflection point in depth the signal-to-noise ratio can theoretically be improved by a factor of $\sqrt{N}$ (Yilmaz, 1987), where N is the number of contributing traces. However, the large proportion of incoherent noise, typical to seismic data, is only one motivation of collecting multi-coverage data. Aside from improving the signal-to-noise ratio, the illumination of one and the same subsurface point by a multitude of different experiments is necessary to obtain suitable information for velocity analysis and inversion.

- **Depth migration**, i. e., a transformation of the time domain records to a depth domain image by placing the reflections at the correct subsurface position and focusing the diffracted energy at the associated diffraction points. Virtually all depth migration procedures demand at least the knowledge of an initial macrovelocity model. In contrast to the short wavelength velocity variation which gives rise to the recorded seismic reflection events, this model can be thought of as representing the long wavelength component of the true subsurface velocity distribution. Information about the velocity model is obtained from the seismic data itself, together with additional geological a priori information.

The order in which these two processes, stacking and depth migration, are applied is not fixed. On the one hand, it is possible to stack the data in the time domain and to apply the migration afterwards. A typical processing chain would be, e. g., NMO/DMO/stack followed by poststack depth migration. On the other hand, the migration can be applied first, before the migrated data is stacked in the depth domain. This proceeding is called prestack depth migration. In practice, both approaches are closely interrelated since the information used to built an initial macrovelocity model for prestack depth migration is usually obtained by stacking in the time domain. At this point, it has to be mentioned that there is also an intermediate process called time migration which is very similar to depth migration but creates a migrated time-domain image of the subsurface. Since no depth axis is introduced a time domain velocity model which is far easier to obtain than its depth domain counterpart suffices for the time migration process.

To understand the concept of macro-model independent seismic imaging which is vitally important for the CRS stack method it is necessary to take a closer look at the model oriented prestack depth migration, first. Various different methods exist, but most of them are based on the assumption that each reflection point in the subsurface can be treated as a diffractor. Utilizing a known macrovelocity model the associated diffraction operator (see Figure 1.6 (c)) is calculated, e. g., by finite-difference methods, and all seismic energy along this operator is summed up. In other words, a summation over all possible reflections at the CRP is carried out, with the assumption that only the true reflection will constructively contribute to the summation result and that everything else will be subject to destructive interference. Under this assumption, prestack depth migration theoretically provides the best possible image of the subsurface. Practically, the required velocity model is not known a priori. It has to be derived from an initial model by means of iterative application of prestack depth migration itself and sophisticated methods to update the velocity model until the migration result is consistent with the data. The latter is achieved when the subsurface position of each reflection point in the migrated image is independent of source and receiver displacement. It is evident that seismic data acquired with a limited number of sources and receivers at the surface can resolve the true velocity distribution of the subsurface only up to a certain degree. Vice versa, a velocity model that is consistent to the prestack data does not need to resolve every detail of the actual velocity distribution. Therefore, certain assumptions according the velocity model to be inverted for are justified. For example, one might assume a model build by homogeneous, isotropic layers or blocks, or the smoothest possible isotropic model without discontinuities that is consistent with the kinematics of the prestack data.

In order to separate the summation of amplitudes from the transformation into the depth domain which requires a velocity model, a macrovelocity model independent stacking approach can be deployed. In the ideal case the stacking process would have to identify and sum up all amplitudes related to one and the same reflection point in depth. In other words, the stack would have to be applied along so-called common-reflection-point (CRP) trajectories. However, a strict identification of the CRP trajectories and their associated reflection points in depth is generally impossible as the exact velocity distribution

of the subsurface would need to be known. A pragmatic solution to solve this problem is to employ an approximate description of the CRP trajectories by parameterizing them in such a way that the parameters can be directly determined from the prestack data. Doing this, allows a summation of the amplitudes pertaining to a certain reflector point performed directly in the prestack data.

The depth location of the reflection points remains unknown and, thus, subject to a subsequent migration algorithm, whereas the offset-dependency of the reflection traveltimes associated with a single CRP then provides the information needed for the construction of a velocity model, apart from borehole measurements and geological a priori knowledge. The parameterization of the CRP response should make as little assumptions as possible regarding the subsurface structure but involve only a reasonable number of free parameters. Furthermore, a sound physical interpretation of these parameters should exist. Such a space-time adaptive, data-driven approach relies on the existence of coherent reflection events in the prestack data. Only if coherent reflection events can be observed in the acquired multi-coverage data, they can be associated with wavefronts that appear at the acquisition surface.

1.4.1 Common-midpoint stack

In the old days of seismic data processing the available computing power was very limited so that the parameterization of reflection events had to be as simple as possible. For this reason, the CMP stack method introduced by Mayne (1962), assumes a horizontally layered medium, where the reflection events measured on different traces in a CMP gather stem from a common-reflection-point in the subsurface located directly beneath the CMP location (see Figure 1.4(a)). Hence, the CRP trajectory is approximated by a line in offset direction and the reflection response of a CRP is described by

$$t^2(h) = t_0^2 + \frac{4h^2}{v_{\text{NMO}}^2} \, , \tag{1.1}$$

using only one parameter, i.e., the well known NMO velocity, which is for such a simple medium equal to the root-mean-square (RMS) velocity.

In CMP processing, seismic traces are grouped into CMP gathers (see Figure 1.1). For selected CMP gathers velocity functions, based on arrival time variations as a function of source-receiver offset, are determined for the most prominent reflection events. An example for this process, called velocity analysis, is given in Figure 1.5. CMP velocity functions are then interpolated throughout the survey area to construct a velocity model of the subsurface. This velocity model is used to perform a normal moveout (NMO) correction of the multi-coverage data. The NMO correction approximates each reflection event by a hyperbola and corrects the traveltimes in a way that reduces this hyperbola to a straight line at $t = t_0$, i.e. the zero-offset (ZO) traveltime. Thus, it reduces the multi-offset reflection times to ZO reflection times, related to hypothetical experiments with coincident shot and receiver locations. After NMO correction, the reflection events in the CMP gather are assumed to be flat so that all traces can be easily summed up, or stacked. If the subsurface geology does not violate the assumptions of the CMP method too strongly, reflection events on the different traces will sum up constructively, producing a single trace with a signal-to-noise ratio that is much higher than that of the individual prestack traces. By repeating this procedure for all CMP gathers in the survey, the prestack data set is replaced by a much smaller poststack data set of much higher signal quality. Note two effects of the simple geometric NMO correction: for far offsets, reflections experience a pulse stretch which artificially lowers their frequency and dipping reflections are over-corrected due to the fact that the asymptotic moveout velocity of a dipping reflection is increased by dividing the real velocity by
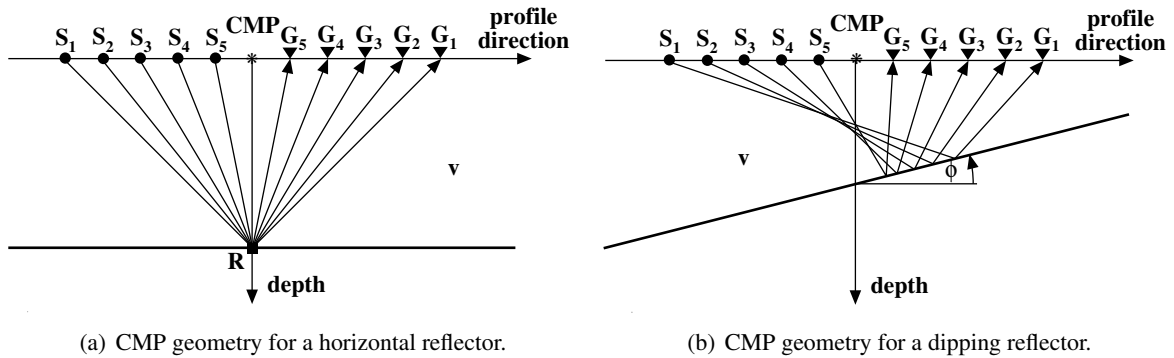
(a) CMP geometry for a horizontal reflector.   (b) CMP geometry for a dipping reflector.

Figure 1.4: In (a) the model consists of a single horizontal reflector embedded into two constant velocity layers. All rays associated with one CMP location illuminate the same subsurface point. In (b) a single dipping reflector separates two constant velocity layers. In this case, the CMP experiment illuminates more than one subsurface point (reflection point dispersal). Figure taken from Müller (1999).

the cosine of the dip. As a consequence, the NMO correction, even given perfect velocity information, is only appropriate for zero-dip reflections.

Later this approach was extended by Levin (1971) to consider plane reflectors with dips by adding a correction term that accounts for the reflection point dispersal depicted in Figure 1.4(b):

$$t^2(h) = t_0^2 + \frac{4\,h^2 \cos^2 \Phi}{v_{NMO}^2} \qquad (1.2)$$

where Φ denotes the dip angle of the reflector. However, this equation does only consider the reflection point dispersal but does not remove it.

Nowadays, the so-called dip moveout (DMO) correction (for further details I refer to Deregowski, 1986; Hale, 1991) is applied to precondition the data for CMP processing. This process can be seen as a partial migration with the aim to remove the influence of the reflector dip from the prestack data in such a way that the reflection response of a CRP is again located within the CMP gather—as in case of a non-dipping reflector. This is done for a specific ZO traveltime by summing up for each offset the contributions of all possible dips along the DMO operator and putting the result into the CMP gather. This is justified by a similar assumption as used by prestack depth migration and many other migration methods. It is assumed that only the amplitudes along the true CRP trajectory will result in a constructive summation of signal whereas the summation along the remaining trajectories will be subject to destructive interaction of noise. A drawback of such a "blind" stack approach is that no additional subsurface information can be obtained that could later complement the NMO velocity. DMO processing has greatly extended the accuracy and usefulness of the CMP method for areas where the geology violates the assumptions of the method. Today, the NMO/DMO/stack approach is commonly used in standard processing.

Migration to zero-offset (MZO) combines both the NMO and the DMO process, but requires the knowledge of the interval velocity model. Since the true CRP trajectory is unknown, the MZO sums up all amplitudes along a group of CRP trajectories belonging to those reflection points that lie on the ZO isochron defined by the two-way ZO traveltime t_0. According to Figure 1.6 (b), where the
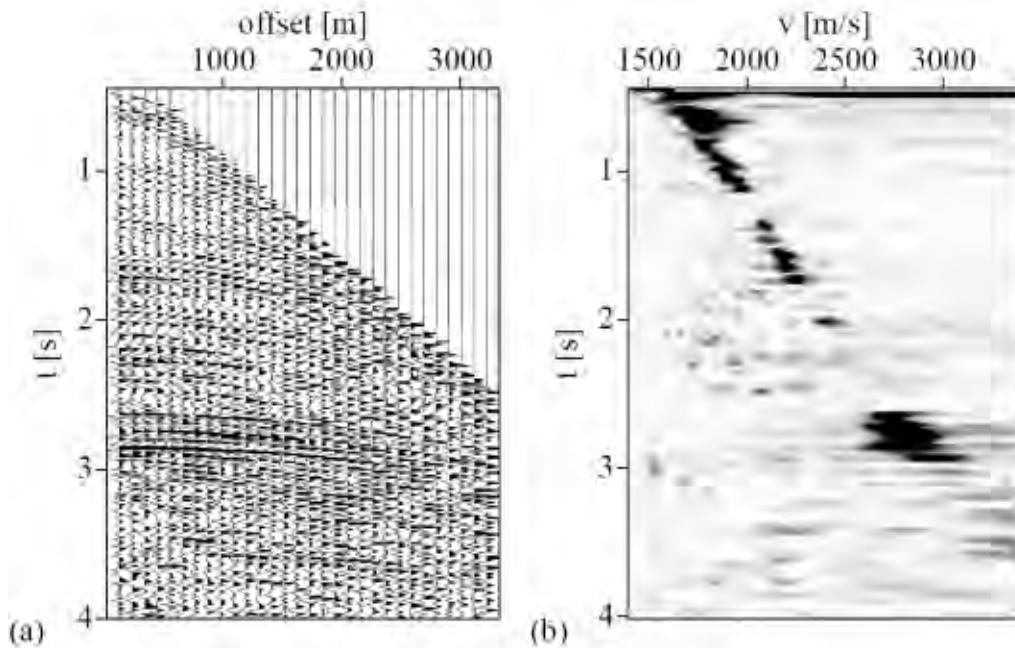
Figure 1.5: Stacking velocity analysis in a CMP gather. (a) Muted CMP gather. (b) Velocity spectrum. Semblance values, obtained along NMO hyperbolas are plotted as a function of zero-offset traveltime and stacking velocity. Maxima (dark) correspond to reflection events in (a). Figure taken from Duveneck (2004).

fan-shaped MZO operator is illustrated for the case of a reflection point R located at a dome-like reflector with a homogeneous overburden, the stacked signal is placed into point P_0 of the ZO section to be simulated. For this case, the ZO isochron is the lower semicircle with the center at x_0 and radius $v_0 t_0 / 2$.

1.4.2 Common-reflection-surface stack

The CMP stack described above employs a second order traveltime approximation in offset direction and assumes homogeneous layers separated by horizontal interfaces. The CRS stack generalizes this concept by involving also the midpoint coordinate and thus accounting for subsurface models with lateral variations, i. e., models with arbitrarily curved reflectors.

The recorded reflection events are described in terms of an analytic second order approximation of the kinematic reflection response of an arbitrarily curved reflector segment in depth. This results in a stacking operator that sums up all amplitudes stemming from a common-reflector-segment. According to Figure 1.6 (d) the summation result is placed at that location in the ZO section which is defined by traveltime and midpoint coordinate of the ZO ray that is reflected at the center of the common-reflector-segment.

The parameters of this analytic function are related to physical properties of this so-called central ray and are determined automatically from the prestack data by means of coherence analysis. As mentioned before, the ideal approach would be to use a second-order approximation of the kinematic reflection response of a reflection point rather than a segment. However, the direct determination of

the parameters from the prestack data that would describe such a CRP trajectory is inherently ambiguous: without information about neighboring reflection points, it is impossible to decide whether a trajectory actually refers to a single CRP or mixes contributions from various reflection points. The concept of reflector segments allows to use a significantly larger part of the coherent reflection event in the prestack data for the parameter search. In addition, the attenuation of coherent noise strongly benefits from the highly increased number of traces that contribute to the stack.

The physical justification to use entire reflector segments is based on the fact that, due to the finite bandwidth of seismic signals, not only reflections from the CRP itself contribute to the measured reflection response associated with the CRP, but also reflections from neighboring points at the reflector located within the so-called Fresnel zone. Nevertheless, there is a trade-off between S/N ratio and the achievable resolution, expecially if the low signal-to-noise ratio of the prestack data demands search and stacking apertures that exceed the size of the Fresnel zone.

Within the last decade, the Common-Reflection-Surface (CRS) stack has established as a promising alternative to conventional methods used so far for stacking and velocity analysis. Originally designed to generate a 2D ZO stack section (Höcht, 1998; Müller, 1999; Mann, 2002), the CRS stack was successfully extended to 3D (Höcht, 2002; Bergler, 2004) and to finite-offset (FO) (Zhang et al., 2001; Bergler, 2001). A special case of the FO CRS stack is the common-offset (CO) CRS stack, which is performed analogously to ZO stacking but generates a stacked CO gather instead of a ZO gather.

Since very little assumptions according to the underlying subsurface model are made, the CRS stack method is referred to the modern macro-model independent methods, which also includes the Polystack method (de Bazelaire, 1988; de Bazelaire and Viallix, 1994), the Multifocusing method (Gelchinsky et al., 1997) and the Common-Focus-Point (CFP) method (Berkhout and Verschuur, 2001). Various aspects of macro-model-independent reflection imaging methods are discussed in Hubral (1999).

As practical experience has shown, these new methods are particularly successful for seismic land-data. Land data acquisition often suffers from rough top-surface topography and complicated near-surface conditions. The resulting poor data quality makes conventional data processing very difficult. Under such circumstances, where simple model assumptions may fail, it is of particular importance to extract as much information as possible directly from the measured data. Besides an improved ZO simulation, the CRS stack determines for every ZO sample several so-called kinematic wavefield attributes as a by-product of the data-driven stacking process. As will be shown, they can be applied both, to improve the stack itself and to support subsequent processing steps. Using these *CRS attributes*, an advanced data-processing workflow can be established leading from time to depth domain, covering a broad range of seismic reflection imaging issues in a consistent manner (Mann et al., 2003). So far, this workflow was limited to data acquired on a planar measurement surface or at least to data for which a planar measurement surface had been simulated by elevation statics. However, conventional elevation statics may introduce a certain error to the stack and—even worse—to the attribute sections, as a vertical emergence of all rays has to be assumed (see Chapter 3). In the case of rough top-surface topography, this error might cause a significant deterioration of the results of the stack, and of all the processing steps based on it. Therefore, an extention of the existing implementations of CRS stack and CRS-stack-based residual static correction that consider the true source and receiver elevations and, thus, omits elevation statics, is subject of this thesis.

Extensions of the Multifocusing and Common-Focusing-Point method that also consider the individual source and receiver elevations have been proposed by Gurevich et al. (2001) and Al-Ali and Verschuur (2006).
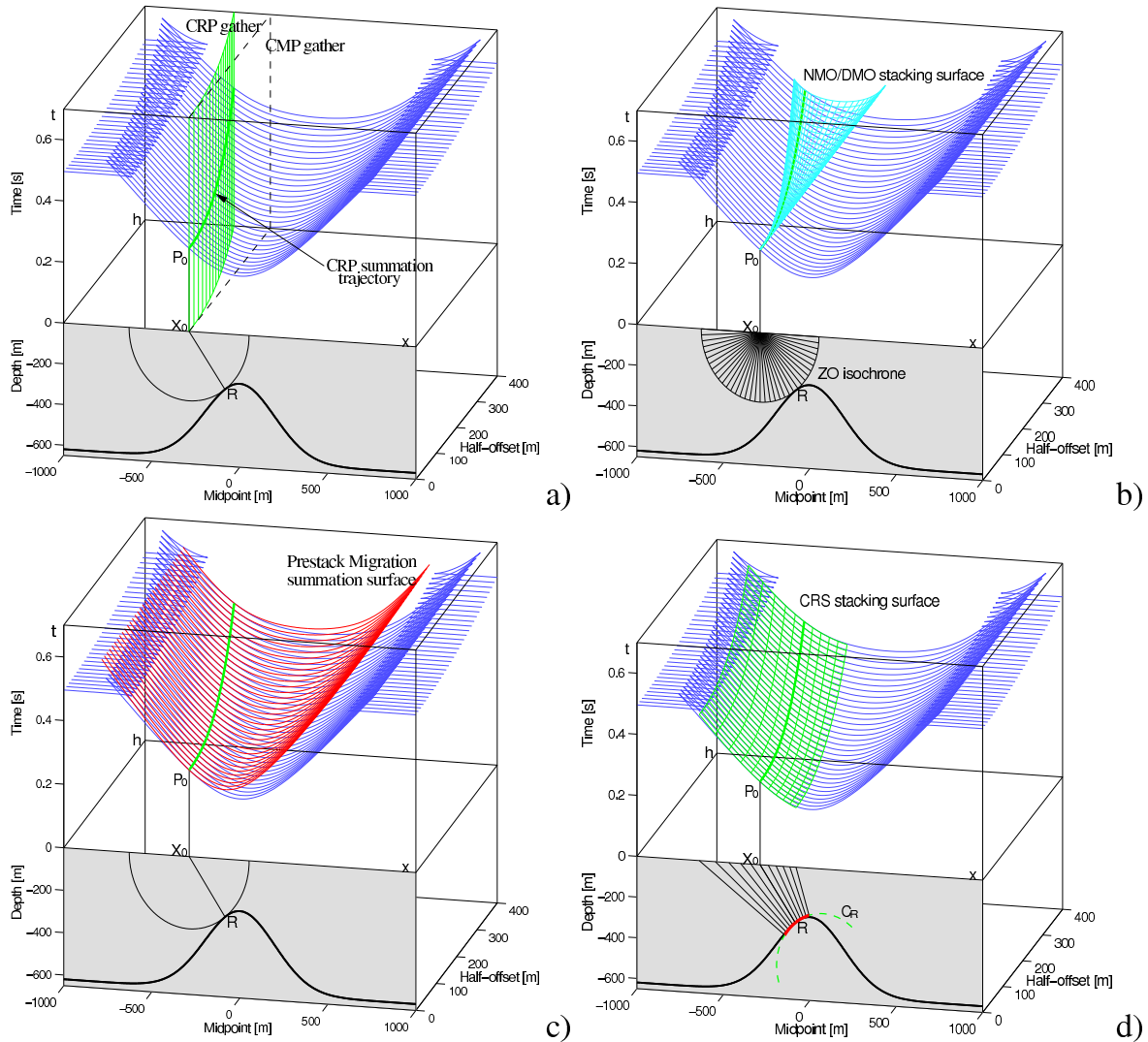
Figure 1.6: Subsurface illumination for different imaging methods. (a) The CMP stack method sums data along the hyperbola in the CMP gather which approximates the reflection response best and places the summation result into point P_0. Since the assumption of a planar and horizontal reflector is violated reflection point dispersal is encountered. In the ideal case summation would have to be performed along the CRP trajectory, shown in green. (b) The NMO/DMO/stack sums up data along the cyan colored stacking surface and places the summation result into point P_0. This stacking surface is equal to the reflection response of the ZO isochrone in the depth domain that is associated with point P_0. (c) In prestack migration data is summed along the red surface that is the kinematic response of a diffractor point at R. In time migration the summation result is assigned to the apex of the red surface in the ZO section. In depth migration it is placed into point R. (d) The CRS stack sums the data along the green surface and assigns the result to point R. This stacking surface results from approximating the true subsurface reflector by a reflector segment that has locally the same curvature as the true reflector. Figure taken from Müller (1999).

13

1.5   Structure of the thesis

In this thesis, the complete theory of the 2D CRS stack for topography is presented, practical and numerical aspects are discussed, and its application is demonstrated on synthetic and real seismic data examples. Beyond focusing on the CRS stack method itself, the integration of the CRS stack into a consistent CRS-stack-based imaging workflow for land data and tests involving the full complexity of the considered time-to-depth imaging process were important issues for the thesis at hand. The following chapters can be roughly divided into three parts: theory (chapters 2-3), implementation (chapters 4-5), and application (chapters 6-7).

The theoretical part starts in Chapter 2 with an introduction to seismic ray theory. In this regard, special emphasis is put on aspects that are relevant for the development of the CRS stack for topography. Using the paraxial ray method, the two-point eikonal, a formula which approximately describes the traveltime difference between a central ray and a ray in its vicinity (paraxial ray), is derived in local ray-centered coordinates and finally transformed to a local Cartesian coordinate system. Based on these results, a CRS traveltime operator for arbitrary topography will be derived in Chapter 3, motivated by a brief discussion on conventional approaches how to handle top-surface topography and complex near-surface conditions. In view of the practical implementation, the CRS stack operator for arbitrary topography will be simplified yielding the CRS stack operators for smoothly curved topography and for planar topography. Chapter 3 is concluded by the presentation of a redatuming procedure that aims at relating the CRS stack results to a fictitious horizontal measurement surface.

The implementation of the CRS stack for topography is discussed in Chapter 4. In principle, a global three parameter optimization problem has to be solved for each point of the ZO section. Three so-called CRS attributes have to be determined that parameterize the CRS stacking operator along which the highest coherence of the data can be obtained. For practical reasons, a cascaded processing scheme is employed starting with the determination of initial attribute values by means of a global three-times-one parameter search considering a reduced CRS stacking operator for smoothly curved topography. For this purpose, small static corrections are necessary to relate the prestack data to a fictitious smoothly curved reference level and appropriate search ranges for the stacking parameters have to be defined. As will be discussed, the initial attribute values enter into an event consistent smoothing process before they are optimized by a local three-parameter optimization considering the true source and receiver elevations. Finally, the implementation of the redatuming procedure is discussed. It provides standardized results for interpretation and further processing by mapping both, stack and attribute sections, to a horizontal redatuming level.

Chapter 5 is devoted to the introduction of the CRS-stack-based imaging workflow for land data and the individual processing steps involved. The concept of CRS-stack-based residual static corrections which is very important in land-data processing will be discussed. Furthermore, an approach for the tomographic inversion of CRS attributes will be presented aiming at the determination of a smooth macrovelocity model needed for a subsequent depth migration. Kirchhoff pre- and poststack depth migration constitutes the final step of the presented workflow. The redatumed CRS stack results serve as input for the poststack depth migration, whereas prestack depth migration is performed directly from topography using the prestack data after residual static correction.

The results achieved for two realistic synthetic data sets and two quite challenging real data sets are presented in chapters 6 and 7. The synthetic data sets were created by the oil industry using finite difference methods. Both of them are well suited to test and further develop the implementation of the CRS-stack-based imaging workflow for land data since they include typical problems of land data

processing in a realistic manner. The first data set resembles a situation quite common for the arid areas of the Arabian Peninsula. The very shallow part of the subsurface model is homogeneous, hence residual static corrections were omitted in this case. Besides this, the complete time-to-depth imaging workflow was conducted including CRS stack for topography, redatuming, tomographic inversion and depth migration. The second data set aims at simulating a situation typical for the overthrust front of the Canadian Foothills. However, similar geological settings can also be found in other foothill areas. The data includes the full spectrum of difficulties that can be encountered in such a case: strongly variable top-surface topography, complicated near-surface conditions, and a very difficult subsurface structure. For this very complex dataset the discussion will be limited on applying the CRS stack and residual static corrections rather than considering the complete workflow including tomographic inversion, and depth migration.

In Chapter 7, two case studies based on real data sets from North Brazil and the Arabian Peninsula are presented. In both cases the complete CRS-stack-based imaging workflow was conducted including CRS stack for topography, residual static corrections, tomographic inversion and pre- and poststack depth migration. The first data example resulted from an ongoing research project conducted in collaboration with the Federal University of Pará (UFPA), Bélem, Brazil. The main issue of this project is to develop a new seismic reflection imaging workflow well suited for the re-processing of existing seismic data with the aim to reevaluate exploration prospects. In this specific case, the seismic data was acquired under difficult conditions many years ago. The main problem encountered was the poor quality of the data, especially with respect to coverage and signal-to-noise-ratio. The second case study presented in this chapter is concerned with a challenging land data set from Saudi Arabia. This data set was selected and distributed to international research teams and contractors by Saudi Aramco, with the purpose to test and further develop new methods to solve specific problems of data processing in the Middle East. These problems are mainly related to the complex near-surface geology of this region. As a matter of fact, the presented data set suffers from rough top-surface topography, a strongly varying weathering layer, and a complex near-surface geology.

Conclusions and outlook on future research concerning the CRS-stack-based imaging workflow for land data and particularly the CRS stack for topography are given in Chapter 8.

Appendix A lists most of the notation used in this thesis. Furthermore, the abbreviations used throughout this thesis are compiled. In **Appendix B** a definition the Fresnel zone is given followed by a brief discussion regarding its estimation by means of CRS attributes and its use in the framework of the CRS stack method. **Appendix C** is concerned with the NMO velocity on non-planar surfaces. For example, a relation between the NMO velocity which is actually measured on a smoothly curved measurement surface and the NMO velocity which would be measured on a fictitious horizontal surface is derived. **Appendix D** is devoted to the hard- and software utilized in the framework of this thesis.

Chapter 2

Theory

In this section I will briefly review the ray-theoretical foundations of the seismic data-processing and imaging methods presented in this thesis. For a profound study on ray theory I refer to Aki and Richards (1980), Popov (2002), and especially Červený (2001). Emphasis will be put on the derivation of a very general second order approximation of the traveltime of rays in the so-called paraxial vicinity of a central ray, e. g. a normal ray, using the concept of paraxial ray theory. The latter allows to extrapolate kinematic and dynamic properties of waves calculated along a given ray into the vicinity of that ray. Throughout this chapter I assume a smoothly varying isotropic elastic medium with continuous second order spatial derivatives of the wave propagation velocity.

2.1 Wave propagation in 3D media

"The propagation of seismic body waves in complex, laterally varying 3D layered structures is a considerably complicated process" (Vlastislav Červený). Getting an exact description would require to solve the elastodynamic wave equation for this very general case with its multitude of degrees of freedom. For inhomogeneous, anisotropic, and perfectly elastic media we find a system of three partial differential equations of second order. Its derivation from linear elastodynamics is well explained in many textbooks (see references given above), and is not repeated here. For the (small-amplitude) displacement vector $\vec{u}$, in the absence of body forces, this equation reads

$$\rho \frac{\partial^2 u_j}{\partial t^2} - \frac{\partial}{\partial x_i}\left(c_{ijkl} \frac{\partial u_k}{\partial x_l} \right) = 0 \,, \tag{2.1}$$

where ρ is the density and c_{ijkl} is the elastic tensor, containing, in the most general case, 21 independent parameters. Both, the elastic tensor and the density are functions of position, $c_{ijkl} = c_{ijkl}(\vec{x})$ and $\rho = \rho(\vec{x})$. Here, and throughout this thesis, lower-case subscripts denote vector or matrix components and range from 1 to 3 while capital subscripts range from 1 to 2, only. In addition, the Einstein summation convention[1] is used.

In an isotropic medium the propagation velocity of waves neither depends on the direction of propagation nor, in case of S-waves, on the direction of polarization. Although, ray theory itself is not

---

[1]Summation is carried out over repeated indices

limited to isotropic media, for most seismic applications, the assumption of an isotropic subsurface is sufficiently accurate. Therefore, I will assume such a medium in the following. In this special case, the components of the elastic tensor can be expressed in terms of two independent elastic moduli, the Lamé parameters λ and μ. In vectorial form the elastodynamic equation for inhomogeneous isotropic perfectly elastic media reads:

$$\rho \frac{\partial^2 \vec{u}}{\partial t^2} = (\lambda + \mu) \, \vec{\nabla} \left(\vec{\nabla} \cdot \vec{u} \right) + \mu \Delta \vec{u} + \vec{\nabla} \lambda \left(\vec{\nabla} \cdot \vec{u} \right) + \vec{\nabla} \mu \times \left(\vec{\nabla} \times \vec{u} \right) + 2 \left(\vec{\nabla} \mu \cdot \vec{\nabla} \right) \vec{u} \,, \qquad (2.2)$$

where Δ is the Laplace operator which stands for $\vec{\nabla} \cdot \vec{\nabla} = \frac{\partial^2}{\partial x_1^2} + \frac{\partial^2}{\partial x_2^2} + \frac{\partial^2}{\partial x_3^2}$ and $\vec{\nabla} = \left(\frac{\partial}{\partial x_1}, \frac{\partial}{\partial x_2}, \frac{\partial}{\partial x_3} \right)^T$ is the Nabla operator, here both given in Cartesian coordinates.

General analytical solutions of equations (2.1) and (2.2) are not known and—even if there would be a solution—barely applicable to practical problems. Thus, the most common approaches to investigate wave propagation in complex media are based either on the direct numerical solution of these equations (e. g., finite-difference method (Kelly et al., 1976) and finite-element method (Strang and Fix, 1973)), or on approximate asymptotic solutions valid only for high frequencies.

Numerical methods are usually applied if the investigated medium is strongly heterogeneous and the computational cost is no crucial issue. Typical problems are related to grid dispersion and reflections from model boundaries or may occur at singular points of the wavefield, e. g., caustics.
However, if the physical properties vary smoothly within the medium, high-frequency approximations solve the elastodynamic wave equation in an efficient and sufficiently accurate way. One of the latter is the so-called *ray method* which is highly developed and widely used, today. Here, the asymptotic high-frequency solution of the elastodynamic equations for each elementary body wave can be sought in the form of a so called ray series (Babich, 1956; Karal and Keller, 1959).

2.1.1 Zero-order ray theory

In the frequency domain, where $\vec{U} = \vec{U}(\vec{x}, \omega)$ denotes the Fourier transform of the particle displacement vector field $\vec{u}(\vec{x}, t)$, equation (2.2) can be rewritten as

$$\omega^2 \rho \vec{U} + (\lambda + \mu) \, \vec{\nabla} \left(\vec{\nabla} \cdot \vec{U} \right) + \mu \Delta \vec{U} + \vec{\nabla} \lambda \left(\vec{\nabla} \cdot \vec{U} \right) + \vec{\nabla} \mu \times \left(\vec{\nabla} \times \vec{U} \right) + 2 \left(\vec{\nabla} \mu \cdot \vec{\nabla} \right) \vec{U} = 0 \,. \qquad (2.3)$$

A possible realization of the ray series solution is a series in inverse powers of the circular frequency ω. In most practical applications in seismology and seismics, only the leading term which is of the order ω^0 is considered. This leads to the *zero order ray theory* which is the underlying concept of all the formulas derived and implemented within the scope of this thesis.

The validity conditions of the zero-order ray theory are an extensively discussed topic (see, e.g., Ben-Menachem and Beydoun (1985), Kravtsov and Orlov (1990), or Červený (2001)). Many investigations on this subject were made in the past. Nevertheless, there are only heuristic criteria to determine whether zero order ray theory is applicable for a particular earth model or not. One of the most commonly used conditions is that the Fourier spectrum of the source wavelet is required to effectively vanish for frequencies

$$\omega < \omega_0 = v(\vec{x})/l_0 \,,$$

where l_0 is the length scale of the inhomogeneity and $v(\vec{x})$ is the wave velocity of the medium. As will be shown below, in the high-frequency limit, compressional and shear waves propagate independently

of each other, as in the case of a homogeneous medium—a prediction which is in full accordance with practical observations.

The main results of this method are the *eikonal* and the *transport equation*. They will be briefly rederived in the following. Solving the eikonal equation will provide us with the so-called *ray tracing system* which describes all kinematic aspects of ray propagation. The solution of the transport equation is omitted as it describes the dynamic properties of the wavefield which are of little importance within the scope of this theses.

In order to construct an approximate high frequency solution of equation (2.3) we use the ray series ansatz, namely a time-harmonic trial solution for $\vec{U} = \vec{U}(\vec{x}, t)$,

$$\vec{U} \approx \sum_{n=0}^{\infty} \frac{\tilde{\vec{U}}_n}{(i\omega)^n} e^{-i\omega\tau} . \tag{2.4}$$

The traveltime from a source to the location $\vec{x}$ is denoted with $\tau = \tau(\vec{x})$. If external forces are neglected, the displacement vector $\tilde{\vec{U}}_n$ depends on the location $\vec{x}$, only.

As mentioned before, the zero-order term of the ray series ansatz is sufficient for most practical applications in seismology and seismics. Thus, we confine our considerations to the first term of equation (2.4), i. e.,

$$\vec{U} = \tilde{\vec{U}} e^{-i\omega\tau} . \tag{2.5}$$

Inserting ansatz (2.5) into equation (2.3) and sorting by the order of ω yields

$$C_0\omega^0 + C_1\omega^1 + C_2\omega^2 = 0 , \tag{2.6}$$

with

$$C_0 = (\lambda + \mu)\,\Delta\tilde{\vec{U}} + \mu\Delta\tilde{\vec{U}} + \left(\vec{\nabla} \cdot \tilde{\vec{U}}\right)\vec{\nabla}\lambda + 2\left(\vec{\nabla}\mu \cdot \vec{\nabla}\right)\tilde{\vec{U}} + \vec{\nabla}\mu \times \left(\vec{\nabla} \times \tilde{\vec{U}}\right) . \tag{2.7}$$

$$C_1 = (\lambda + \mu)\left[\left(\vec{\nabla} \cdot \tilde{\vec{U}}\right)\vec{\nabla}\tau + \vec{\nabla}\left(\tilde{\vec{U}} \cdot \vec{\nabla}\tau\right)\right] + \mu\left[2\left(\vec{\nabla}\tau \cdot \vec{\nabla}\right)\tilde{\vec{U}} + (\Delta\tau)\,\tilde{\vec{U}}\right]$$
$$+ \left(\tilde{\vec{U}} \cdot \vec{\nabla}\tau\right)\vec{\nabla}\lambda + \left(\vec{\nabla}\mu \cdot \vec{\nabla}\tau\right)\tilde{\vec{U}} + \left(\vec{\nabla}\mu \cdot \tilde{\vec{U}}\right)\vec{\nabla}\tau , \tag{2.8}$$

$$C_2 = -\rho\tilde{\vec{U}} + (\lambda + \mu)\left(\vec{\nabla}\tau \cdot \tilde{\vec{U}}\right) + \mu\left(\vec{\nabla}\tau\right)^2\tilde{\vec{U}} , \tag{2.9}$$

Since equation (2.6) has to be fulfilled for all frequencies, each coefficient C_i has to vanish independently. For high frequencies ω, the second and third term in equation (2.6) dominate over the first term, which is therefore neglected in high frequency approximations. As a consequence of this C_0 can be used to evaluate the validity of the zero-order ray series assumption (Červený, 2001). To take this term into account more rigorously, a trial solution in the form of equation (2.4) may be used instead of expression (2.5).

Solving condition $C_1 = 0$ yields the transport equation which governs the dynamic aspects of wave propagation. Solving condition $C_2 = 0$ lead to the before-mentioned eikonal equation that describes the kinematic aspects of wave propagation. On its solution we will focus in the following.

19

2.1.2 The eikonal equation

Evaluating the condition $C_2 = 0$ is most convenient and intuitive if we reformulate it as an eigenvector problem of the matrix

$$\Gamma_{ij} = \frac{\lambda + \mu}{\rho} \frac{\partial \tau}{\partial x_i} \frac{\partial \tau}{\partial x_j} + \frac{\mu}{\rho} \delta_{ij} \left(\vec{\nabla} \tau \right)^2 , \qquad (2.10)$$

which is known as Christoffel matrix for isotropic inhomogeneous media. Denoting the identity matrix by $\underline{I}$ equation $C_2 = 0$ is equivalent to

$$\left(\underline{\Gamma} - \underline{I} \right) \tilde{\vec{U}} = 0 . \qquad (2.11)$$

According to the laws of linear algebra, the necessary condition for the existence of a non-trivial solution is

$$\det \left(\underline{\Gamma} - \underline{I} \right) = 0 , \qquad (2.12)$$

which results in the two eigenvalues

$$E_1 = \frac{\lambda + 2\mu}{\rho} \left(\vec{\nabla} \tau \right)^2 \qquad \text{and} \qquad E_2 = E_3 = \frac{\mu}{\rho} \left(\vec{\nabla} \tau \right)^2 . \qquad (2.13)$$

These eigenvalues correspond to the two different wave-types that propagate independently in the high-frequency limit. E_1 is related to a quasi longitudinal polarized wave. E_2 and E_3 represent two mutual perpendicular, quasi transversal polarized waves. In inhomogeneous media, the P-wave is not purely compressional, longitudinal or irrotational and the S-wave is not purely shear, transverse or equivoluminal. For this reason we use the terms P- and S-wave according to the classical seismological definition, where the P-wave is the first (primae) and the S-wave is the second (secundae) wave that arrives.

Inserting equations (2.13) into equation (2.11) yields that both eigenvalues have to be equal to one. This finally leads to the eikonal equations for P- and S-waves

$$\left(\vec{\nabla} \tau \right)^2 = \frac{1}{\alpha^2} \qquad \text{and} \qquad \left(\vec{\nabla} \tau \right)^2 = \frac{1}{\beta^2} , \qquad (2.14)$$

introducing the P-wave velocity $\alpha = \sqrt{(\lambda + 2\mu)/\rho}$ and the S-wave velocity $\beta = \sqrt{\mu/\rho}$.

Generally speaking, the above couple of first order nonlinear partial differential equations describes the propagation of discontinuities of the wavefield, which can be interpreted as wavefronts that correspond to propagating P waves or S waves. In mathematics such equations are usually solved for τ in terms of characteristics (e. g. Herzberger, 1958; Bleistein, 1984). The characteristics of the eikonal equation are trajectories, described by a system of ordinary differential equations which can be solved easily by standard numerical procedures. The main advantage of this formalism is that the traveltime along such a trajectory can be obtained by a simple integration.

2.1.3 Rays as characteristics of the eikonal equation

Since the following derivations are equally valid for both wave types we introduce the more general quantity v to denote either the P-wave or the S-wave velocity. If we combine both equations (2.14)

and substitute the gradient of the traveltime τ by the slowness vector $\vec{p}$ we can set up the so-called Hamiltonian of the system

$$\mathcal{H} = \mathcal{H}(\vec{x}, \vec{p}(\vec{x})) = \vec{p}^2 - \frac{1}{v^2} = 0. \tag{2.15}$$

According to the method of characteristics there is a system of seven first-order ordinary differential equations, known as the characteristic equations or the Hamiltonian system, which are equivalent to the eikonal equation:

$$\frac{d\vec{x}}{d\xi} = \vec{\nabla}_{\vec{p}}\mathcal{H}, \qquad \frac{d\vec{p}}{d\xi} = -\vec{\nabla}\mathcal{H}, \qquad \text{and} \qquad \frac{d\tau}{d\xi} = \vec{p} \cdot \vec{\nabla}_{\vec{p}}\mathcal{H}, \tag{2.16}$$

with ξ increasing monotonously along the curve $\vec{x} = \vec{x}(\xi)$, for which equation (2.15) is satisfied and which is called a characteristic of this equation. In physical terms, the characteristics of the eikonal equation are called rays. For this purpose, equations (2.16) are referred to as ray-tracing system. The six equations for the so-called canonical coordinates $\vec{x}$ and $\vec{p}$ are in general coupled and must be solved together. The seventh equation for the traveltime τ along the ray is independent from the others and can be solved once the characteristic is known.

The Hamiltonian $\mathcal{H}$ can be formulated in various different ways, resulting in alternative formulations of the ray-tracing system. If we divide both sides of equation (2.15) by two we obtain,

$$\mathcal{H} = \frac{\vec{p} \cdot \vec{p} - \frac{1}{v^2}}{2}, . \tag{2.17}$$

Inserting this into equations (2.16) results in the simplest ray-tracing system that can be obtained,

$$\frac{d\vec{x}}{d\xi} = \vec{p}, \qquad \frac{d\vec{p}}{d\xi} = \frac{1}{2}\vec{\nabla}\left(\frac{1}{v^2}\right), \qquad \text{and} \qquad \frac{d\tau}{d\xi} = \frac{1}{v^2}. \tag{2.18}$$

Here the ray-parameter $d\xi = v^2 d\tau$ can be seen as the "natural variable along the ray".

Multiplying both sides of equation (2.15) by v and inserting into equation (2.16) results in the ray-tracing system:

$$\frac{d\vec{x}}{d\xi} = \vec{p}^{-\frac{1}{2}}\vec{p}, \qquad \frac{d\vec{p}}{d\xi} = \vec{\nabla}\left(\frac{1}{v}\right), \qquad \text{and} \qquad \frac{d\tau}{d\xi} = \frac{1}{v}, \tag{2.19}$$

where the ray-parameter ξ is equal to the arclength $ds = v d\tau$.

It is also possible to use the traveltime directly as ray-parameter. Therefore we rewrite equation (2.15) in the following way:

$$\mathcal{H} = \frac{1}{2}\ln(\vec{p}^2) + \ln v = \frac{1}{2}\ln(v^2\vec{p}). \tag{2.20}$$

According to equation (2.16) the corresponding ray tracing system reads

$$\frac{d\vec{x}}{d\xi} = \vec{p}^{-2}\vec{p}, \qquad \frac{d\vec{p}}{d\xi} = -\vec{\nabla}\ln v, \qquad \text{and} \qquad \frac{d\tau}{d\xi} = 1. \tag{2.21}$$

2.2 Paraxial ray method

Dynamic ray-tracing is a powerful approach, nowadays frequently applied to evaluate high-frequency seismic wavefields in laterally inhomogeneous layered structures or to solve inverse seismic problems (e. g. Duveneck, 2004). Various coordinate systems can be used to express the dynamic ray-tracing system. However, its simplest and for the following derivations most suitable form can be obtained in ray-centered coordinates. Therefore, we will limit our derivations to these coordinates throughout this section. The eikonal equation in ray-entered coordinates will be used to derive a simple system of linear ordinary differential equations of the first order known as the *paraxial ray-tracing system*. The term "paraxial" has his seeds in optics were it represents the vicinity of the axis of the optical system. In our case it denotes the vicinity of a so-called *central ray*. The paraxial ray tracing system provides a linear description of the *paraxial rays* in terms of properties of a central ray, which is assumed to be known. This is done by using the *paraxial assumption* saying that the ray tracing system of a particular ray is also approximately valid in the close vicinity of this ray. The *dynamic ray tracing system* can be immediately obtained from the paraxial ray tracing system. Both systems are closely connected: their system matrices are identical, only the computed quantities have a different physical meaning. The dynamic ray tracing system provides dynamic information which is very useful, e. g., to calculate the geometrical spreading for true amplitude imaging (Červený and Hron, 1980; Hubral et al., 1995). Solving the dynamic ray-tracing system for arbitrary initial conditions leads to the *ray propagator matrix* $\underline{\underline{\Pi}}$, which describes, in a very convenient way, the the second-order traveltime moveout of paraxial rays in terms of quantities that refer to the central ray only.

2.2.1 Ray-centered coordinates

The ray-centered coordinates are a special kind of curvilinear orthogonal coordinates which allow a very convenient description of wave propagation in terms of paraxial ray theory. These coordinates are regular in a certain vicinity of the central ray. The extent of this region of regularity depends on the curvature of the central ray.

In order to define the ray centered coordinate system q_1, q_2, q_3, we assume according to Figure 2.1 a given ray Ψ in a smooth medium with a known trajectory $\vec{x}(s)$, determined, for example, with the ray-tracing system (2.19). One coordinate, without loss of generality q_3, may correspond to any monotonic parameter ξ along the ray. For the sake of simplicity we use $\xi = s$, with s being the arclength along the ray measured with respect to the origin S. In order to define the two remaining coordinate axes q_1 and q_2, we establish, as depicted in Figure 2.1, at any point P along that ray two mutually orthogonal unit vectors $\vec{e_1}(s)$ and $\vec{e_2}(s)$ in the plane normal to the ray through $P(s)$. The orientation of these two unit vectors along the ray is described by the following differential equations:

$$\frac{d\vec{e_I}}{ds} = \vec{\kappa_I}(s)\vec{t}(s) \qquad I = 1, 2 \,, \tag{2.22}$$

with $\vec{t}(s)$ being a unit vector tangent to the ray in $P(s)$. $\kappa_1(s)$, $\kappa_2(s)$ are to be specified in the following in such a way that the coordinate system is *orthogonal*. Consequently, a point in the vicinity of the central ray can be described by the three coordinates (q_1, q_2, s) as

$$\vec{r}(q_1, q_2, s) = q_1\vec{e_1}(s) + q_2\vec{e_2}(s) + \vec{r}(0, 0, s) \,. \tag{2.23}$$

Using $\vec{t}(s) = d\vec{r}(0, 0, s)/ds$, an infinitesimal line segment dS is given by the relation

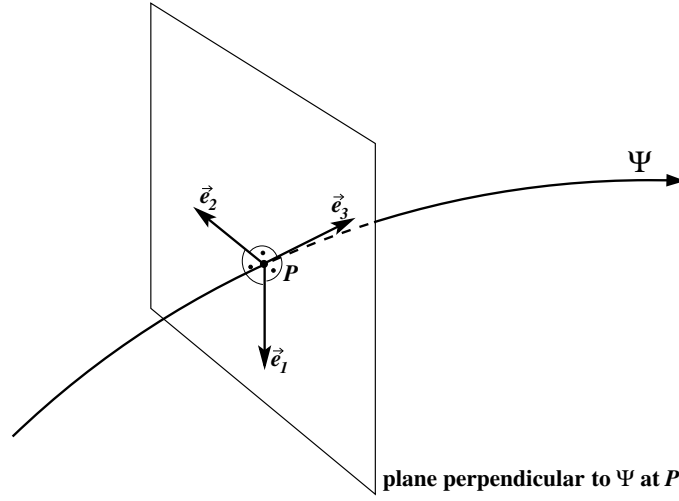$$dS^2 = d\vec{r} \cdot d\vec{r} = dq_1{}^2 + dq_2{}^2 + h^2ds^2 \,, \tag{2.24}$$

Figure 2.1: Definition of ray-centered coordinates: The ray-centered coordinate system (q_1, q_2, q_3) is curvilinear and orthogonal. It is defined along the ray Ψ that constitutes the q_3 axis of the system. For any fixed point P along this ray, the straight coordinate lines q_1 and q_2 are mutually perpendicular and situated in the plane normal to the ray at P. It follows that the ray Ψ itself is specified by $q_1 = q_2 = 0$ and that the coordinate plane q_3=const is tangent to the wavefront. Figure modified from Červený (2001).

with the scale factor

$$h = 1 + \kappa_1(s)q_1 + \kappa_2(s)q_2 \,. \tag{2.25}$$

For the slowness vector in ray-centered coordinates we can write

$$\vec{\nabla}\tau = \left(\frac{\partial \tau}{\partial q_1}, \frac{\partial \tau}{\partial q_2}, h^{-1}\frac{\partial \tau}{\partial s} \right)^T \,. \tag{2.26}$$

The superscript T denotes transposition. Inserting this into equations (2.14) for a general velocity v results in the eikonal equation in ray-centered coordinates

$$p_1{}^2 + p_2{}^2 + h^{-2}p_3{}^2 = v^{-2} \,, \tag{2.27}$$

where $p_i := \partial \tau / \partial q_i$ and, thus, is in general not identical to the components of the slowness vector (2.26).

The number of equations in the associated ray-tracing system

$$\frac{d\vec{q_i}}{ds} = \frac{\partial \mathcal{H}}{\partial p_i}, \quad \frac{dp_i}{ds} = -\frac{\partial \mathcal{H}}{\partial q_i}, \quad \text{with} \quad i = 1, 2, 3 \,, \tag{2.28}$$

can be reduced from six to four by using the eikonal equation to eliminate one of the three equations for p_i and by taking the arclength s to be equal to x_3.

Solving equation (2.27) for p_3 yields so-called reduced Hamiltonian $\hat{\mathcal{H}}$:

$$p_3 = h \sqrt{\frac{1}{v_2} - p_1{}^2 - p_2{}^2} := -\hat{\mathcal{H}}(q_1, q_2, q_3, p_1, p_2) \,. \tag{2.29}$$

With the reduced Hamiltonian $\hat{\mathcal{H}}$ we can establish a new formulation for $\mathcal{H}$ given by

$$\mathcal{H} = p_3 + \hat{\mathcal{H}} = 0 \, . \tag{2.30}$$

Inserting $\mathcal{H}$ into ray-tracing system (2.28) yields the reduced ray-tracing system

$$\frac{d\vec{q}_I}{ds} = \frac{\partial \hat{\mathcal{H}}}{\partial p_I} \, , \quad \frac{dp_I}{ds} = -\frac{\partial \hat{\mathcal{H}}}{\partial q_I} \, , \quad \text{with} \quad I = 1, 2 \, . \tag{2.31}$$

Due to the condition $\partial q_3 / \partial s = 1$, the coordinate q_3 is equal to the arclength s along the ray, and p_3 can be directly calculated from $p_3 = -\hat{\mathcal{H}}$. The reduced ray-tracing system can be used, in case q_3 varies strictly monotonously along the ray, i. e., if the ray has no turning point with respect to the q_3 direction.

In ray-centered coordinates, the right hand side of the above equations must vanish, since the coordinate system is attached to an already known ray with the coordinates $q_1 = q_2 \equiv 0$ and $p_1 = p_2 \equiv 0$. From this condition $\kappa_1(s)$ and $\kappa_2(s)$ can be obtained:

$$\kappa_I(s) = \frac{1}{V} V_I \, , \tag{2.32}$$

where $V = v|_{(0,0,s)}$ and $V_I = \frac{\partial v}{\partial q_I}|_{(0,0,s)}$.

The scaling factor h now reads

$$h = [1 + V_{-1}(V_1 q_1 + V_2 q_2)] \, . \tag{2.33}$$

Please note: unit vectors $\vec{e}_i$ have very important properties for the description of seismic wave fields in inhomogeneous isotropic media. Among others, they determine the direction of the displacement vector and, thus, the polarization of high-frequency seismic body waves propagation in laterally varying isotropic structures.

2.2.2 Paraxial ray-tracing

In the ray-centered coordinate system the phase-space coordinates q_I, p_I of a ray in the close vicinity of a known central ray ($q_{I_0} = 0$ and $p_{I_0} = 0$) are given by

$$q_I = q_{I_0} + \Delta q_{I_0} = \Delta q_{I_0} \quad \text{and} \quad p_I = p_{I_0} + \Delta p_{I_0} = \Delta p_{I_0} \, . \tag{2.34}$$

This so-called paraxial ray can be described by a second order approximation of the eikonal equation around the central ray. Inserting (2.34) into the Hamiltonian system (2.31) of the central ray and expanding the right hand side of (2.31) into a Taylor series up to the first order leads to the linear system of equations

$$\begin{aligned}
\frac{d\Delta q_{I_0}}{ds} &= \sum_{J=1}^{2} \left(\frac{\partial^2 \mathcal{H}}{\partial p_I \partial q_J} \Delta q_{J_0} + \frac{\partial^2 \mathcal{H}}{\partial p_I \partial p_J} \Delta p_{J_0} \right) , \\
\frac{d\Delta p_{I_0}}{ds} &= - \sum_{J=1}^{2} \left(\frac{\partial^2 \mathcal{H}}{\partial q_I \partial q_J} \Delta q_{J_0} + \frac{\partial^2 \mathcal{H}}{\partial q_I \partial p_J} \Delta p_{J_0} \right) .
\end{aligned} \tag{2.35}$$

Finally, inserting equations (2.29) and (2.30) into equations (2.35) and substituting Δq_{I_0} and Δp_{I_0} by q_I and p_I yields the paraxial ray-tracing system in ray-centered coordinates

$$\frac{dq_I}{ds} = v p_I \, , \quad \frac{dp_I}{ds} = -v^{-2} \frac{\partial v}{\partial q_1 \partial q_I} q_J \, . \tag{2.36}$$
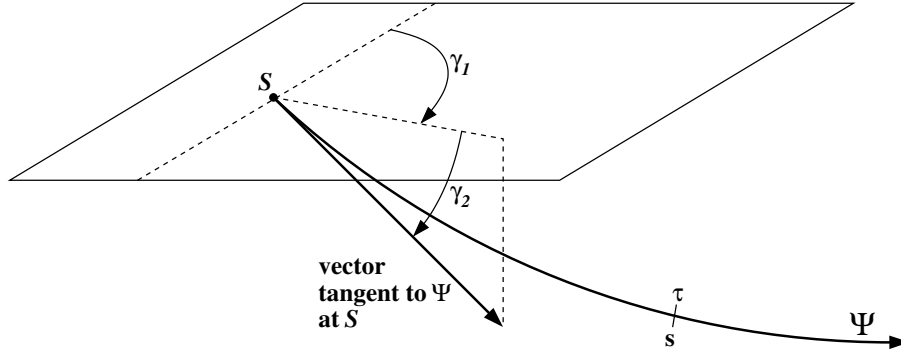
Figure 2.2: Definition of ray coordinates: for a wavefront emanating from a point source at S, an arbitrary ray of the associated ray field can by specified by the two ray parameters γ_1 and γ_2, defined, e. g., as the two take-off angles in S. The traveltime τ, the arclength s, or any other parameter varying monotonically along the ray Ψ can be chosen for γ_3. Figure modified from Koglin (2005).

Alternatively, system (2.35) can be written in the more compact form

$$\frac{d\vec{\eta}}{ds} = \underline{\underline{S}}\vec{\eta}, \tag{2.37}$$

by introducing

$$\vec{\eta} = (q_1, q_2, p_1, p_2)^T \quad \text{and} \quad \underline{\underline{S}} = \begin{pmatrix} \mathbf{O} & v^2\mathbf{I} \\ -v^{-1}\mathbf{V} & \mathbf{O} \end{pmatrix}, \tag{2.38}$$

where the submatrices of the so-called system matrix $\underline{\underline{S}}$ are $V_{IJ} = \frac{\partial^2 v}{\partial q_1 \partial q_J}|_{(0,0,s)}$, the identity matrix $I_{IJ} = \delta_{IJ}$, and the zero matrix $0_{IJ} = 0$.

2.2.3 Dynamic ray-tracing

Dynamic ray-tracing in ray centered coordinates aims at calculating the first partial derivatives of phase-space coordinates q_I and p_I along a known central ray with respect to its initial parameters. As initial parameters, e. g., the phase-space coordinates at the initial point of the central ray can be chosen or, as will be done in the following, the so-called *ray-parameters* γ_1 and γ_2. For a point source the latter might be chosen as two take-off angles at the source as depicted in Figure 2.2. Alternatively, for a propagating wavefront for which the corresponding rays are perpendicular in isotropic media, γ_1 and γ_2 could, e. g., specify the curvilinear coordinates of a point at this wavefront. Due to the fact that the partial derivative $\partial/\partial\gamma$ commutes with d/ds we easily obtain from the paraxial ray-tracing system (2.36) the dynamic ray-tracing system

$$\frac{d}{ds}\left(\frac{\partial q_I}{\partial \gamma}\right) = v\frac{\partial p_I}{\partial \gamma}, \quad \frac{d}{ds}\left(\frac{\partial p_I}{\partial \gamma}\right) = -v^{-2}\frac{\partial v}{\partial q_I \partial q_J}\frac{\partial q_I}{\partial \gamma}. \tag{2.39}$$

Using again the system matrix $\mathbf{S}$ and introducing the two transformation matrices $\mathbf{Q}$ and $\mathbf{P}$

$$Q_{IJ} = \frac{\partial q_I}{\partial \gamma_I}, \quad P_{IJ} = \frac{\partial p_I}{\partial \gamma_I}, \tag{2.40}$$

the dynamic ray-tracing system (2.39) can be written as

$$\frac{d}{ds}\left(\begin{array}{c}\mathbf{Q}\\ \mathbf{P}\end{array}\right) = \underline{\mathbf{S}}\left(\begin{array}{c}\mathbf{Q}\\ \mathbf{P}\end{array}\right). \tag{2.41}$$

If we compare system (2.41) to the paraxial ray-tracing system (2.37) we find that they are identical in form, but describe different properties.

2.2.4 The ray propagator matrix

For a linear system of equations such as the paraxial ray-tracing system (2.37) a general solution can be formulated in terms of a fundamental matrix, as long as the latter is not singular for any s along the central ray. In this case, we can introduce the 4x4 integral matrix $\underline{\underline{\mathbf{\Pi}}}(s, s_0)$ which satisfies the condition $\underline{\underline{\mathbf{\Pi}}}(s_0, s_0) = \underline{\mathbf{I}}$, the 4x4 identity matrix, and solves

$$\frac{d}{ds}\underline{\underline{\mathbf{\Pi}}} = \underline{\underline{\mathbf{S}\mathbf{\Pi}}}. \tag{2.42}$$

By means of this so-called ray-propagator matrix we can write a solution of equation (2.37) for any initial condition $\Delta\eta(s_0)$ as

$$\eta(s) = \underline{\underline{\mathbf{\Pi}}}(s, s_0)\eta(s_0). \tag{2.43}$$

It is shown, e. g., in Červený (2001) that the ray-propagator matrix $\underline{\underline{\mathbf{\Pi}}}$ can be composed of two of the four independent solutions of equation (2.41) as

$$\underline{\underline{\mathbf{\Pi}}}(s - s_0) = \left(\begin{array}{cc}\mathbf{Q_1}(s, s_0) & \mathbf{Q_2}(s, s_0)\\ \mathbf{P_1}(s, s_0) & \mathbf{P_2}(s, s_0)\end{array}\right). \tag{2.44}$$

The submatrices $(\mathbf{Q_1}, \mathbf{P_1})^T$ of the ray-propagator matrix $\underline{\underline{\mathbf{\Pi}}}$ solve system (2.41) for the initial conditions $(\mathbf{I_2}, \mathbf{O_2})$, known in case of ray-centered coordinates as *normalized plane wave initial conditions*. $(\mathbf{Q_2}, \mathbf{P_2})^T$ is a solution for the so called *normalized point source* initial conditions $(\mathbf{O_1}, \mathbf{I_1})$.

A similar formulation in the global Cartesian coordinate system called the surface-to-surface ray propagator matrix $\underline{\mathbf{T}}$ was presented by Bortfeld (1989). The mutual relationship between the $\underline{\mathbf{T}}$ and the $\underline{\underline{\mathbf{\Pi}}}$ matrix was discussed in Hubral et al. (1992). Some useful properties of these matrices, namely their symplecticity, the so-called chain rule, and their associated inverse ray propagator matrices, are given in Červený (2001).

The elements P_{IJ} of matrix $\mathbf{P}$ can be written as

$$P_{IJ} = \frac{\partial p_I}{\partial \gamma_J} = \sum_{K=1}^{2}\frac{\partial p_I}{\partial q_K}\frac{q_K}{\gamma_J} = \sum_{K=1}^{2}\frac{\partial^2 \tau}{\partial q_I \partial q_K}\frac{q_K}{\gamma_J} = \sum_{K=1}^{2}M_{IK}Q_{KJ}, \tag{2.45}$$

where $\mathbf{M} = \mathbf{P}\mathbf{Q}^{-1}$ is the matrix of the second derivatives of traveltime with respect to q_1 and q_2.
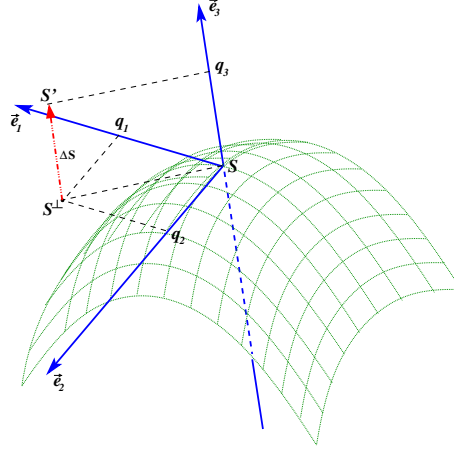
Figure 2.3: A wavefront (depicted in green) that propagates in $\vec{e}_3$-direction and crosses the point $S(0,0,s)$ on the central ray at the traveltime $\tau(S)$. The tangent plane spanned by the ray-centered unit vectors $\vec{e}_1$ and $\vec{e}_2$ contains the point $S^\perp(q_1,q_2,s)$ on a paraxial ray where the wavefront crosses at time $\tau(S^\perp)$. The point $S'(q_1,q_2,s+\Delta s)$ will be reached by the wavefront at time $\tau(S')$. Figure modified from Zhang (2003).

2.3 Paraxial traveltimes

In the vicinity of a central ray it is, of course, possible to determine an exact solution for rays and their traveltimes by standard ray-tracing. However, this demands the full knowledge of the subsurface structure. For practical reasons, we are only interested in approximate solutions for paraxial rays and their traveltimes that can be calculated from properties along the central ray, only. For this purpose we derived how the 2×2 matrix $\mathbf{M}(\mathbf{s})$ can be computed in terms of the 2×2 matrices $\mathbf{Q}(s)$ and $\mathbf{P}(s)$ and how matrices $\mathbf{Q}(s)$ and $\mathbf{P}(s)$ can be calculated by dynamic ray-tracing. Assuming the matrix $\mathbf{M}(s)$ to be known along the central ray a simple quadratic expansion of traveltime $\tau(q_1,q_2,s)$ can be established:

$$\tau(q_1,q_2,s) = \tau(0,0,s) + \frac{1}{2}\vec{q}^T\mathbf{M}(s)\vec{q} \quad \text{with} \quad \vec{q} = (q_1,q_2)^T , \tag{2.46}$$

in which the linear term vanishes as the wavefront is perpendicular to the central ray (see Figure 2.3).

In the following, we will modify equation (2.46) in order to obtain a more flexible and efficient quadratic expansion of traveltime $\tau(q_1,q_2,q_3)$ not only in q_1 and q_2 but also in q_3 direction.

For this purpose we consider a point S' with the ray-centered coordinates $(q_1,q_2,s+\Delta s)^T$ in the close vicinity of the central ray, i.e., $q_1 \neq 0$ and $q_2 \neq 0$. Then, the traveltime along a paraxial ray passing through point S' can be approximated from the traveltime at a point S with the ray-centered coordinates $(0,0,s)^T$ as

$$\tau(S') = \tau(S) + \left.\frac{\partial\tau}{\partial q_I}\right|_S q_I + \left.\frac{\partial\tau}{\partial s}\right|_S \Delta s + \frac{1}{2}\left.\frac{\partial^2\tau}{\partial q_I\partial q_I}\right|_S q_I q_I + \frac{1}{2}\left.\frac{\partial^2\tau}{\partial s^2}\right|_S \Delta s^2 . \tag{2.47}$$

From the definition of ray-centered coordinates follows that the projection of the slowness vector onto the plane tangent to the wavefront has to vanish, i.e.,

$$\left.\frac{\partial\tau}{\partial q_I}\right|_S = 0 . \tag{2.48}$$

27

Consequently, the first and second derivatives of τ with respect to s in S read

$$\left.\frac{\partial \tau}{\partial s}\right|_S = \frac{1}{v(S)} \qquad \text{and} \qquad \left.\frac{\partial^2 \tau}{\partial s^2}\right|_S = -\frac{1}{v^2(S)}\frac{\partial v(S)}{\partial s}. \tag{2.49}$$

Inserting equations (2.48) and (2.49) into equation (2.47) and taking the definition of $\mathbf{M}$ as the matrix of the second derivatives of τ with respect to q_I (see equation (2.45)) into account we finally obtain for the paraxial traveltime in the vicinity of S:

$$\tau(S') = \tau(S) + \frac{1}{v(S)}\Delta s - \frac{1}{2v^2(S)}\frac{\partial v(S)}{\partial s}\Delta s^2 + \frac{1}{2}m_{IJ}(S)q_I q_J. \tag{2.50}$$

2.3.1 Paraxial traveltimes in local ray-centered Cartesian coordinates

Ray-centered coordinates are well suited for the theoretical description of the properties of paraxial rays as they provide results in a compact form that is easy to comprehend. However, for the practical implementation Cartesian coordinates are often demanded since they are more flexible and numerically very efficient. Therefore, we establish a local ray-centered Cartesian coordinate system y_1, y_2, y_3 with origin in S. According to to Figure 2.4 the unit vectors $\vec{j}_1$, $\vec{j}_2$, and $\vec{j}_3$ of the local ray-centered Cartesian coordinate system are chosen to be identical with the unit vectors $\vec{e}_1$, $\vec{e}_2$, and $\vec{e}_3$ of the ray-centered coordinate system in S and the coordinates of point S' in the vicinity of S are given by

$$\left.\vec{r}(\vec{y})\right|_{S'} = \left.\vec{r}\right|_S + y_1\vec{j}_1 + y_2\vec{j}_2 + y_3\vec{j}_3, \tag{2.51}$$

with $\left.\vec{r}\right|_S$ denoting the position of the origin S.

It follows from equations (2.23) and (2.24) that $ds = h^{-1}dy_3$. Consequently, we find

$$\frac{\partial}{\partial s} = h\frac{\partial}{\partial y_3}, \qquad \Delta s = h^{-1}y_3 \approx \left(1 - \frac{1}{v}\frac{\partial v}{\partial y_I}\right)y_I y_3, \qquad \Delta s^2 \approx y_3^2, \qquad \text{and} \qquad m_{IJ}^{(y)} = m_{IJ}. \quad (2.52)$$

Substituting these relations into equation (2.50) yields for the paraxial traveltimes in ray-centered Cartesian coordinates

$$\tau(S') = \tau(S) + \frac{1}{v(S)}y_3 - \frac{1}{2v^2(S)}\frac{\partial v(S)}{\partial y_3}y_3^2 - \frac{1}{v^2(S)}\frac{\partial v(S)}{\partial y_I}y_I y_3 + \frac{1}{2}m_{ij}(S)y_I y_J. \tag{2.53}$$

Alternatively, this can be expressed in matrix and vector notation:

$$\tau(S') = \tau(S) + \vec{y}^T\vec{p}^{(y)}(S) + \frac{1}{2}\vec{y}^T\underline{\mathbf{M}}^{(y)}(S)\vec{y}, \tag{2.54}$$

using

$$\vec{p}^{(y)}(S) = \begin{pmatrix} p_1^{(y)}(S) \\ p_2^{(y)}(S) \\ p_3^{(y)}(S) \end{pmatrix} = \begin{pmatrix} 0 \\ 0 \\ \frac{1}{v(S)} \end{pmatrix}, \tag{2.55}$$

and

$$\underline{\mathbf{M}}^{(y)}(S) = \left.\begin{pmatrix} m_{11}^{(y)} & m_{12}^{(y)} & -\frac{1}{v^2}\frac{\partial v}{\partial y_1} \\ m_{21}^{(y)} & m_{22}^{(y)} & -\frac{1}{v^2}\frac{\partial v}{\partial y_2} \\ -\frac{1}{v^2}\frac{\partial v}{\partial y_1} & -\frac{1}{v^2}\frac{\partial v}{\partial y_2} & -\frac{1}{v^2}\frac{\partial v}{\partial y_3} \end{pmatrix}\right|_S. \tag{2.56}$$
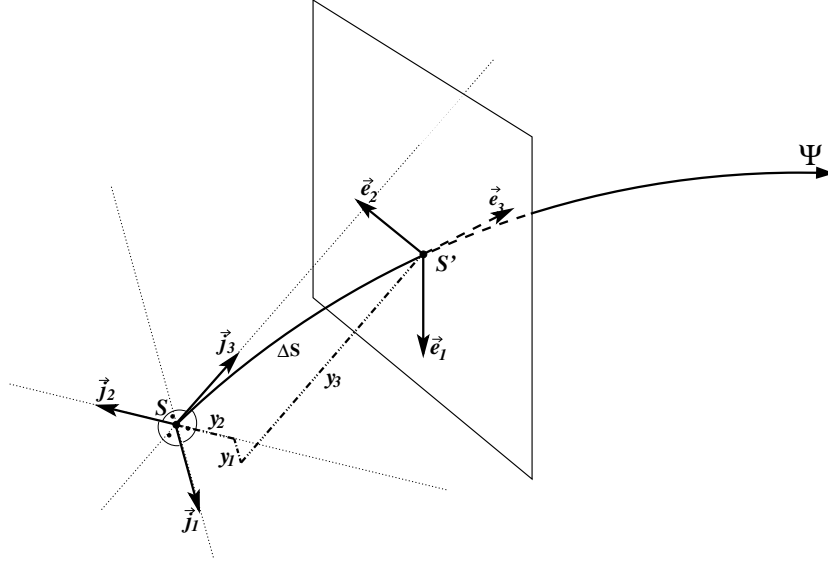
Figure 2.4: In the origin $S(0,0,0)^T$ the unit vectors $\vec{j}_1$, $\vec{j}_2$, and $\vec{j}_3$ of the local ray-centered Cartesian coordinates and the unit vectors $\vec{e}_1$, $\vec{e}_2$, and $\vec{e}_3$ of the ray-centered coordinate system are identical. Point S' has the local ray-centered Cartesian coordinates $(y_1, y_2, y_3)^T$ whereas its local ray-centered Cartesian coordinates read $(q_1, q_2, s + \Delta s)^T$. The quantities y_1, y_2, and y_3 are depicted as dash-dotted, dash-double-dotted, and dash-triple-dotted lines, respectively. Figure modified from Koglin (2005).

2.3.2 The two-point eikonal

In reflection seismics sources and receivers are usually located at the same measurement surface. A wave, emitted from a source at the surface travels along a ray downwards until it is reflected and starts its way back to the surface were it is finally recorded at a receiver. The ray propagator matrix $\mathbf{\Pi}$ derived in Section 2.2.4 connects the properties of the ray field and traveltime field at different points of the central ray. Due to the so-called chain rule (see Červený, 2001) we can find a ray-propagator matrix for the whole raypath from source to receiver, i.e., for both the downgoing and the upgoing parts. Thus, a reflection point has not to be considered explicitly to establish a formula that approximately describes the traveltime difference (moveout) between a central ray from S to R and a paraxial ray S' and R' in its vicinity.

From Figure 2.5 we obtain for the traveltime difference between the central and the paraxial ray

$$
\begin{aligned}
\Delta\tau &= \Delta\tau(R, R') - \Delta\tau(S, S') \\
&= (\tau(R') - \tau(R)) - (\tau(S') - \tau(S)) .
\end{aligned}
\tag{2.57}
$$

Using equation (2.53) to express the traveltimes in $S, S', R,$ and R' in equation (2.57) yields for the traveltime moveout in local ray-centered Cartesian coordinates:

$$
\begin{aligned}
\Delta\tau =\ & \left(\frac{y_3(R')}{v(R)} - \frac{1}{2v^2(R)} \frac{\partial v(R)}{\partial y_3} y_3(R')^2 - \frac{1}{v^2(R)} \frac{\partial v(R)}{\partial y_I} y_I(R') y_3(R') + \frac{1}{2} y_I(R') y_J(R') m_{IJ}(R) \right) \\
& - \left(\frac{y_3(S')}{v(S)} - \frac{1}{2v^2(S)} \frac{\partial v(S)}{\partial y_3} y_3(S')^2 - \frac{1}{v^2(S)} \frac{\partial v(S)}{\partial y_I} y_I(S') y_3(S') + \frac{1}{2} y_I(S') y_J(S') m_{IJ}(S) \right) .
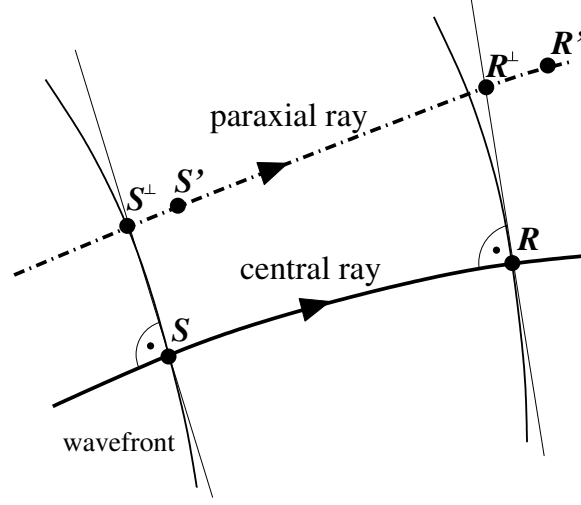\end{aligned}
\tag{2.58}
$$

29

Figure 2.5: Paraxial ray from S' to R' in the vicinity of the central ray from S to R. $S^\perp$ and $R^\perp$ are the intersection points of the paraxial ray with a plane tangent to the wavefront in S and R, respectively.

The ray propagator matrix $\mathbf{\Pi}$ is assumed to be known along the central ray from S to R. For a point source in S matrix $\mathbf{\Pi}$ at R has the following form:

$$\underline{\underline{\mathbf{\Pi}}}(S,R) = \begin{pmatrix} \mathbf{Q_1}(S,R) & \mathbf{Q_2}(S,R) \\ \mathbf{P_1}(S,R) & \mathbf{P_2}(S,R) \end{pmatrix}. \tag{2.59}$$

Considering $S^\perp$ and $R^\perp$, the intersection points of the paraxial ray with the tangent plane to the wavefront passing through S and R, matrix $\mathbf{\Pi}$ provides a linear relationship between the phase-space coordinates $\vec{q}(S^\perp)$, $\vec{p}(S^\perp)$ and $\vec{q}(R^\perp)$, $\vec{p}(R^\perp)$ that reads

$$\begin{pmatrix} \vec{q}(R^\perp) \\ \vec{p}(R^\perp) \end{pmatrix} = \underline{\underline{\mathbf{\Pi}}}(S,R) \begin{pmatrix} \vec{q}(S^\perp) \\ \vec{p}(S^\perp) \end{pmatrix}, \tag{2.60}$$

or after inserting relation (2.59)

$$\vec{q}(R^\perp) = \mathbf{Q}_1\vec{q}(S^\perp) + \mathbf{Q}_2\vec{p}(S^\perp) \qquad \text{and} \qquad \vec{p}(R^\perp) = \mathbf{P}_1\vec{q}(S^\perp) + \mathbf{P}_2\vec{p}(S^\perp). \tag{2.61}$$

According to Section 2.2.4, the first term on the right hand side of both equations has to vanish for a point source at S and the matrix of second derivatives of traveltimes at R due to the point source at S can be written as

$$m_{IJ}(S,R) = \frac{\partial p_I(R^\perp)}{\partial p_K(S^\perp)} \frac{\partial p_K(S^\perp)}{\partial q_J(R^\perp)} = \left(\mathbf{P}_2\mathbf{Q}_2^{-1}\right)_{IJ}, \tag{2.62}$$

if we choose p_1 and p_2 as the initial ray coordinates at $S^\perp$. Vice versa, we find for the matrix of the second derivatives of traveltime at S due to a point source at R

$$m_{IJ}(R,S) = \frac{\partial p_I(S^\perp)}{\partial p_K(R^\perp)} \frac{\partial p_K(R^\perp)}{\partial q_J(S^\perp)} = \left(\mathbf{Q}_1\mathbf{Q}_2^{-1}\right)_{IJ} = \left(\mathbf{Q}_2^{-1}\mathbf{Q}_1\right)_{IJ}. \tag{2.63}$$

Using equations (2.61), (2.62), and (2.63) we can express the slowness in $R^\perp$ and $S^\perp$ in the following way:

$$\vec{p}(S^\perp) = -\mathbf{M}(R,S)\,\vec{y}(S^\perp)\mathbf{Q}_2\,\vec{y}(R^\perp) \qquad \text{and} \tag{2.64a}$$

$$\vec{p}(R^\perp) = -\mathbf{Q}_2^{-1T}\vec{y}(S^\perp) + \mathbf{M}(S,R)\,\vec{y}(R^\perp). \tag{2.64b}$$

According to equation (2.46) the slowness vectors in $S^\perp$ and $R^\perp$ can be approximated by

$$p_I(S^\perp) = \frac{\partial \tau(S^\perp)}{\partial q_I} = \frac{\partial \tau(S^\perp)}{\partial y_I} \approx m_{IJ}(S)\, y_J \qquad \text{and} \qquad (2.65a)$$

$$p_I(R^\perp) = \frac{\partial \tau(R^\perp)}{\partial q_I} = \frac{\partial \tau(R^\perp)}{\partial y_I} \approx m_{IJ}(R)\, y_J \,. \qquad (2.65b)$$

Substituting in equation (2.58) the right hand sides of equations (2.65a) and (2.65b) by the left hand sides of equations (2.64a) and (2.64b) yields for the traveltime moveout of the paraxial ray

$$
\begin{aligned}
\Delta\tau = \;& \left(\frac{y_3(R')}{v(R)} - \frac{1}{2v^2(R)} \frac{\partial v(R)}{\partial y_3} y_3(R')^2 - \frac{1}{v^2(R)} \frac{\partial v(R)}{\partial y_I} y_I(R')\, y_3(R') \right) \\
& - \left(\frac{y_3(S')}{v(S)} - \frac{1}{2v^2(S)} \frac{\partial v(S)}{\partial y_3} y_3(S')^2 - \frac{1}{v^2(S)} \frac{\partial v(S)}{\partial y_I} y_I(S')\, y_3(S') \right) \\
& + \tfrac{1}{2} y_I(R')\, m_{IJ}(S,R)\, y_J(R') + \tfrac{1}{2} y_I(S')\, m_{IJ}(R,S)\, y_J(S') \\
& - \tfrac{1}{2} y_I(R') \left(\mathbf{Q}_2^{-1T} \right)_{IJ} y_J(S') - \tfrac{1}{2} y_I(S') \left(\mathbf{Q}_2^{-1T} \right)_{IJ} y_J(R')
\end{aligned}
\qquad (2.66)
$$

Alternatively, we can combine the last two terms by introducing the 4x4 matrix $\mathbf{R}$ and re-write this equation in vector and matrix notation:

$$
\begin{aligned}
\Delta\tau = \;& \vec{y}^T(R')\, \vec{p}^{(y)}(R) - \vec{y}^T(S')\, \vec{p}^{(y)}(S) \\
& + \tfrac{1}{2} \vec{y}^T(R')\, \underline{\mathbf{M}}(S,R)\, \vec{y}(R') + \tfrac{1}{2} \vec{y}^T(S')\, \underline{\mathbf{M}}(R,S)\, \vec{y}(S') \\
& - \vec{y}^T(S')\, \underline{\mathbf{R}}(S,R)\, \vec{y}(R') \,,
\end{aligned}
\qquad (2.67)
$$

with

$$
\underline{\mathbf{M}}(S,R) = \begin{pmatrix} m_{11}(S,R) & m_{12}(S,R) & -\frac{1}{v^2(R)}\frac{\partial v(R)}{\partial y_1} \\ m_{21}(S,R) & m_{22}(S,R) & -\frac{1}{v^2(R)}\frac{\partial v(R)}{\partial y_2} \\ -\frac{1}{v^2(R)}\frac{\partial v(R)}{\partial y_1} & -\frac{1}{v^2(R)}\frac{\partial v(R)}{\partial y_2} & -\frac{1}{v^2(R)}\frac{\partial v(R)}{\partial y_3} \end{pmatrix}, \qquad (2.68a)
$$

$$
\underline{\mathbf{M}}(R,S) = \begin{pmatrix} m_{11}(R,S) & m_{12}(R,S) & -\frac{1}{v^2(S)}\frac{\partial v(S)}{\partial y_1} \\ m_{21}(R,S) & m_{22}(R,S) & -\frac{1}{v^2(S)}\frac{\partial v(S)}{\partial y_2} \\ -\frac{1}{v^2(S)}\frac{\partial v(S)}{\partial y_1} & -\frac{1}{v^2(S)}\frac{\partial v(S)}{\partial y_2} & -\frac{1}{v^2(S)}\frac{\partial v(S)}{\partial y_3} \end{pmatrix}, \text{ and} \qquad (2.68b)
$$

$$
\underline{\mathbf{R}}(S,R) = \begin{pmatrix} \mathbf{Q}_2^{-1} & & 0 \\ & & 0 \\ 0 & 0 & 0 \end{pmatrix}. \qquad (2.68c)
$$

2.3.3 The two-point eikonal in local Cartesian coordinates

For practical applications it is most convenient to express the two-point eikonal in right handed local Cartesian coordinates (x_1, x_2, x_3) in which the x_3 axis points in opposite depth direction. As depicted in Figure 2.6 we establish such a coordinate system both at the source point S and at the receiver point R of the central ray. Compared to the local ray-centered Cartesian coordinate systems, the local Cartesian coordinate systems are rotated by the two azimuth angles of the central ray at S and R, respectively. The azimuth angles in S might be denoted by β_S, θ_S and those in R by β_R, θ_R.
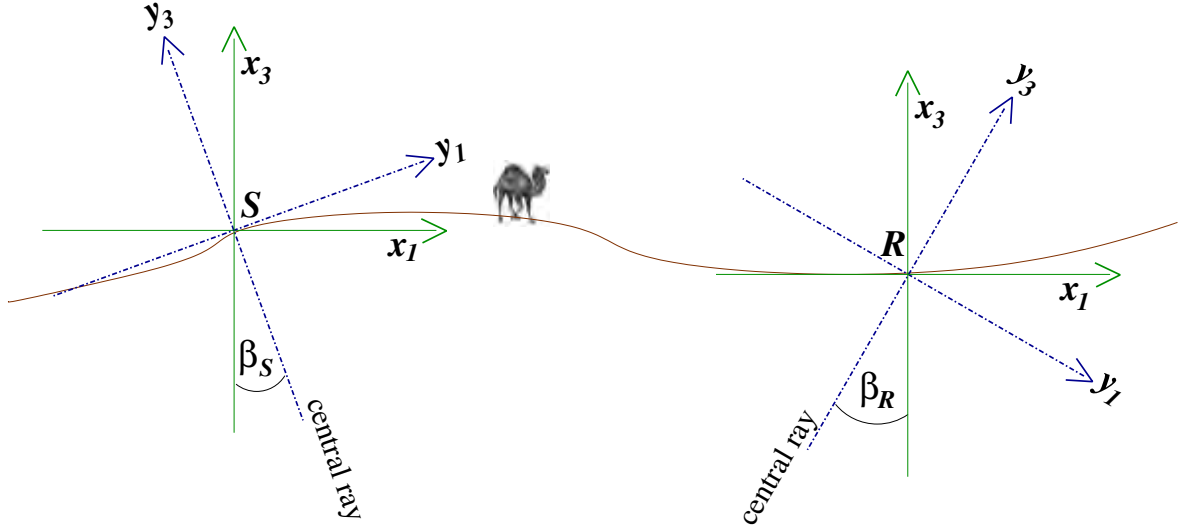
Figure 2.6: Local Cartesian coordinate system in S and R with x_3 axis pointing in opposite depth direction compared to the associated local ray-centered Cartesian coordinate systems. For the sake of simplicity, the y_2 and x_2 axes are omitted. The emergence angles β_S and β_R are measured counter-clockwise with respect to the x_3 axis. In the depicted case β_S has a positive value and β_R a negative one.

Introducing the two rotation matrices

$$\underline{\mathbf{D}}(S) = \begin{pmatrix} \cos\theta_S \cos\beta_S & \sin\theta_S \cos\beta_S & \sin\beta_S \\ -\sin\theta_S & \cos\theta_S & 0 \\ \cos\theta_S \sin\beta_S & \sin\theta_S \sin\beta_S & -\cos\beta_S \end{pmatrix} \quad \text{and} \tag{2.69a}$$

$$\underline{\mathbf{D}}(R) = \begin{pmatrix} \cos\theta_R \cos\beta_R & \sin\theta_R \cos\beta_R & \sin\beta_R \\ -\sin\theta_R & \cos\theta_R & 0 \\ \cos\theta_R \sin\beta_R & \sin\theta_R \sin\beta_R & -\cos\beta_R \end{pmatrix}, \tag{2.69b}$$

the transformation matrices of S' and R' from local Cartesian ray-centered coordinates to the chosen local Cartesian coordinates read

$$\begin{pmatrix} y_1(S') \\ y_2(S') \\ y_3(S') \end{pmatrix} = \underline{\mathbf{D}}(S) \begin{pmatrix} x_1(S') \\ x_2(S') \\ x_3(S') \end{pmatrix} \quad \text{and} \quad \begin{pmatrix} y_1(R') \\ y_2(R') \\ y_3(R') \end{pmatrix} = \underline{\mathbf{D}}(R) \begin{pmatrix} x_1(R') \\ x_2(R') \\ x_3(R') \end{pmatrix}. \tag{2.70}$$

Applying this coordinate transformation to equation (2.67) finally yields the two-point eikonal in local Cartesian coordinates:

$$\begin{aligned} \tau(S',R') =& \ \tau(S,R) + \Delta\tau \\ =& \ \tau(S,R) + \vec{x}^T(R')\,\vec{p}^{(x)}(R) - \vec{x}^T(S')\,\vec{p}^{(x)}(S) \\ & + \tfrac{1}{2}\vec{x}^T(R')\,\underline{\mathbf{M}}^{(x)}(S,R)\,\vec{x}(R') \\ & + \tfrac{1}{2}\vec{x}^T(S')\,\underline{\mathbf{M}}^{(x)}(R,S)\,\vec{x}(S') \\ & - \vec{x}^T(S')\,\underline{\mathbf{R}}^{(x)}(S,R)(R)\,\vec{x}(R'), \end{aligned} \tag{2.71}$$

where the slowness vectors in local Cartesian coordinates, $\vec{p}^{(x)}(S)$ and $\vec{p}^{(x)}(R)$ are given by

$$\vec{p}^{(x)}(S) = \underline{\mathbf{D}}^T(S)\,\vec{p}^{(y)}(S) \qquad \text{and} \qquad \vec{p}^{(x)}(R) = \underline{\mathbf{D}}^T(R)\,\vec{p}^{(y)}(R)\,, \tag{2.72}$$

and the matrices $\underline{\mathbf{M}}^{(x)}$ and $\underline{\mathbf{R}}^{(x)}$ are calculated from

$$
\begin{aligned}
\underline{\mathbf{M}}^{(x)}(S,R) &= \underline{\mathbf{D}}^T(R)\,\underline{\mathbf{M}}(S,R)\,\underline{\mathbf{D}}(R)\,, & (2.73)\\
\underline{\mathbf{M}}^{(x)}(R,S) &= \underline{\mathbf{D}}^T(S)\,\underline{\mathbf{M}}(R,S)\,\underline{\mathbf{D}}(S)\,, & (2.74)\\
\underline{\mathbf{R}}^{(x)}(S,R) &= \underline{\mathbf{D}}^T(S)\,\underline{\mathbf{R}}(S,R)\,\underline{\mathbf{D}}(R)\,. & (2.75)
\end{aligned}
$$

Chapter 3

Common-Reflection-Surface stack for topography

The influence of the top-surface topography on the recorded traveltimes is one of the specific problems of land data processing. Besides this, sparse data coverage, a low signal-to-noise ratio, and complex geological structures at target depth as well as close to the measurement surface have to be handled. The very general formulation of the CRS stacking operator allows for a spatial aperture with large fold which makes this approach particularly suitable for complex onshore data. Conventional processing workflows typically apply surface consistent field static corrections, briefly discussed in the following, aiming at the removal of both the top-surface topography and the complex near-surface geology by relating the data to a horizontal reference level below the actual measurement surface. However, this approach tents to corrupt the extracted NMO velocities as well as the CRS attributes, if the assumption of vertical raypaths is not perfectly fulfilled between planar reference level and measurement surface. Thus, putting the focus on topography handling, two different 2D ZO CRS stacking operators that directly consider the top-surface topography will be derived in this chapter. For comparison, also the conventional 2D ZO CRS stack operator for a planar measurement surface, e. g., the marine case, will be rederived. As will be shown, the latter can serve as a kind of reduced stacking operator in case of smoothly curved topography—a property quite useful for the practical implementation presented in the next chapter.

3.1 Topography handling by field static corrections

The term field static correction has its roots in the early days of seismics. At that time such corrections were applied by the field crew during land-data acquisition in order to check the data quality and to facilitate a first interpretation. Today, field static corrections are part of the data preprocessing and usually denoted as datum or elevation static corrections. In most cases of marine data acquisition, it is not necessary to apply field statics since the low-velocity layer (LVL) at the sea bottom is usually thin and homogeneous and the ocean surface provides a planar measurement surface with virtually constant near-surface velocity. Nevertheless, in case of ocean bottom seismics (Yilmaz, 2001; Flueh et al., 2002; Boelsen and Mann, 2005) and conventional surveys in areas of rapidly changing water-bottom topography and/or very pronounced weathering layer, marine field static corrections are computed in
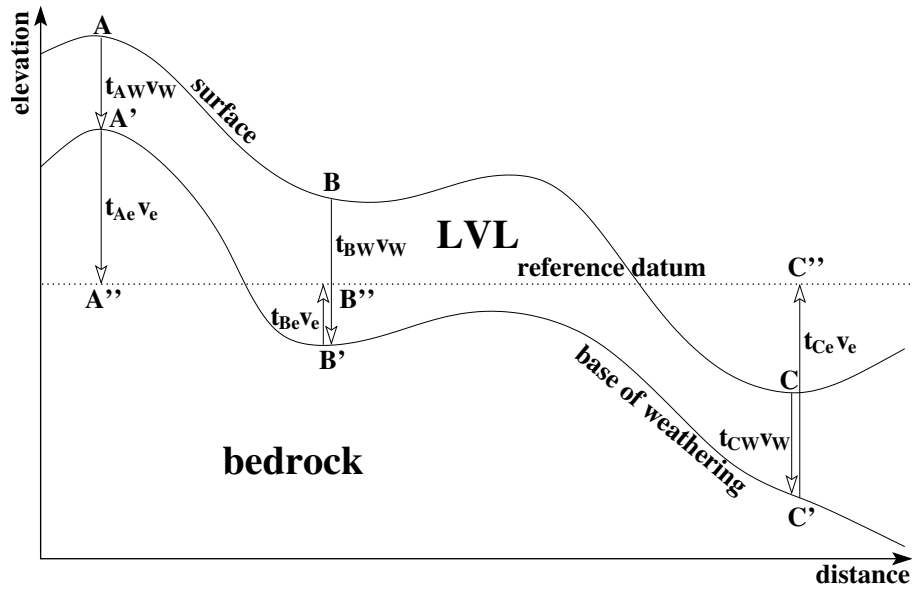
Figure 3.1: Field static corrections to a planar reference datum, depicted for the source or receiver locations A, B, and C, according to Koglin et al. (2006). The total static correction time related to a specific trace, e. g., with source location A and receiver location B is computed as the sum of the weathering corrections t_{AW} and t_{BW} and the elevation corrections t_{Ae} and t_{Be}. The weathering correction aims at eliminating the influence of the LVL and to relate the traveltimes to those measured at a floating datum that coincides with the base of the weathering layer (A', B', C'). Finally, elevation correction maps the traveltimes from this floating datum to a planar reference datum (A'', B'',C''). The wave propagation velocities of the weathering layer and of the underlying bedrock, v_w and v_e, as well as the depth of the weathering layer have to be determined by suitable methods like, e. g., refraction statics or uphole measurements.

analogy to the field static corrections for the onshore case. Figure 3.1 schematically shows how field static corrections are applied:

- in a first step, the influence of the weathering layer to the traveltimes is virtually removed by subtracting[1] for each trace a time shift that accounts for the vertical traveltime between acquisition surface and base of weathering. For this purpose it is necessary to know both the thickness and the average velocity of the weathering layer. The resulting traveltimes are then related to the base of weathering which is usually a floating datum.

- in a second step a new reference datum is introduced by subtracting for each trace a time shift that accounts for the vertical traveltime between the base of weathering and the chosen reference datum.

---

[1]There is no general agreement according to the sign convention of static correction time shifts. Throughout this thesis static corrections are subtracted which means that we have a positive value if the new source or receiver position is located below the original one and a negative value if it is located above.

Finally, the static correction time of a certain trace is given by the sum of the static correction times associated with its source and receiver locations. According to Figure 3.1 we find

$$t_{\text{fstat}}(AB) = t_{\text{AW}} + t_{\text{Ae}} + t_{\text{BW}} + t_{\text{Be}} = -\frac{\overline{AA'}}{v_w} - \frac{\overline{A'A''}}{v_e} - \frac{\overline{BB'}}{v_w} + \frac{\overline{B'B''}}{v_e} \,, \qquad (3.1)$$

where v_w and v_e are the wave propagation velocities of the weathering layer and the underlying bedrock and t_{AW}, t_{BW} and t_{Ae}, t_{Be} are the associated traveltimes within these two layers.

In many cases it is possible to choose a planar reference datum. However, there are two often antithetical conditions that should not be strongly violated:

1. the static corrections should be as small as possible to minimize the systematic error that is caused by the not perfectly vertical ray paths. On the first sight, it seems that subtraction of positive static time shifts produces traveltimes which are too large for non-zero offset, if the wave propagates obliquely through the top-layer and not perfectly vertical like the correction assumes. However, Figure 3.2 shows that it is also necessary to consider the consequence of keeping offset and midpoint fixed, which is implicitly included in the assumption of vertical emergence. Accordingly, subtracting the static correction Δt_{fstat} results for non-zero offset in too small instead of too large traveltimes. Since this error in general increases with offset, static corrections result in such a case in NMO velocities that are higher than those NMO velocities which would actually be measured at the new datum. Cox (1999) calls this error *residual NMO* which leads to a deviation of the hyperbolic relationship between the reflection traveltimes in the CMP gather and, thus, to incorrect NMO velocities (see also Profeta et al., 1995).

2. the reference datum should always be below the complex features of the near-surface geology, preferably atop constant velocity layers, in order to reduce the complexity of the measured wave-field.

If it is not possible to find an appropriate planar reference datum, e. g., because of large changes in elevation along the seismic line, a floating datum can be used for the processing but it has to be taken into account that in this case the NMO velocities are strongly influenced by the curvature of the floating datum (see Appendix C). There are several methods how to reduce this effect. One option is to split the static correction in one part which is applied before the NMO correction and one part which is applied afterwards. Before the NMO correction a time shift is applied to every trace in the CMP gather which is the difference between the individual time shift corresponding to a planar reference level and the average of this time-shift for all traces in the CMP gather. After the NMO correction the average time shift in the CMP gather is applied to the stacked trace resulting in a stack section which is related to a planar reference surface.

As will be shown in the following sections, the presented CRS stack approach can directly handle the top-surface topography problem. Thus, pure elevation statics are rendered unnecessary. However, the experience with complex real data sets, such as those presented in Chapter 7, has proven that the influence of a strongly variable near-surface geology cannot always be removed by residual static corrections, only. As a matter of fact, field static corrections are still necessary, if large static time shifts caused by strong near-surface inhomogeneities completely destroy the continuity of the seismic events in a certain area so that stacking fails there completely and as a consequence no basis for residual static correction exists. Furthermore, static time shifts, caused by large scale inhomogeneities in the near-surface, change smoothly along the line and therefor cannot be detected by residual static
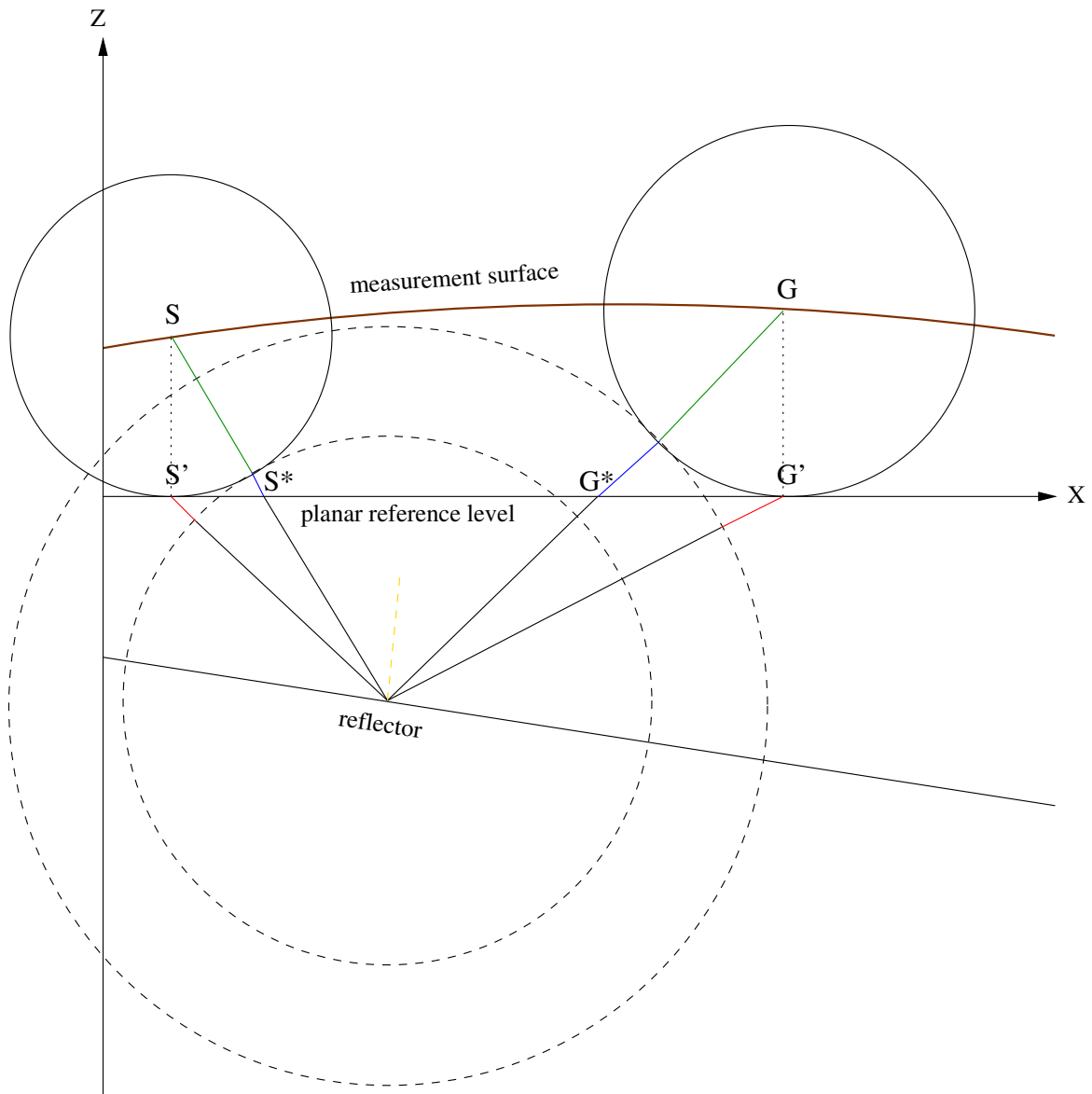
Figure 3.2: Visualization of the systematic traveltime error introduced by static corrections if the assumption of surface consistency is not fulfilled. Two homogeneous layers separated by a planar dipping reflector are depicted together with the surface consistent and not surface consistent field static corrections from the actual measurement surface to a planar reference level below. To visualize the static time shifts, distance and traveltime are displayed simultaneously assuming units in which the velocity has the value one. It can be observed that, on the one hand, the surface consistent static correction $t_{\text{fstat}} = t(S, S') + t(G, G')$ is, due to the non-vertical ray-path, too small (blue line segment) to obtain the traveltime $t^*(m^*, h^*)$ from S^* to G^*, the fictitious source and receiver locations at the new datum that pertain to the ray that joins S and G. However, on the other hand, the correction $t_{\text{fstat}} = t(S, S') + t(G, G')$ is too large (red line segment) to yield the searched-for traveltime $t'(m, h)$ from S' to G'. Since this error in general increases with offset, it leads to a deviation of the hyperbolic relationship between the reflection traveltimes in the CMP gather and, thus, to distorted NMO velocities.
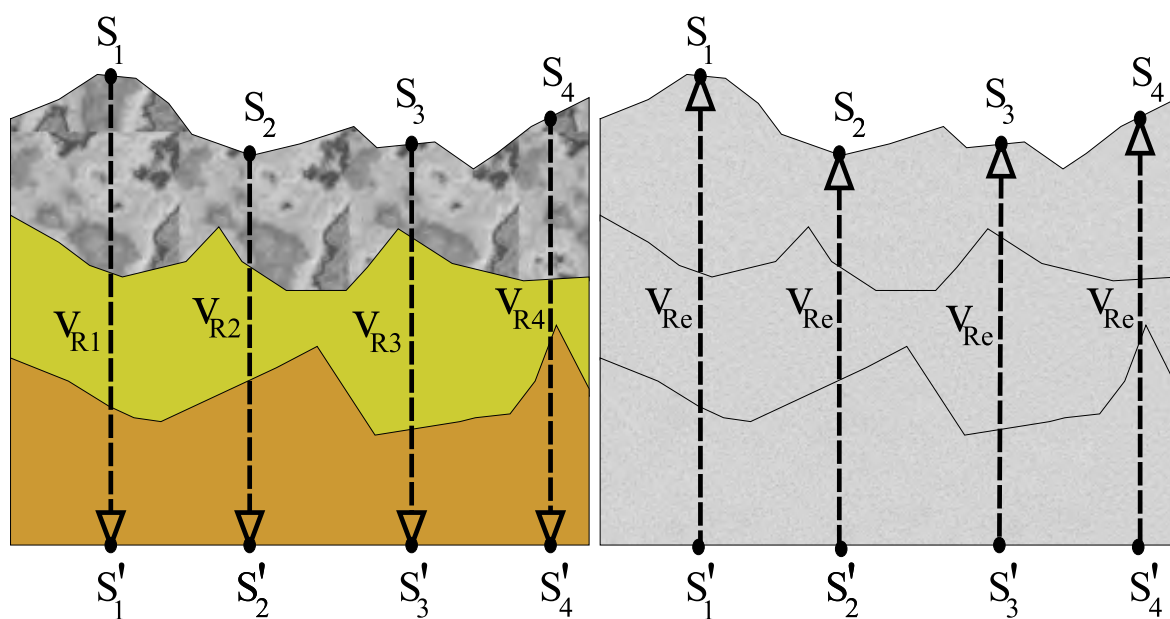
Figure 3.3: To restore the original topography after the application of field static corrections, inverse elevation statics are applied using a constant replacement velocity v_{Re} equal to the average value of those velocities used for the field-static correction ($v_{R1}, v_{R2}, v_{R3}, v_{R4}$).

corrections as they do not disturb the continuity of the wave field but influence shape and location of the imaged reflections, only. Thus, to omit field static corrections completely is only possible if the inhomogeneities in the near-surface are more or less randomly distributed and the resulting time-shifts are still small enough to allow the detection of at least some coherent events. In any other case field static corrections are necessary to remove the influence of the near-surface geology as far as possible before the processing itself can be started.

Now, the question remains, how the inhomogeneity of the near-surface geology can be removed by field static corrections without loosing the benefits one can achieve from processing directly from topography? The error which is introduced to the data by field static corrections, if the assumption of vertical ray paths is not completely met, was already discussed. As can be observed in Figure 3.2, it is a geometrical error that is caused by not considering the true emergence angle but assuming the ray to emerge vertically. Of course, if one would apply this static correction downwards to the planar reference level and afterwards back to the actual topography using the same velocity even the largest angle deviation would not matter. Consequently we can reduce this error at least to a certain extent if we restore the original geometry by going back to the actual topography with a velocity that does not differ too much from the velocity used for the static correction (e. g., the refractor-velocity). This process is illustrated in Figure 3.3 for a constant replacement velocity v_{Re}. If necessary also a laterally variable replacement velocity can be used that changes smoothly along the line. In fact, even a replacement velocity that differers at some locations about 50% from the velocity used for the field static correction still minimizes the error introduced to the NMO velocity and the CRS attributes.

3.2 CRS stack considering the top-surface topography

Today, 3D data acquisition and processing is frequently applied and has become routine for the oil companies and their contractors. Nevertheless, 2D acquisition is still in use. Particularly in onshore exploration, there are many cases were 2D surveys are conducted, e. g., due to economic reasons or because the topographic features or the infrastructure of the target area do not allow 3D surveys. In principle, a 3D survey is always required if the subsurface structure varies arbitrarily in all three dimensions. However, geologic structures, particularly in sedimentary basins, often exhibit a horizontal direction in which the medium parameters are virtually constant. Such a medium can be described by a so-called 2.5D model for which wave-propagation in a vertical plane of symmetry simplifies considerably. 2D acquisition should always be carried through along a line that lies within this plane to avoid the problem of out-of-plane reflections. Therefore, all 2D seismic imaging procedures are based on this assumption since only in this case, the observation plane coincides with the plane of symmetry and the 2.5D medium can be fully imaged. Otherwise, if the acquisition line is not parallel to the plane of symmetry the observation plane would be, in general, different for each point of the subsurface image.

In recent years, two different 2D CRS stacking operators that consider the top-surface topography have been proposed:

- Chira et al. (2001) and Heilmann (2002) assumed a smoothly curved measurement surface for which the elevation of all source and receiver points contributing to an individual stack trace can be approximated by a parabola. This approach is attractive from the computational point of view as it allows to adopt most parts of the conventional CRS stack implementation. In particular, the pragmatic attribute search strategy using three one-parameter searches to determine the optimal stacking operator can be maintained. However, small elevation statics are still required in order to relate the data to the chosen smoothly curved reference datum.

- Zhang (2003) presented a more general CRS stacking operator that directly considers the true elevation of every source and receiver. This approach demands far more computational effort, as at least two of the three attributes have to be searched for simultaneously due to the higher complexity of the stacking operator. On the other hand, no elevation statics are required and the elevations of the emergence points of the simulated zero-offset rays can be chosen—within certain limits—arbitrarily. A similar approach based on the methodology of *Multifocusing* was presented by Gurevich et al. (2001) and Al-Ali and Verschuur (2006).

In the following, I will rederive both stacking operators starting from the very general second order traveltime approximation (2.71) for paraxial rays in 3-D media, derived in Chapter 2 and here repeated for convenience:

$$
\begin{aligned}
\tau(S',R') = {} & \tau(S,R) + \Delta\tau \\
= {} & \tau(S,R) + \vec{x}^T(R')\,\underline{\mathbf{D}}^T(R)\,\vec{p}^{(y)}(R) - \vec{x}^T(S')\,\underline{\mathbf{D}}^T(S)\,\vec{p}^{(y)}(S) \\
& + \tfrac{1}{2}\vec{x}^T(R')\,\underline{\mathbf{D}}^T(R)\,\underline{\mathbf{M}}(S,R)\,\underline{\mathbf{D}}(R)\,\vec{x}(R') \\
& + \tfrac{1}{2}\vec{x}^T(S')\,\underline{\mathbf{D}}^T(S)\,\underline{\mathbf{M}}(R,S)\,\underline{\mathbf{D}}(S)\,\vec{x}(S') \\
& - \vec{x}^T(S')\,\underline{\mathbf{D}}^T(S)\,\underline{\mathbf{R}}(S,R)\,\underline{\mathbf{D}}(R)\,\vec{x}(R')\ .
\end{aligned}
\tag{3.2}
$$

Equation (3.2) is valid for arbitrary source and receiver locations and depends on attributes of the central ray, only. Zhang et al. (2001) has shown how a CRS stack operator for 3D media, arbitrary top-surface topography, and central rays with finite offsets can be derived from this equation. However,

due to the high complexity of equation (3.2) and the large number of parameters that have to be known for each central ray, this operator is inapplicable to most practical problems of seismic data processing.

To facilitate a practical implementation it is possible to simplify equation (3.2) by considering a specific measurement configuration, only. There are various possibilities, e. g. for stacking of 3D data acquired on a planar measurement surface with constant near-surface velocity and central rays having coincident source and receiver locations, the reader is referred to Höcht (2002) and Bergler (2004). For a 2D survey on a planar measurement surface with constant near-surface velocities in S and R and central rays having a constant but finite offset, I refer to Bergler (2001).

3.2.1 CRS stack operator for arbitrary topography

In order to simplify equation (3.2) to obtain a 2D ZO traveltime approximation for arbitrary topography the following assumptions according to survey design and subsurface structure are made:

1. sources and receivers are located along a straight line oriented, without loss of generality, in x_1-direction.
   $\Rightarrow x_2$ is zero for all source and receiver points.

2. 2.5 D subsurface structure, medium parameters vary only in x_1-direction.
   $\Rightarrow$ all derivatives in x_2 direction and the azimuth angle θ vanish.

3. constant near surface velocity v_0.
   $\Rightarrow v(S) = v(R) := v_0$ and all derivatives of v_0 vanish.

4. central rays have coincident source and receiver location $S = R := X_0$.
   $\Rightarrow$ i. $\beta_S = \beta_R := \beta_0$ and the rotation matrices $\mathbf{D}(R)$ and $\mathbf{D}(S)$ are equal to $\mathbf{D}(\mathbf{X_0})$ with

$$\mathbf{D}(\mathbf{X_0}) = \begin{pmatrix} \cos\beta_0 & 0 & \sin\beta_0 \\ 0 & 1 & 0 \\ \sin\beta_0 & 0 & -\cos\beta_0 \end{pmatrix}.$$

$\Rightarrow$ ii. the downgoing and upgoing wavefield associated with the central ray propagates along the same path but in opposite directions, thus the slowness vectors $\vec{p}^{(x)}(R)$ and $\vec{p}^{(x)}(S)$ coincide but have opposite signs:

$$\vec{p}^{(x)}(R) = -\vec{p}^{(x)}(S) := p_0^{(x)}(X_0) = \begin{pmatrix} \sin\beta_0/v_0 \\ 0 \\ -\cos\beta_0/v_0 \end{pmatrix}$$

$\Rightarrow$ iii. similarly we find for matrices $\underline{\mathbf{M}}^{(x)}(S,R)$ and $\underline{\mathbf{M}}^{(x)}(S,R)$

$$\underline{\mathbf{M}}^{(x)}(S,R) = \underline{\mathbf{M}}^{(x)}(R,S) := \underline{\mathbf{M}}^{(x)}(X_0).$$

If we apply these confinements to the parabolic traveltime expression (3.2), it simplifies to

$$
\begin{aligned}
\tau(S',R')^{ZO} \quad = \quad & \tau(S,R)^{ZO} \; + \; \vec{x}^T(R') \cdot \vec{p}_0^{(x)}(X_0) \; - \; \vec{x}^T(S') \cdot \vec{p}_0^{(x)}(X_0) \\[2mm]
& + \quad \frac{1}{2}\,\vec{x}^T(R') \cdot \mathbf{M}^{(x)}(X_0) \cdot \vec{x}(R') \\[2mm]
& + \quad \frac{1}{2}\,\vec{x}^T(S') \cdot \mathbf{M}^{(x)}(X_0) \cdot \vec{x}(S') \\[2mm]
& - \quad \vec{x}^T(S') \cdot \mathbf{R}^{(x)}(R,S) \cdot \vec{x}(R'),
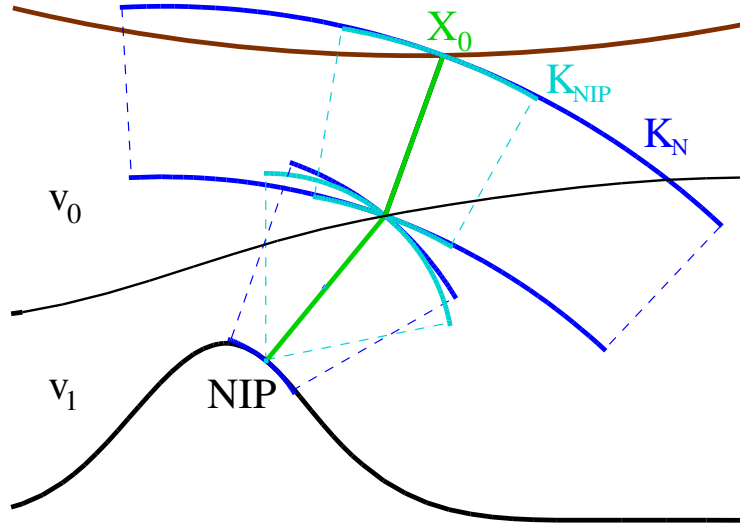\end{aligned}
\tag{3.3}
$$

Figure 3.4: ZO situation: The central ray shown in green hits the reflector perpendicularly at the normal incidence point (NIP). Consequently, the down-going and up-coming ray paths are identical. The wavefronts of the NIP-wave depicted in light-blue and the normal-wave depicted in blue travel along the central ray emerging at the coincident source and receiver point X_0 with the wavefront curvatures K_{NIP} and K_N, respectively. For the illustration, the wavefronts are approximated by circular segments with the corresponding curvature of the wavefronts at the central ray. The measurement surface depicted in brown is a smooth curve with negative curvature K_0 in X_0.

with

$$\underline{\mathbf{M}}^{(x)}(X_0) = \begin{pmatrix} \cos^2\beta_0 \left(\mathbf{Q}_1\mathbf{Q}_2^{-1}\right)_{11} & 0 & \sin\beta_0 \, \cos\beta_0 \left(\mathbf{Q}_1\mathbf{Q}_2^{-1}\right)_{11} \\ 0 & 0 & 0 \\ \sin\beta_0 \, \cos\beta_0 \left(\mathbf{Q}_1\mathbf{Q}_2^{-1}\right)_{11} & 0 & \sin^2\beta_0 \left(\mathbf{Q}_1\mathbf{Q}_2^{-1}\right)_{11} \end{pmatrix},$$

and

$$\underline{\mathbf{R}}^{(x)}(R,S) = \begin{pmatrix} \cos^2\beta_0 \left(\mathbf{Q}_2^{-1}\right)_{11} & 0 & \sin\beta_0 \, \cos\beta_0 \left(\mathbf{Q}_2^{-1}\right)_{11} \\ 0 & 0 & 0 \\ \sin\beta_0 \, \cos\beta_0 \left(\mathbf{Q}_2^{-1}\right)_{11} & 0 & \sin^2\beta_0 \left(\mathbf{Q}_2^{-1}\right)_{11} \end{pmatrix},$$

where the identity

$$m_{ij}(X_0) = \left(\mathbf{P}_2\mathbf{Q}_2^{-1}\right)_{ij} = \left(\mathbf{Q}_1\mathbf{Q}_2^{-1}\right)_{ij} \tag{3.6}$$

was used.

According to Hubral (1983) the ray propagator matrix $\mathbf{\Pi}$ along the ZO central ray can be expressed by the wavefront curvatures of two hypothetical eigenwaves, namely the normal-incidence-point wave (NIP-wave) and the normal wave (N-wave). Both curvatures are measured at X_0; the sign convention is given in Figure 3.5. In the 2D case, the 2×2 wavefront curvature matrices of these hypothetical waves reduce to scalars K_{NIP} and K_N and the expression for matrix $\mathbf{\Pi}$ reads

$$\mathbf{\Pi}(S,R) = \frac{1}{K_{\mathrm{NIP}} - K_{\mathrm{N}}} \begin{pmatrix} K_{\mathrm{NIP}} + K_{\mathrm{N}} & 2v_S \\ \frac{2K_{\mathrm{NIP}}K_{\mathrm{N}}}{v_S} & K_{\mathrm{NIP}} + K_{\mathrm{N}} \end{pmatrix}. \tag{3.7}$$
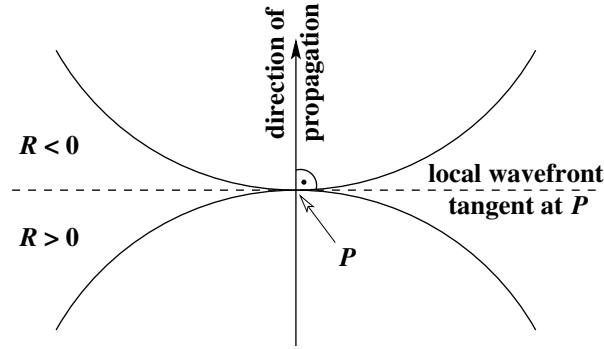
Figure 3.5: Sign convention of wavefront curvatures according to Hubral (1983): By definition, a wavefront curvature is positive if the wavefront is lagging behind its tangent plane. Vice versa, if the wavefront is ahead of its tangent plane, the wavefront curvature is negative. Figure taken from Koglin (2005).

As depicted in Figure 3.4, the NIP-wave is related to a point source located at the (unknown) reflection point in depth, whereas the N-wave is related to an exploding reflector experiment for the reflector segment (or CRS) under consideration. The attribute K_{NIP} characterizes the overburden along the central ray which, in turn, is parameterized by its emergence location X_0, its emergence angle β_0, and the zero-offset traveltime $\tau_0 := \tau(S', G')^{ZO}$. In contrast, the attribute K_N additionally depends on the reflector curvature.

In seismics, the source and receiver locations, $\vec{x}(S')$ and $\vec{x}(G')$, are usually described in terms of *midpoint* and *half-offset* coordinates, labeled $\vec{m}$ and $\vec{h}$ according to the relations

$$\vec{m}(S',G') = \begin{pmatrix} m_x \\ m_z \end{pmatrix} = \frac{1}{2} \begin{pmatrix} x_1(G') + x_1(S') \\ x_3(G') + x_3(S') \end{pmatrix} \tag{3.8}$$

and

$$\vec{h}(S',G') = \begin{pmatrix} h_x \\ h_z \end{pmatrix} = \frac{1}{2} \begin{pmatrix} x_1(G') - x_1(S') \\ x_3(G') - x_3(S') \end{pmatrix}. \tag{3.9}$$

Since all following considerations will be limited to the 2D case, the term x-axis will be used as synonym to x_1-axis and the term z-axis will be used instead of x_3-axis.

For the practical application, where the source and receiver coordinates of the entire survey are related to the same coordinate system, it is more appropriate to use global Cartesian coordinates rather than the local Cartesian coordinates used so far. For this reason, we denote the emergence point of the central ray in a global coordinate system by ray $\vec{m_0} = (m_{x_0}, m_{z_0})^T$ and introduce the midpoint displacement vector $\Delta\vec{m} = \vec{m} - \vec{m_0}$.

With the propagator matrix expressed in terms of the wavefront curvatures (3.7), the parabolic form of the traveltime surface can be rewritten as

$$
\begin{aligned}
\tau_{\text{par}}(\Delta\vec{m}, \vec{h}) \;=\; & \tau_0 - \frac{2}{v_0}\,(\Delta m_x \sin\beta_0 + \Delta m_z \cos\beta_0) \\
& + \; \frac{K_{\text{N}}}{v_0}\,(\Delta m_x \cos\beta_0 - \Delta m_z \sin\beta_0)^2 \\
& + \; \frac{K_{\text{NIP}}}{v_0}\,(h_x \cos\beta_0 - h_z \sin\beta_0)^2 \; .
\end{aligned}
\tag{3.10}
$$

For exploration seismics, practical experience and systematic studies, e. g. Ursin (1982), suggested that a hyperbolic form of the traveltime approximation is a better approximation to the real traveltime response than the parabolic approximation given by equation (3.10). This was later also approved by the work of Höcht (1998), Jäger (1999), Müller (1999), and Bergler (2001).

Taking the square of both sides of equation (3.10) and retaining only terms up to second order leads to the hyperbolic formulation of the paraxial traveltime in global Cartesian coordinates:

$$
\begin{aligned}
\tau^2_{\text{hyp}}(\Delta\vec{m}, \vec{h}) \;=\; & \left(\tau_0 - \frac{2}{v_0}\,(\Delta m_x \sin\beta_0 + \Delta m_z \cos\beta_0)\right)^2 \\
& + \; \frac{2\,\tau_0\,K_{\text{N}}}{v_0}\,(\Delta m_x \cos\beta_0 - \Delta m_z \sin\beta_0)^2 \\
& + \; \frac{2\,\tau_0\,K_{\text{NIP}}}{v_0}\,(h_x \cos\beta_0 - h_z \sin\beta_0)^2 \; .
\end{aligned}
\tag{3.11}
$$

3.2.2 CRS stack operator for smoothly curved topography

Equations (3.10) and (3.11) are quite compact and provide an accurate and very natural description of the topography. Nevertheless, the computational cost connected with their practical evaluation is relatively high. Therefore we will simplify this traveltime approximation by assuming a smoothly curved measurement surface. For this purpose, we establish in every point X_0 a local Cartesian coordinate system as depicted in Figure 3.6, with origin in X_0 and $\hat{x}$-axis being tangent to the surface at X_0. In the local coordinate system the $\hat{z}$-component of any source or receiver point in the vicinity of X_0 can be approximated up to the second order by the relation

$$
\hat{z}(\hat{x}) = -\frac{K_0}{2}\hat{x}^2 \,, \quad \text{with} \quad K_0 = -\left.\frac{d^2\hat{z}}{d\hat{x}^2}\right|_{x_0}
\tag{3.12}
$$

being the local curvature of the measurement surface in X_0. Please note that, in case of an undulating topography the assumption of a parabolic-measurement surface with apex in X_0 becomes more and more inaccurate for larger offsets. Particularly, if X_0 is located close to an inflection point of the topography, where a sign-change of the curvature K_0 occurs, the validity range of this assumption is very limited. In the local coordinate system the location of two points S and G in the vicinity of X_0 reads

$$
\begin{pmatrix} \hat{x}(S) \\ \hat{z}(S) \end{pmatrix} = \begin{pmatrix} m_{\hat{x}} - h_{\hat{x}} \\ -\frac{K_0}{2}(m_{\hat{x}} - h_{\hat{x}})^2 \end{pmatrix} \quad \text{and} \quad \begin{pmatrix} \hat{x}(G) \\ \hat{z}(G) \end{pmatrix} = \begin{pmatrix} m_{\hat{x}} + h_{\hat{x}} \\ -\frac{K_0}{2}(m_{\hat{x}} + h_{\hat{x}})^2 \end{pmatrix} .
\tag{3.13}
$$
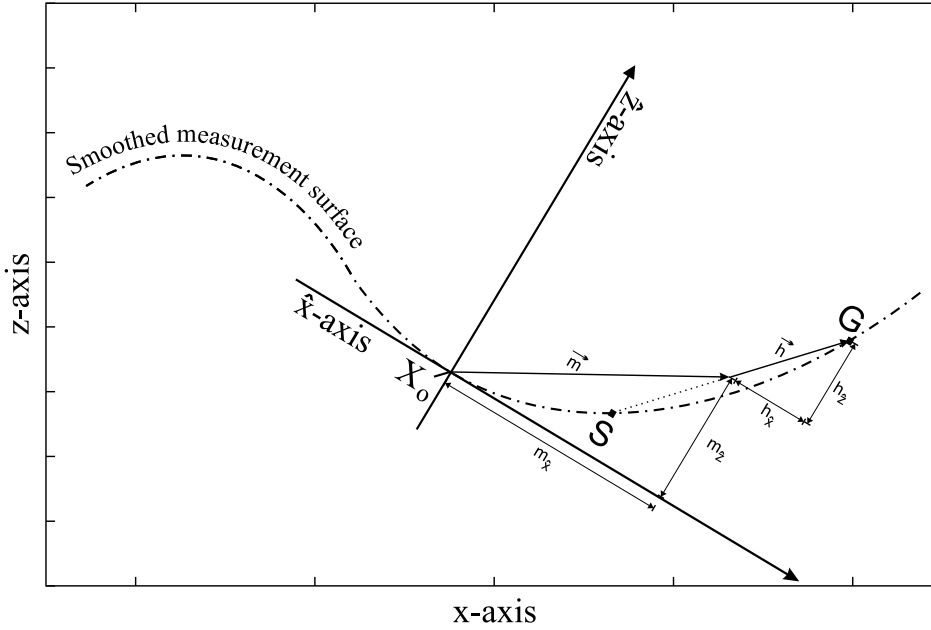
Figure 3.6: Local Cartesian coordinate system with origin in X_0 and $\hat{x}$-axis tangent to the measurement surface in X_0.

For the corresponding midpoint and half-offset vectors we find, according to Figure 3.6,

$$\vec{m}(S,G) = \begin{pmatrix} m_{\hat{x}} \\ m_{\hat{z}} \end{pmatrix} = \frac{1}{2} \begin{pmatrix} \hat{x}(G) + \hat{x}(S) \\ \hat{z}(G) + \hat{z}(S) \end{pmatrix} = \begin{pmatrix} m_{\hat{x}} \\ -\frac{K_0}{2}(m_{\hat{x}}^2 + h_{\hat{x}}^2) \end{pmatrix}, \tag{3.14a}$$

$$\vec{h}(S,G) = \begin{pmatrix} h_{\hat{x}} \\ h_{\hat{z}} \end{pmatrix} = \frac{1}{2} \begin{pmatrix} \hat{x}(G) - \hat{x}(S) \\ \hat{z}(G) - \hat{z}(S) \end{pmatrix} = \begin{pmatrix} h_{\hat{x}} \\ -K_0 m_{\hat{x}} h_{\hat{x}} \end{pmatrix}. \tag{3.14b}$$

Denoting the dip angle of the measurement surface in X_0 with respect to a global z-axis by α_0 we obtain for Δm_z and h_z after a simple rotation of the coordinate system:

$$\Delta m_x = m_{\hat{x}} \cos \alpha_0 - m_{\hat{z}} \sin \alpha_0 \,, \qquad\qquad h_x = h_{\hat{x}} \cos \alpha_0 - h_{\hat{z}} \sin \alpha_0 \,, \tag{3.15a}$$

$$\Delta m_z = m_{\hat{x}} \sin \alpha_0 + m_{\hat{z}} \cos \alpha_0 \,, \qquad\qquad h_z = h_{\hat{x}} \sin \alpha_0 + h_{\hat{z}} \cos \alpha_0 \,. \tag{3.15b}$$

From equations (3.14a), (3.14b), and (3.15a) we can derive

$$m_{\hat{x}} = \frac{\Delta m_x}{\cos \alpha_0} - \frac{\sin \alpha_0}{\cos \alpha_0} \frac{K_0}{2}(m_{\hat{x}}^2 + h_{\hat{x}}^2) \quad \text{and} \quad h_{\hat{x}} = \frac{h_x}{\cos \alpha_0} - \frac{\sin \alpha_0}{\cos \alpha_0} K_0 m_{\hat{x}} h_{\hat{x}}. \tag{3.16}$$

Multiplying the above equations by $m_{\hat{x}}$ and $h_{\hat{x}}$, respectively, we find the second order approximation

$$m_{\hat{x}}^2 = \frac{\Delta m_x^2}{\cos^2 \alpha_0} \,, \qquad h_{\hat{x}}^2 = \frac{h_x^2}{\cos^2 \alpha_0} \,, \quad \text{and} \quad m_{\hat{x}} h_{\hat{x}} = \frac{\Delta m_x h_x}{\cos^2 \alpha_0} \,. \tag{3.17}$$

45

Together with equations (3.14a), (3.14b), (3.15b) and (3.16), this leads to the following expressions:

$$\Delta m_z = \frac{\sin\alpha_0 \Delta m_x}{\cos\alpha_0} - \frac{K_0}{2\cos^3\alpha_0}(\Delta m_x^2 + h_x^2) \,, \tag{3.18}$$

$$h_z = \frac{\sin\alpha_0 h_x}{\cos\alpha_0} - \frac{K_0}{\cos^3\alpha_0}\Delta m_x h_x \,. \tag{3.19}$$

Inserting equations (3.18) and (3.19) into equation (3.10) and retaining only terms up to the second order yields the parabolic CRS traveltime operator for smoothly curved topography

$$
\begin{aligned}
\tau_{\text{par}}(\Delta m_x, h_x) = {} & \tau_0 + \frac{2\,\Delta m_x}{v_0\,\cos\alpha_0}\ \sin(\beta_0 + \alpha_0) \\[2mm]
& + \frac{\Delta m_x^2}{v_0\,\cos^2\alpha_0}\ \left(K_{\text{N}}\ \cos^2(\beta_0 + \alpha_0) - K_0\ \cos(\beta_0 + \alpha_0)\right) \\[2mm]
& + \frac{h_x^2}{v_0\,\cos^2\alpha_0}\ \left(K_{\text{NIP}}\ \cos^2(\beta_0 + \alpha_0) - K_0\ \cos(\beta_0 + \alpha_0)\right) \,.
\end{aligned}
\tag{3.20}
$$

By squaring both sides and keeping again only terms up to the second order, we obtain the hyperbolic CRS traveltime operator for smoothly curved topography:

$$
\begin{aligned}
\tau_{\text{hyp}}^2(\Delta m_x, h_x) = {} & \left(\tau_0 + \frac{2\,\Delta m_x}{v_0\,\cos\alpha_0}\ \sin(\beta_0 + \alpha_0)\right)^2 \\[2mm]
& + \frac{2\,\tau_0\,\Delta m_x^2}{v_0\,\cos^2\alpha_0}\ \left(K_{\text{N}}\ \cos^2(\beta_0 + \alpha_0) - K_0\ \cos(\beta_0 + \alpha_0)\right) \\[2mm]
& + \frac{2\,\tau_0\,h_x^2}{v_0\,\cos^2\alpha_0}\ \left(K_{\text{NIP}}\ \cos^2(\beta_0 + \alpha_0) - K_0\ \cos(\beta_0 + \alpha_0)\right) \,.
\end{aligned}
\tag{3.21}
$$

3.2.3 CRS stack operator for planar topography

A ZO CRS stack operator for planar topography can easily be obtained from equation (3.21) or equation (3.20). By setting $K_0 = 0$ and $\alpha_0 = 0$ in equation (3.21) we obtain the well-known hyperbolic traveltime operator for a planar measurement surface (e. g. Hubral et al., 1993a). It reads, in different notation,

$$
\begin{aligned}
\tau_{\text{hyp}}^2(\Delta m_x, h_x) = {} & \left(t_0 + \frac{2}{v_0}\,\Delta m_x\,\sin\beta_0\right)^2 + \frac{2\,\tau_0}{v_0}\,K_{\text{N}}\,\cos^2\beta_0\,\Delta m_x^2 \\[2mm]
& + \frac{2\,\tau_0}{v_0}\,K_{\text{NIP}}\,\cos^2\beta_0\,h_x^2 \,.
\end{aligned}
\tag{3.22}
$$

In the same way we obtain from equation (3.20) the parabolic traveltime operator for a planar measurement surface:

$$
\begin{aligned}
\tau_{\text{par}}(\Delta m_x, h_x) = {} & \tau_0 + \frac{2}{v_0}\,\Delta m_x\,\sin\beta_0 + \frac{1}{v_0}\,K_{\text{N}}\,\cos^2\beta_0\,\Delta m_x^2 \\[2mm]
& + \frac{1}{v_0}\,K_{\text{NIP}}\,\cos^2\beta_0\,h_x^2 \,.
\end{aligned}
\tag{3.23}
$$

Note that the emergence angle β_0 in equations 3.22 and 3.23 is related to the surface normal instead of being related to the depth direction.

3.2.4 Comparison of the different CRS stack operators

Comparing the traveltime operators for a planar and a smoothly curved measurement surface one can observe that we have in both cases two-dimensional second order equations of parabolic or hyperbolic form. Thus, the second order reflection response of an arc-shaped reflector segment in depth can be described by the same kind of surface (see Figure 1.6(d)) either if measured on a planar or a smoothly curved topography. In contrast to this, traveltime surfaces that are described by equations (3.10) and (3.11) are usually much more complicated. An example for the hyperbolic operator in case of a rough top-surface topography and a subsurface model similar to the one used for Figure 1.6 is depicted in Figure 3.7.
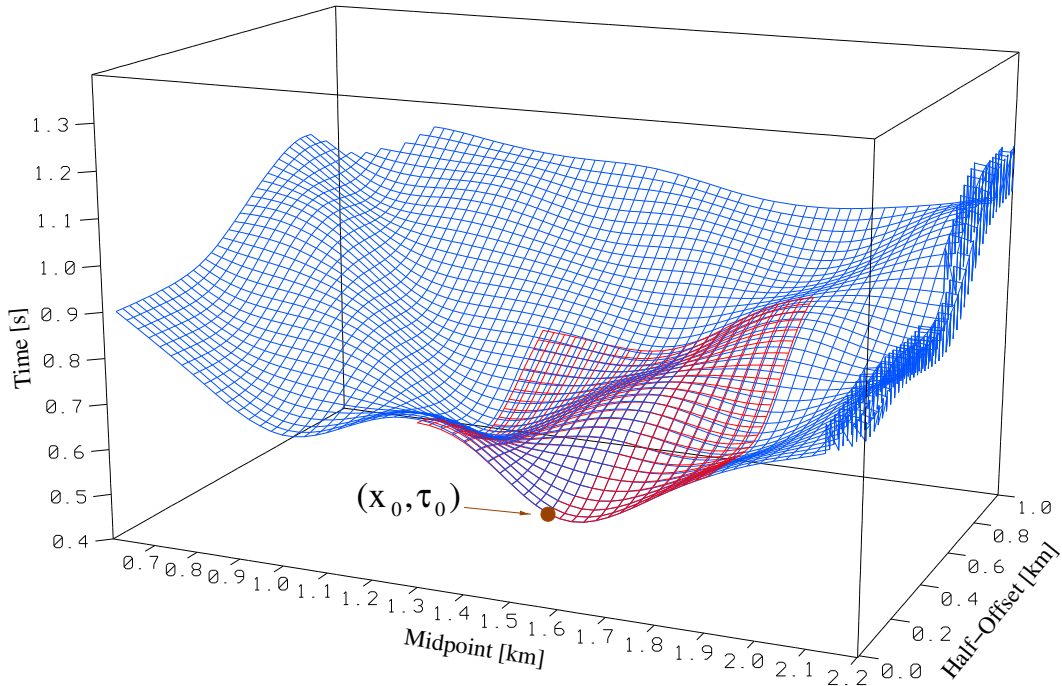
Figure 3.7: The hyperbolic CRS stack operator for arbitrary topography (red] compared to the forward modeled reflection response of a dome-like structure in depth (blue). For the sake of simplicity, the rough measurement surface and the subsurface model have been omitted. Figure according to Zhang (2003).

Both, for planar and smoothly curved top-surface topography the previously derived CRS traveltime operators can be rewritten in a Taylor series as

$$\tau_{par} = \tau_0 + A\,\Delta m_x + B\,\Delta m_x^2 + C\,h_x^2 \quad \text{and} \quad \tau_{hyp}^2 = (\tau_0 + A\,\Delta m_x)^2 + 2\tau_0 B\,\Delta m_x^2 + 2\tau_0 C\,h_x^2, \quad (3.24)$$

with the coefficients A, B, and C given by Table 3.1.

It follows from this observation that both traveltime operators describe the same type of surface in the (m, h, t) space and that it is possible to use an operator as simple as the one for a planar measurement surface also in case of a smoothly curved measurement surface. As will be discussed in Chapter 4 in more detail, this has certain advantages from the implementational point of view since far less

Planar measurement surface	Smoothly curved measurement surface
$A = \frac{2}{v_0} \sin \beta_0$	$A = \frac{2}{v_0 \, \cos \alpha_0} \, \sin(\beta_0 + \alpha_0)$
$B = \frac{1}{v_0} \, K_{\mathrm{N}} \, \cos^2 \beta_0$	$B = \frac{\cos^2(\beta_0 + \alpha_0)}{v_0 \, \cos^2 \alpha_0} \left[K_{\mathrm{N}} - \frac{K_0}{\cos(\beta_0 + \alpha_0)} \right]$
$C = \frac{1}{v_0} \, K_{\mathrm{NIP}} \, \cos^2 \beta_0$	$C = \frac{\cos^2(\beta_0 + \alpha_0)}{v_0 \, \cos^2 \alpha_0} \left[K_{\mathrm{NIP}} - \frac{K_0}{\cos(\beta_0 + \alpha_0)} \right]$

Table 3.1: Taylor coefficients of the CRS stacking operators for planar and smoothly curved measurement surfaces.

additions and multiplications are needed to calculate the traveltime surfaces during the stack and, in particular, during the stacking parameter search. Introducing the stacking parameters, β_0^*, K_{NIP}^*, and K_{N}^* to describe the traveltime surface in case of smoothly curved topography, the hyperbolic CRS stacking operator reads

$$
\begin{aligned}
\tau_{\mathrm{hyp}}^2(\Delta m_x, h_x) \;=\; & \left(t_0 + \frac{2}{v_0} \, \Delta m_x \, \sin \beta_0^* \right)^2 \\
& + \; \frac{2 \, \tau_0}{v_0} \, K_{\mathrm{N}}^* \, \cos^2 \beta_0^* \, \Delta m_x^2 \\
& + \; \frac{2 \, \tau_0}{v_0} \, K_{\mathrm{NIP}}^* \, \cos^2 \beta_0^* \, h_x^2 .
\end{aligned}
\tag{3.25}
$$

It is obvious that β_0^*, K_{NIP}^*, and K_{N}^* are no wavefield attributes but stacking parameters only, since equation (3.25) considers neither influence of the local dip nor of the local curvature of the measurement surface. However, comparing the coefficients A, B, and C given by Table 3.1 reveals the mutual relationship between these stacking parameters and the wavefield attributes β_0, K_{NIP}, and K_{N}:

$$
\sin(\beta_0 + \alpha_0) = \cos \alpha_0 \sin \beta_0^* \, ,
\tag{3.26a}
$$

$$
K_{\mathrm{N}} = \frac{K_{\mathrm{N}}^* \cos^2 \alpha_0 \cos^2 \beta_0^* + K_0 \sqrt{1 - \cos^2 \alpha_0 \sin^2 \beta_0^*}}{1 - \cos^2 \alpha_0 \sin^2 \beta_0^*} \, , \text{ and}
\tag{3.26b}
$$

$$
K_{\mathrm{NIP}} = \frac{K_{\mathrm{NIP}}^* \cos^2 \alpha_0 \cos^2 \beta_0^* + K_0 \sqrt{1 - \cos^2 \alpha_0 \sin^2 \beta_0^*}}{1 - \cos^2 \alpha_0 \sin^2 \beta_0^*} \, .
\tag{3.26c}
$$

Please note that β_0^* becomes complex if $\left| \frac{1}{\cos \alpha_0} \sin(\beta_0 + \alpha_0) \right| > 1$, again demonstrating that it does not represent a physical emergence angle.

For the practical implementation of the 2D ZO CRS stack presented in the following chapter the real wavefront attributes β_0, K_{NIP}, and K_N are substituted by β_0^*, K_{NIP}^*, and K_{N}^* resulting in stack operator (3.25) having the same form as equation (3.22). This reduced operator is used instead of equation (3.21) for the time-consuming parameter search, where the optimal stacking surface is determined by coherence analysis. Afterwards, the correct wave-field attributes are calculated from the resulting stacking parameters by means of equations (3.26). Doing this, the run-time can be shortened. However, it has to be considered that physically reasonable search limits, valid for the true wavefield attributes, have to be transfered into those limits valid for the actually searched-for pseudo attributes.
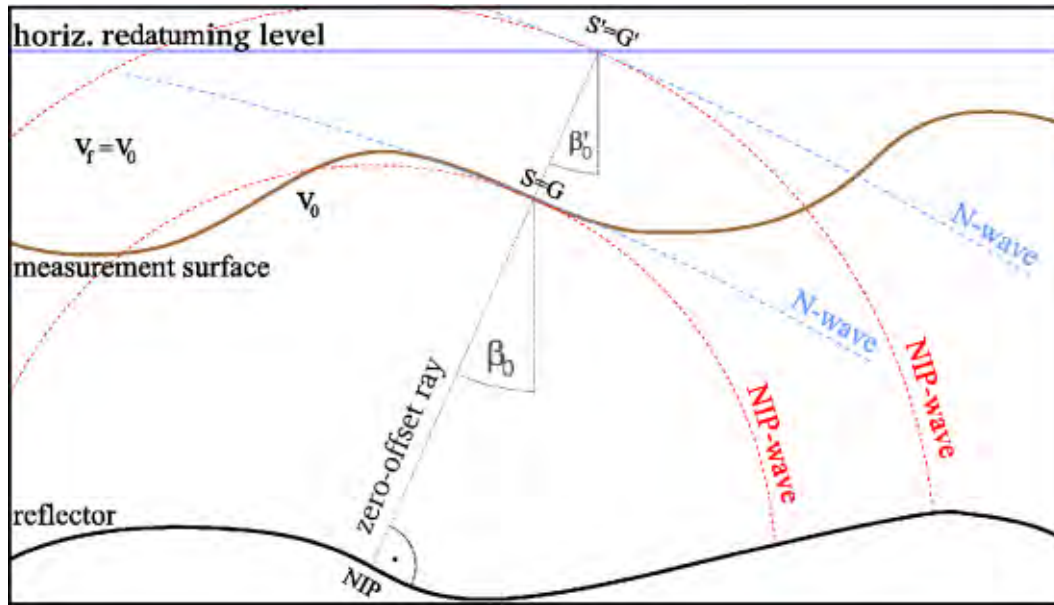
Figure 3.8: Redatuming: To remove the influence of the top-surface topography from the obtained ZO and attribute sections, a situation is simulated where all central rays emerge on the same horizontal redatuming level. This process is shown here for one central ray. In order to keep the figure simple, only the situation $v_0 = $ const is displayed. In this case the replacement velocity v_f can be chosen to be equal to v_0 so that no refraction at the measurement surface has to be considered.

3.3 Redatuming to a horizontal reference level

The 2D CRS stack aims at producing a time domain image of the subsurface structure, i.e. the ZO section, and furthermore at providing additional information in the form of kinematic wavefield attribute sections, namely the β_0, the K_N, and the K_{NIP} sections. It is evident that these output sections should not depend on the characteristics of the measurement surface. In case of the CRS stack operator for arbitrary topography (3.11) it is possible to relate all simulated ZO rays to the same emergence-point elevation z_{RD} by choosing $m_{z0} = z_{RD}$ for the calculation of the z-component of the midpoint displacement $\Delta m_z = m_z - m_{z0}$. Thus the redatuming is inherent to the stacking procedure. However, if the CRS stack operator for smoothly curved top-surface topography is used, one obtains output sections which are related to the smoothly curved measurement surface. As will be discussed in the next chapter, an explicit redatuming procedure has to be applied to the obtained results due to the cascaded parameter-search strategy utilized by the presented implementation.

For this purpose, the ZO traveltimes, the amplitudes and also the attribute values have to be transfered to those values which would be measured at the horizontal reference level. In the following, all values that pertain to the horizontal redatuming level are denoted with a prime. The key information for this procedure is the knowledge of the take-off angle β_0, which is provided by the CRS stack. If the redatuming level is assumed to be above the actual topography, it is possible to choose an arbitrary velocity v_f for the fictitious layer between topography and new datum. If the near-surface velocity is constant along the line, the most convenient choice is to set v_f equal v_0, because this avoids that the topography has to be considered as an additional interface. For varying v_0 Snell's Law has to

49

be applied to derive β_0', the take-off angle at the fictitious coincident source and receiver point X_0'. Knowing the take-off angles and the wave velocity within the fictitious layer, it is not difficult to forward propagate the Normal- and NIP-wave fronts up to the redatuming level.

To map the coincident source and receiver point X_0 of a ZO ray from the original measurement surface to its corresponding location X_0' at the redatuming level, one has to transfer its coordinates x_0 and z_0 to their new values x_0' and z_0'. Of course, z_0' is given by the elevation of the new datum. To transfer x_0, the emergence angle of the central ray after being refracted at the measurement surface needs to be known. This angle is equal to β_0' if both are measured with respect to the depth direction. Relating both angles to the measurement surface normal by introducing the local dip of the measurement surface α_0 yields, according to Snell's Law,

$$\frac{v_0}{v_f} = \frac{\sin{(\beta_0 + \alpha_0)}}{\sin(\beta_0' + \alpha_0)} \; , \tag{3.27}$$

which leads to

$$\beta_0' = \arcsin\left(\frac{v_f}{v_0} \sin{(\beta_0 + \alpha_0)}\right) - \alpha_0 \; . \tag{3.28}$$

Denoting the vertical distance between X_0 and X_0' by Δz, the relation between x_0 and x_0' reads

$$x_0' = x_0 + \Delta z \tan\beta_0' \; . \tag{3.29}$$

Similar trigonometric considerations result for t_0 and t_0',

$$t_0' = t_0 + \frac{2\Delta z}{v_f \cos\beta_0'} \; . \tag{3.30}$$

The amplitude value $A'(t_0', x_0')$ as it would be measured at the redatuming level can be approximatively calculated from its value at the real measurement surface $A(t_0, x_0)$ and the associated NIP- and N-wave curvatures. According to Vieth (2001), the geometrical spreading factor for 2.5D media can be estimated from the CRS attributes by the following relation:

$$|\mathcal{L}_2| = \sqrt{\frac{2}{v_0}\left|\frac{1}{K_{NIP} - K_N}\right|} \; . \tag{3.31}$$

Consequently the amplitude value corresponding to the redatuming level reads

$$A' = A \, \frac{|\mathcal{L}_2(K_{NIP}', K_N')|}{|\mathcal{L}_2(K_{NIP}, K_N)|} \; . \tag{3.32}$$

In order to transfer the values of the wavefield attributes K_N, K_{NIP} to those values which would be measured at the redatuming level, we have to use the *refraction law* (Hubral and Krey, 1980), that gives us the curvature of the N- and NIP-wave, respectively, after passing the measurement surface

$$K_{N,NIP}^f = \frac{K_{N,NIP} v_f \cos^2{(\beta_0 + \alpha_0)}}{v_0 \cos^2(\beta_0' + \alpha_0)} + \frac{K_0}{\cos^2(\beta_0' + \alpha_0)}\left(\frac{v_f}{v_o}\cos{(\beta_0 + \alpha_0)} - \cos(\beta_0' + \alpha_0)\right) \; , \tag{3.33}$$

where $K_{N,NIP}^f$ are the refracted wavefront curvatures on the upper side of the measurement surface.

Subsequently, we use the *transmission law* (Hubral and Krey, 1980) to propagate the wave-fronts of the N- and NIP-wave through the fictitious layer above the real measurement surface, up to the redatuming level:

$$\frac{1}{K'_{N,NIP}} = \left(\frac{1}{K^f_{N,NIP}} + \frac{1}{2} v_f t_f \right) ,$$

(3.34)

with the two-way traveltime within the fictitious layer

$$t_f = t'_0 - t_0 = \frac{2\Delta z}{v_f \cos \beta'_0} .$$

(3.35)

Inserting equations (3.33) and (3.35) into (3.34) leads to the final equations for the wavefront curvatures K'_N and K'_{NIP}, measured at the redatuming level

$$\frac{1}{K'_{N,NIP}} = \left(\frac{\cos^2(\beta'_0 + \alpha_0)}{K_{N,NIP} \frac{v_f}{v_0} \cos^2 (\beta_0 + \alpha_0) + K_0 \left(\frac{v_f}{v_o} \cos \beta_0 - \cos \beta_{0'} \right)} + \frac{\Delta z}{\cos \beta'_0} \right) .$$

(3.36)

Chapter 4

Implementation

This chapter is devoted to the practical implementation of the 2D ZO CRS stack for topography. The developed source code was written in an object oriented way employing the widely-used programming language C++ (Stroustrup, 1997). It is mainly an extention of the existing 2D ZO CRS stack program for planar topography discussed in Mann (2002). During the last years, the latter was applied and further developed in several academic and commercial research projects so that a high level of sophistication could be achieved. Consequently, the 2D ZO CRS stack code for topography was implemented with the intention to preserve the generality and the high degree of automatization of the original implementation. In this chapter, I will focus on the extensions and changes that had to be made rather than going into details of the quite extensive implementation. A very simple synthetic dataset will be used to visualize important aspects of the presented processing scheme.

4.1 Determination of the stacking parameters

In the preceeding chapter, a second order approximation of the kinematic reflection response of an arbitrarily curved reflector segment in depth was derived. If we limit the associated traveltime surface adequately in offset and midpoint direction we obtain a stacking operator along which the energy reflected at this specific reflector segment can be summed up constructively. However, since the depth and curvature of the reflector segment are unknown, every reasonable combination of the three wavefront attributes β_0, K_{NIP}, and K_N might parameterize the searched for reflection event. Thus, finding the optimum stacking parameters for every sample of the ZO section to be simulated is the main problem that has to be solved. In order to tackle this global optimization problem we have to define a suitable objective function, which measures the fit of the stacking operator to the (unknown) reflection event in the prestack data. For this purpose, a direct comparison of the kinematic reflection traveltimes is not attractive as it would require the manual picking of reflection events in the usually noisy pre-stack data. Therefore, a statistical approach was chosen for the current implementation based on the coherence of the prestack data along the stacking operator. This criterion can be evaluated in a fully automated way which facilitates an entirely data-driven determination of the CRS attributes. To measure the coherence the well-known *semblance* (Neidell and Taner, 1971) is used.

To find the best fitting operator by brute force, i. e. by evaluating the semblance for every possible attribute triple, is virtually impossible considering the typically huge size of seismic multi-coverage

data sets used, e. g. for hydrocarbon exploration. Thousands of traces might be located inside the considered stacking aperture which makes the coherence analysis very time-consuming, particularly, since the same process has to be applied independently for the tens of thousands samples of the ZO section. Unfortunately, many established optimization algorithms, like the gradient method or the Newton method, are not applicable, since derivatives of the objective function are not available.

Several alternative methods to solve this non-linear global optimization problem have been published for the case of planar topography: Anticipating a smooth behavior of the objective function, Müller et al. (1998) and Birgin et al. (1999b) proposed to determine initial CRS stacking parameters by means of three individual one-parametric searches followed by a local three-parameter optimization to identify the optimal CRS stacking parameter triplets. For the local three-parameter optimization Birgin et al. (1999b) suggested the so-called *Spectral Projected Gradient optimization method* (Birgin et al., 1999a) while Müller et al. (1998) applied a *Moving Polyhedron search* (Nelder and Mead, 1965). Due to the tremendous increase in computing power, global two-plus-one (Garabito and Paschoal, 2003) and even three parameter optimization methods (Salvatierra et al., 2003) came again into focus during the last years. Garabito and Paschoal (2003) use a *Simulated Annealing algorithm* (Kirkpatrick et al., 1983) to determine β_0 and K_{NIP} simultaneously from the prestack data assuming $K_N = K_{NIP}$; subsequently they determine K_N in a global one-parameter search also applied in the prestack data. Finally, a *Quasi Newton method* (Gill et al., 1981) is used for a local three-parameter optimization of the obtained attribute triple. Salvatierra et al. (2003) employ the so-called *Box Euclidian Trust Region algorithm* (see, e. g., Andretta et al., 2005) for a three parameter search combined with the use of Lissajous curves in order to escape from local maxima. A direct comparison of these methods is difficult to conduct since success or failure of a certain optimization strategy highly depends on the data set to which it is applied. During the last years, the pragmatic search strategy of Müller et al. (1998) proved to be efficient and sufficiently accurate in a large number of applications to real and synthetic data. Nevertheless, there was also enough evidence given to suggest that a more sophisticated search strategy could be helpful to tap the full potential of the CRS stack method. Although the simulated annealing algorithm showed very promising results in the field of CRS processing of 3D data, the practical experience with alternative search strategies is still very limited. Thus more studies on this topic might be expedient for future research.

4.2   Cascaded processing scheme for topography

Considering arbitrary top-surface topography an initial three-times-one parameter search as proposed by Müller et al. (1998) and Birgin et al. (1999b) is not directly applicable, since there is no specific subset of the data for which CRS stack operator (3.11) depends on one parameter only. A first implementation (Zhang, 2003) that employed a global two-parameter search within shot gathers turned out to be very unstable in case of noisy data and far too time consuming for the given hardware resources. The latter was also the cause why a global three parameter optimization was not considered for the presented implementation—although it might be recommended for future implementations that can make use of a modern multi-CPU cluster.

The current implementation assumes for the initial parameter search a smoothly curved top-surface topography. In this case it is possible to use the reduced stacking operator for smoothly curved topography (3.25) which is identical in form to the one for planar topography. This facilitates the application of a three-times-one parameter search very close to the one proposed by Müller et al. (1998) and
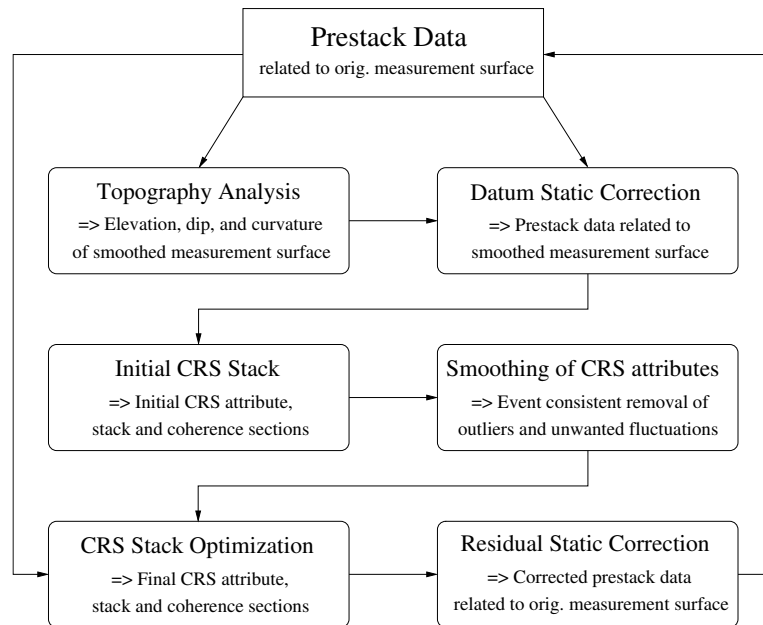
Figure 4.1: Processing scheme to handle topography in CRS stack and residual static correction.

Birgin et al. (1999b). Since for most land data surveys, the assumption of a smoothly curved topography is not met a priori, datum static corrections (see Section 1.3) are used to transfer the data from the real topography to a fictitious smoothly curved measurement surface. This approach is very similar to conventional land data processing, where usually a planar measurement surface is simulated by static corrections. The datum static correction for every source and receiver location is calculated from the near-surface velocity and the differences in elevation of the true source and receiver points and their vertical projections onto the smoothly curved reference surface. The latter is obtained by smoothing the original measurement surface in a suitable way: on the one hand, it has to be considered that the larger the scale of the smoothing the larger the elevation static corrections which have to be applied. On the other hand, the surface has to be smooth enough such that for every single stacking process the elevations of all contributing sources and receivers can be well approximated by a parabola with apex in X_0. After the smooth reference surface is defined, its local dip and curvature are determined for every CMP location. As mentioned before, these values are needed to calculate suitable search ranges for the stacking parameters and to convert the latter afterwards to the searched-for kinematic wavefield attributes.

When the initial CRS stack for smoothly curved top-surface topography is finished, event-consistent smoothing (Hertweck et al., 2005) of the obtained attributes can be helpful to remove fluctuations and outliers. The latter are mainly caused by the limitations of the initial search strategy and should be removed as far as possible before a local optimization is applied. Finally, the local optimization with the CRS stack operator for arbitrary topography (3.11) is applied using the original, i. e. uncorrected, prestack data. For this purpose a simultaneous three-parameter search using the Moving Polyhedron algorithm (Nelder and Mead, 1965) is conducted. The objective function to be maximized is, as in the case of single-parameter searches, semblance (Neidell and Taner, 1971). A subsequent CRS-based residual static correction (Koglin and Ewig, 2003; Koglin, 2005) further optimizes the stack results. A flowchart of this pragmatic processing scheme is depicted in Figure 4.1.

4.3   Surface analysis and static correction

For land data processing it has to be considered that the sources and receivers often do not strictly follow a straight line as it should theoretically be the case for 2D data. In such situations, the top-surface topography or the infrastructure prevents the acquisition from being performed along a straight line, resulting in a so-called *crooked line*. In particular the sources, i.e., large-scale explosives or vibrator trucks require easy access to roads, while geophones with their negligible size can be placed far less restricted. If the deviations of the midpoints from the line of regression through all source and receiver locations are relatively small compared to the maximum offset used in processing, the source and receiver locations can be projected to the line of regression without further corrections. However, doing this artificially reduces the offset by the factor $\cos\gamma$, with γ being the angle between the original offset vector and the straight line. As a consequence of this, certain errors are introduced to the important relation between offset and traveltime. The presented CRS stack implementation employs the more sophisticated approach to project for each trace only the midpoint location while keeping the original offset value (for details see Mann, 2002). For the topography extension of the CRS stack, it is necessary that besides the horizontal x- and y-coordinates also the elevation of each source and receiver point can be obtained from the respective trace header information. According to the cascaded processing scheme discussed in the last section, the initial CRS stack employing the traveltime operator for smoothly curved topography is the first processing step to be conducted. As mentioned before, a local parabolic approximation is used to describe the elevation of sources and receivers within the stacking aperture. Therefore, the actual measurement surface has to be smoothed in order to find a reference level for which this assumption is valid. Before the smoothing can be started the source and receiver coordinates have to be projected onto the straight line so that a 2D distribution of surface locations results. These projected source and receiver locations are in general different from those which are later used by the stack, which considers the projected midpoints and the original offset values. The case of different elevations for sources and receivers with coincident projected x-coordinate is possible. This happens for instance, if the vibrator trucks have to drive around a steep hill but the receivers are laid out across it. To have a unique reference level for the subsequent processing, the mean value is assigned to this point.

In literature one can find many different approaches how to smooth a given 2D distribution of points with respect to a certain axis (see, e.g. Press et al., 1992). It depends on the typical characteristics of the distribution which is assumed and on the purpose of the smoothing, which method is favorable. The method chosen for this implementation had to fulfill the following criteria:

- the obtained surface should be sufficiently smooth to allow, for each point X_0, to describe all source and receiver elevations within a certain stacking aperture by the local dip and curvature of a parabola with apex in in X_0, according to equation (3.12).

- the difference between the original and the smoothed measurement surfaces should be as small as possible to minimize the error introduced by surface consistent datum static corrections.

- the utilized smoothing algorithm should demand besides the source and receiver coordinates only the stacking aperture in order to work fully automated, i.e. without user interaction.

The approach chosen for this implementation requires some computational effort, but seemed to me
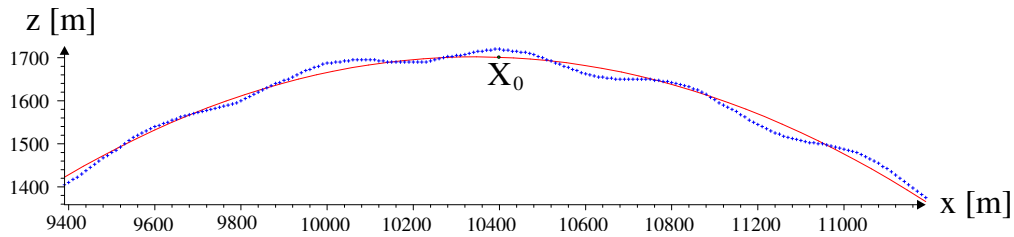
Figure 4.2: The dip, curvature, and elevation in X_0 of the smooth reference level are determined by fitting a circular arc (red) to the source and receiver locations within the stacking aperture (blue).

to be the most natural way to fulfill these criteria. For every CMP location $X_0(x,z_0)$ a circle[1] is fitted to those source and receiver points that lie within the respective stacking aperture (see Figure 4.3). The objective function to be minimized for this fitting process is given by:

$$S(z_0, \alpha_0, K_0) = \sum_{j=1}^{n} |d_j|, \tag{4.1}$$

with n being the number of source and receiver points within the stacking aperture, and d_j being the vertical distance of the jth source or receiver point to the circle defined by z_0, α_0, and K_0. For every CMP location $X_0(x_0, z_0)$, the vertical position z_0 is defined by the circle that minimizes equation (4.1). After these circles are determined, each source or receiver location is vertically projected onto the smoothed surface build by the CMPs. This smoothing algorithm is iteratively applied to the updated source and receiver locations until the average distance of the source and receiver points to the circles has fallen below a certain threshold. Then the process is finished: the new source and receiver locations define the smooth reference surface and the circles determined in the final iteration provide the elevations of the CMPs and those dip and curvature values that define the best fitting parabolas.

The velocity model depicted in Figure 4.3 and the corresponding synthetic data-set were created to conduct first tests of the presented implementation. The subsurface structure is very simple. It is build by four homogeneous layers separated by horizontal interfaces. The top-surface topography resembles the three cases discussed so far and is therefore well suited for testing. On the left hand side it is smoothly curved, undulating on a large scale. On the right hand side the topography is planar. In the region between these two parts small scale undulations have been added to the major trend. It is mainly this part that has to be smoothed before the initial CRS stack can be applied. A comparison between the original and the smoothed measurement surface is depicted in Figure 4.4(a). The local dip and curvature, i. e. the dip and curvature of the best fitting parabola for the respective stacking aperture, are depicted in Figures 4.4(b) and 4.4(c). Furthermore, the datum static corrections necessary to relate the original prestack data to the smoothed reference level are depicted in Figure 4.4(d).

---

[1]Close to its apex, a parabola is well approximated by a circle so that the differences in the resulting dip and curvature are negligible. Circles are used, because an arbitrarily oriented parabola is very inconvenient to handle since it has no unique explicit description in a Cartesian coordinate system in which none of the two axes is tangential at the apex. In principle, one could define, in a first step, a local coordinate system for each parabola by estimating the local dip α_0 which indicates its inclination to the global coordinate system. Optimum values for the curvature and the apex elevation of a parabola could be determined in a second step. However, this approach is due to the split search neither more accurate nor more stable than fitting circles for which three parameters, e. g.radius and x- and z-coordinates of the midpoint, have to be determined simultaneously.
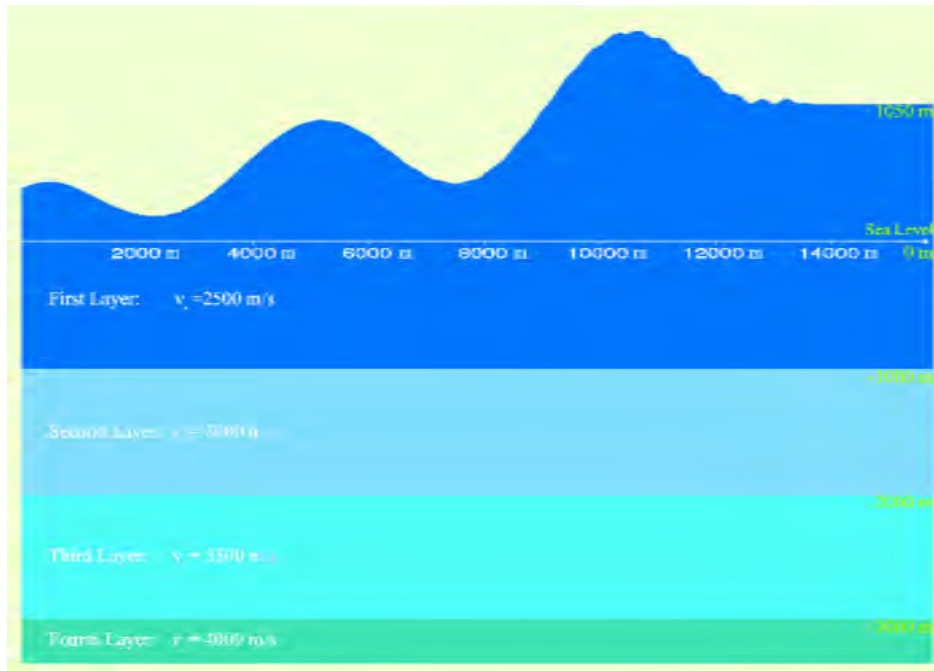
Figure 4.3: ENI/Syndata: Velocity model. For first tests of the extended CRS stack implementation a simple subsurface structure was chosen so that bugs and features can easily be distinguished. The synthetic data and the underlying velocity model were kindly provided by Eni E&P, Italy.

(a) Original and smoothed measurement surfaces.

(b) Dip angle of the smoothed reference level.

(c) Curvature of the smoothed reference level.

(d) Datum static corrections.
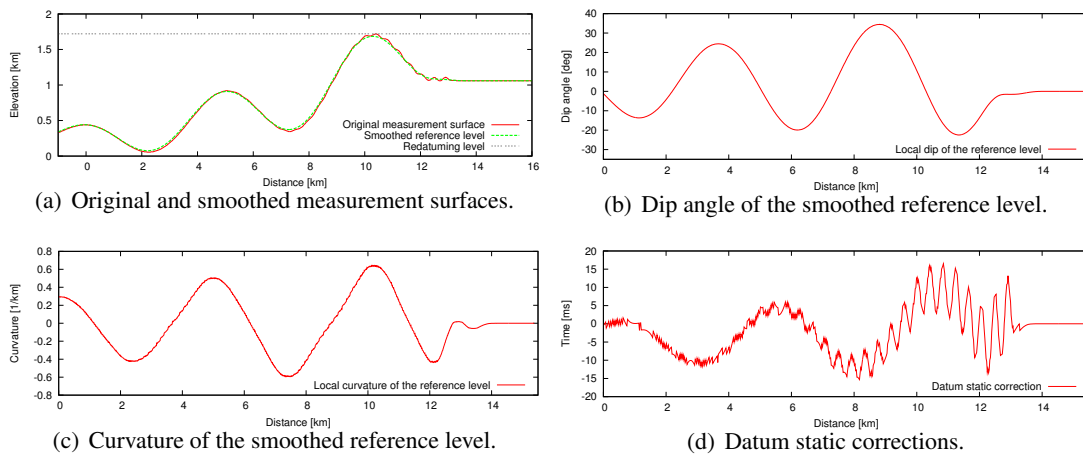
Figure 4.4: (a) Comparison between original and smoothed measurement surfaces. An aperture of 1200 m was considered for the smoothing, i. e., the range of ± 600 m around each surface point X_0 shall be approximated by a parabola with apex in X_0. The small reduction of the long-scale undulation results from the trade off between minimizing the static corrections and minimizing the total deviation of the surface points within a chosen aperture from the local parabolic approximation. (b) Local dip angle of the smoothed reference level . (c) Local curvature of the smoothed reference level. (d) Datum static corrections calculated from the near-surface velocity v_0 = 2500 m/s and the vertical distance between the original and smoothed measurement surfaces.

4.4 Initial CRS stack for smoothly curved topography
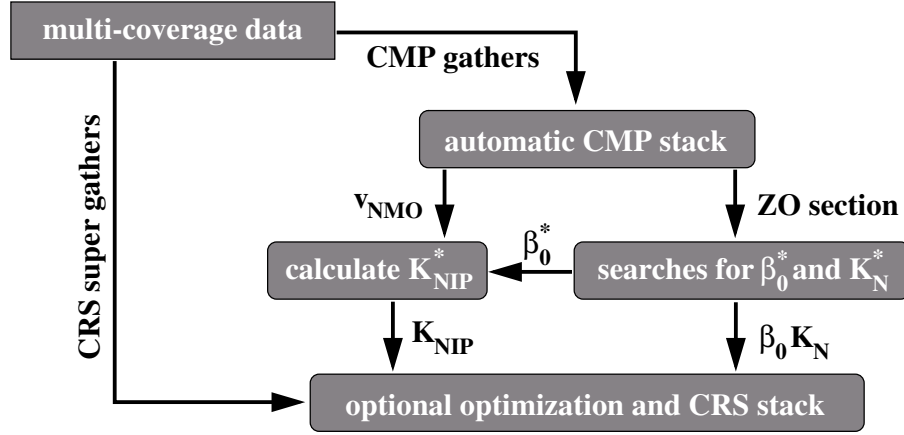
Figure 4.5: Pragmatic search strategy for the initial wavefield attributes: a smoothly curved measurement surface is assumed. The values of β_0, K_{NIP} and K_N are calculated from the stacking parameters β_0^*, K_{NIP}^* and K_N^* according to equations (3.26). Figure modified from Mann (2002)
.

In Section 3.2.4 it was shown that the reduced CRS stack operator for smoothly curved topography (3.25) can substitute the original operator (3.21) that explicitly considers the dip and curvature of the measurement surface, since both operators describe the same kind of traveltime surface. Due to the fact that the attribute search is the most time consuming part of the CRS stack process, this reduced operator is used for the determination of the best-fitting stacking operator. On the one hand, doing this saves several arithmetic operations in the innermost loop where the traveltimes corresponding to a certain triple of attributes are calculated for the subsequent coherence analysis. Furthermore, the number of required parameters is reduced from six ($t_0, v_0, m_x, h_x, \alpha_0, K_0$) to four ($t_0, v_0, m_x, h_x$). On the other hand, the reduced run-time involves the necessity to convert the obtained stacking parameters β_0^*, K_{NIP}^* and K_N^* to the physically interpretable wavefield attributes β_0, K_{NIP} and K_N according to equations (3.26a,b,c) and to transfer the attribute search limits to those limits valid for these apparent attributes.

4.4.1 Search strategy

For details on the employed search strategy, depicted in Figure 4.5, I refer to Müller (1999) and Mann (2002). As mentioned before the global optimization is split into three one-parameter searches applied in specific 2-D subsections of the 3-D prestack data:

- **Automatic CMP stack**: The CMP gather is the only 2D subset of the datacube for which the CRS operator depends on one (combined) parameter, only. Consequently, the first of the three one-parameter searches is applied here. According to Section 3.2.4 the hyperbolic CRS operator for smoothly curved topography and $\Delta m_x = 0$, given by equation (C.1), can be re-written using

the parameters β_0^* and K_{NIP}^*:

$$\tau_{\text{CMP}}^2(0, h_x) = \tau_0^2 + \frac{2\,\tau_0}{v_0}\,K_{\text{NIP}}^*\,\cos^2\beta_0^*\,h_x^2 = \tau_0^2 + \frac{4\,h_x^2}{v_{\text{NMO}}^2}\,, \tag{4.2}$$

with

$$v_{\text{NMO}}^2 = \frac{2\,v_0}{\tau_0\,K_{\text{NIP}}^*\,\cos^2\beta_0^*} \tag{4.3}$$

Please note: $(4/v_{NMO}^2)$ is defined as the coefficient of the h_x^2 term of the hyperbolic second order approximation of the traveltimes in the CMP gather. As a consequence of this, its value is independent of the specific formulation of this traveltime approximation, i.e. does not depend on whether traveltime formula (3.22), (3.25), or (3.21) is used.

For a single CMP gather, the second order traveltime approximation reduces to a simple hyperbola[2] and the CRS stack operator gets identical with the classical CMP stack operator, discussed in Section 1.4.1. Most implementations of the CMP stack determine the stacking velocity semi-manual and only for the prominent events in certain CMP gathers. Afterwards the stack is conducted using a smooth stacking velocity field generated by inter- and extrapolation of the determined stacking velocity values. Contrary to this, the automatic CMP stack determines the stacking velocity fully automatic by coherence analysis and applies this procedure independently for every sample of the ZO section. Finally, the resulting NMO velocity section and CMP stack section provide the input for the second parameter search.

Here and throughout the entire thesis the terms stacking velocity and normal-moveout (NMO) velocity are used synonymously. Strictly speaking, only for homogeneous layers separated by plane horizontal interfaces, v_{NMO} can be seen as the average, here root-mean-square (RMS), velocity of the reflector's overburden (see Appendix C). There are cases in which the subsurface structure causes the NIP wavefront to emerge as a plane wave, e.g. a concave low velocity lense, resulting in an infinite NMO velocity. Even imaginary values of v_{NMO} can occur if K_{NIP} gets negative, e.g. because the NIP-wave passes an odd number of caustics on its way to the surface. In order to handle such cases the actual search parameter was chosen to be the squared inverse of the NMO velocity, i.e. the squared stacking slowness p_{NMO}^2, since this parameter is always real and finite, unless there is no caustic very close to the surface, which is very unlikely.

- **linear ZO search**: the previously simulated ZO section is well suited to determine the emergence angle and NIP wavefront curvature due to its significant azimuth difference to the CMP gather and its increased signal-to-noise ratio. In the ZO section ($h_x = 0$), the hyperbolic CRS operator for a smoothly curved topography, expressed in terms of β_0^* and K_N^* reads:

$$
\begin{aligned}
\tau_{\text{ZO}}^2(\Delta m_x, 0) \;=\; & \left(\tau_0 + \frac{2}{v_0}\,\sin\beta_0^*\,\Delta m_x\right)^2 \\
& + \;\frac{2\,\tau_0}{v_0}\,K_{\text{N}}^*\,\cos^2\beta_0^*\,\Delta m_x^2\,.
\end{aligned}
\tag{4.4}
$$

Choosing a sufficiently small midpoint aperture, e.g. 30% of the full midpoint aperture, the contribution of the second term in equation (4.4) becomes negligible. In other words, K_N^* is

---

[2]Turns to elliptic shape, in the rare cases of $v_{\text{NMO}}^2 < 0$.

assumed to be zero. Taking the square-root on both sides results in the so called *plane wave approximation*

$$\tau_{\mathrm{PW}}(\Delta m_x, 0) = \tau_0 + \frac{2}{v_0} \sin\beta_0^* \, \Delta m_x \,. \tag{4.5}$$

This linear expression solely depends on the parameter β_0^* and allows a one-parameter search for its optimum value. A subsequent stack results in a ZO section very similar to the result of a so-called slant stack, which is mainly a linear radon transformation of the CMP stack section. Knowing β_0^* and v_{NMO} allows to calculate K_{NIP}^* from equation (4.3). Subsequently, β_0 and K_{NIP} can be calculated from equations (3.26). Now, only K_N^* remains to be determined.

- **hyperbolic ZO search**: after finding the optimum value for the parameter β_0^*, the best fitting hyperbolic operator (4.4) can be determined in a one-parameter search using the full midpoint aperture. The curvature of the normal wave K_N and the so-called hyperbolic ZO stack section results from this step. The implementation of this search is more demanding than in case of the two previous searches as the stacking hyperbola is in general not symmetric to the midpoint location X_0 which makes the choice of the sampling interval of tested stacking operators more involved. Furthermore the upper search limits for K_N and K_N^*, respectively, are difficult to choose whereas the lower limit of K_N is obviously zero. For a homogeneous medium K_N can never be larger that K_{NIP}, because $K_N = K_{NIP}$ signifies a diffraction. However, in real situations larger values can be observed. Therefore, according to Mann (2002), the upper search limit for K_N is chosen in such a way that the slope of the stacking operator does not exceed $\pm 1/v_0$ which is the slope of the direct waves traveling in x- and $-x$-direction, respectively.

After the three kinematic wavefield attributes are determined for every sample of the ZO section it is possible calculate the associated CRS stack operator for each of this samples and to conduct the so-called initial CRS stack.

4.4.2 Search-range estimation

It is very important for the efficiency and for the success of the search strategy described in the previous section that the search ranges of the stacking parameters are defined in an appropriate way. However, in case of top-surface topography, the interfering influences of subsurface structure and measurement surface characteristics make the choice of the search limits more involved. In this matter, the fact that the stacking parameters β_0^*, K_N^* and K_{NIP}^* depend on the local dip and curvature of the measurement surface, leads to a considerable complication. Furthermore, as follows from equation (C.1), also the determined NMO velocity is strongly influenced by the shape of the measurement surface, particularly by its curvature (see Appendix C). In case of homogeneous layers separated by horizontal reflectors the influence of the topography on the obtained NMO velocities can nicely be observed. The strongly fluctuating NMO velocities obtained by the automatic CMP stack for the model depicted in Figure 4.3 are displayed in Figure 4.6. Below the hilltops the NMO velocity becomes imaginary since the traveltime of the reflection events decreases with offset.

Processing real data, it is often necessary to exclude for instance very small NMO velocities from the search, as this velocities are related to multiples. However, the stacking velocity related to a certain multiple varies lateral with the local dip and curvature of the measurement surface and the search limits have to account for this effect. In order to solve this problem, I related the actual search limits to those limits that would hold if the real measurement surface would be replaced by a horizontal
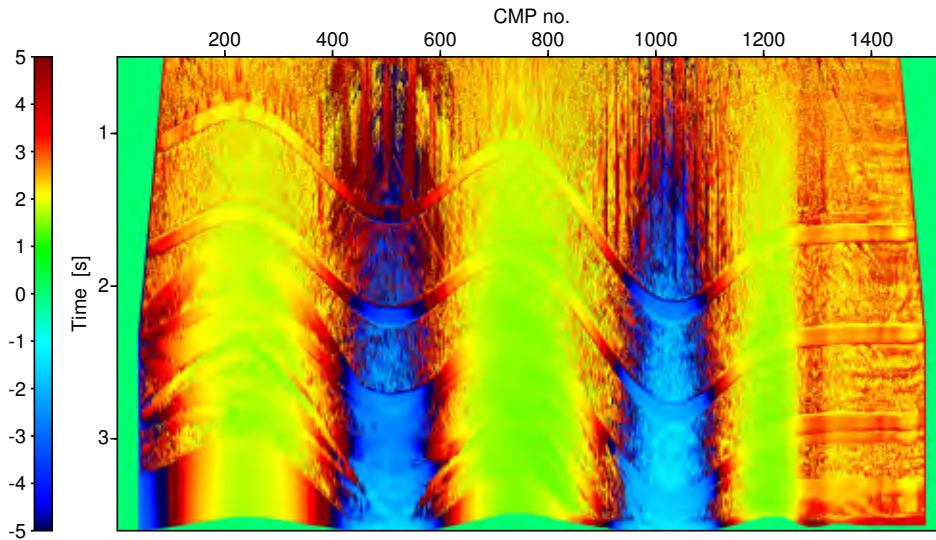
Figure 4.6: ENI/Syndata: NMO velocity [km/s] obtained by the automatic CMP stack. Note that the *signed square root*, $\sqrt{a} := sign(a) \sqrt{|a|}$, taken from v_{NMO}^2 was used to also visualize imaginary values of the stacking velocity resulting from negative values of v_{NMO}^2.

measurement surface. How to choose such topography independent search limits is well known from the conventional 2D CRS stack for a planar measurement surface (see Mann, 2002). To derive the relations, between the actual search limits and those *reference limits* is the purpose of this section. For the model depicted in Figure 4.3 a comparison between the forward modeled stacking parameters and the associated search limits, calculated from topography independent reference limits can be found in Heilmann (2002).

In the presented implementations K_{NIP}^* and K_{NIP}, respectively, are no direct search parameters. They are computed from the obtained values of v_{NMO} and β_0^*, according to equation (4.3) and (3.26a). Therefore, search limits of K_{NIP} and K_{NIP}^* will not explicitly be discussed, but similar derivations as for K_N and K_N^* would hold in this case, too.

Search range of the NMO velocity

The NMO velocity is the first parameter which has to be determined during the initial attribute search. As mentioned before, the values of the NMO velocity are strongly affected by the dip and particularly by the curvature of the measurement surface. For the conventional CRS stack a multitude of experience exists how the search limits of the NMO velocity can be chosen with respect to an assumed subsurface model. Consequently zero-dip NMO velocity limits (or limits for K_{NIP}) can easily be derived from the v_{NMO} and β_0 limits by means of equation (C.6). These zero-dip NMO velocity limits that hold for the conventional CRS stack, shall serve in the following as a unified, acquisition independent, basis, from which the v_{NMO} search limits that hold for the actual measurement surface, can be derived. Of course the zero-dip NMO velocity limits can be replaced by RMS velocity limits, if the conditions under which the RMS velocity is defined are supposed to be met.

To find a relation between the limits of the actually measured NMO velocity and the zero-dip NMO velocity range mentioned above, we have to analyze equation (C.8a). The first observation is that one

has to know the take off angle β_0 in order to calculate the searched-for NMO velocity limits from the respective zero-dip NMO velocity limits. This leads to a severe problem, because, as stated above, the NMO velocity is the first parameter that is determined and thus the angle β_0 is still unknown at this stage. Unfortunately it is hardly possible to permute the order in which the parameters are determined.

To find a solution, we have to look at the situation more closely. Actually, we are not searching the limiting values of v_{NMO}, but the limits of the coefficient of the h^2-term of the traveltime, which depends, according to equation (4.2), on v_{NMO}^{-2}. If we call the inverse of v_{NMO} NMO slowness p_{NMO}, then we have to find infimum and supremum of the function

$$ p_{NMO}^2 = \frac{2v_0 \cos^2{(\beta_0 + \alpha_0)} - K_0 t_0 \cos{(\beta_0 + \alpha_0)}\ v_{NMO,ZD}^2}{2v_0 \cos^2{\alpha_0} v_{NMO,ZD}^2} \ , \tag{4.6} $$

which is the inverse of equation (C.8a). This function of $v_{NMO,ZD}^2$ and β_0 describes a surface in the 3D space. To determine infimum and supremum we have to evaluate equation (4.6) at the borders of the search ranges of $v_{NMO,ZD}$ and β_0 as well as potential extrema within these ranges. The condition for the extrema reads

$$ \frac{\partial p_{NMO}^2}{\partial (v_{NMO,ZD}^2)} = 0 \quad \text{and} \quad \frac{\partial p_{NMO}^2}{\partial \beta_0} = 0 \ . \tag{4.7} $$

The first of the two conditions above can be evaluated without problems. If we take the derivative of p_{NMO} with respect to $v_{NMO,ZD}^2$, we obtain

$$ \frac{\partial p_{NMO}^2}{\partial (v_{NMO,ZD}^2)} = - \frac{\cos^2{(\beta_0 + \alpha_0)}}{\cos^2{\alpha_0} v_{NMO,ZO}^4} \ . \tag{4.8} $$

Equation (4.8) only vanishes for $\beta_0 + \alpha = \pm \pi/2$, i. e. for the obviously pointless case of grazing rays emerging tangentially to the acquisition surface. Thus, there are nor extrema and inflection points in all relevant cases such that p_{NMO}^2 is a strictly monotonous function of $v_{NMO,ZD}^2$ with pole in $v_{NMO,ZD}^2 = 0$. It decreases for positive $v_{NMO,ZD}^2$ values and increases for negative $v_{NMO,ZD}^2$ values. Consequently, the infimum and supremum lie at the borders of the p_{NMO}^2 surface, at

$$ p_{NMO}^2 = p_{NMO}^2 \left(\left(v_{NMO,ZD}^2 \right)^{min}, \beta_0 \right) \quad \text{and} \quad p_{NMO}^2 = p_{NMO}^2 \left(\left(v_{NMO,ZD}^2 \right)^{max}, \beta_0 \right) \ , \tag{4.9} $$

where $\left(v_{NMO,ZD}^2 \right)^{min}$ and $\left(v_{NMO,ZD}^2 \right)^{max}$ are the pre-estimated limiting values of the squared zero-dip NMO velocity. Depending on the assumed subsurface model $\left(v_{NMO,ZD}^2 \right)^{min}$ can be either positive or negative.

The first derivative of p_{NMO}^2 with respect to β_0 reads

$$ \frac{\partial p_{NMO}^2}{\partial \beta_0} = \frac{\sin{(\beta_0 + \alpha_0)}\,(K_0 t_0 v_{NMO,ZD}^2 - 4v_0 \cos{(\beta_0 + \alpha_0)})}{2v_0 v_{NMO,ZD}^2 \cos^2{\alpha_0}} \ . \tag{4.10} $$

If we set this equation equal to zero, solve for $(\beta_0 + \alpha_0)$, and consider that the extrema have to lie at the $v_{NMO,ZD}^{min,max}$ borders of the p_{NMO}^2 surface we find,

$$ (\beta_0 + \alpha_0)^{(1)} = 0 \quad \text{and} \quad \cos{(\beta_0 + \alpha_0)^{(2)}} = \left(\frac{K_0 t_0 (v_{NMO,ZD}^{min,max})^2}{4v_0} \right) = \frac{K_0}{2K_{NIP}^{min,max}} \ , \tag{4.11} $$
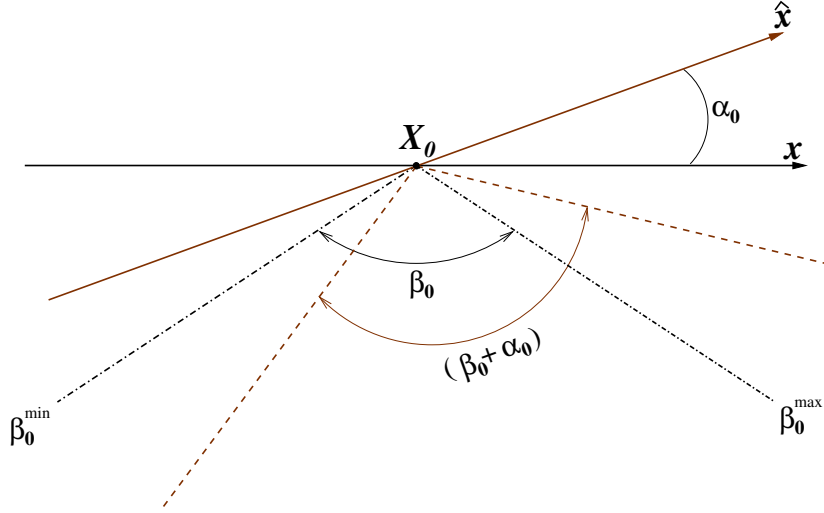
Figure 4.7: The $\hat{x}$-axis of the local Cartesian coordinate system tangent to the measurement surface in X_0 (brown) has the (positive) dip α_0 with respect to the horizontal x-axis of the global coordinate system (black). To keep the figure simple, the z-axes and $\hat{z}$-axis are omitted. The search range $[-60°, 60°]$ of the take-off angle β_0 and the range of the corresponding $(\beta_0 + \alpha_0)$ values is depicted. Since a maximum value for $(\beta_0 + \alpha_0)$ that is larger than $\pi/2$ or a minimum value smaller than $-\pi/2$ is not to be expected the corresponding range of $(\beta_0 + \alpha_0)$ is limited by $\pm\pi/2$.

were we have used equation (C.6) to express $\left(v_{NMO,ZD}^2\right)^{min,max}$ in terms of $K_{NIP}^{min,max}$, according to

$$K_{NIP}^{max} = \frac{2v_0}{t_0(v_{NMO,ZD}^{min})^2} \quad \text{and} \quad K_{NIP}^{min} = \frac{2v_0}{t_0(v_{NMO,ZD}^{max})^2} \; . \tag{4.12}$$

At this point, we have to consider the limits of the search range of the take-off angle β_0, depicted in Figure 4.7. In case of a smoothly curved measurement surface with local dip α_0 it results:

$$-\pi/2 \le \left(\beta_0^{min} + \alpha_0\right) \le (\beta_0 + \alpha_0) \le \left(\beta_0^{max} + \alpha_0\right) \le \pi/2 \; . \tag{4.13}$$

Due to this limitation, the second solution for $(\beta_0 + \alpha_0)$, i.e., $(\beta_0 + \alpha_0)^{(2)}$, is only valid for,

$$\frac{K_0}{2K_{NIP}^{min,max}} \ge \min\left(\cos\left(\beta_0^{min} + \alpha_0\right), \cos\left(\beta_0^{max} + \alpha_0\right)\right) \; . \tag{4.14}$$

If this condition is met, we get possible candidates for infimum and supremum, which read

$$C^{(21)} = p_{NMO}^2((v_{NMO,ZD}^2)^{min}, (\beta_0 + \alpha_0)^{(2)}) \, , \quad C^{(22)} = p_{NMO}^2((v_{NMO,ZD}^2)^{max}, (\beta_0 + \alpha_0)^{(2)}) \; . \tag{4.15}$$

Otherwise, if $(\beta_0 + \alpha_0)^{(2)}$ lies outside of the considered range and possible infima and suprema, which correspond to this solution, lie at the respective edges of the $p_{NMO}^2(v_{NMO,ZD}^2, \beta_0)$ surface. These are

$$\begin{aligned}
C^{(a)} &= p_{NMO}^2((v_{NMO,ZD}^2)^{min}, \left(\beta_0^{min} + \alpha_0\right)) \, , \quad C^{(b)} = p_{NMO}^2((v_{NMO,ZD}^2)^{min}, \left(\beta_0^{max} + \alpha_0\right)) \text{ and} \\
C^{(c)} &= p_{NMO}^2((v_{NMO,ZD}^2)^{max}, \left(\beta_0^{min} + \alpha_0\right)) \, , \quad C^{(d)} = p_{NMO}^2((v_{NMO,ZD}^2)^{max}, \left(\beta_0^{max} + \alpha_0\right)) \; .
\end{aligned} \tag{4.16}$$

The first solution $(\beta_0 + \alpha_0)^{(1)}$ is always valid and yields

$$C^{(11)} = p_{NMO}^2((v_{NMO,ZD}^2)^{min}, (\beta_0 + \alpha_0)^{(1)}) \,, \quad C^{(12)} = p_{NMO}^2((v_{NMO,ZD}^2)^{max}, (\beta_0 + \alpha_0)^{(1)}) \,. \quad (4.17)$$

To make things clearer, I will discuss an example of how, according to our derivations, the maximum and minimum values of the NMO velocity are obtained. If, e.g.,

$$\frac{K_0}{2K_{NIP}^{min}} \ge \min\left(\cos(\beta_0^{min} + \alpha_0), \cos(\beta_0^{max} + \alpha_0)\right) \,, \quad \text{and} \quad \frac{K_0}{2K_{NIP}^{max}} < \min\left(\cos(\beta_0^{min} + \alpha_0), \cos(\beta_0^{max} + \alpha_0)\right) \,,$$

then we have the possible solutions $\{C^{(11)}, C^{(12)}, C^{(a)}, C^{(b)}, C^{(22)}\}$.

The solution $C^{(21)}$ is not valid, because the value of $(\beta_0 + \alpha_0)^{(2)}$, which results for $K_{NIP} = K_{NIP}^{max}$ lies outside the considered range. Consequently, $C^{(21)}$ has to be replaced by $C^{(a)}$ and $C^{(b)}$. Thus, the limiting values for v_{NMO}^2 are

$$\left(v_{NMO}^2\right)^{max} = \frac{1}{\left(p_{NMO}^2\right)^{min}} = \frac{1}{\min\{C^{(1)}, C^{(2)}, C^{(a)}, C^{(b)}, C^{(4)}\}} \,, \quad \text{and}$$

$$\left(v_{NMO}^2\right)^{min} = \frac{1}{\left(p_{NMO}^2\right)^{max}} = \frac{1}{\max\{C^{(1)}, C^{(2)}, C^{(a)}, C^{(b)}, C^{(4)}\}} \,.$$

The actual determination of infimum and supremum is performed numerically by evaluating and comparing all possible candidates.

Please note, as mentioned before, all above derivations hold also for the RMS velocity, which is nothing more than the zero-dip NMO velocity for a special subsurface structure. Thus, if the subsurface can be assumed to be constituted of homogeneous layers, separated by planar and parallel reflectors, RMS velocity limits can be used instead of zero-dip NMO velocity limits, simply by substituting $v_{NMO,ZD}$ by v_{RMS} in the equations above.

Search range of β_0 and β_0^*

In case of the conventional CRS stack for a planar measurement surface, β_0 and, thus, also its search range are related to the surface normal and the limits of the search range are constant along the measurement surface.

However, for a smoothly curved measurement surface it makes no sense to allow values for $(\beta_0 + \alpha_0)$ that are larger than 90° or smaller than −90° (see Figure 4.7). If we denote the limits of the search range in case of a horizontal measurement surface by $\beta_0^{max,g}$ and $\beta_0^{min,g}$ we obtain the search limits β_0^{max} and β_0^{min} by the following relation:

$$\beta_0^{max} = \min\left(\beta_0^{max,g} \,, \frac{\pi}{2} - \alpha_0\right) \quad \text{and} \quad \beta_0^{min} = \max\left(\beta_0^{min,g} \,, -\frac{\pi}{2} - \alpha_0\right) \,. \quad (4.18)$$

Inserting these limits into equation (3.26a) results in the search limits of β_0^* that read:

$$\beta_0^{*max} = \arcsin\left(\frac{\sin\left(\min\left(\beta_0^{max,g} \,, \frac{\pi}{2} - \alpha_0\right)\right)}{\cos\alpha_0}\right) \,, \quad (4.19a)$$

$$\beta_0^{*min} = \arcsin\left(\frac{\sin\left(\max\left(\beta_0^{min,g} \,, -\frac{\pi}{2} - \alpha_0\right)\right)}{\cos\alpha_0}\right) \,. \quad (4.19b)$$

65

As mentioned before, β_0^* has, under certain circumstances, complex values. Such a situation is always given if the modulus of the argument of the arcus sine in the equations above is larger than one. Consequently, in any case were complex β_0^* are possible, the respective limiting values have to be complex, too.

Search range of K_N and K_N^*

If we use K_N^* instead of K_N as search parameter of the hyperbolic ZO search and consequently do not consider the actual dip and curvature of the measurement surface, we have to transfer the search range that holds for K_N in order to get a appropriate search range for K_N^*. If we solve equation (3.26b) for K_N^* and insert at the righthand-side the search limits of K_N, we get

$$K_N^{*max} = \frac{K_N^{max}\left(1 - \cos^2\alpha_0 \sin^2\beta_0^*\right) - K_0\sqrt{1 - \cos^2\alpha_0 \sin^2\beta_0^*}}{\cos^2\alpha_0 \cos^2\beta_0^*} \, , \tag{4.20a}$$

and

$$K_N^{*min} = \frac{K_N^{min}\left(1 - \cos^2\alpha_0 \sin^2\beta_0^*\right) - K_0\sqrt{1 - \cos^2\alpha_0 \sin^2\beta_0^*}}{\cos^2\alpha_0 \cos^2\beta_0^*} \, , \tag{4.20b}$$

Please note, that the use of these relations demands that β_0 is already determined. In all current implementations of the 2D ZO CRS stack K_N is the last parameter that is searched for. Otherwise, a procedure similar to the v_{NMO} search-range determination, presented in Section 4.4.2, would be necessary.

4.4.3 Search and stacking apertures

The choice of an appropriate aperture that limits the traveltime operator both during the attribute search and during the stacking process is very important to achieve an optimum resolution and signal-to-noise ratio as well as reliable attributes. In this regard it would be desirable to have certain criteria that allow to define these apertures in a data-driven way. However, it is evident that the CRS attributes are not yet available before the initial search and thus, optimum apertures derived from the CRS attributes do not exist at this early stage. At the first sight, a possible solution for this problem could be to calculate individual search apertures for every tested attribute triple. Unfortunately, this is not practical because the conducted coherence analysis is very sensitive to the number of contributing traces so that coherence values calculated with different apertures are not comparable. For this reason, user-defined apertures are necessary for the initial attribute search, but can be checked afterwards using the obtained attributes. In this regard, the only search process which directly benefits from the CRS attributes is the local three-parameter optimization. Here, it makes sense to use the initial attributes to calculate well-suited search aperture limits for the optimization even though the user-defined aperture is still necessary to limit the number of contributing traces at locations where the attributes are not reliable.

Contrary to the search process, it is always possible to use the attributes to limit the aperture for the stacking process. However, it has to be considered that search and stacking apertures should not differ too much because otherwise it cannot be guaranteed that the determined attributes define the best fitting stacking operator. In case of the presented implementation both was realized: for the initial

(a) ZO aperture.   (b) CMP aperture.   (c) CRS aperture.
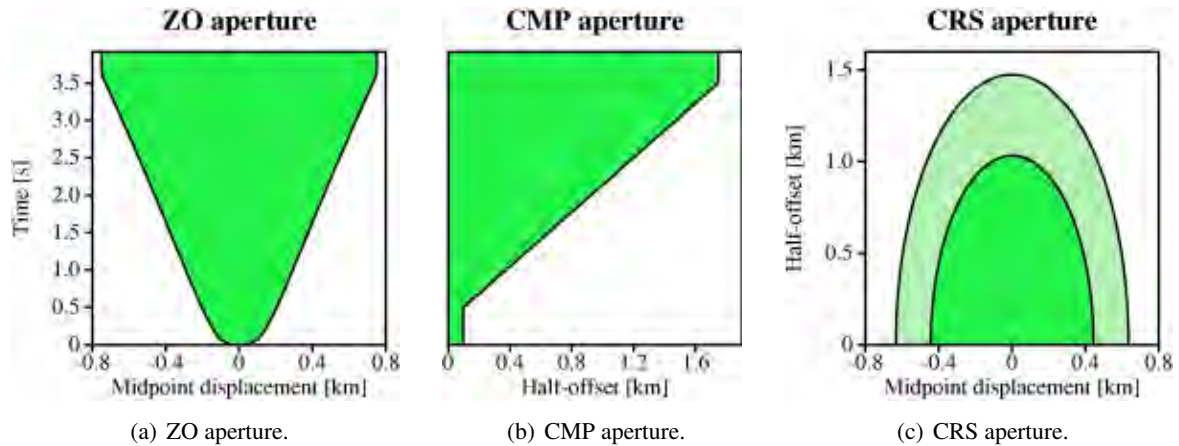
Figure 4.8: Slices of the CRS aperture. (a) shows an example of a common-offset slice, here at $h = 0$, i.e., the ZO aperture for a dominant frequency of 30 Hz and an average velocity ranging from 1.5 km/s to 3 km/s. The minimum ZO aperture is set to 50 m and the maximum to 750 m. (b) represents a common-midpoint slice, i.e., the CMP aperture. Between the points (t_0, h)=(0.5 s, 0.1 km) and (3.5 s, 1.75 km) this aperture increases linearly. Outside this area, the CMP aperture is extrapolated constantly. (c) is a time slice at $t_0 = 3$ s and illustrates the spatial extent of the CRS aperture. The shaded area is the part of the aperture that is tapered. The inner ellipse is usually 70% of the outer ellipse that basically covers the projected second Fresnel zone for ZO (taken from Mann, 2002).

stack as well as for the optimized stack an additional stack section based on apertures derived from the attributes is generated besides the conventional stack section based on the user defined aperture.

Let us take a closer look at the criteria we have at hand to define the optimum apertures in offset and midpoint direction. Apart from the run-time which linearly increases with the number of traces that contribute, there are mainly two points that have to be taken into account:

1. the size of the Fresnel zone (see Appendix B) which defines the area containing rays with signals that interfere constructively at the receiver. This criterion defines the maximum aperture which can be used without loss of lateral resolution.

2. the size of the paraxial vicinity for which the employed second-order traveltime approximation is sufficiently valid to ensure a constructive summation of reflected energy. This criterion defines the aperture for which a maximum signal-to-noise ratio can be achieved by stacking.

Unfortunately, the second criterion is difficult to evaluate. It strongly depends on the complexity of the unknown subsurface structure and so far, no relation between the stacking parameters itself and the range of validity of the associated second-order traveltime approximation could be established. As a consequence, only empirical knowledge can be applied in this regard and there is still the experience of the user required to decide whether the second order approximation is fulfilled or not. Thus, it remains only the Fresnel zone as candidate for a data-driven criteria to limit the extent of the traveltime operator. For this purpose it is most suitable to consider the so-called *projected Fresnel zone*, i.e. the

time-domain counterpart of the interface Fresnel zone[3]. According to Appendix B its approximate size W_F estimated by means of the CRS attributes reads

$$\frac{W_F}{2} = |x_m - x_0| = \frac{1}{\cos \alpha} \sqrt{\frac{v_0 \, T}{2 \, |K_N - K_{NIP}|}} \; . \tag{4.21}$$

Due to the missing offset dependency of equation (B.4) no criterion for the midpoint aperture for finite offset can be derived from this. Nevertheless, it is well suited to define an optimum midpoint aperture for ZO. A detailed analysis of this problem can be found in Mann (2002).

Midpoint aperture

It was already mentioned that user-defined apertures are necessary since reliable attributes are not available at every stage of the processing and for every sample of the ZO section. As is depicted in Figure 4.8(a), the midpoint aperture is linearly interpolated between user-defined minimum and maximum midpoint apertures valid for minimum and maximum traveltimes. After the initial search, the projected Fresnel zone is calculated from the obtained attributes and considered for a separate initial stack, which can later be compared to the one computed within the user-given midpoint aperture. Furthermore, a quality-control section that displays the size of the projected Fresnel zone is generated which should not diverge too much from the user-given aperture.
For the local optimization of the initial attributes, the projected Fresnel zone estimated from the initial attributes is used to restrict the midpoint aperture. As in case of the initial stack, a quality control section with the value of the projected Fresnel zone, a stack section according to the user-defined midpoint aperture and a stack section using a midpoint aperture defined by means of the projected Fresnel zone are generated.

Offset aperture

Since there is no possibility to derive appropriate limits for the offset aperture in a data-driven manner, user-defined limits are the only choice. At least, there is a multitude of experience from conventional CMP stack or NMO/DMO/stack processing, how to choose these limits with respect to specific sub-surface structures. As a rule of thumb, the offset should not be larger than the depth which is assumed for the respective traveltime. As depicted in Figure 4.8(b) the time-dependent offset aperture is defined by two pairs of aperture and traveltime values. For traveltimes within these two limits, the aperture is linearly interpolated; for traveltimes that lie outside this range the aperture is extrapolated constantly. For the stack along the entire, spatial CRS operator, either with the initial or the optimized attributes, an extended definition of the offset aperture is used by the current implementation. As depicted in Figure 4.8(a), the maximum offset is limited by an elliptic aperture in the midpoint/offset plane with the half-axes given by the above described midpoint and offset apertures, respectively.

4.5 Event-consistent smoothing

In the previous section it was discussed how a triple of kinematic wavefield attributes is determined independently for each sample of the ZO section. Compared to conventional approaches working with

---

[3](Interface) Fresnel zone (after Sheriff, 2002): the portion of a reflector from which reflected energy can reach a detector within one-half wavelength of the first reflected energy

smooth stacking velocity models based on selected CMP locations and reflection events, it provides more detailed information about the subsurface structure. However, this is only one side of the medal, on the other side outliers and fluctuations can be observed in the attribute sections that are mainly caused by limitations of the three-times-one parameter search, a variable data quality along the line and random effects stemming from the discrete nature of the in- and output data. At this stage, it makes sense to take advantage of the fact that a smooth behavior of the subsurface structure can always be expected to a certain extent. Therefore, event-consistent smoothing of the initial attributes is well justified (see also: Mann and Höcht, 2003) and even more since the smoothed attributes are not the final result, but will undergo a further optimization which can restore local changes of the attributes if they provide a higher coherence with the data.

The employed smoothing algorithm is based on the combined application of mean and median filters within volumes aligned with reflection events (Hertweck et al., 2005). The information about slopes of events in the time domain is readily available from the CRS attributes themselves and allows to avoid the mixing of intersecting events. In detail, for every point P in the ZO section, the following steps are performed:

1. A parallelogram-shaped window of user-defined vertical and horizontal extention is centered around P and aligned with the local dip of the reflection event. The latter is equivalent to the horizontal slowness p of the associated normal ray which can be calculated from the emergence angle β_0 and the near-surface velocity[4] v_0 used by the CRS stack. It holds

$$p = \frac{1}{2} \frac{\partial t}{\partial x_m} \bigg|_{(x_m = x_0, h = 0)} = \frac{sin\beta_0}{v_0} \ . \tag{4.22}$$

   In order to enable the use of a laterally variable near-surface velocity, the implementation was extended at this point to support this feature by reading the near-surface velocity from the trace-header information of the input sections instead of considering a constant user-defined value.

2. The coherence values associated with the samples located within this tilted window are used to reject samples with unreliable, possibly unphysical attribute values: each sample that does not exceed a user-defined coherence threshold is excluded from the smoothing process.

3. The horizontal slowness p, calculated from β_0 and v_0, provides a criterion to avoid the mixing of different events, especially in case of conflicting dip situations: only ZO samples with similar horizontal slowness are accepted for the smoothing process, again controlled by a given threshold, which the modulus of the difference in p must not exceed. At this point the horizontal slowness p has to be evaluated instead of the emergence angle β_0 in order to allow for a laterally variable near-surface velocity.

4. The attribute values associated with the remaining ZO locations enter into a median filter, i. e. they are sorted by magnitude and discriminated if located outside a user-defined fraction of all values centered around the median. Finally the remaining values of each attribute are subject to arithmetic averaging.

5. The averaged attribute values are assigned to the considered ZO sample P.

---

[4]Please note, the horizontal slowness itself is independent of the near-surface velocity v_0 whereas the correct determination of the emergence angle β_0 requires the knowledge of v_0. As a consequence, the event consistency of the smoothing algorithm remains valid even if a wrong near-surface velocity was chosen for the CRS stack.

As a result, the smoothing algorithm works in an event-consistent manner and does not imply any loss of information about the parameterized reflection events (e. g., Mann and Duveneck, 2004). Thus, even in the case of conflicting dip situations, it often provides significantly improved input for the subsequent local optimization. In the case of complex near-surface conditions which often lead to a strongly variable data quality, this intermediate processing step proved especially successful.

4.6 Three-parameter optimization considering the true topography

As mentioned before, the wavefield attributes determined by the three-times-one parameter search described above cannot be expected to be exactly the same as those optimum values that a global three parameter search would yield. For this reason, the conventional CRS stack for planar topography employs a local three parameter optimization. In case of topography there are even more reasons for such a final optimization:

- The CRS stack approach for a smoothly curved measurement surface applied for the initial search and stack process has its weakness at inflection points of the topography where the assumption of a locally parabolic shape fails.

- The datum-static corrections introduce small traveltime errors for rays with non-zero emergence angles which can deteriorate the extracted attributes to a certain extent.

To compensate these drawbacks, both, the local three-parameter optimization and the final stacking are applied to the original, i. e., uncorrected, prestack data and make use of the more accurate traveltime operator for arbitrary topography (3.11).

The CRS operator for arbitrary topography has the important feature that the elevation of the emergence point X_0 of each ZO ray to be simulated can be chosen arbitrarily. This property provides the link to the initial results, since this allows to chose their smoothly curved reference level as the reference level of the optimization, too. Consequently, the ZO rays to be simulated are identical in both cases. Therefore, it can be expected that the CRS attributes obtained in the previous step are close to their optimum values and, thus, well suited as initial values for a local three-parameter optimization using equation (3.11). The objective function to be maximized is, as in the case of single-parameter searches, semblance (Neidell and Taner, 1971), a measure of the coherence of the prestack data along the stacking operator.

As mentioned before, the presented implementation utilizes the *flexible polyhedron search* by Nelder and Mead (1965). During the last years, the latter proved to be robust and stable in numerous examples when applied in the CRS stack for planar topography. For a scalar objective function $f(\vec{x})$, where $\vec{x}$ is a vector with $n \geq 2$ components, this local optimization algorithm propagates a polyhedron with $n + 1$ vertices through the n-dimensional parameter space. Starting with a given polyhedron, the method only requires the values of the objective function f at the vertices $\vec{x}_i$ and at internally calculated new potential vertex locations. Derivatives of the objective function are not required. In this case, where the objective function depends on the three attributes, i. e. β_0, K_{NIP}, and K_N, a moving tetrahedron is used. The evolution of shape and position of this tetrahedron during the iterations performed is controlled by three basic operations: reflection at the center of gravity, expansion, and contraction. All in all, there are six different transformations that can be applied to the tetrahedron in each iteration:

(a) Coherence after initial attribute search.   (b) Coherence after optimization.
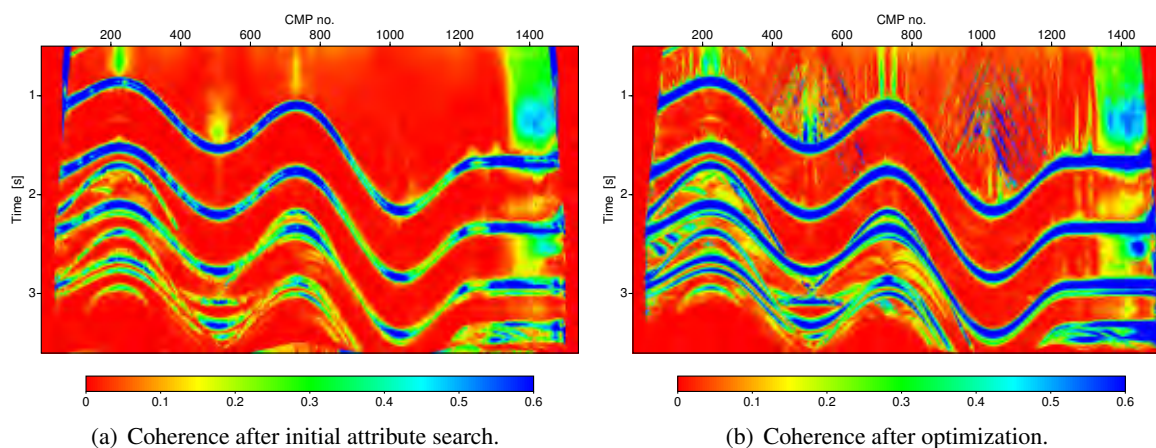
Figure 4.9: (a) Coherence section after initial attribute search. (b) Coherence section after optimization. It is obvious that the coherence in general, but especially at inflection points of the topography, could be significantly increased by directly considering the topography during the optimization.

reflection, reflection and expansion, contraction, reflection and contraction, reduction, reflection and reduction. These transformations enable the tetrahedron to propagate through the parameter space (reflection) with the option to increase and decrease its propagation velocity (expansion and contraction, respectively). In the vicinity of the searched-for minimum or on narrow maxima, the tetrahedron is also able to shrink (reduction). For details on this algorithm and on adaptations that had to be made for the CRS stack implementation, I refer to Himmelblau (1972) and Mann (2002).

For the simple synthetic data example used in this chapter, a comparison between the coherence obtained by the initial stack and by the optimization is depicted in Figure 4.9. A significant increase of coherence can be observed, particularly at the inflection points of the topography and at the right hand side of the model where the measurement surface is undulating on a small lateral scale. The optimized stack result is depicted in Figure 4.10. To confine the spatial extent of the stacking operator used for parameter search and stack, the projected first Fresnel zone calculated from the initial attributes was taken into account. The strong acquisition footprint caused by the top-surface topography is obvious. The surface multiples that are contained in the data can be distinguished from the inter layer multiples by the fact that they show two-times the acquisition footprint.

The attribute sections that resulted from the local three-parameter optimization of the initial attributes are depicted in Figure 4.11, together with a NMO velocity section which was calculated from the latter using equation (C.3). In this case the NMO-velocity corresponds to a horizontal measurement surface through X_0 and coincides with the RMS-velocity (see Appendix C). As expected, the emergence angle is virtually zero along each of the reflection events. The same holds for the N-wave curvature to which the laterally variable vertical distance to the measurement surface has no influence in this case. In contrast to this, the values of the NIP-wave radius and of the NMO-velocity obviously depend on the elevation of the associated emergence point of the simulated ZO ray. For the very shallow part of the first reflection, at the left hand side of the image, the time dependent search aperture was a little bit too narrow to ensure a stable determination of R_{NIP}, which can be better seen at the v_{NMO} section. The multiples contained in the data exhibit significantly lower NMO velocities than primary reflections with similar traveltime and, thus, could be attenuated by using more restrictive search limits.
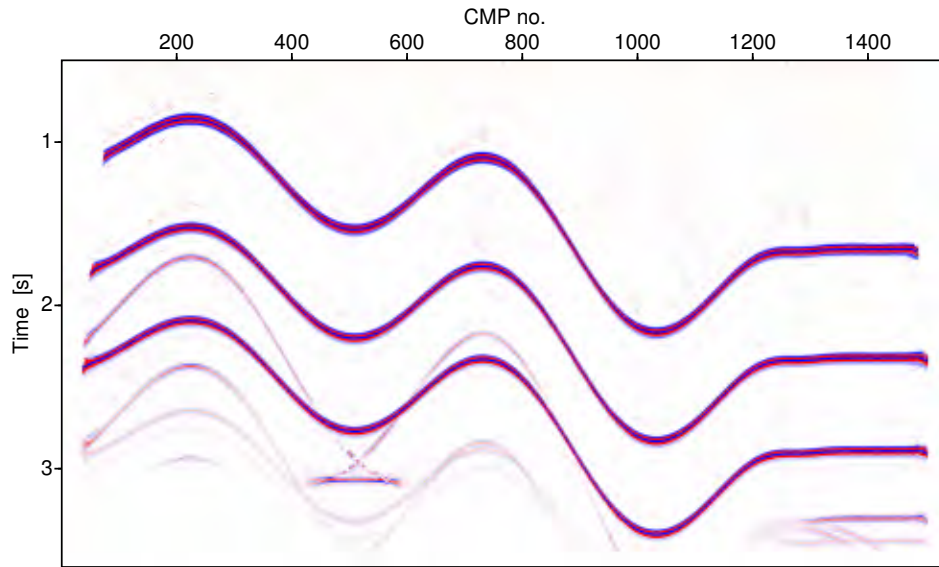
Figure 4.10: Optimized CRS stack section. The stack was performed using the projected Fresnel zone to confine the midpoint aperture.

(a) Emergence angle (°).

(b) NIP-wave radius (km).

(c) N-wave curvature (1/km).

(d) Normal moveout velocity (km/s).
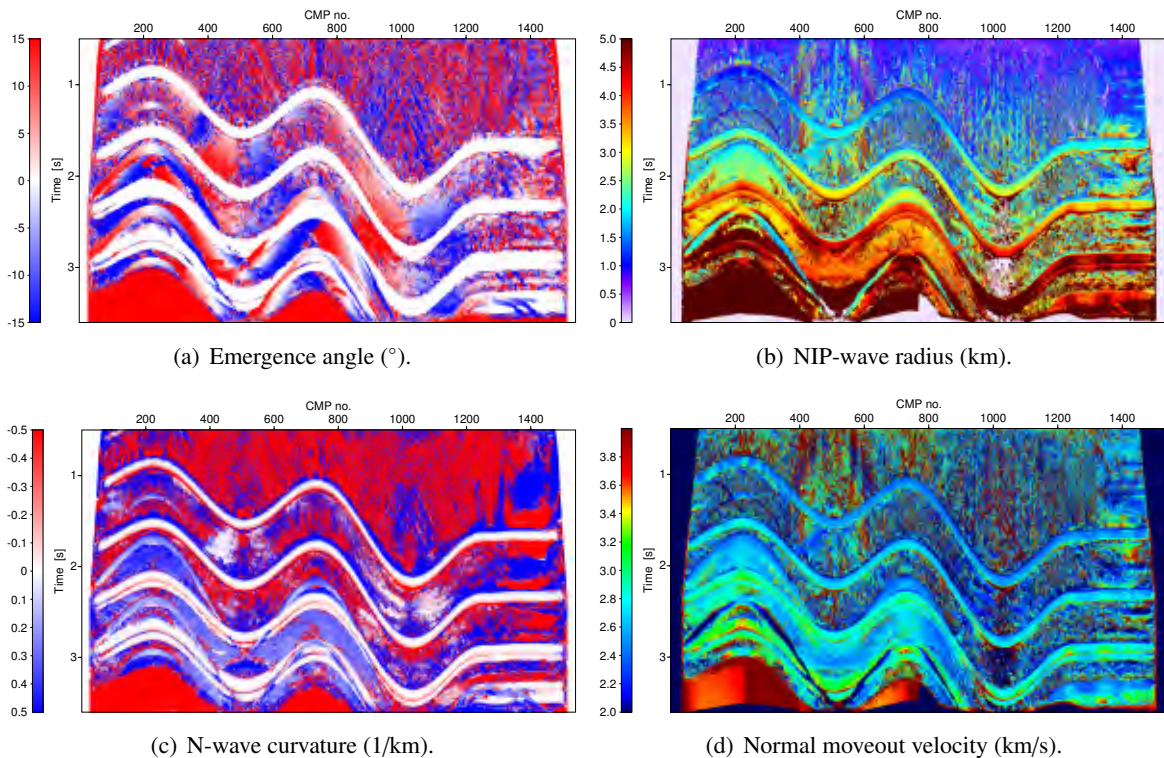
Figure 4.11: (a) Due to the horizontal layering all simulated ZO rays emerge vertically at the measurement surface. (b) For a horizontally layered structure, R_{NIP} increases linearly with depth so that the acquisition footprint is clearly observable (c) Due to the planar layering, the N-wave propagates as a planar wave with $K_N = 0$, so that no acquisition footprint is observable in this case. (d) The NMO velocity calculated from the optimized attributes, according to equation (C.3), coincides in this case with the RMS velocity.

4.7 Redatuming of the CRS stack results

Floating datum sections are no appropriate input for interpretation or further processing: the acquisition footprint, inherently contained in the stack and attribute sections makes the structural interpretation cumbersome and the use of the extracted CRS attributes, e.g. for tomographic inversion, difficult. For this purpose, a redatuming procedure (see also Section 3.3) was implemented that relates the CRS stack results, i.e. stack, attribute and coherence sections, to a fictitious horizontal measurement surface. The elevation of the reference level can be chosen arbitrarily; the default value is 10 m above the highest point of the topography. In general it is recommended to chose the horizontal reference level above the actual topography. The only case where downward redatuming would be preferable is the case of a constant velocity layer between the actual measurement surface and the redatuming level below. Otherwise, a laterally variable redatuming velocity would have to be considered for the redatuming process which is not supported by the current implementation. It was already discussed in Section 3.3 that each simulated ZO ray, specified by its traveltime t_0 and its coincident source and receiver location $X_0(x_0, z_0)$, has to be extrapolated to the chosen redatuming level where it emerges at time t_0' and location $X_0'(x_0', z_0')$. Furthermore, we have to consider that besides emergence point and traveltime also the respective amplitude value and the three wavefront attributes may alter their values while mapped from the actual measurement surface to the redatuming level.

For the practical implementation of this mapping process, the discrete nature of the stack and attribute sections has to be considered. In general, neither x_0', calculated according to equation (3.29), nor the new traveltime t_0' calculated according to equation (3.30) matches a regular grid of ZO samples. In most cases the point (m_x', t_r) will be located in between four grid-points. Thus, a strategy has to be defined on how to handle the assignment of a stacked amplitude or attribute value to the grid.

In case of amplitudes, this is done by distributing its new value onto the surrounding grid points according to their respective distance to its actual position. This is justified because stacked amplitudes are related to elastic energy, which is an extensive property.

Looking at the wavefield attributes it is obvious that for intensive properties like angles, radii or even velocities such a procedure does not make sense. One approach to solve this problem would be to place the attribute value on each of the surrounding grid points, if there is not already a value stored with a higher associated coherence. This method has the disadvantage that it produced some kind of smoothed attribute sections with less resolution than the unredatumed input.

The presently utilized method is to calculate the new attribute-value A_g' on a grid point by its former value A_g and the newly added value, called A_n. The coherence values, which are associated with those three values are C_g' and C_g for new and old grid values and C_n for the coherence of the added sample. The relations between these variables are

$$A_g' = \frac{C_g A_g + C_n A_n}{C_g + C_n} \quad \text{and} \quad C_g' = C_g + C_n, \tag{4.23}$$

which is simply a coherence-weighted average. The advantage of this method is that contributions by attribute values with a higher coherence are much stronger, since they can be expected to be more accurate. The extra computational cost can be neglected as the runtime of the redatuming is far less than that of the stacking operation or the attribute search. A grid point which does not receive any input sample at all is clearly indicated as being empty by assigning a value that is far outside of the expected attribute range. For the simple synthetic data example used throughout this chapter the redatumed stack section is displayed in Figure 4.10. A redatuming velocity of 2.5 km/s was used and the traveltimes are related to a horizontal reference level at $z = 1710$ m. For the primary reflections

(a) Optimized CRS stack section after redatuming.

(b) Emergence angle (°) after redatuming.

(c) NIP-wave radius (km) after redatuming.

(d) N-wave curvature (1/km) after redatuming.

(e) Normal moveout velocity (km/s) after redatuming.
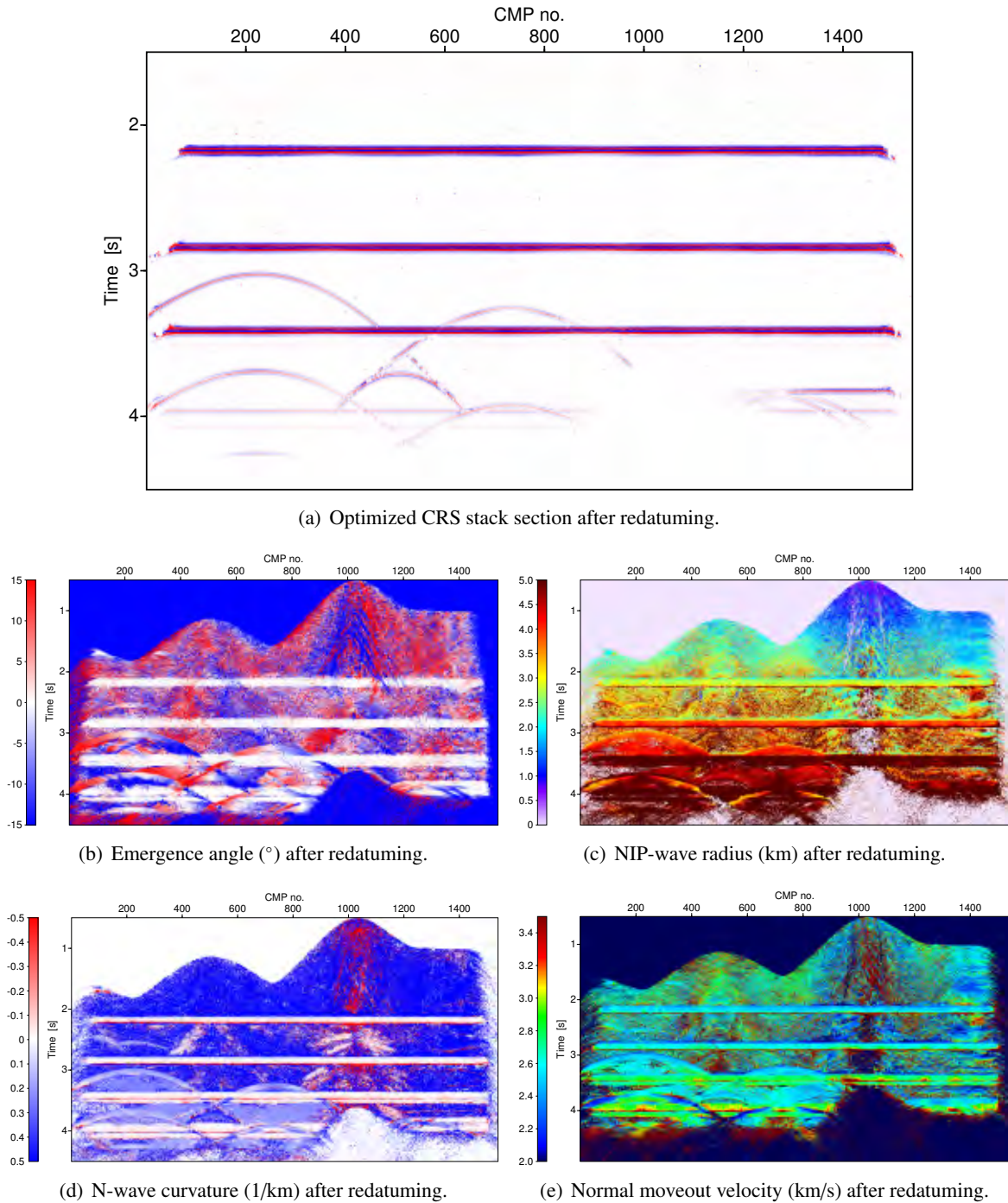
Figure 4.12: After redatuming the optimized stack (a) and attribute sections (b-e) are related to a horizontal reference level at $z = 1710$ m. A redatuming velocity of 2.5 km/s was used. Due to the horizontal layering the emergence angles of the simulated ZO rays (b) are equal to zero, i. e. these rays emerge vertically at the measurement surface. For a horizontally layered structure, R_{NIP} should be laterally constant if related to a horizontal measurement surface. The actual fluctuations of R_{NIP} that can be observed in (c) are caused by the noise in the data, the influence of the multiples, and border effects. Due to the horizontal layering, the N-waves propagate as planar waves so that the N-wave curvature in (d) equals zero for all events. The NMO velocity after redatuming (e) coincides in this case with the RMS velocity related to the planar reference level.

and for the internal multiples, the acquisition footprint is completely removed. The surface multiples are not flat after the redatuming since they carried twice the acquisition footprint of the primaries. The sections of β_0, R_{NIP}, K_N, and v_{NMO} after redatuming are depicted in Figure 4.12. It can be observed that there are still some speckles along the reflection events that are obviously dislocated. They stem from unreliable attribute values determined at the borders of the data set that are associated a high coherence value due to a low number of contributing traces, only. This effect could be omitted by excluding ZO samples from the redatuming for which the number of contributing traces is below a certain threshold.

Chapter 5

CRS-stack-based imaging workflow

It was already discussed that besides an improved ZO simulation, the decisive advantage of the CRS stack method compared to conventional methods is that for every ZO sample three kinematic wavefield attributes are obtained as a by-product of the data-driven stacking process. In the previous two chapters it was demonstrated how these attributes can be used to estimate optimum stacking apertures, to apply event consistent smoothing to the initial attribute sections, and to redatum the CRS stack results to a chosen reference level. However, besides improving the stack itself, the CRS attributes are also very important in view of subsequent processing steps. Using this additional information, an advanced data-processing workflow can be established leading from time to depth domain and covering a broad range of seismic reflection imaging issues in a consistent manner. The major steps of this workflow are displayed in Figure 5.1. A CRS-based approach for residual static correction provides improved prestack data which serve as input for new iterations of the CRS stack process or for prestack depth migration. To bridge the gap between time and depth domains a tomographic inversion method makes use of the CRS attributes to determine a smooth macrovelocity model well suited for the subsequent migration. Finally, pre- and poststack depth migration make use of the CRS attributes to define optimum migration apertures. A true-amplitude limited-aperture time migration using CRS attributes is under current development (Spinner, 2006) and will further complement this workflow in the near future together with a very promising approach to determine velocity updates from the residual moveout of reflectors within so-called common image gathers (Klüver, 2006).

First tests on synthetic data (Hertweck et al., 2003) and an extensive case study carried out in the framework of a commercial exploration project (Heilmann et al., 2004) proved the great potential of CRS stacking followed by CRS-stack-based tomographic inversion and depth migration. However, two important problems of land data processing, the top-surface topography and complex near-surface conditions were not covered by these examples and not yet considered in the original workflow. To use the full potential the CRS stack method, especially for these difficult cases where conventional processing methods might fail, the workflow was extended by the CRS stack for topography and CRS-stack-based residual static corrections. A first test on a quite simple synthetic dataset, where there was no need for residual static corrections, was already presented in Chapter 4. Results of CRS-stack based imaging for more realistic synthetic data are presented in Chapter 6. Its further application to quite complicated land-data sets from North Brasil and the Arabian Peninsula, posing severe problems in view of signal-to-noise ratio, topography and near-surface structures, will be discussed in Chapter 7.
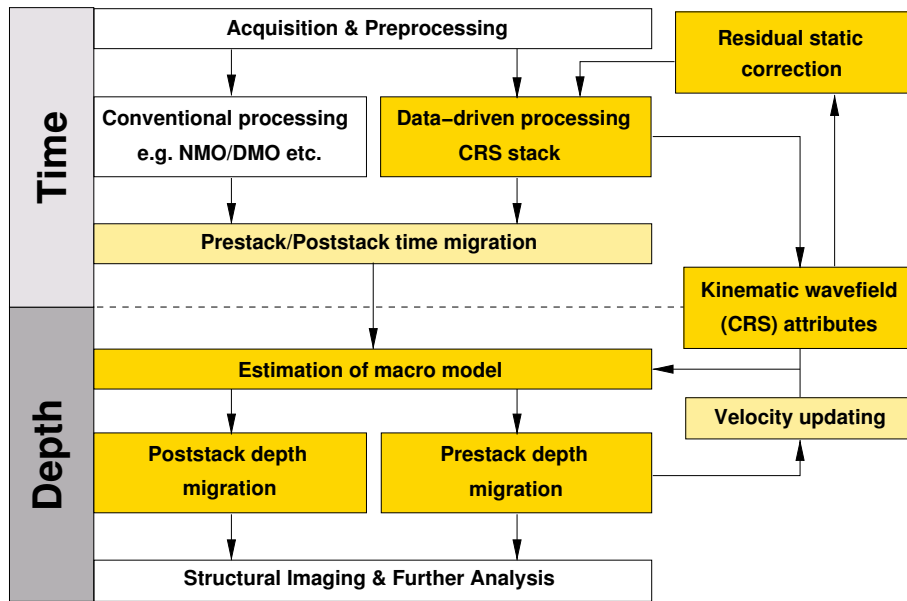
Figure 5.1: CRS stack based imaging: Major steps of seismic-reflection data processing in time and depth domain. Imaging procedures that can be incorporated in the CRS-stack-based imaging workflow are highlighted in yellow. Dark yellow indicates processes applied and discussed in this thesis. Figure modified after Hertweck (2004).

5.1 CRS-stack-based residual static corrections

It was already mentioned in Section 1.3 that resolving the near-surface structures can be a very difficult task, particularly in deserts or mountainous areas where the near-surface conditions change rapidly and on a broad scale. In such cases, the sampling of the near-surface model used to calculate the field static corrections is often not sufficiently dense due to the practically unavoidable lack of a priori information. Therefore, the field static corrections fail to compensate the entire effect of the topography and near-surface structure (see Figure 5.2) and residual static corrections are necessary which try to estimate these time shifts by data-driven geostatistical procedures.

Today, there are many different approaches to determine residual static corrections. The so called *traveltime picking methods* are very common in practice. The latter are based on a two-step procedure. In the first step, static time shifts are estimated for the individual traces, e. g., by cross-correlating each trace in question against a reference trace or pilot trace. In most cases, common midpoint sorted data is used for which the pilot trace typically consists of the stack of the remaining traces in the CMP gather. Optionally, neighboring CMP gathers can be included to construct the pilot trace in order to increase the stability in case of sparse data or a high noise level. The time shift for a given seismogram can be expressed as

$$T_{ij} = S_i + R_j + G_k + M_k x_{ij}^2, \qquad (5.1)$$

where S_i denotes the ith source static, R_j the jth receiver static and G_k the time shift related to the kth CMP position. Furthermore, M_k, denotes the residual normal moveout coefficient and x_{ij} the source-receiver spacing (offset).

In the second step the time shifts T_{ij} are separated into surface-consistent source and receiver statics, S_i and R_j, for instance by least-squares fitting (Taner et al., 1974).
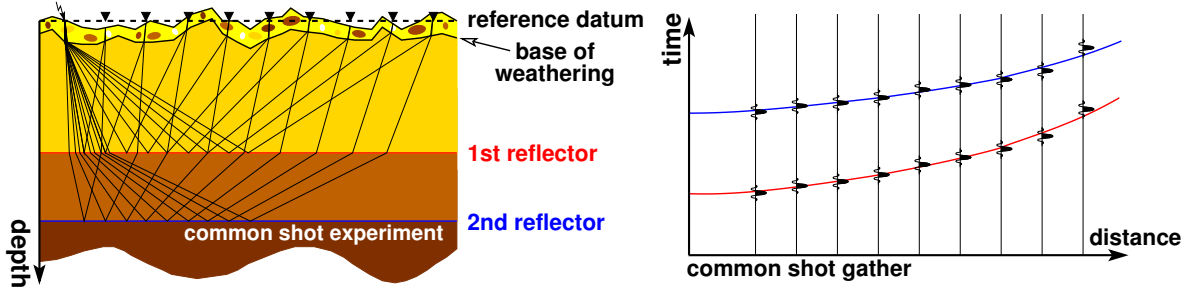
Figure 5.2: Residual statics in a shot gather: on the left hand side the acquisition geometry of a common shot experiment is displayed. If the near-surface model which is used for the field static correction does not resolve the full complexity of the actual conditions residual statics remain in the data. On the right hand side of this figure, the resulting common shot gather is depicted. The residual time-shifts are clearly observable comparing the vertical position of the wavelets with their ideal location indicated by the red and blue lines. Figure taken from Koglin (2005).

To reduce the sensitivity to errors in the presence of noise and ambiguities within the cross correlation results Ronen and Claerbout (1985) proposed an alternative approach based on the estimation of residual static corrections by maximizing the stack-power function. The latter describes nothing more than the stacked amplitude $S(x)$, where $x = (x_1, x_2, \ldots, x_M)$ denoting the vector of the source and receiver statics. This one-step method immediately yields surface-consistent static corrections. Usually, the static parameters are successively determined by local maximization and subsequent application of the correction giving the best improvement of the stack-power. According to Normark (1993), the change in stack-power $\Delta S(\delta x_j)$ for a perturbation of the jth static parameter (δx_j), which affects a subset of CMP gathers C_j, is estimated as

$$\Delta S(\delta x_j) = 2 \sum_{c \in C_j} \phi^{pf}_{c(\delta x_j)}, \qquad \text{with} \qquad \phi^{pf}_{c(\delta x_j)} = \sum_t p_{ct} f_{c(t+(\delta x_j))}, \qquad (5.2)$$

where f_{ct} is the trace influenced by the jth static parameter and t indicates the sample numbers. Furthermore, p_{ct} denotes the partial stack of the cth CMP gather which is a stack of all traces in the gather except f_{ct}. Finally, $\phi^{pf}_{c(\delta x_j)}$ is the cross-correlation between f_{ct} and p_{ct}. This expression is equivalent to the super-trace correlation of Ronen and Claerbout (1985). The static solution is determined iteratively. In most cases, about ten iterations, defined as a perturbation of all static parameters, are necessary before convergence is achieved. In contrast to traveltime picking methods which involve only one or a limited number of CMP gathers, the time shifts obtained by the stack-power maximization technique are based on several CMP gathers. The latter constitutes an important advantage, particularly in case of sparse data or data with low signal-to-noise ratio since more traces contribute to an individual time shift. A serious drawback of stack-power maximization might be its significant demand on the data storage facilities, because all data are preferably kept in the main memory during the optimization.

A general problem which can affect both of the presented methods is that so-called cycle skips occur when the static corrections are large compared to the dominating period in the data. In such cases local optimization can be inadequate for the stack-power maximization since it might be trapped in local maxima of the objective function. In order to find the global solution, Rothman (1985, 1986) suggested the use of a Monte Carlo optimization technique called simulated annealing. This method

was originally introduced by Kirkpatrick et al. (1983) to solve the problem of the successful growth of crystals. Even though, simulated annealing is a very effective global optimization method its computational cost is high compared to a local optimization. For this purpose, Dahl-Jensen (1989) proposed to enhance the global character of the local search, by estimating the static parameters in random order. Alternatively, Normark (1993) suggested to enlarge the operational field for local optimization, based on stack-power maximization in the frequency domain.

As mentioned before, the traveltime picking methods often use several neighboring CMP gathers for the construction of a pilot trace which can increase both accuracy and stability of the determined time shifts. This strategy can also be applied in the stack-power maximization technique, and the same benefits as in the traveltime picking method can be expected. However, combining neighboring CMP gathers usually requires the assumption that the structural dips are limited. As will be shown in the following, this problem can be solved by a residual static correction technique based on the CRS stack method (Koglin, 2005; Koglin et al., 2006).

The CRS-based residual static correction methodology is an iterative process close to the super-trace cross-correlation method by Ronen and Claerbout (1985). The cross-correlations are performed within so-called CRS supergathers, consisting of all moveout-corrected prestack traces within the spatial stacking aperture, instead of being confined to individual CMP, common-shot, or common-receiver gathers. The moveout correction makes use of the previously obtained attributes and considers the true source and receiver elevations. Thus, elevation static correction can be omitted that may introduce non surface-consistent errors of the same scale as the searched-for residual statics. Due to the spatial extent of the employed stacking operator, a supergather contains many neighboring CMP gathers. For each considered supergather, corresponding to a particular ZO location, the moveout correction will, in general, be different. Since each prestack trace is included in many different supergathers it contributes to far more cross-correlations than in methods using individual gathers, only. The cross-correlations of the stacked pilot trace and the moveout corrected prestack traces are summed up for each shot and receiver location. This summation is performed for all supergathers contained in the specified target zone. The searched-for residual time shifts are then expected to be associated with the maxima in the cross-correlation stacks. After the residual statics are obtained from the cross correlation results, the prestack traces are time shifted with the corresponding total time shifts. The total time shift of a certain trace is simply the sum of the static time shifts of source and receiver.

If the CRS stack results obtained by using the corrected prestack data are not yet satisfactory, another iteration of residual static correction can be applied to the corrected prestack data either with or without repeating the attribute search process. In the first case, I recommend to update the CRS attributes by a complete repetition of the entire CRS stack process. The initial attribute search is much faster than the optimization, thus repeating only the optimization does not save much time compared to a complete CRS stack iteration and, in particular, does not guaranty that the optimum attributes for the corrected data are determined. Particularly in gaps of reflection events that might be filled by the residual static corrections the attributes are often too far from their optimum values to be corrected by a local optimization, only.

In certain cases it might seem attractive to omit a repetition of the CRS stack completely, since the CRS stack process itself is about ten times as time-consuming as the residual static correction procedure. However, if the results of the first iteration are still far from being optimal it might be insufficient to rely on the CRS attributes determined for the uncorrected data because the determined time shifts between neighboring traces might be too large so that the CRS stack probably failed to detect actually contiguous events and their corresponding attributes. Therefore, I would recommend further iterations of residual static corrections without further updating of the CRS attributes—if at all—then for final
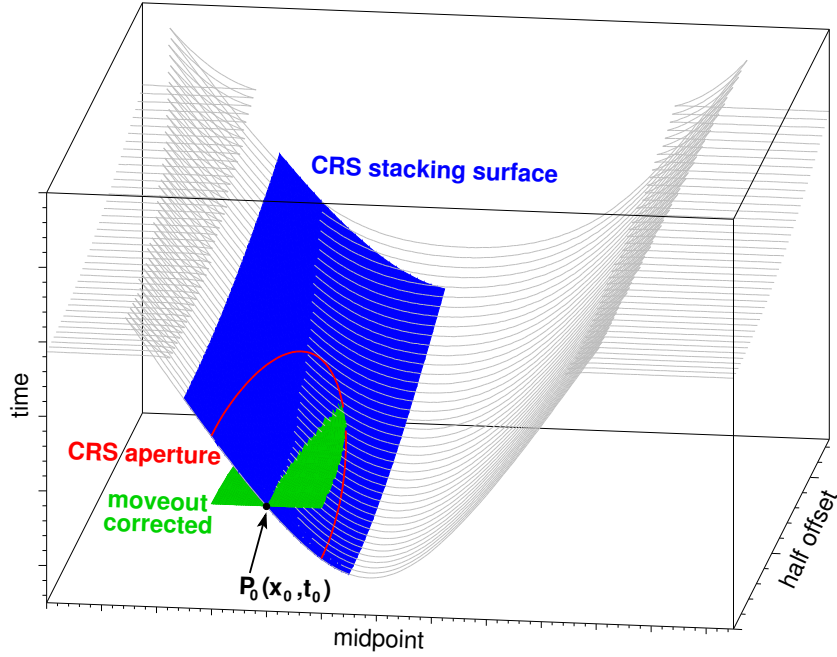
Figure 5.3: CRS moveout correction for the ZO sample $P_0(x_0, t_0)$, according to Koglin et al. (2006). For a dome-like reflector segment in depth the forward-modeled spatial reflection event is depicted in gray as a family of common-offset reflection events. The CRS stacking operator defined by the attribute triplet β_0, K_{NIP}, and K_{N} is depicted in blue. With the knowledge of these attributes, the reflection event can be flatted at time t_0 by subtracting the moveout according to equation (5.3). It results the moveout-corrected supergather, depicted in green, which was confined for display by a user-defined stacking aperture (red).

iterations only, where significant residual time shifts are not anymore expected.

5.1.1 Moveout correction

To correct the traveltime moveout of a certain reflection event, the half-offset $\vec{h}$ and midpoint $\Delta\vec{m}$ dependency of the traveltimes have to be eliminated. This dependency can be estimated for every time sample of the ZO section by means of the associated CRS traveltime operator (3.11) determined during the previously applied CRS stack and defined by a certain attribute triplet. Thus, each reflection event can be approximately transformed into a horizontal plane at ZO traveltime t_0 by subtracting the moveout

$$t_{\mathrm{moveout}}(\Delta\vec{m}, \vec{h}) = t_{\mathrm{hyp}}(\Delta\vec{m}, \vec{h}) - t_0 \tag{5.3}$$

from all traces contained within the respective stacking aperture. The latter ensemble of traces defines the so-called moveout corrected CRS supergather depicted in Figure 5.3. The moveout correction is performed for every sample of the ZO section.
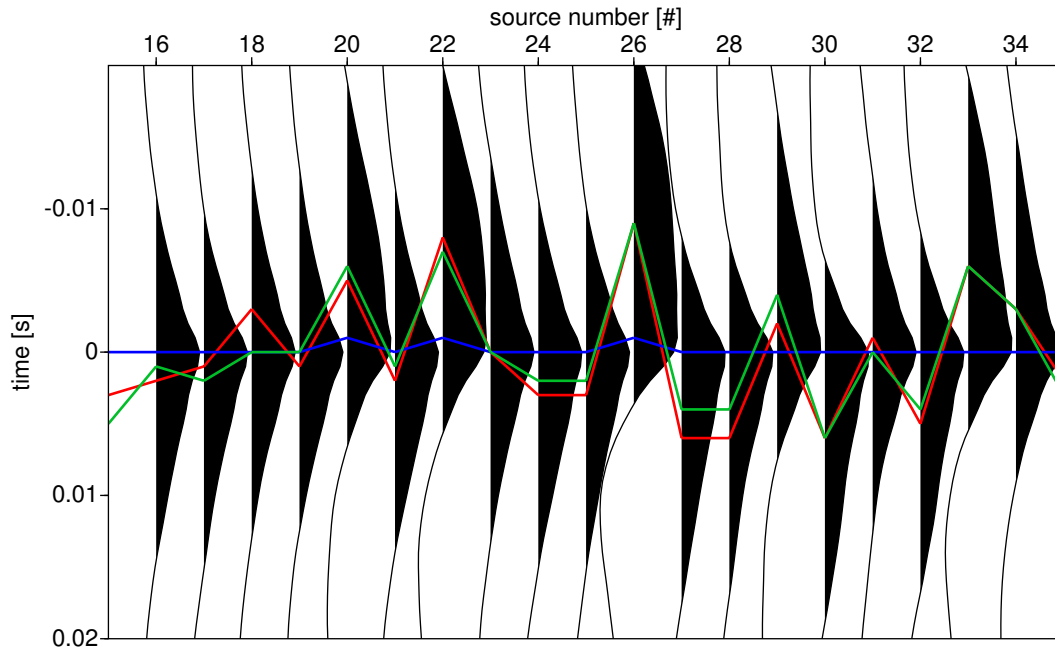
Figure 5.4: Example for asymmetric correlation stacks, according to Koglin et al. (2006). The red line displays artificial time shifts which were added to a real data set. The blue line shows the estimated time shifts obtained by picking the global maxima whereas the green line shows the estimated time shifts obtained by picking the center of a region around the maximum which is specified by having at least 20% of the maximum value.

5.1.2 Cross correlation

After the moveout correction, the traces are assumed to be still misaligned due to the surface-consistent residual time shifts of the source and receiver locations. Thus, for each CRS supergather, the cross correlations are performed between the corresponding trace of the simulated ZO section, i.e., the pilot trace, and every single moveout-corrected trace contained in the supergather. Afterwards, a cross correlation stack is produced for each source and receiver location by summing up all correlation results of traces that have a certain source or receiver location in common. It is evident that the individual correlation results of traces that have for instance the source position in common also contain the contributions of the various receiver locations involved. However, as for the super traces correlation method by Ronen and Claerbout (1985) it is assumed that those contributions which are not related to the considered surface location are randomly distributed around zero and thus cancel out during the summation.

In principle, the searched for residual static time shift should be associated with the time shift that corresponds to the maximum of the summed correlation results. However, after systematic tests on synthetic and real data, Koglin et al. (2006) suggested that for the practical application picking of the center of a region around the maximum which is specified by having at least, e. g., 20% of the maximum value is more appropriate than picking the maximum itself (see Figure 5.4). Additionally, the traces to be cross correlated can be weighted with the coherence value of the pilot trace. This emphasizes the actual reflection events compared to the surrounding noise.

The tapering effect of cross correlations (see Cox, 1999; Koglin, 2005) can be compensated if, in contrast to standard cross correlation, the windows of moveout corrected traces or of moveout corrected

and pilot traces to be correlated are enlarged by up to the maximum time shift Δt of the calculated cross correlations. Thus, during the correlation less values are zeroed out so that the tapering effect of the cross correlations is reduced. Furthermore, a normalization process similar to the one optionally performed prior to the CRS attribute search (see Mann, 2002) can be applied before the correlation to balance the amplitudes of the input traces. Normalization after the correlation based on its power can be applied before the correlation stack to balance the influence of each contribution. However, none of the two normalizations were applied in the presented case.

At the boundary of the dataset or at acquisition gaps the number of traces contributing to the cross correlation stacks might be inadequate to provide a reliable result. Therefore, a threshold for the minimum number of contributing traces and for the maximum residual static time shift was implemented to discriminate such outliers. The threshold for the maximum residual time shift also reduces the likelihood of cycle skips.

5.2 Tomographic inversion

In laterally inhomogeneous media, velocity model building is one of the crucial steps of seismic depth imaging. A suitable macrovelocity model is essential, both for the correct positioning of the reflection events in the subsurface and—in case of prestack depth migration—to obtain an optimally focused image. There are many different approaches which differ, e. g., in the criterion used to evaluate the quality of the current model, the way model updates are determined, or in the assumptions made concerning the resulting velocity model (blocky, layered, smooth, etc.).

Today, migration velocity methods based on *residual moveout analysis* in common image gathers are widely used. These methods employ the criterion that prestack depth migration should produce reflector images that have the same depth for every migrated common-offset gather, i. e. the depth of a certain reflector has to be offset-independent (e. g. Deregowski, 1990; Liu and Bleistein, 1995). An alternative approach that is also based on prestack depth migration is the so-called *depth focusing analysis* which makes use of the criterion that a reflection event should focus at zero traveltime if backward propagated within the correct velocity model (e. g. Jeannot and Faye, 1986; MacKay and Abma, 1992).

Besides these methods which work directly in the migrated domain, time domain methods like the classical *reflection tomography* are the most commonly used approach to determine a macrovelocity model (e. g. Bishop et al., 1985; Farra and Madariaga, 1987). Here, global model updates are determined that minimize the misfit between picked traveltimes and their forward modeled counterparts. Unfortunately, the latter usually demands the assumption of continuous reflectors—often across the entire model—and furthermore involves tremendous effort in picking the traveltimes along continuous events in the often noisy prestack data. In order to minimize these drawbacks so-called *stereo tomography* was proposed by Billette and Lambaré (1998). This approach makes use of the slopes and traveltimes of only locally coherent events in common-shot and common receiver gathers. As a consequence no interfaces have to be introduced in the model and picking along continuous events can be omitted.

The tomographic inversion method employed in the CRS-stack-based imaging workflow combines some of the advantages of the above mentioned methods. Firstly introduced and implemented by Duveneck (2004), it aims at obtaining a smooth but laterally inhomogeneous velocity model from picked ZO travel times and the associated slopes and curvatures of locally coherent events. This kinematic information can be obtained from the CRS stack results: the attributes K_{NIP} and β_0 determined for
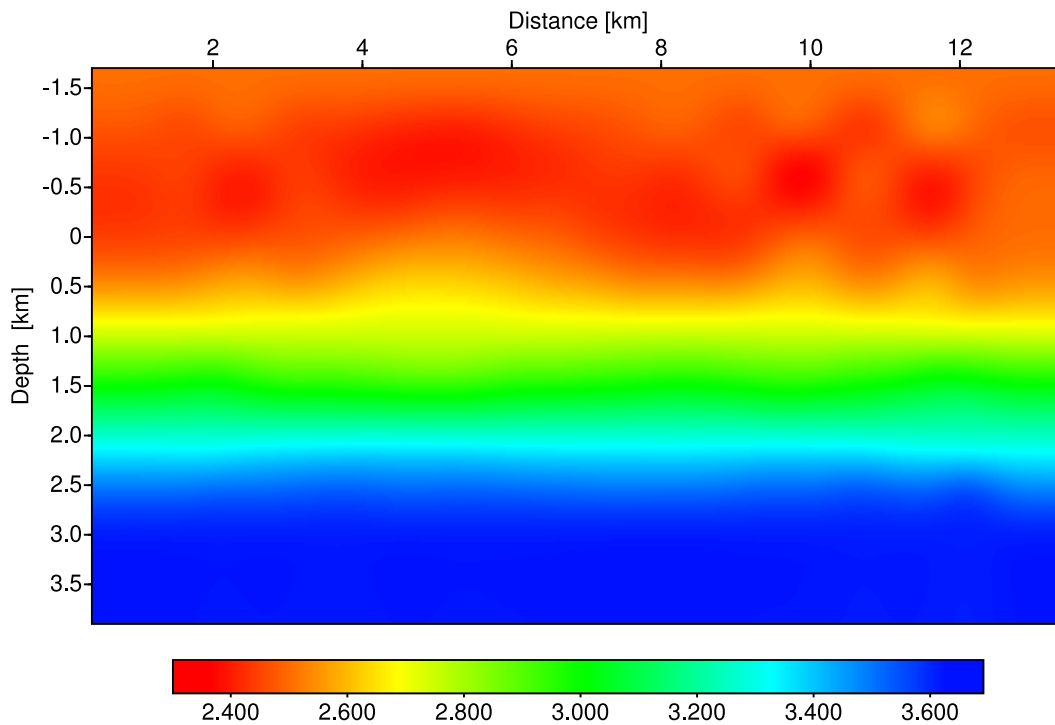
Figure 5.5: Smooth macrovelocity model [km/s] obtained by tomographic inversion of redatumed CRS stack results of the ENI/Syndata. Generally, a good consistency to the original velocity model depicted in Figure 4.3 can be observed. Small deviations from the actual velocities are visible presumably caused by remaining influences of the topography and the multiples.

every sample of the ZO section are related to the hypothetical NIP wave at a given ZO location and can be used to describe the approximate multi-offset reflection response of a common reflection point in the subsurface. Topography does not have to be considered by the inversion since the redatuming procedure provides stack and attribute sections related to a planar reference level. The replacement velocity used for the redatuming can be incorporated as a priori information into the inversion process. The primary criterion for the inversion is that the NIP wave focuses at zero traveltime at the NIP if propagated into the subsurface in a correct model. From the assumption of a smooth and isotropic velocity distribution in the subsurface which is necessary to make paraxial ray theory applicable follows vice versa the secondary criterion: the velocity distribution has to be as smooth as possible. The latter serves mainly to improve the stability of the inversion. Since picking is performed in the simulated ZO section, the effort related to this process is considerably reduced compared to other tomography methods that demand picking in the prestack data. Furthermore, using the coherence value connected to each sample of the ZO section picking can be performed in a highly automated way (Klüver and Mann, 2005). The misfit between picked and forward-modeled attributes is iteratively minimized in the least-squares sense. To obtain the forward-modeled attributes dynamic ray-tracing is used. To give a first example, the smooth macrovelocity model obtained from the redatumed CRS stack results of the simple synthetic dataset (ENI/Syndata) discussed in the previous chapter is depicted in Figure 5.5.

5.2.1 Data and model parameters

A velocity model is considered to be consistent with the measured data if for each of n chosen data points

$$D_i(x_0, t_0, \beta_0, R_{NIP}) \quad \text{with} \quad i = 1, \ldots, n_{data}$$

a reflector element can be found with a dip and location that allows: (a) the associated normal ray to emerge at x_0 with emergence angle β_0 and (b) the NIP-wavefront to emerge at x_0 with radius R_{NIP}. This consistency criterion allows together with the demanded smoothness of the model to pose an inversion problem. The straightforward formulation of the inversion problem would have been, to trace the normal rays downwards in β_0 direction with wavefront curvature K_{NIP} and to check if they focus at zero traveltime. However, since the picked values of β_0 and K_{NIP} cannot be expected to be exact due to noise in the data and other mutilating influences it is a more stable approach to start ray-tracing at the CRP. In this case, the position of the CRPs and the starting directions of the corresponding normal-rays have to be considered as part of the model to be inverted for, along with the velocity distribution. For practical purposes and to make the inversion independent from the near-surface velocity v_0 the second spatial derivative of the traveltime of the NIP wave at x_0, i. e.,

$$M = \frac{\cos^2 \beta_0}{v_0 \, R_{NIP}} \quad \text{and} \quad p = \sin \beta_0 / v_0 \,,$$

i. e., the horizontal component of the slowness vector are chosen as parameters for the inversion instead of β_0 and R_{NIP}. As was shown in Section 2.3.1, solving the dynamic ray-tracing system for a normal ray, M can be expressed using the elements P_2 and Q_2 of the ray-propagator matrix $\mathbf{\Pi}$ in the ray centered coordinate system as $M = P_2/Q_2$. Thus the approximate CRP response in the vicinity of a normal ray at any location along the ray can be directly modeled by dynamic ray-tracing.

Each CRP of the velocity model is described by the coordinates x, z and the local dip-angle θ, which specifies the direction of the normal ray. A two dimensional B-spline function (e. g., de Boor, 1978) can be used to describe the smooth velocity model itself:

$$v(x, z) = \sum_{j=1}^{n_x} \sum_{k=1}^{n_z} v_{jk} \gamma_j(x) \, \gamma_k(z) \,, \tag{5.4}$$

where $\gamma_j(x)$ and $\gamma_k(z)$ are the B-spline functions and n_x and n_z are the number of node points in horizontal and vertical direction, respectively. Thus the model is described by the parameters

$$(x, z, \theta)_i \,, \quad vjk, \quad \text{with} \quad i = 1, \ldots, n_{data}, \ j = 1, \ldots, n_x, \text{ and } k = 1, \ldots, n_z \,.$$

5.2.2 Solution of the inverse problem

The model and data parameters described above shall be represented by the data vector $\vec{d}$ and the model vector $\vec{m}$. The vector of the modeled data shall be denoted by $\vec{d}_{mod} = f(\vec{m})$, in which the non-linear operator f represents the dynamic ray-tracing. According to this notation, the aim of the inversion is to find a model vector $\vec{m}$ that minimizes the misfit between the data vector $\vec{d}$ and the vector of the modeled data $\vec{d}_{mod}$. The cost-function of this minimization, i. e. the least-squares misfit $S(\vec{m})$, can be written as

$$S(\vec{m}) = \frac{1}{2} \left\| \vec{d} - f(\vec{m}) \right\|_D^2 = \frac{1}{2} \Delta \vec{d}^T(\vec{m}) \, \mathbf{C}_D^{-1} \Delta \vec{d}(\vec{m}) \,, \tag{5.5}$$

where $\Delta\vec{d} = \vec{d} - f(\vec{m})$ denotes the difference between picked data $\vec{d}$ and modeled data $\vec{d}_{mod}$. The matrix C is assumed to be diagonal and serves to assign individual weights to the data components.

A widely used approach to solve such non-linear minimization problems is find a solution by iteratively applied minimization of the locally linearized problem. Starting with an user-defined initial model $\vec{m}_0$, a sequence of n model updates $\Delta\vec{m}_n$ is calculated and applied—hoping that the process converges to the global minimum of S. Linearizing the model operator f by introducing the matrix of the Fréchet derivatives yields

$$f(\vec{m}) \approx f(\vec{m}_n) + \mathbf{F}\Delta\vec{m}, \quad \text{with} \quad \mathbf{F} = \frac{\partial(x_0, t_0, M, p)}{\partial(x, z, \theta, v)}. \tag{5.6}$$

In this case the individual Fréchet derivatives can be obtained during forward modeling (see, Duveneck and Hubral, 2002) using ray-perturbation theory (e. g., Farra and Madariaga, 1987). Now we can approximate the gradient of S by

$$\Delta_m S \approx -\mathbf{F}^T \mathbf{C}_D^{-1}(\Delta\vec{d}(\vec{m}_n)) - \mathbf{F}\,\Delta\vec{m})\,. \tag{5.7}$$

A necessary condition for a minimum of the misfit function $S(\vec{m})$ is that its gradient vanishes. Setting $\Delta_m S = 0$ leads to the relation

$$\mathbf{F}^T\mathbf{C}_D^{-1}\Delta d = \mathbf{F}^T\,\mathbf{C}_D^{-1}\,\mathbf{F}\Delta m\,, \tag{5.8}$$

which provides a least-squares solution for Δm if the inverse of $\mathbf{F}^T\,\mathbf{C}_D^{-1}\,\mathbf{F}$ exists. However, in practical application $\mathbf{F}$ is mostly ill conditioned since the model components are not sufficiently constrained by the data. Thus, the condition that the model has to be as smooth as possible has to be taken into account by minimizing the second derivative of the velocity field. Applying this smoothness criterion as an additional constraint for the velocity field $v(x, z)$ results in a cost function with additional regularization term:

$$S(\vec{m}) = \frac{1}{2}\Delta\vec{d}^{\,T}(\vec{m})\,\mathbf{C}_D^{-1}\Delta\vec{d}(\vec{m}) + \frac{1}{2}\vec{\epsilon}\,\vec{m}_{(v)}^T\,\mathbf{D}''\,\vec{m}_{(v)}\,, \tag{5.9}$$

where $\vec{m}_{(v)}$ is the part of the model parameter vector $\vec{m}$ that contains the B-spline coefficients v_{jk} and $\vec{\epsilon} = (\epsilon_1, \epsilon_2, \epsilon_3)^T$ serves as weight of the regularization term. Furthermore, matrix $\mathbf{D}''$ is assumed to be positive definite. It is related to the second spatial derivatives of v and to v itself and is defined according to the following equation:

$$\int_x \int_z \epsilon_1\left(\frac{\partial^2 v(x, z)}{\partial z^2}\right)^2 + \epsilon_2\left(\frac{\partial^2 v(x, z)}{\partial x^2}\right)^2 + \epsilon_3 v(x, z)^2 dz\,dx = \vec{m}_{(v)}^T\mathbf{D}''\vec{m}\,. \tag{5.10}$$

For further details on matrix $\mathbf{D}''$ I refer to Duveneck (2004).

Linearizing $f(\vec{m})$ according to equation (5.6) and evaluating the condition $\Delta S(\vec{m}) = 0$ results in the matrix equation

$$\hat{\mathbf{F}}\Delta\vec{m} = \Delta\hat{\vec{d}}, \tag{5.11}$$

with

$$\hat{\mathbf{F}} = \begin{pmatrix} \mathbf{C}_D^{-\frac{1}{2}}\,\mathbf{F} \\ [\mathbf{0}, \mathbf{B}] \end{pmatrix} \quad \text{and} \quad \Delta\hat{\vec{d}} = \begin{pmatrix} \mathbf{C}_D^{-\frac{1}{2}}\Delta\vec{d}(\vec{m}_n) \\ -[\mathbf{0}, \mathbf{B}]\,\vec{m}_n \end{pmatrix}. \tag{5.12}$$

$[\mathbf{0}, \mathbf{B}]$ is a rectangular matrix satisfying the condition $\vec{\epsilon}\,\mathbf{D}'' = \mathbf{B}^T\mathbf{B}$. Finally, the searched-for model update $\Delta\vec{m}$ is obtained from solving equation (5.11) in the least-squares sense. Due to the large size of the matrices involved, the LSQR-algorithm (Paige and Saunders, 1982b,a) is used. The latter is attractive from the computational point of view since this algorithm works very efficient by taking advantage of the sparsity of $\mathbf{F}$ and by omitting any explicit matrix inversion.

5.3 Kirchhoff depth migration

Even though a number of different migration methods exist, each based on a different imaging condition, most migration methods employ, in one way or another, the scalar wave equation and follow the principle of wavefield continuation. The so-called exploding reflector concept which assumes the recorded wavefield as originating from exploding reflectors in the subsurface and traveling through a medium with half the actual velocity is often used for poststack migration. Here, the wavefront shape of an exploding reflector at time $t = 0$ coincides with the shape of the reflector itself. It results the imaging condition that the reflector location in the subsurface can be obtained by backward continuing the measured wavefield in time and evaluating it at $t = 0$. This concept applies also to prestack migration where the source- and the receiver side has to be taken into account during the wavefield continuation.

The Kirchhoff- or diffraction-summation migration which is applied in this thesis is based on an integral solution of the wave equation and usually performed in the time domain. Other migration approaches are based on finite difference solutions of the wave equation, applied either in the space-time or the space-frequency domain (e. g., Claerbout, 1985). Migration can also be carried out in the frequency wavenumber domain (e. g., Stolt, 1978; Gazdag, 1978; Stoffa et al., 1990). For a detailed treatment of different migration algorithms I refer to Claerbout (1985).

The algorithmic framework of Kirchhoff migration goes back to the days of Hagedoorn (1954) who presented a graphical migration scheme based on surfaces of maximum convexity (see, e. g. Bleistein, 1999). It was many years later that his work was related to the wave equation and the Kirchhoff integral[1] and got therefore known as "Kirchhoff migration" (see, e. g. Schneider, 1978). The basic idea of Kirchhoff migration is to treat every subsurface point M located on a sufficiently dense grid as a diffraction point, to stack all recorded energy that would stem from this diffractor and to place the result in M. The diffraction traveltime surface of a single subsurface point, called *Huygens surface*, contains all points N in the time domain for which the traveltime equals the sum of traveltimes from the source and from the receiver to a depth point M,

$$t = \tau_D(x_S, x_G|M) = \tau_D(x_S|M) + \tau_D(x_G|M) \,. \tag{5.13}$$

The Kirchhoff migration process corresponds to an integration of the recorded wavefield along the Huygens surface $\tau_D(x_S, x_G)$ for each depth point M:

$$V(M) \propto \int\limits_{x_1}^{x_2} \int\limits_{h_1}^{h_2} dx_m \, dh \, W(x_m, h|M) \, \partial_t^{1/2} \, U(x_m, h, t) \bigg|_{t=\tau_D(x_m,h)}, \tag{5.14}$$

where U is the recorded wavefield, V denotes the migrated image, W is an optional migration weight employed, e. g., for true amplitude migration and $\partial_t^{1/2}$ is a temporal half-derivative.

This *diffraction stack* process is depicted in Figure 5.6(b) for a single common offset gather; performed in the prestack data for all common offset gathers one speaks of *prestack migration* otherwise if performed only in a stacked, typically ZO, section it is called *poststack migration*. In the former case, the summation in offset direction is usually postponed and applied in a second step since the

---

[1]The Kirchhoff integral describes the forward propagation of seismic waves within a known subsurface model. However, the inverse process, i. e. backward propagation, cannot be described by the Kirchhoff integral itself but by the Porter-Bojarski integral (Langenberg, 1986). Kirchhoff migration performs this adjoint operation by forward propagating the recorded wavefield in reverse direction, i. e. back to the origin of the assumed diffraction.

offset dependency of the depth of the migrated reflector images serves as criterion to evaluate and to update the underlying macrovelocity model. To define the respective diffraction stack operator for each point M, the configuration-specific diffraction-traveltime surface (prestack migration) or curve (poststack migration) has to be calculated using an a-priori given macrovelocity model. The latter can be performed, e. g., by using a finite-differences eikonal solver to compute the kinematic part of the Green's function of a point source located at the diffraction point M. In order to perform a so-called *true amplitude migration* the dynamic part of the Green's function serves to calculate a true-amplitude weight factor which is applied during the stack to remove the effect of geometrical spreading from the output amplitudes. Assuming all other influences on the amplitude such as, e. g., transmission loss or source-receiver coupling effects to be modest or corrected, the migrated amplitudes then become a measure of the angle-dependent reflection coefficient. Based on Kirchhoff migration and demigration, its asymptotic inverse process, a unified approach for 3D true amplitude seismic reflection imaging was introduced by Hubral et al. (1996) and Tygel et al. (1996).

Although a lot of different migration algorithms have been developed since the time of Hagedorn, e. g. wave-equation migration, reverse-time migration, and frequency wave number migration, Kirchhoff migration is still frequently used due to its great flexibility and well established mathematical foundations. The latter allows, e. g., target-oriented and amplitude preserving processing even of irregular datasets, without much additional effort. These properties and the moderate computational expense demanded by Kirchhoff migration made this approach very attractive for academic research so that an independent and quite extensive implementation of Kirchhoff migration and demigration was developed at Karlsruhe University (see, e. g., Jäger and Hertweck, 2002). This implementation was later included into the CRS-stack-based imaging workflow to perform the depth domain imaging part.

In case of an irregular acquisition surface there is—similar as for stacking—a considerable advantage in migrating the data directly from topography without shifting them to a flat or floating datum (Gray and Marfurt, 1995). One reason for this is that irregular topography is usually associated with highly contorted near-surface formations. Imaging these formations is crucial to tying geologic (e. g. outcrop) control to the seismic data. However, imaging these beds requires a level of precision in processing that redatuming (of prestack data) usually does not allow. For this purpose, the basic implementation was later extended to facilitate prestack migration directly performed from topography (Jäger et al., 2003). Contrary to prestack migration, poststack migration can make use of the redatumed CRS stack results so that there is no need to consider the actual topography and the planar reference level can be used instead. The poststack migration result for the simple synthetic dataset (ENI/Syndata) discussed in the previous chapter is depicted in Figure 5.6(c). The depth position of the reflectors matches very well the reflector depth in the original velocity model, depicted in Figure 4.3. Only small undulations of the reflector depths are visible presumably caused by remaining influences of topography and multiples on the used macrovelocity model.

A further improvement, which was recently implemented, is to limit the aperture of the migration operator to the size of the first projected Fresnel zone centered around the so-called stationary point, where the migration operator is tangent to the actual reflection even. This limited aperture is calculated from the wavefield attributes produced by the CRS stack and approximates the size of the first projected Fresnel zone. The use of such an aperture commonly reduces the time consumption particularly for prestack migration and also reduces the so-called diffraction-smiles. For further discussion on this issue, I refer to Schleicher et al. (1997).
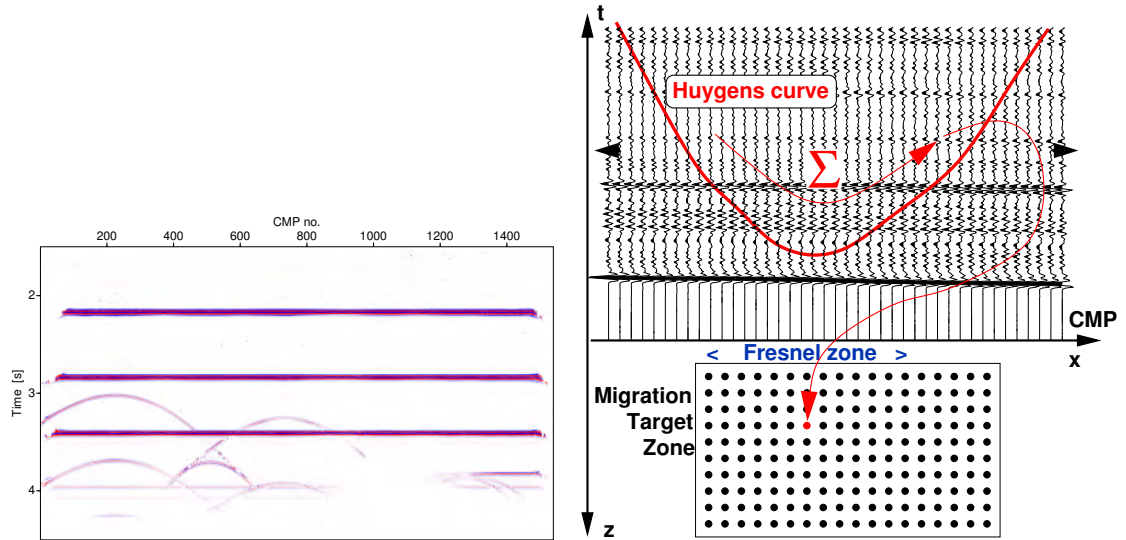
(a) Optimized CRS stack result after redatuming.

(b) Kirchhoff migration operator for a single depth point.
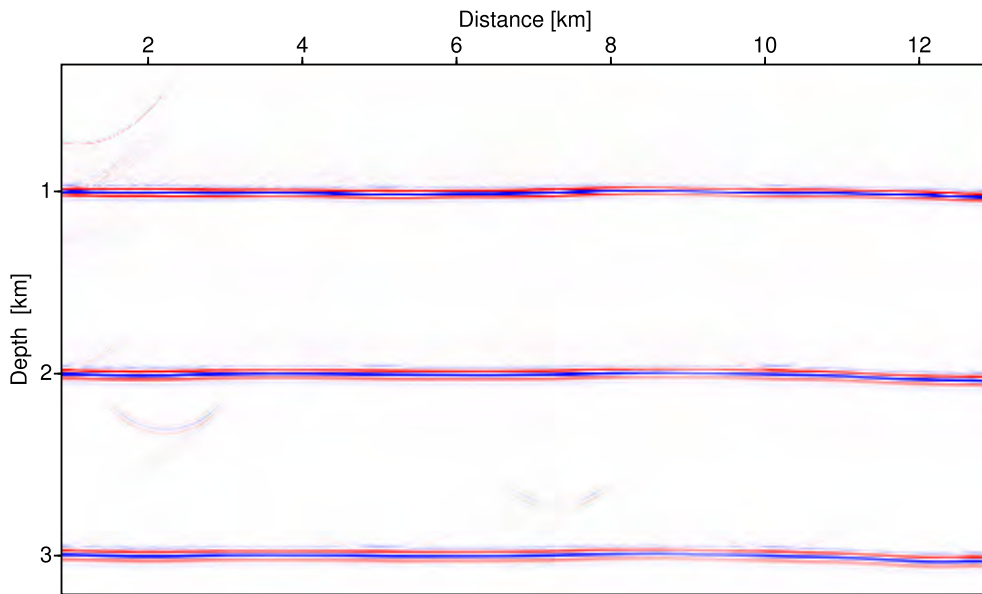
(c) Poststack depth migration result.

Figure 5.6: (a) Optimized CRS stack section after redatuming obtained for the ENI/Syndata. (b) Kirchhoff migration operator for a single depth point depicted in red. For limited aperture migration the summation is confined to the Fresnel zone indicated in blue. (c) Poststack depth migration results of the redatumed CRS stack section depicted in (a).

Chapter 6

Synthetic data examples

This chapter is devoted to the presentation of results achieved for two quite complex synthetic data sets. These data sets were created by the oil industry using finite difference (FD) modeling schemes to simulate typical problems encountered in land data processing. The main advantage of using FD methods instead of ray-tracing for modeling seismic data lies in the fact that the obtained data is more realistic since the complete wavefield is considered instead of individual rays only. The highly increased computational effort involved in FD modeling is worthwhile particularly for complicate models like those presented in this chapter. Both of them are well suited to test and further develop the implementation of the presented CRS-stack-based imaging workflow for land data since they include the most important problems of land data processing in an realistic manner. The first data set resembles a situation quite common for the arid areas of the Arabian Peninsula. Since the very shallow part of the subsurface model is homogeneous residual static corrections were omitted in this case. Besides this, the complete time-to-depth imaging workflow was conducted including CRS stack for topography, redatuming, tomographic inversion and depth migration. The second dataset resembles a situation typical for data acquired in the foothills of large mountains. It includes the full spectrum of difficulties that can be encountered in such a case: strongly variable top-surface topography, complex near surface conditions and a very difficult subsurface structure. Besides this, the CMP fold is rather sparce, including 38 traces only. Considering the time-frame of this thesis, I focused on applying the CRS stack followed by residual static corrections rather than trying to carry through the complete workflow including tomographic inversion and depth migration.

6.1 Synthetic data example A

The synthetic data set used for this section was created by the national Saudi Arabian oil company, Saudi Aramco. The primarily intention was to examine prestack migration schemes involving top-surface topography. Later it was kindly provided to me with the purpose of testing the extended CRS-stack-based imaging workflow for land data.

6.1.1 Model and survey design

The data was modeled using a finite difference scheme (explicit 4th order in space, 2nd order in time) and is based on a complicated velocity model resembling a true subsurface structure common to
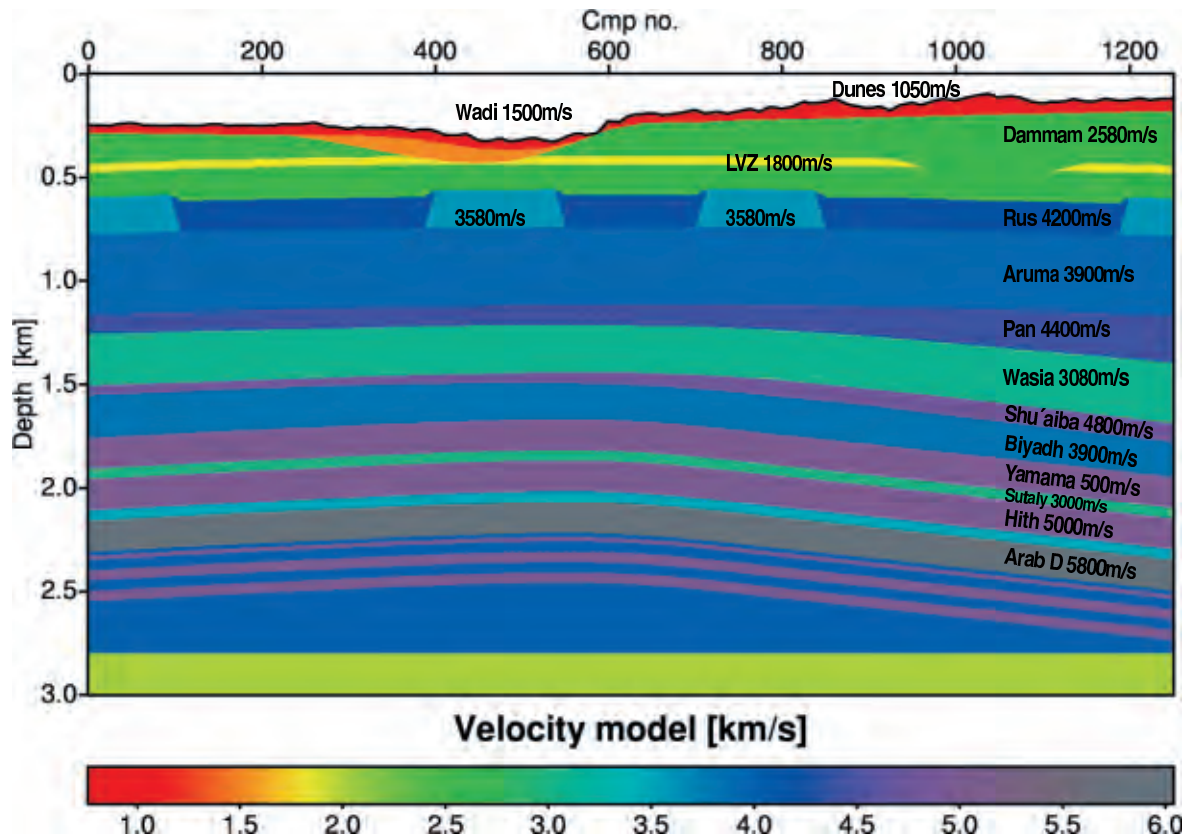
Figure 6.1: Velocity model used by Saudi Aramco to generate the synthetic prestack data. The names of the original layers resembled by this model are given, according to Alkhalifah and Bagaini (2006). The black line indicates the measurement surface.

Saudi Arabia. An image of this velocity model model, annotated according to Alkhalifah and Bagaini (2006)[1], is depicted in Figure 6.1, where the names of the original geological layers resembled by this model are given. There are approximately twenty homogeneous layers of variable thickness. In general, the interval velocities increase with depth, varying between 1050 and 6000 m/s. However, there are about ten different velocity-inversions present. Three blocky structures of unusual high velocity are integrated into the regular layers at a depth of 0.7 km. According to Alkhalifah and Bagaini (2006) "includes the velocity model, built by Saudi Aramco, several of the near-surface seismic challenges encountered in the Arabian Peninsula: rugged topography, sand dunes, large lateral velocity variations in the near-surface due to low-velocity dry riverbeds (also called wadis) filled with unconsolidated sediments interposed between shallow limestone or outcropping formations, and velocity inversions (LVZ in Figure 6.1). The sharp decrease of overburden velocities (depth between 200 m and 800 m), often due to partial dissolution of the anhydrite that composes the Rus formation in Figure 6.1, also complicates conventional seismic data processing. Near-surface scattering due to caves and to vugs in the shallow limestone formations is another important wave phenomenon that occurs in this geological setting but it is not modeled in this dataset". All in all, the elevations are ranging from -328 m to -96 m. However, the elevations do not vary smoothly but change rapidly along the surface

---

[1] Alkhalifah and Bagaini (2006) use this dataset to present an alternative approach to handle top-surface topography by means of a prestack wavefield extrapolation operator, the Topographic Datuming Operator (TDO), which allows redatuming based on the straight rays approximation.

Shot and receiver geometry	Number of shots		625
	Shot interval		16 m
	Maximum number of receivers		375
	Receiver interval		16 m
	Number of traces		199 593
Midpoint and offset geometry	Number of CMP bins		1250
	Maximum CMP fold		188
	Full offset range		-2992…2992 m
Recording parameters	Recording time		2 s
	Sampling interval		4 ms
	Dominant frequency		30 Hz
	Maximum frequency		50 Hz

Table 6.1: Information on the prestack data, obtained from the trace-headers.

as can be observed in Figure 6.3, where a comparison between the original measurement surface and its smoothed counterpart is displayed. The latter constitutes the smooth reference level for the CRS stack; the horizontal redatuming level is also displayed.

A so-called *split spread acquisition* (offset +/-2992 m) was simulated with a shot interval of 16 m equal to the receiver interval, and a point source Ricker wavelet with a central frequency of 20 Hz. More information concerning the prestack data is compiled in Table 6.1.1. Different to the real data examples presented in the next chapter no irregularities of the acquisition geometry are encountered such as deviation of sources or receivers from the straight line or missing shots and receivers caused by insufficient coupling or other environmental difficulties. The raw CMP gather shown in Figure 6.2 highlights some of the features of this dataset. The rugged topography has created short wavelength statics and despite the fact that the deep target reflectors are flat or have small dips the moveout is far from being hyperbolic due to the overburden lateral velocity variations. Multiple reflections, which are mostly generated at the bottom of the sand dunes, contaminate the raw data. Due to the fact that their moveout significantly differs from that of the target reflections, they could be attenuated using the target reflector velocities as NMO velocity constraints. However, this was not performed for the presented results; also no attempt has been made to attenuate them in the prestack domain.

6.1.2 CRS stack for topography

The first step of the conducted workflow was the application of the CRS stack for topography under consideration of a laterally variable near-surface velocity. In detail, the following processing sequence was carried through:

- *Topography and near-surface velocity analysis.* The actual measurement surface was smoothed using a smoothing aperture of 1200 m equal to the size of the maximum offset aperture later considered by the CRS stack. This ensures that each point at the smoothed reference level can be well approximated by a parabola with apex at the center of the stacking aperture (see Section 4.4.3). A comparison between the smoothed and the actual measurement surface is depicted
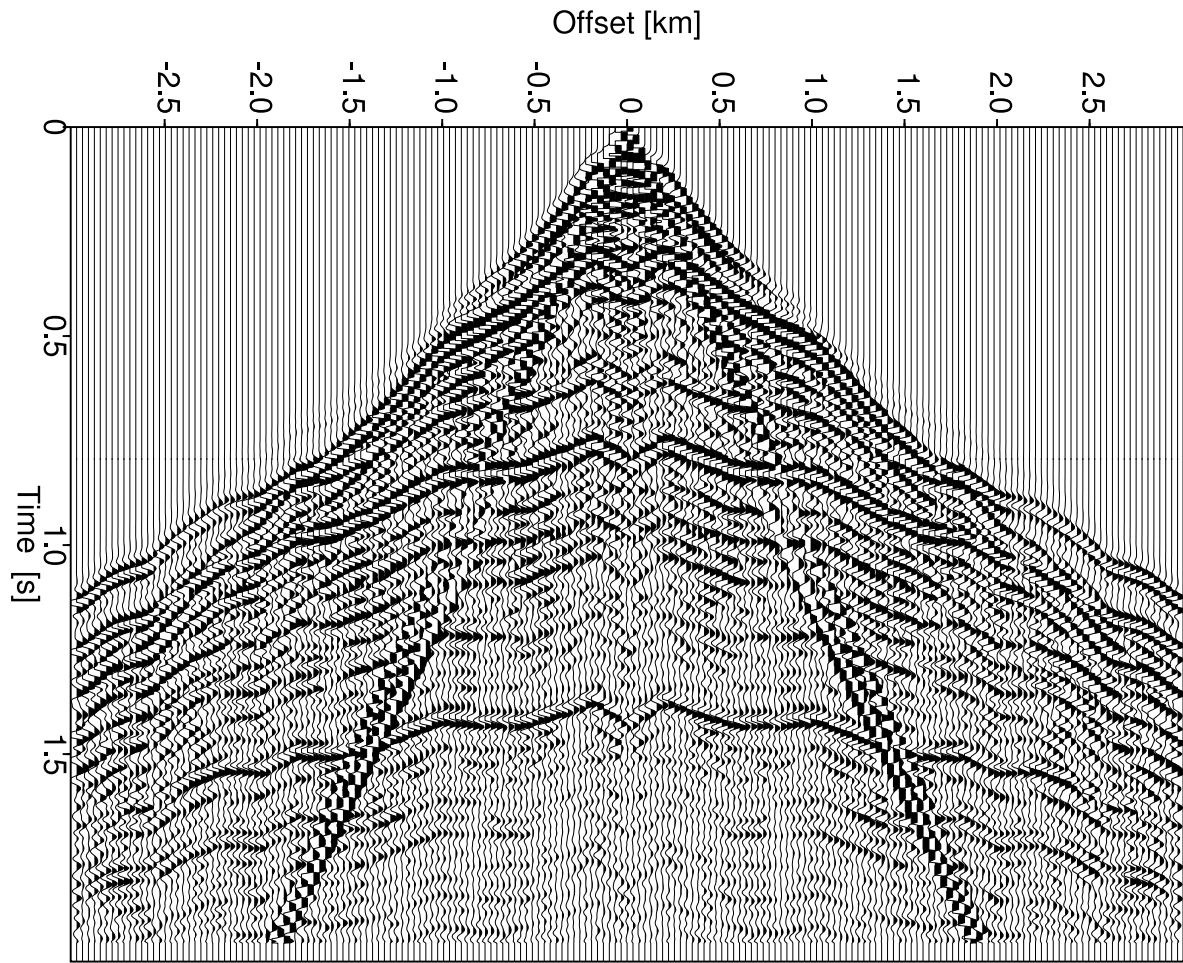
Figure 6.2: SaudiAramco/Syndata: CMP gather from CMP no. 600, at distance 4.8 km. The reflection travel times are strongly influenced by the top-surface topography so that their moveout is far from being hyperbolic
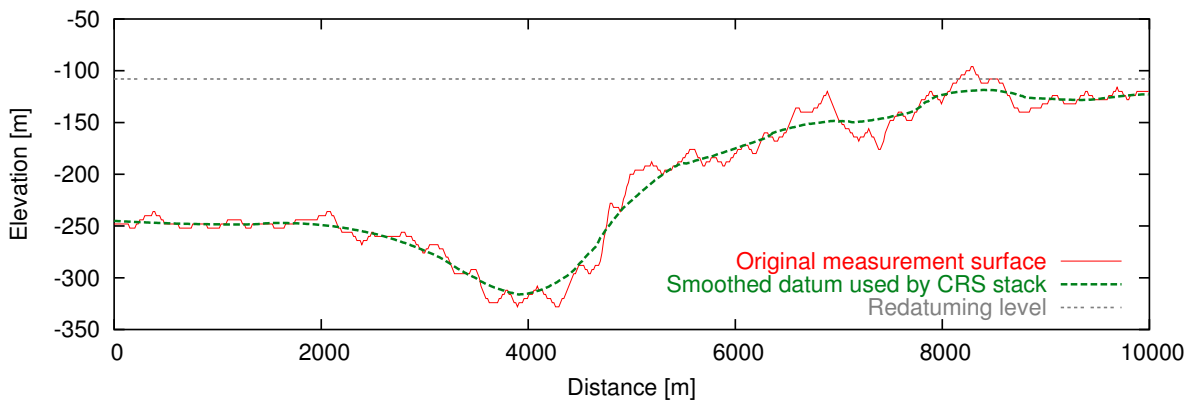
Figure 6.3: Comparison between original and smoothed measurement surface. The horizontal surface at $z = -108$ m was used as reference level for the redatuming.
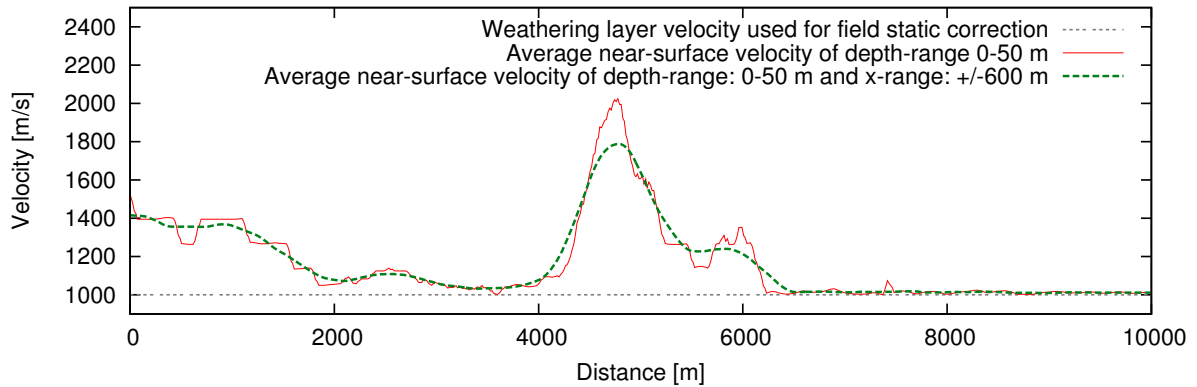
Figure 6.4: A constant weathering layer velocity of 1000 m/s was used for the field static corrections employed by the initial CRS stack. The near-surface velocity vertically averaged for a depth-range of 0 to 50 m is depicted in red, whereas a laterally smoothed value of this average near-surface velocity was used as near-surface velocity v_0 by the CRS stack.

in Figure 6.3. The variable near-surface velocity $v_0(m_x)$ was extracted from the velocity model depicted in Figure 6.1 by locally averaging the near-surface velocity of the first 50 m depth and smoothing the obtained values laterally using again a smoothing aperture of 1200 m equal to the size of the maximum offset aperture (see Figure 6.4).

- *Small scale static corrections.* It can be observed by looking at Figure 6.1 that the measurement surface is covered by a homogeneous layer of variable thickness and a very low velocity of 1050 m/s. Since the distance between the smoothed and the actual measurement surface is very small at most locations the velocity of this uppermost layer was used for the static corrections.

- *Initial CRS stack.* A time dependent offset aperture was employed linearly increasing from 100 m at 0.2 s to 1200 m at 1.5 s. Emergence angle values within the range of ±60° were considered during the search. The NMO velocity was sought for within the range of 500 to 6500 m/s. The midpoint aperture increased from 100 m at minimum traveltime to 500 m at maximum traveltime. For the plane-wave search only 30% of this aperture were used. For the sake of brevity initial CRS stack results are not displayed.

- *Event consistent smoothing.* For the parallelogram shaped smoothing window a spatial half-width of 24 m and a temporal half-width of 8 ms was chosen. The maximum angle deviation for samples to be accepted was two degree and a minimum coherence value of 0.4 was utilized as coherence threshold. For each ZO sample smoothing was only applied if 80% of the samples within the surrounding window fulfilled these criteria.

- *Optimization.* Optimization was carried through for every sample of the ZO section even though the number of samples to be optimized could have been reduced by defining a time dependent coherence threshold below which no optimization is performed. The latter can be advantageous for very large data sets for which time is a crucial factor. The resulting stack section is depicted in Figure 6.5. A strong acquisition footprint is visible. The size of the projected Fresnel zone calculated from the initial attributes was used to limit the search aperture. The final stacking aperture was limited by the projected Fresnel zone calculated from the optimized attributes. The percentage increase of coherence achieved by the optimization is depicted in Figure 6.6.

- *Redatuming.* The horizontal redatuming level was chosen ten meters above the highest peak of the smoothed reference surface, i. e. at an elevation of -108 m. The average near-surface velocity in the target zone, i. e. 1165 m/s, was used as redatuming velocity. The optimized stack section after redatuming is depicted in Figure 6.7. The coherence and attribute sections after redatuming are depicted in Figures 6.8 to 6.11. The NMO velocity section calculated from the optimized attributes after redatuming is depicted in Figure 6.12.

Discussion of the results The stack section after redatuming shows a high signal-to-noise ratio and very continuous events. It can be observed that the low-velocity zone beneath the wadi and the low redatuming velocity used to fill up this valley, caused a syncline shape of the reflection events in this region. This will later be corrected by the depth migration. From the primary reflections most of the acquisition footprint is removed, only the surface multiple starting at $t \approx 0.25$ s on the right hand side of the image still reflects the rough measurement surface. Diffractions that stem from the corners of the shallow blocky structures at $t \approx 0.5$ s can be observed. The flanks of these rectangular structures are nearly vertical after the redatuming. The coherence section depicted in Figure 6.8 shows very high coherence values even for times greater than 1 s. For the display of the attribute sections, Figures 6.9 to 6.12, a coherence threshold of 0.2 was used to mask out unreliable attribute. According to Figure 6.9, most of the emergence angles are close to $0°$, except where the surface-multiple and the steep flanks of the three blocks are present. The NIP-wave radii generally increase with time for most of the section. There is one exception below the lens-like basin structure in the center of Figure 6.10. The radius turns negative here because this very basin structure with its convex boundary and extremely low velocity inverts the curvature of the corresponding NIP-wave. As expected, the N-wave curvature displayed in Figure 6.11 is generally very close to 0 m. However, there are small variations between CMP no. 400 and 700 due to the influence of the basin structure. The NMO velocity section (see Figure 6.12) was calculated from the optimized values of β_0 and R_{NIP} according to equation (C.3). In this case, the NMO-velocity differs from the actual stacking velocity but corresponds to a horizontal measurement surface through the respective emergence point of the simulated ZO ray (see Appendix C). For display, I used the *signed square root*, $\sqrt{a} := sign(a) \sqrt{|a|}$, taken from v_{NMO}^2 to also visualize imaginary values of the stacking velocity resulting from negative values of v_{NMO}^2. The depicted values of v_{NMO} show a similar behavior as the section with the NIP wave radius since the small variation of the emergence angles is negligible compared to the strong variation of R_{NIP}. Below the basin structure, the NMO velocity becomes imaginary, which means that the traveltime of the reflection events decreases with offset.

6.1.3 CRS-stack-based tomographic inversion

The second step of the conducted imaging workflow was to determine a smooth macrovelocity model via CRS-stack-based tomographic inversion. In detail, the following steps were involved:

- *Manual picking within the redatumed CRS stack results.* Input for the tomographic inversion process were 200 samples of the redatumed CRS stack section together with their associated values of emergence angle β_0 and NIP-wave radius R_{NIP}. The latter were picked interactively. To save time and to avoid difficulties at the boarders of the model, the target area was reduced to the range between CMP no. 125 and CMP no. 875. The individual pick locations are displayed in Figure 6.13. There, a certain gap in the picks below the blocky structures which is more than 0.2 s wide can be noticed cased by the lack of coherent reflections in that region. Another

difficulty that was encountered was the necessity to consider a lateral variable velocity gradient for the initial velocity model.

- *Tomographic inversion.* Starting from a laterally variable gradient model, the inversion converged quickly. The inverted macrovelocity model depicted in Figure 6.14 consists of 377 B-spline nodes. In vertical direction 29 node points with 100 m spacing and in horizontal direction 13 node points with 500 m spacing were used. A smaller grid was tested but did not lead to better results. The redatuming level at a depth of 108 m constitutes the upper border of the model.

Discussion of the results. As a result of the subsequent depth migration, it can be suggested that the smooth macrovelocity model depicted in Figure 6.14 is kinematically consistent with the interval velocity model used to generate the data. To resolve the complex structure of the original interval velocity model with its fine layering and various velocity inversions was neither expected nor intended since a smooth macrovelocity model is sufficient to calculate the traveltime tables needed by the subsequent migration.

6.1.4   Kirchhoff type poststack depth migration

The final step of the conducted workflow was a Kirchhoff poststack depth migration. Since the time frame for processing this dataset was quite narrow, prestack migration from topography was omitted. The following steps were performed:

- *Calculation of diffraction traveltime tables.* For the sake of simplicity, the necessary traveltime tables were generated from the macrovelocity model determined in the previous step by means of paraxial ray-tracing using the Seismic Un*x[2] (SU) module RAYT2D.

- *Poststack depth migration.* Poststack depth migration was carried out using the SU module SUKDMIG2D after a high cut filter with a corner frequency of 40 Hz was applied to the input traces. The lateral migration aperture was limited to 200 m and a migration angle aperture of 60° was chosen.

Discussion of the results. In general, the reflectors in the depth migrated image exhibit the correct shape and are located at the correct depth positions, according to the initial model displayed in Figure 6.1. A slightly wrong curvature of the reflectors below the wadi and the rectangular high-velocity structure can be observed. Furthermore, the planar reflector at the bottom of the original model shows erroneously a similar curvature as the reflectors above. This is caused by the fact that no picks from the associated reflection event contributed to the determination of the macrovelocity model.

---

[2]developed by the Colorado School of Mines (see, e. g., Cohen and Stockwell, 2000)
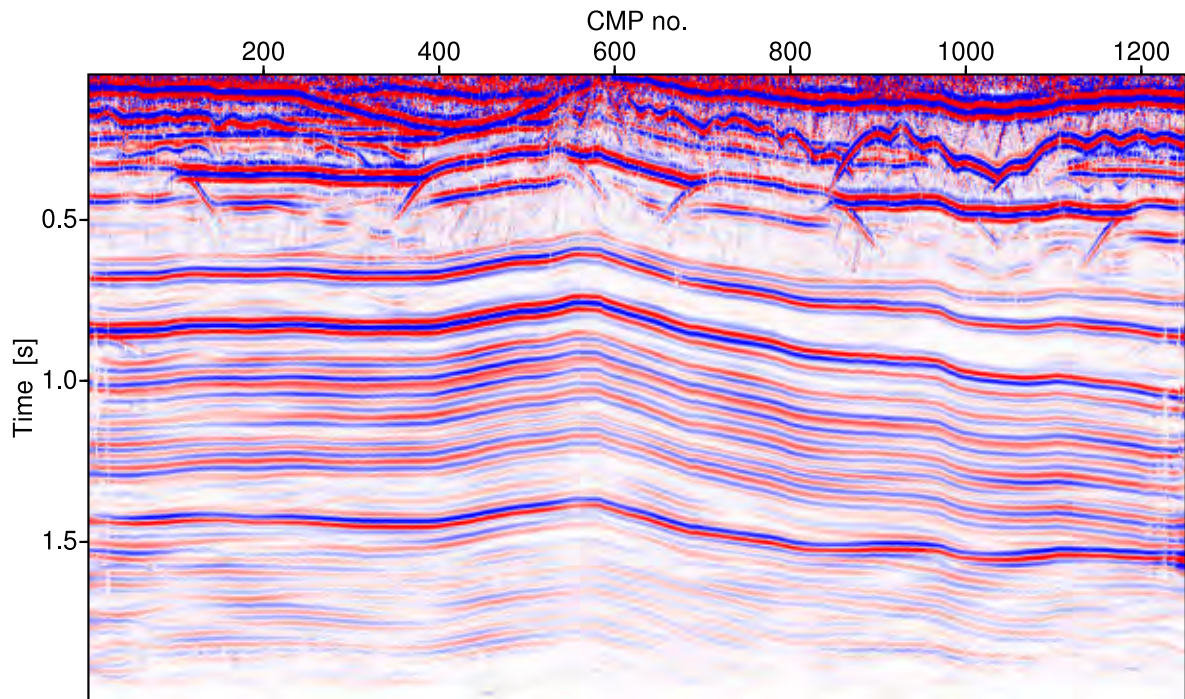
Figure 6.5: Result of optimized CRS stack restricted to the projected first Fresnel zone. The simulated ZO traveltimes are related to the smoothed reference level.
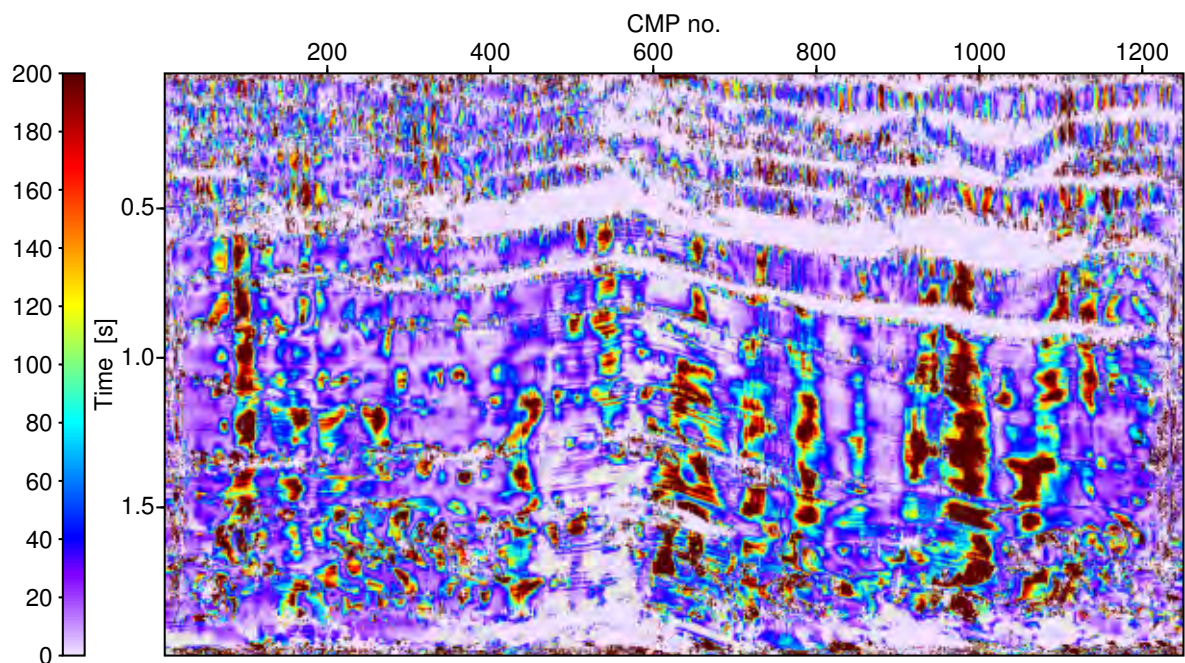
Figure 6.6: Percentage increase of coherence between initial and optimized CRS stack result.
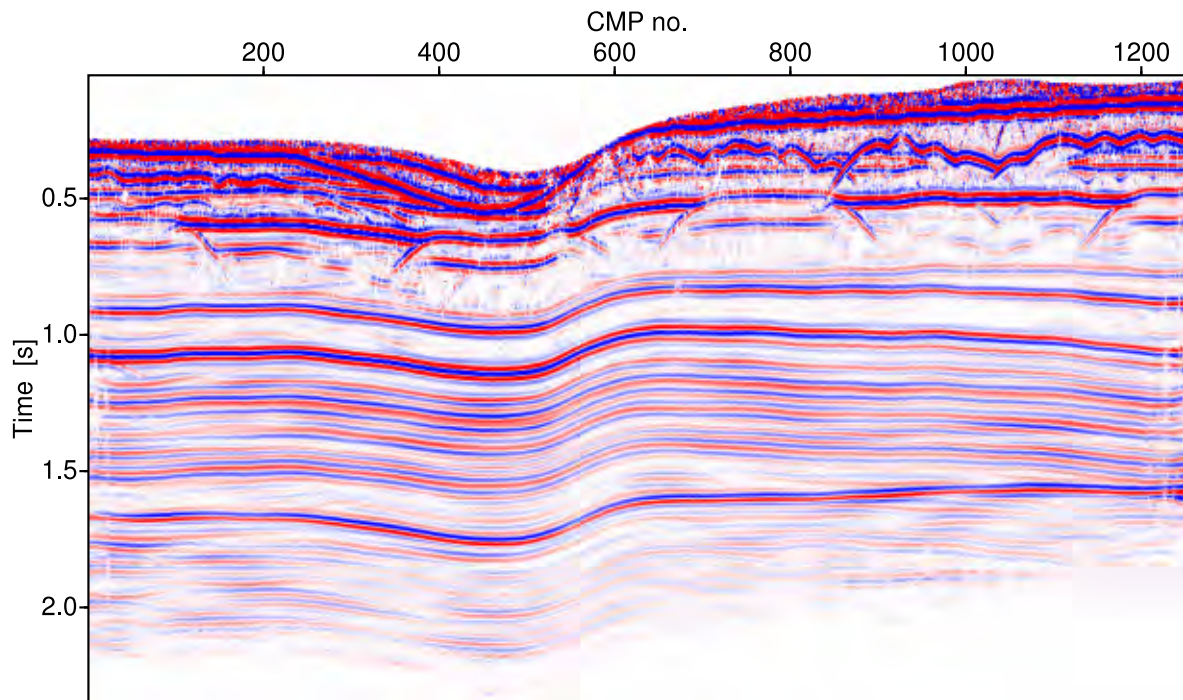
Figure 6.7: Result of optimized CRS stack restricted to the projected first Fresnel zone after redatuming. The redatuming procedure relates the achieved results to a fictitious horizontal measurement surface at $z = -108$ m.
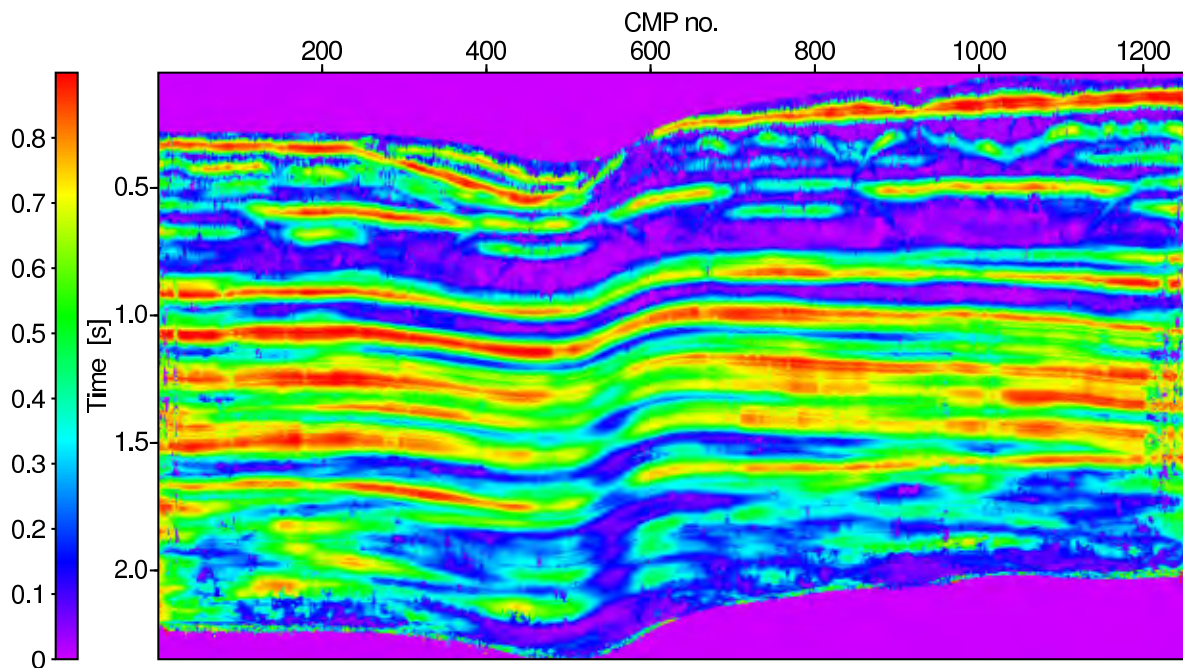
Figure 6.8: Coherence, associated with the optimized CRS stack, related to a fictitious horizontal measurement surface at at $z = -108$ m.
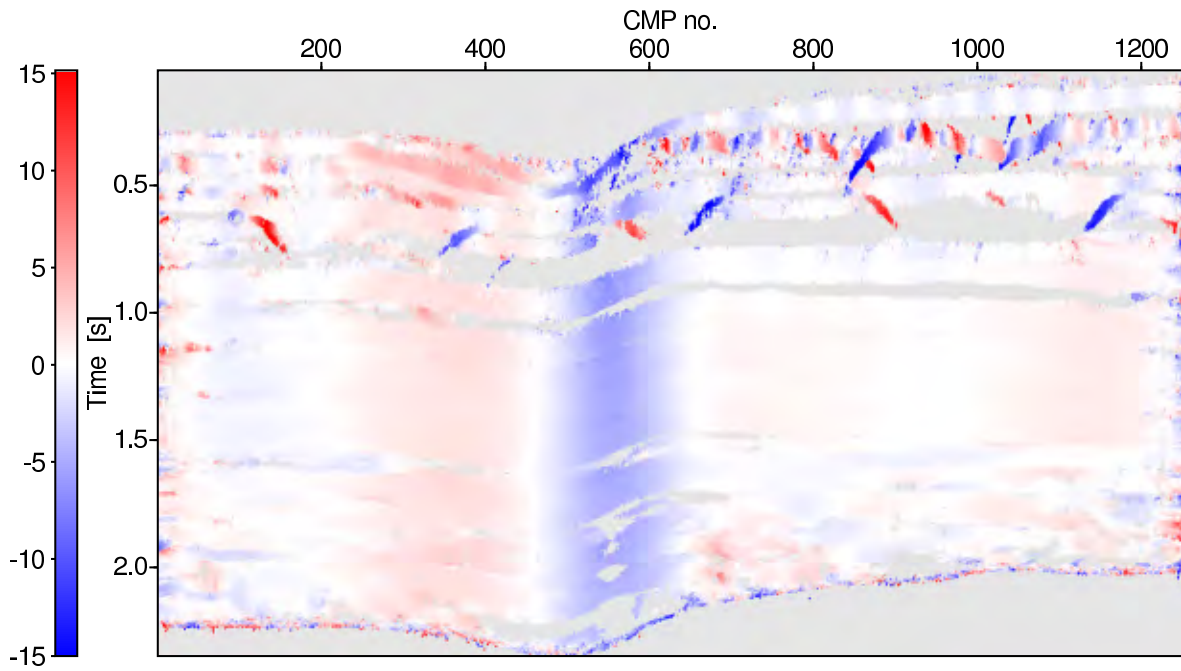
Figure 6.9: Emergence angle of the simulated ZO rays [deg], related to a fictitious horizontal measurement surface at at $z = -108$ m. ZO samples with very low coherence value are masked out (gray), as they are not expected to be related to reliable attributes.
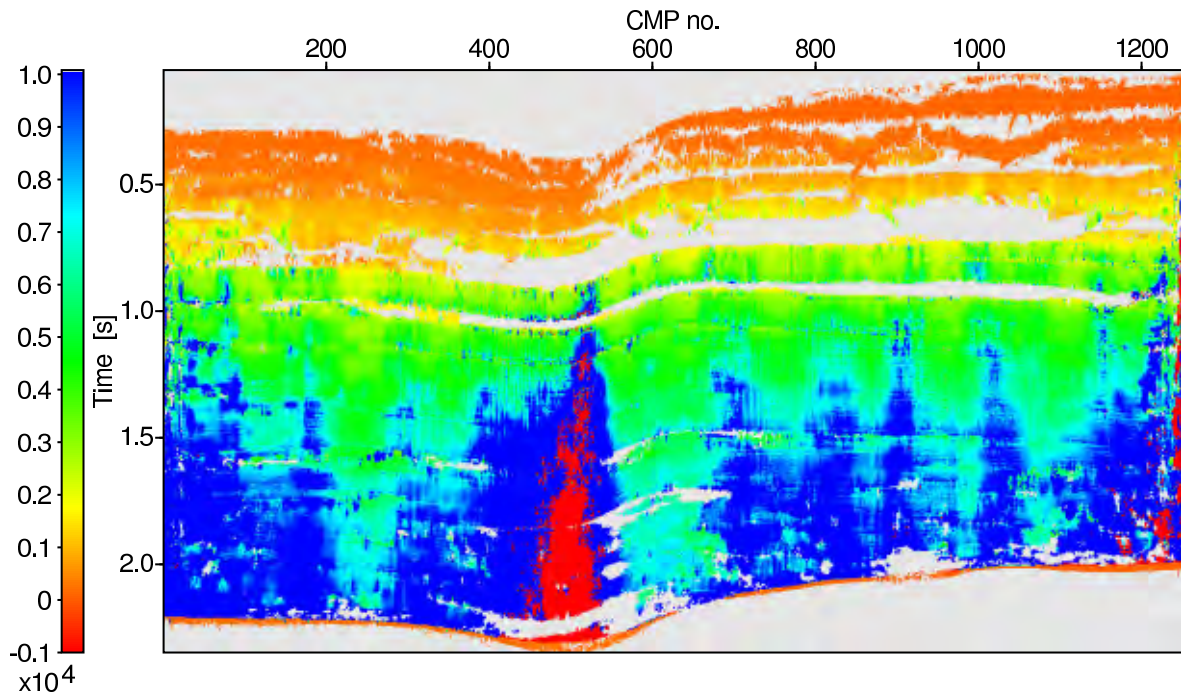
Figure 6.10: Radius of the Normal-Incidence-Point (NIP) wavefront [m], related to a fictitious horizontal measurement surface at at $z = -108$ m. ZO samples with very low coherence value are masked out (gray), as they are not expected to be related to reliable attributes.
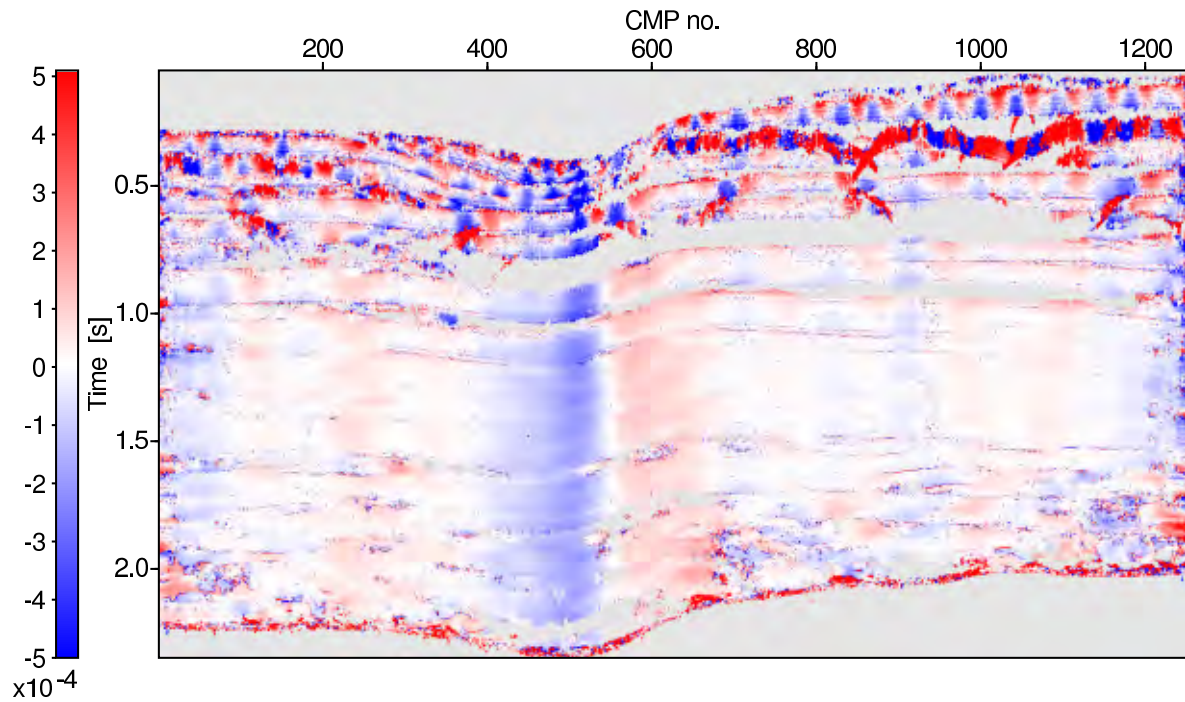
Figure 6.11: Curvature of the normal wave [1/m], related to a fictitious horizontal measurement surface at at $z = -108$ m. ZO samples with very low coherence value are masked out (gray), as they are not expected to be related to reliable attributes.
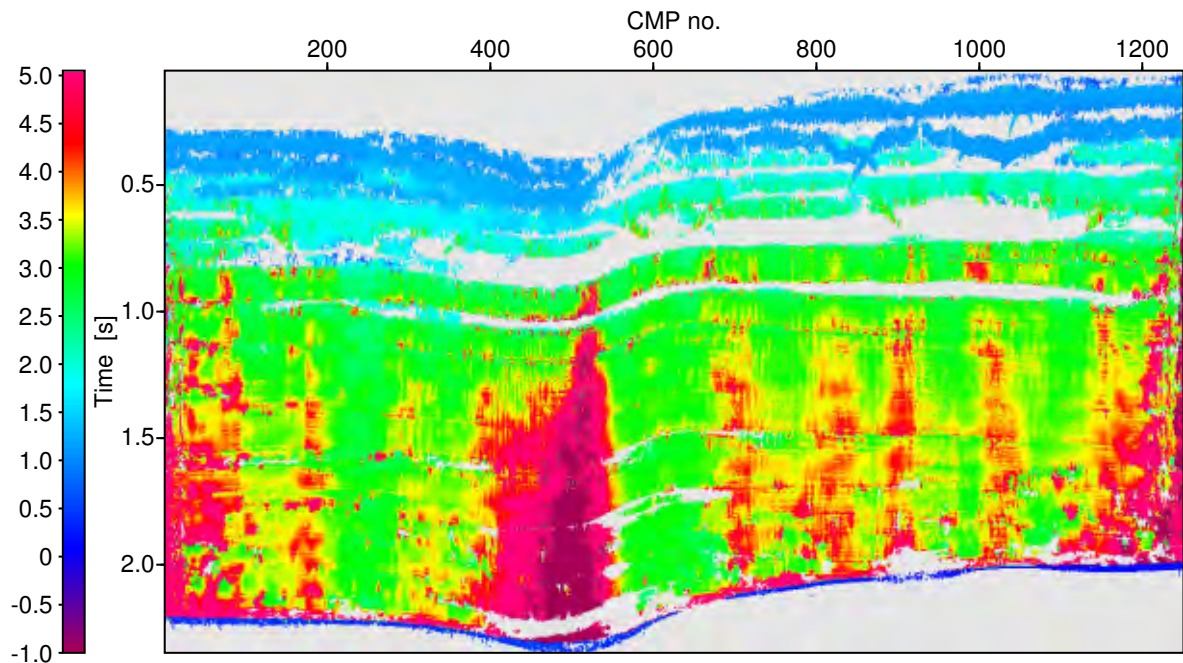
Figure 6.12: NMO velocity [km/s] calculated from optimized CRS attributes and related to a fictitious horizontal measurement surface at $z = -108$ m. To be able to visualize also imaginary values of the NMO velocity the *signed square root* of v_{NMO}^2 is depicted. Thus, negative values correspond to imaginary value of v_{NMO}. ZO samples with very low coherence value are masked out (gray), as they are not expected to be related to reliable attributes.
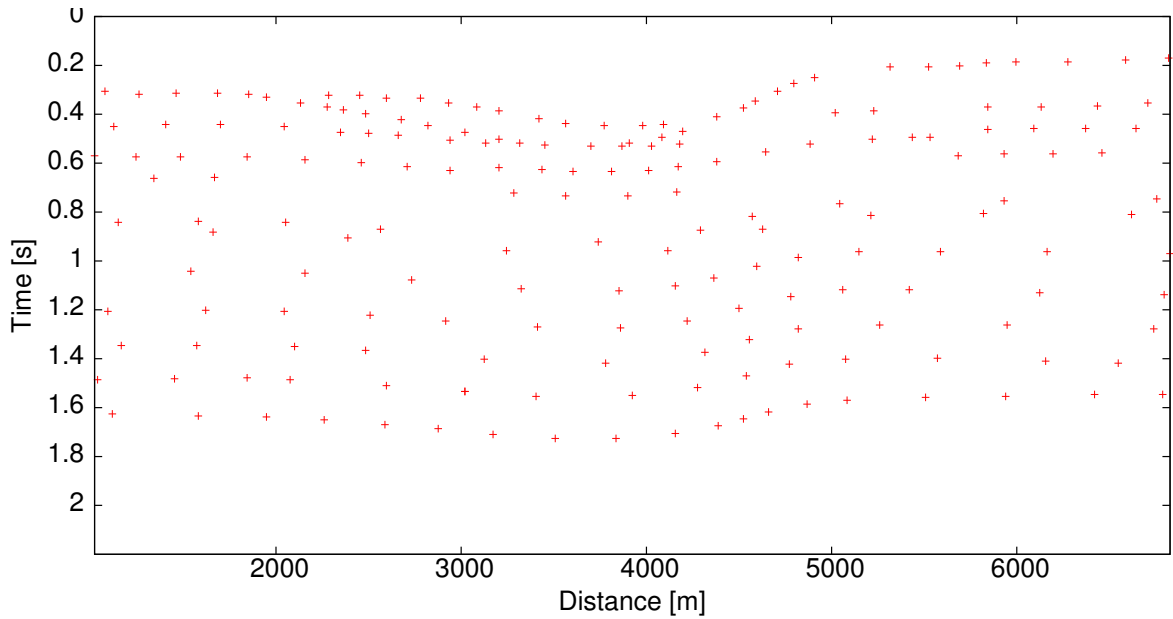
Figure 6.13: Red crosses indicate the position of the redatumed ZO samples from which traveltime, midpoint position, emergence angle, and NIP-wave radius were extracted to serve as input for the tomographic inversion.
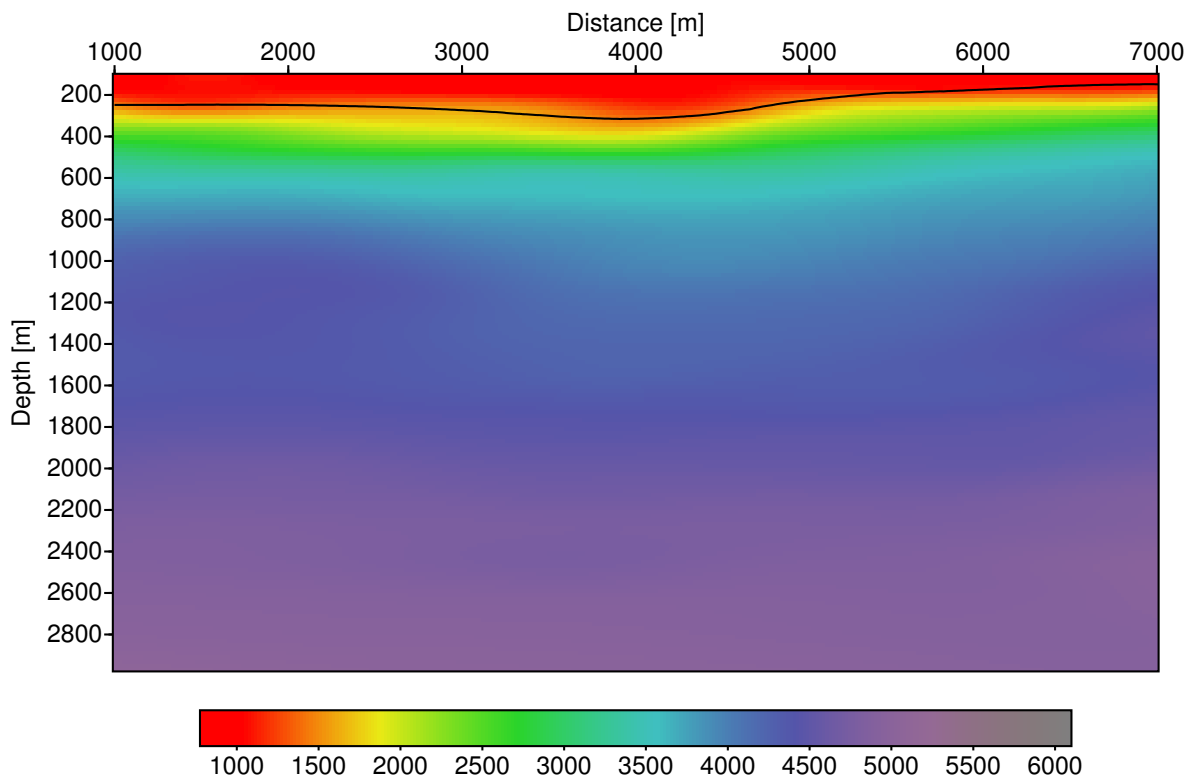
Figure 6.14: Smooth macrovelocity model [m/s] resulting from the tomographic inversion of CRS attributes.
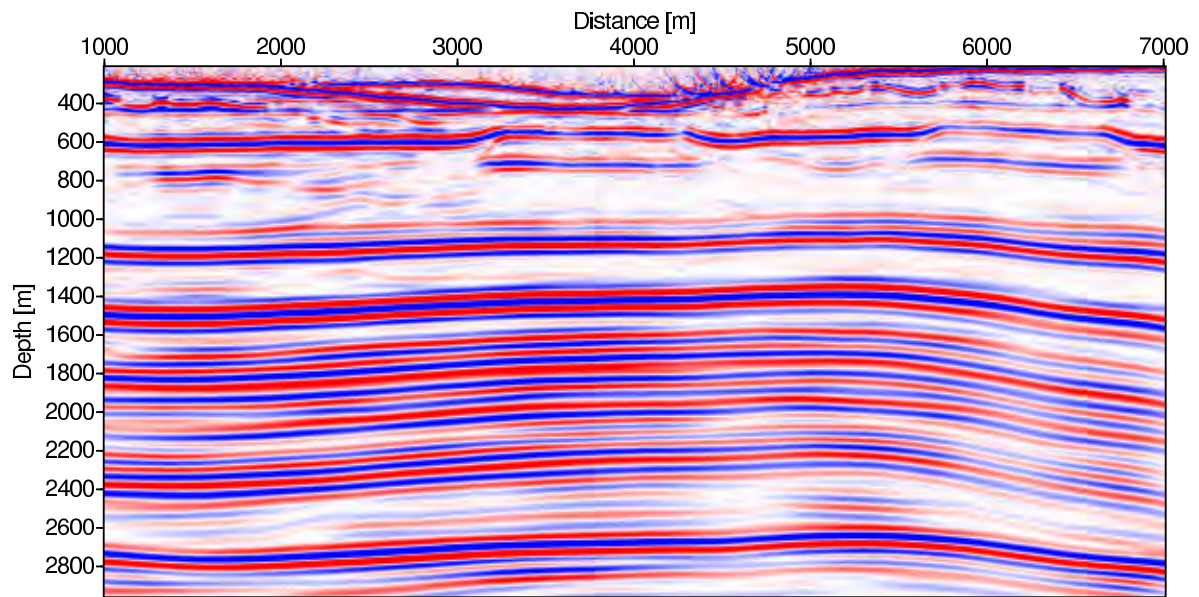
Figure 6.15: Poststack depth migration result of the optimized CRS stack section after redatuming depicted in Figure 6.7. The smooth macrovelocity model, depicted in Figure 6.14, was used to generate the necessary diffraction traveltime tables.

6.2 Synthetic data example B

The synthetic data set presented in this section was created 1997 by S. H. Gray, mainly with the purpose of testing static correction and migration schemes (see, e.g., Gray, 2005). Later it was kindly provided to us by J. A. Dellinger to test our implementation of the CRS stack for topography including CRS-stack-based residual static corrections. The velocity model used to create the prestack data is depicted in Figure 6.16. It aims at simulating a situation typical for the overthrust front of the Canadian Foothills. However, similar geological settings can be found in many other foothill areas of this world, too. The data set discussed in this section was the first data on which the CRS stack for topography was tested in combination with CRS-stack-based residual static corrections. For this purpose a residual static correction module, based on a stand-alone program (see, e.g., Koglin and Ewig, 2003), was included in the CRS stack implementation and extended to consider topography and laterally variable near-surface velocities.
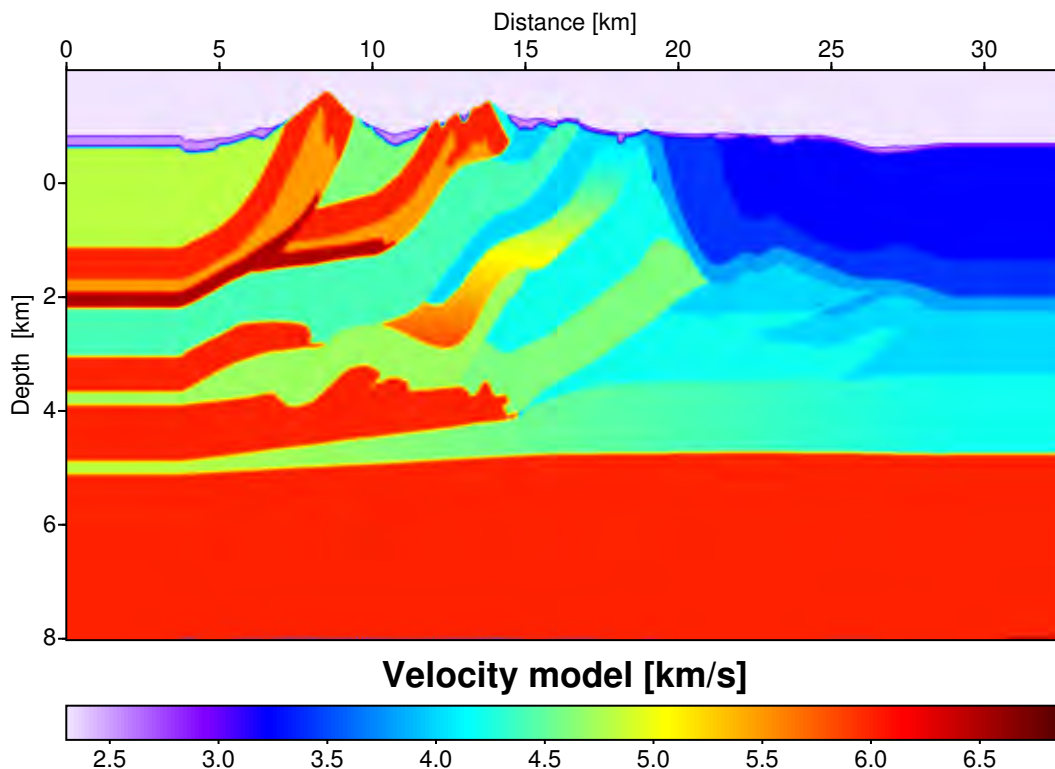
Figure 6.16: Velocity model used to create the prestack data. The model corresponds to a Canadian Foothills setting, featuring typical variations in topography, near-surface velocity, and subsurface velocity. The light purple shaded area at the top is above topography.

6.2.1 Model and survey design

The model can be roughly divided into three parts: the lower foreland margin on the right hand side is signified by a mostly planar topography and a quite simple subsurface structure, the transition zone starting at km 30 exhibits smooth topographic changes and an already complicated subsurface structure with very steep layering. Finally, the left hand side of the model is dominated by steep foothills
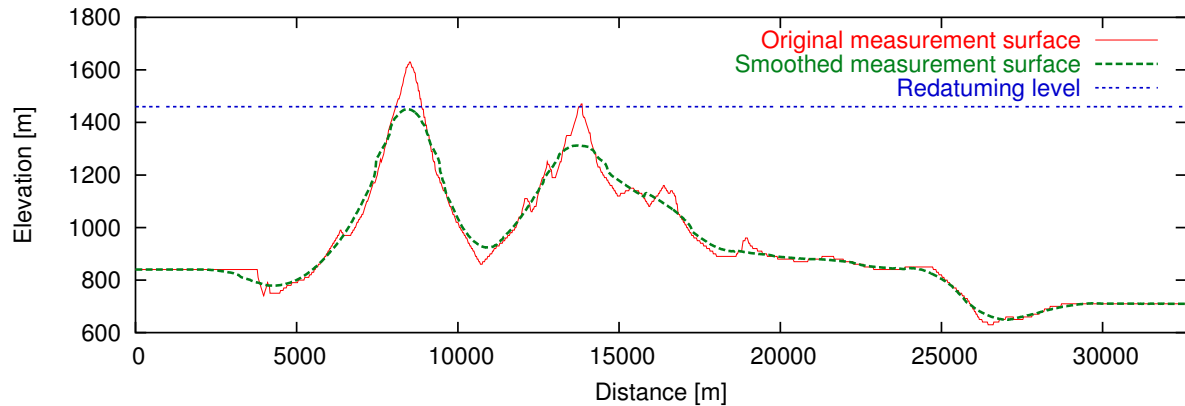
Figure 6.17: Comparison between original and smoothed measurement surface. The horizontal surface at $z = 1459$ m was used as reference level for the redatuming.

characterized by a very rough top-surface topography with an overall change of nearly 800 m, complicated near-surface conditions with high-velocity thrust sheets (red) piercing the surface next to low-velocity layers (blue), and a structurally complex subsurface with deep hydrocarbon targets, large velocity contrasts and several velocity inversions. Obviously, it is the this part that poses the largest problems for data processing. The simulated survey has a total length of 32 600 m. Its highest point has an elevation of 1 630 m, whereas the lowest point lies at 630 m. A magnified view of this topography is shown in Figure 6.17. The smoothed surface depicted in green was used as floating reference level for the CRS stack results. The planar surface (blue) indicates the horizontal reference datum to which these results were subsequently mapped by the redatuming procedure. For the fictitious layer between the floating datum and the horizontal reference level a constant redatuming velocity of 3300 m/s was chosen. Similar as for the previous data example a split spread acquisition was simulated. To account for the very steep structures a large offset range (-3762 m to 3738 m) was considered. A quite large shot interval of 100 m, typical for acquisition in difficult environments, was chosen together with a receiver interval of 25 m. The resulting maximum CMP fold is 38 traces, which is relatively sparce compared to the previous data example. To highlight some of the features of this dataset a CMP gather at km 15 is shown in Figure 6.18. For display, automatic gain control with a window size of 0.5 s was used to amplify deeper reflections. The rugged topography and the strongly fluctuating near-surface velocities have created short wavelength statics. It is obvious that due to the topography and the lateral variations of the near-surface velocity the moveout is far from being hyperbolic. For small offsets even a negative moveout can be observed. The trace-header information of the prestack data concerning the geometry of the virtual survey is given in Table 6.2.1. Different to the real data examples presented in the next chapter no irregularities of the acquisition have to be faced such as deviation of sources or receivers from the straight line or missing shots and receivers caused by insufficient coupling or other environmental difficulties.

6.2.2 CRS stack for topography and residual static corrections

The workflow conducted for this data set included CRS stack considering topography and variable near-surface velocity, followed by five iterations of residual static corrections, a final application of
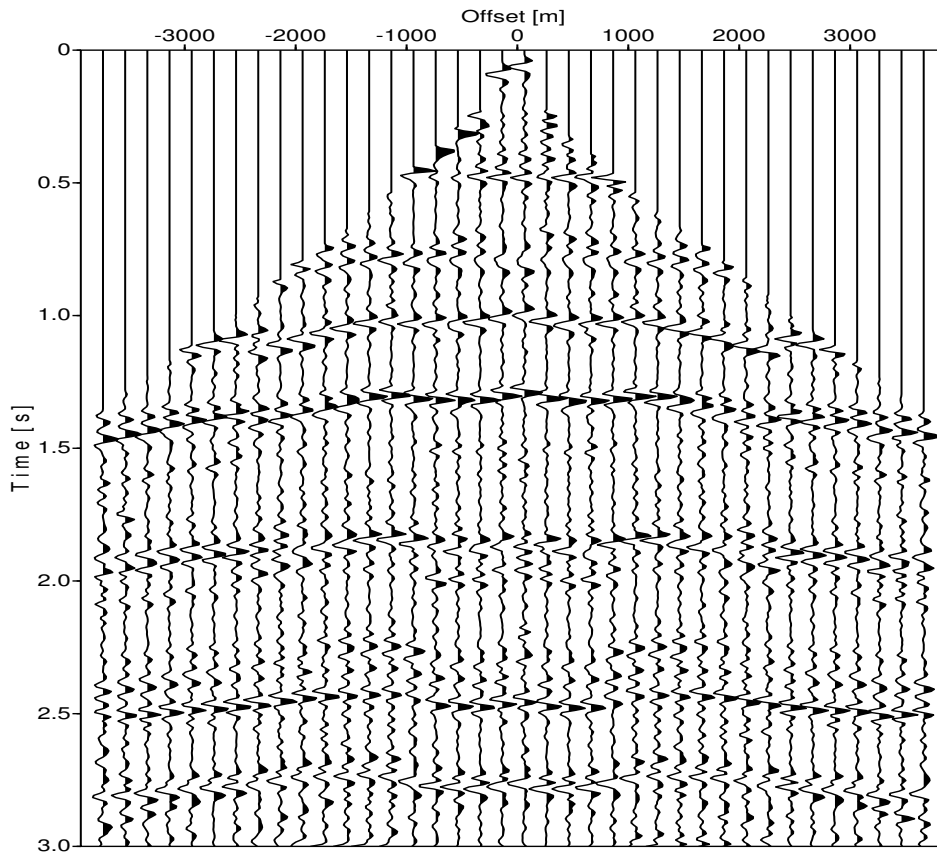
Figure 6.18: CMP gather from km 15. The reflection travel times are strongly influenced by the top-surface topography and the near-surface conditions so that their moveout is far from being hyperbolic. Even negative moveout can be observed for small offsets.

	Number of shots	252
Shot and	Shot interval	100 m
receiver	Maximum number of receivers	301
geometry	Receiver interval	25 m
	Number of traces	75 852
Midpoint and	Number of CMP bins	2309
offset	Maximum CMP fold	38
geometry	Full offset range	-3762…3738 m
	Recording time	4.096 s
Recording	Sampling interval	8 ms
parameters	Dominant frequency	18 Hz
	Maximum frequency	40 Hz

Table 6.2: Information on the prestack data, obtained from the trace-headers.
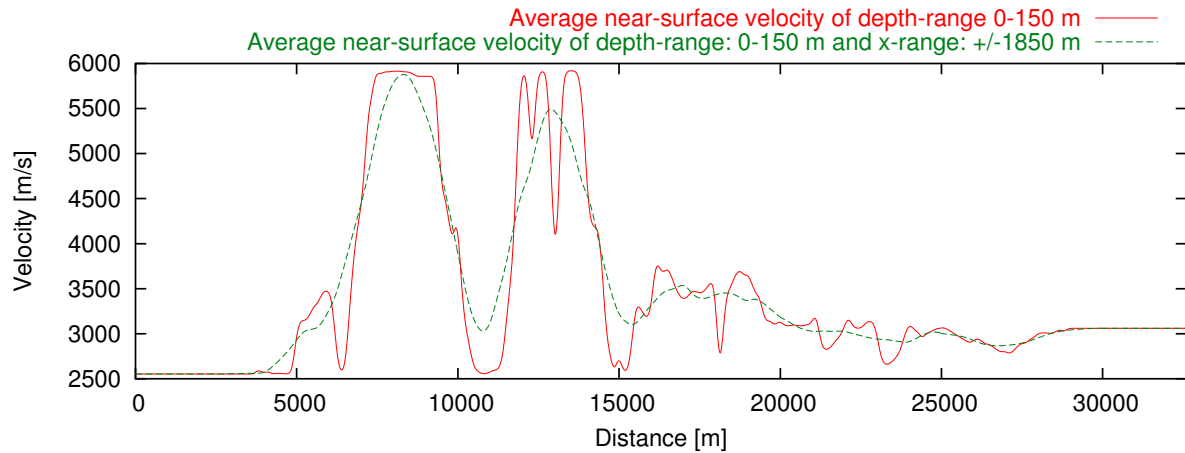
Figure 6.19: The near-surface velocity vertically averaged for a depth-range of 0 to 150 m is depicted in red. The laterally smoothed and vertically averaged near-surface velocity depicted in green was used as near-surface velocity v_0 for the CRS stack.

the CRS stack using the corrected data and redatuming to a horizontal reference level. To account for the strong fluctuations of the near-surface velocity, ranging from 2.5 km/s to nearly 6.0 km/s, the average value of the near-surface velocity within the maximum offset aperture was used for attribute determination, stacking and residual static correction. The local near-surface velocity used for the small scale static corrections applied for the initial stack and its laterally averaged value that serves as v_0 in equations (3.11) and (3.21) are depicted in Figure 6.19. In detail, the following processing sequence was carried through:

- *Topography and near-surface velocity analysis.* The actual measurement surface was smoothed using a smoothing aperture of 3700 m equal to the size of the maximum offset aperture later considered by the CRS stack. This ensures that each point at the smoothed reference level can be well approximated by a parabola with apex at the center of the stacking aperture (see Section 4.4.3). A comparison between the smoothed measurement surface and the actual topography is depicted in Figure 6.17. The variable near-surface velocity $v_0(m_x)$ was extracted from the velocity model depicted in Figure 6.16 by locally averaging the near-surface velocity of the first 150 m depth and smoothing the obtained values laterally using again a smoothing aperture of 3700 m equal to the size of the maximum offset aperture (see Figure 6.19). This time, a larger depth range for extracting the near-surface velocities was used than in the previous data example (150 m instead of 50 m) to account for the larger changes in elevation and for the larger offset range.

- *Small scale static corrections.* In order to be more consistent with the situation encountered in real data processing, where only limited information concerning the near-surface velocity field is available, the field static corrections used for the initial CRS stack were calculated by means of the averaged near-surface velocities of the first 150 m instead of extracting the average velocity actually valid for the applied static correction. The total time shifts of the individual traces ranged from -71 ms to 52 ms.

- *Initial CRS stack.* A time dependent offset aperture was employed linearly increasing from 150 m at 0.1 s to 3700 m at 1.5 s. The reason for choosing such a large offset aperture was, on the one hand, the sparse CMP fold and, on the other hand, the necessity to image very steep reflections. The latter was also the cause why emergence angle values within the range of ±80° were considered during the search. The NMO velocity was sought for within the range of 1000 m/s to 7500 m/s. The midpoint aperture increased from 10 m at minimum traveltime to 1200 m at maximum traveltime. For the plane-wave search only 30% of this aperture were used. For the sake of brevity initial CRS stack results are not displayed.

- *Event consistent smoothing.* For the parallelogram shaped smoothing window a spatial half-width of 37.5 m and a temporal half-width of 16 ms was chosen. The maximum angle deviation for samples to be accepted was 3° and a time dependent coherence threshold linearly decreasing from 0.13 for minimum traveltime to 0.03 for maximum traveltime had to be exceeded. For each ZO sample smoothing was only applied if 80% of the samples within the surrounding window fulfilled these criteria.

- *Optimization.* Optimization was carried through for every sample of the ZO section even though the number of samples to be optimized could have been reduced by defining a time dependent coherence threshold below which no optimization is performed. The latter can be advantageous for very large data sets for which time is a crucial factor. The size of the projected Fresnel zone calculated from the initial attributes was used to limit the search aperture. The final stacking aperture was limited by the projected Fresnel zone calculated from the optimized attributes. The resulting stack section is depicted in Figure 6.20.

- *Residual static correction.* Five iterations of residual static corrections were conducted, each of them followed by an optimization of the CRS attributes applied to the updated, i. e. corrected, data set. After the last iteration the initial CRS stack was repeated before the final optimization. The traveltime window used for the cross-correlations spread from 0.35 s to 3.2 s. The maximum shift for a certain source or receiver location was limited to 50 ms per iteration. Source or receiver time shifts determined from cross correlation stack with less than 500 contributing traces were not considered. The total residual static time shifts for the source and for the receiver locations are depicted in Figure 6.21. The stack and coherence sections resulting from the final iteration of the CRS stack applied to the corrected prestack data are depicted in Figures 6.22 and 6.24.

- *Redatuming.* The horizontal redatuming level was chosen 10 m above the highest peak of the smoothed reference surface, i. e. at an elevation of 1459 m. The average near-surface velocity in the target zone, i. e. 3491 m/s, was used as redatuming velocity. The optimized stack section after redatuming is depicted in Figure 6.25. The attribute sections after redatuming and the associated NMO velocity section after redatuming are depicted in Figures 6.26 to 6.29.

Discussion of the results. The stack section after residual static correction (see Figure 6.7) clearly images most of the wave impedance contrasts contained in the velocity model. Besides this, several diffractions from edges of structures with limited lateral extent can be observed. The most prominent event in the section stems from the reflector at about 5 km depth. It is followed by internal multiples. The steep flanks of the high-velocity thrust sheets have been resolved nearly up to the surface. The same holds also for the deeper thrust sheets in the collision zone and the very steep interface between this area and the tectonically undisturbed area at the right hand side of the model. Only at distance

14.5 km a vertical disruption of the events can be observed that might be caused by the cycle-skip in the residual static time shifts (see Figure 6.21) applied for this location. The coherence section depicted in Figure 6.24 emphasizes this indication.

Comparing the stack sections before and after application of residual static corrections a significant increase of signal-to-noise ratio and event continuity can be observed. On the right hand side and at the left border of the stack section, the stack result without residual static corrections is already quite satisfactory, showing a good signal to noise ratio and clearly imaged reflections. However, below the steep foothills where the high-velocity thrust sheets reach the surface the reflections are still obscured by remaining short wavelength statics. The latter are caused by the strongly fluctuating near-surface conditions which cannot be fully compensated by the current CRS stack approach, especially not as long as the same v_0 is used for each trace within the stacking aperture according to equation (3.11). Fortunately, this limitation can be largely compensated by means of CRS-stack-based residual static corrections as long as the deviation between actual reflection response and stacking operator are small enough to allow the determination of at least some coherent events. This is further demonstrated by the large percentage increase of coherence between the optimization results before and after residual static correction, depicted in Figure 6.6.

Both, for the redatumed attribute sections (Figures 6.26, 6.27, and 6.28), and for the redatumed NMO velocity section (Figure 6.26), a time dependent coherence threshold was used to mask out ZO samples that are not expected to be related to reliable attribute values since they do not correspond to a coherent reflection event. Nevertheless, there is still some coherent noise left in the very shallow part of the sections, particularly at the right hand side of the figures. Besides this, the attribute values are smooth along the events and show the expected behavior. It can be concluded that the redatuming removed the acquisition footprint to a certain extent as can be seen, e. g., by comparing the deepest reflection events at the right hand side of Figures 6.22 and 6.25. Obviously, this does not mean that now all of the time-domain images of the reflections would have the same shape as the depth domain reflectors, especially not for such a complex model. This can only be achieved by a subsequent depth migration using a correct macrovelocity model. Unfortunately, the limited time frame of this thesis did not allow to extent the applied imaging workflow to the depth domain, since the macrovelocity model determination for such a difficult model had to be expected to be very time consuming.
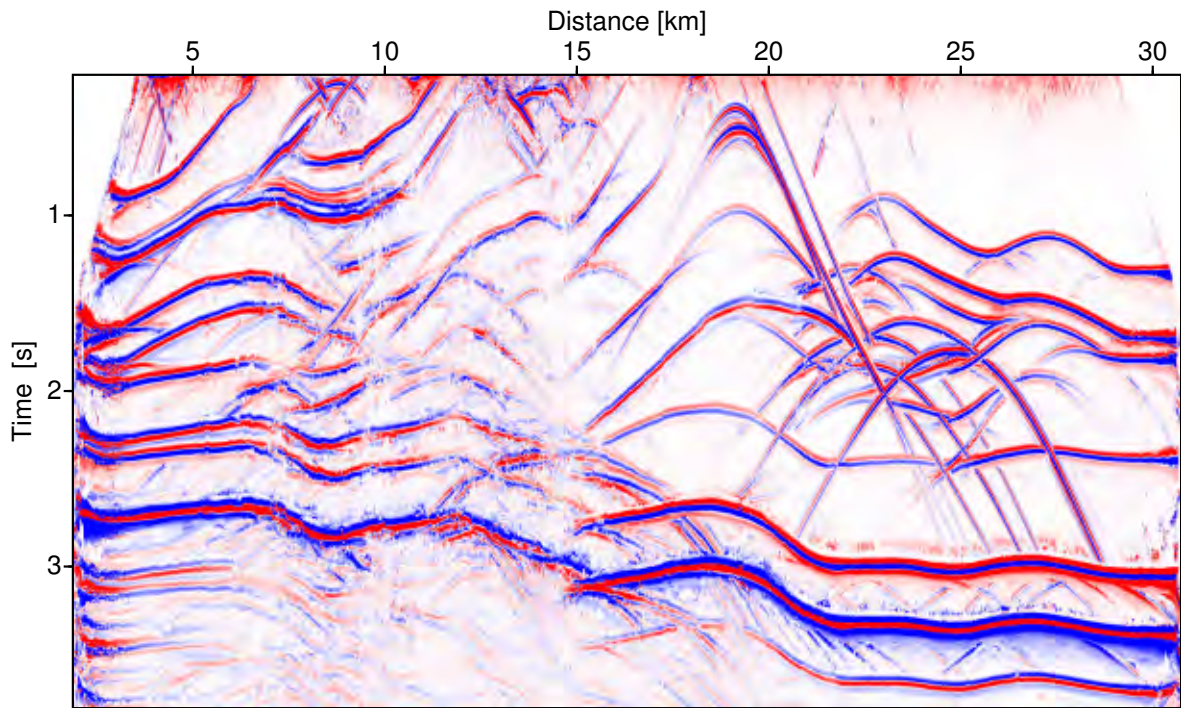
Figure 6.20: Result of optimized CRS stack restricted to the projected first Fresnel zone. The simulated ZO traveltimes are related to the smoothed reference level.
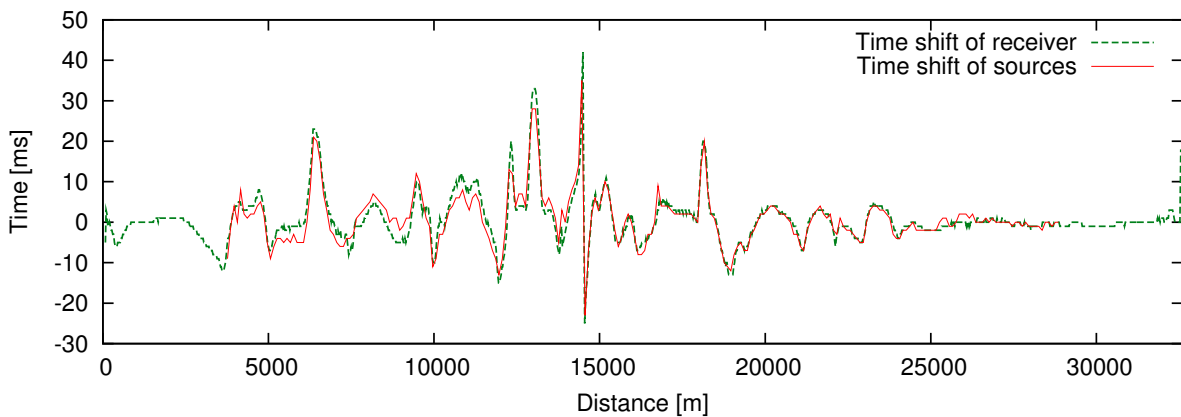
Figure 6.21: Accumulated static time shifts for the individual source and receiver locations after five iterations of residual static corrections. The large time shift at the right border is caused by an insufficiently large number of traces contributing to the cross-corelation stacks. An unwanted cycle-skip at 14500 m can be observed.

110
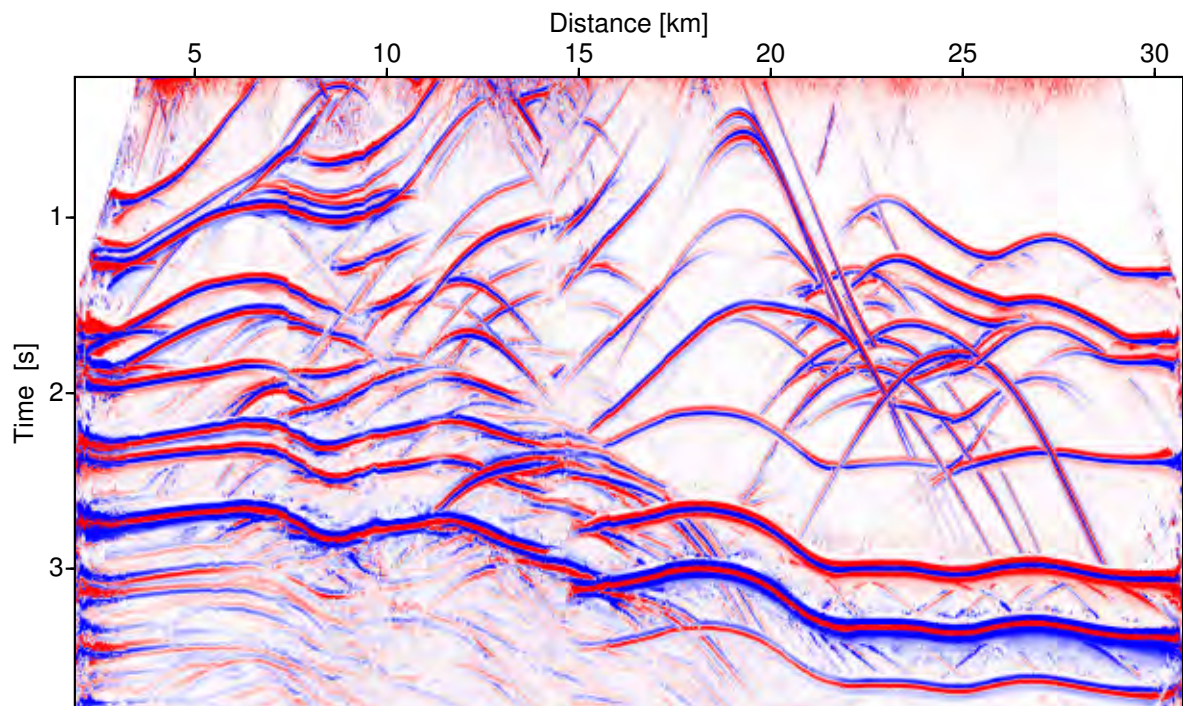
Figure 6.22: Result of optimized CRS stack restricted to the projected first Fresnel zone after five iterations of residual static correction.
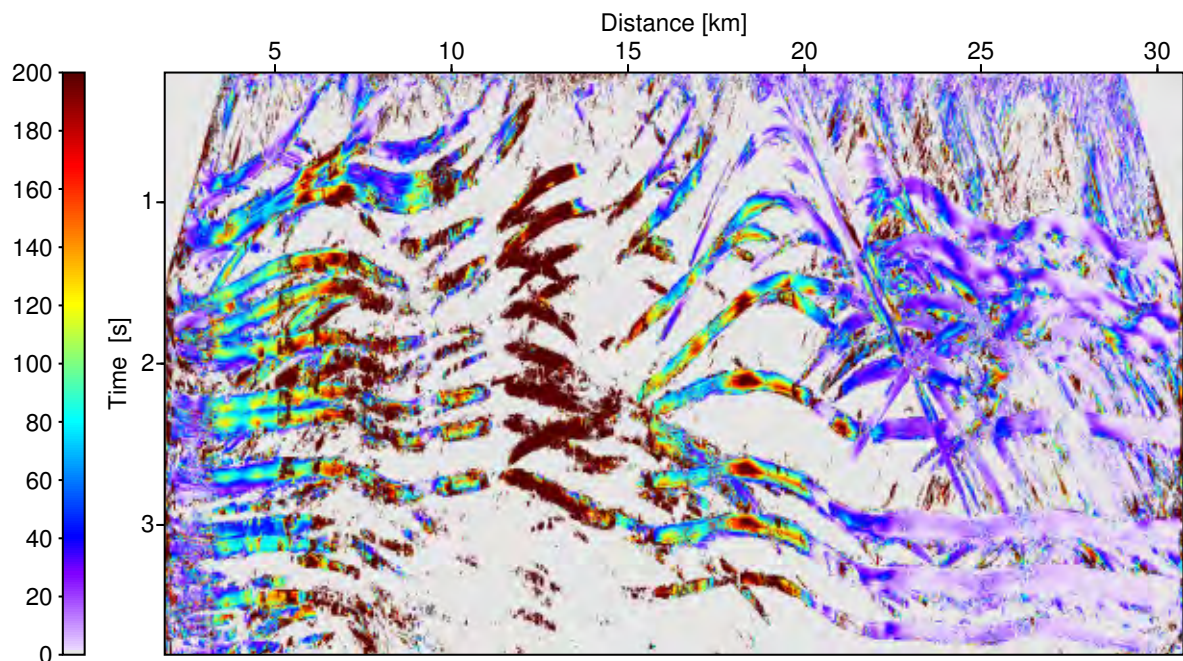
Figure 6.23: Percentage increase of coherence between optimized CRS stack before and after residual static correction.
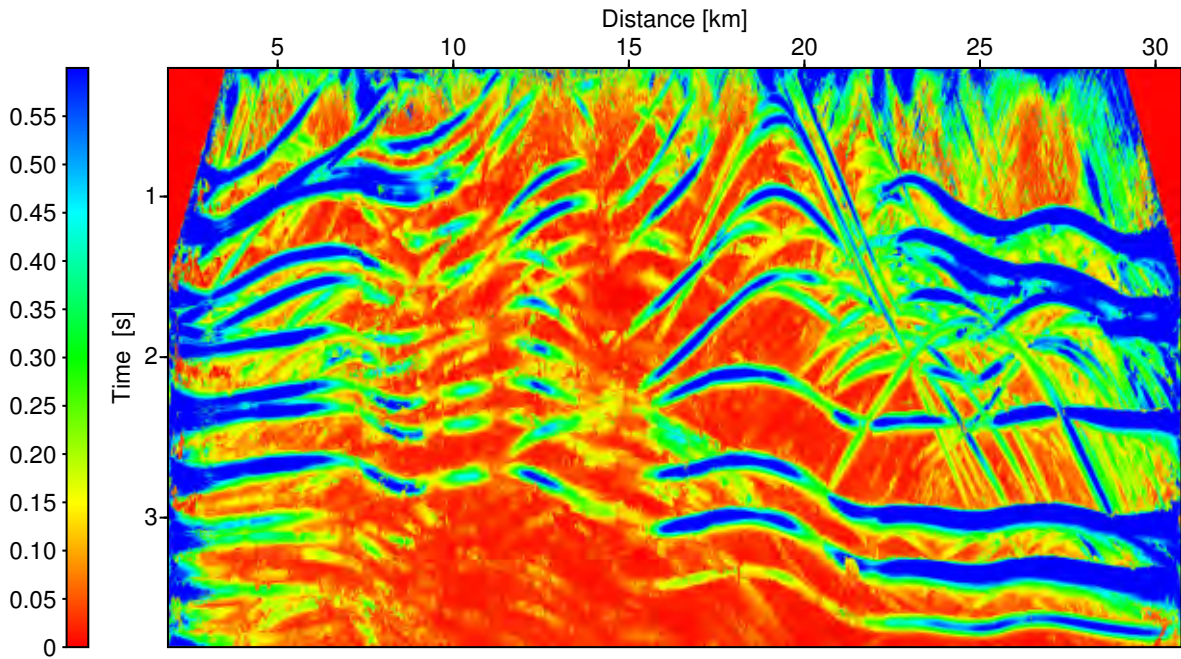
Figure 6.24: Coherence associated with the optimized CRS stack after residual static correction.
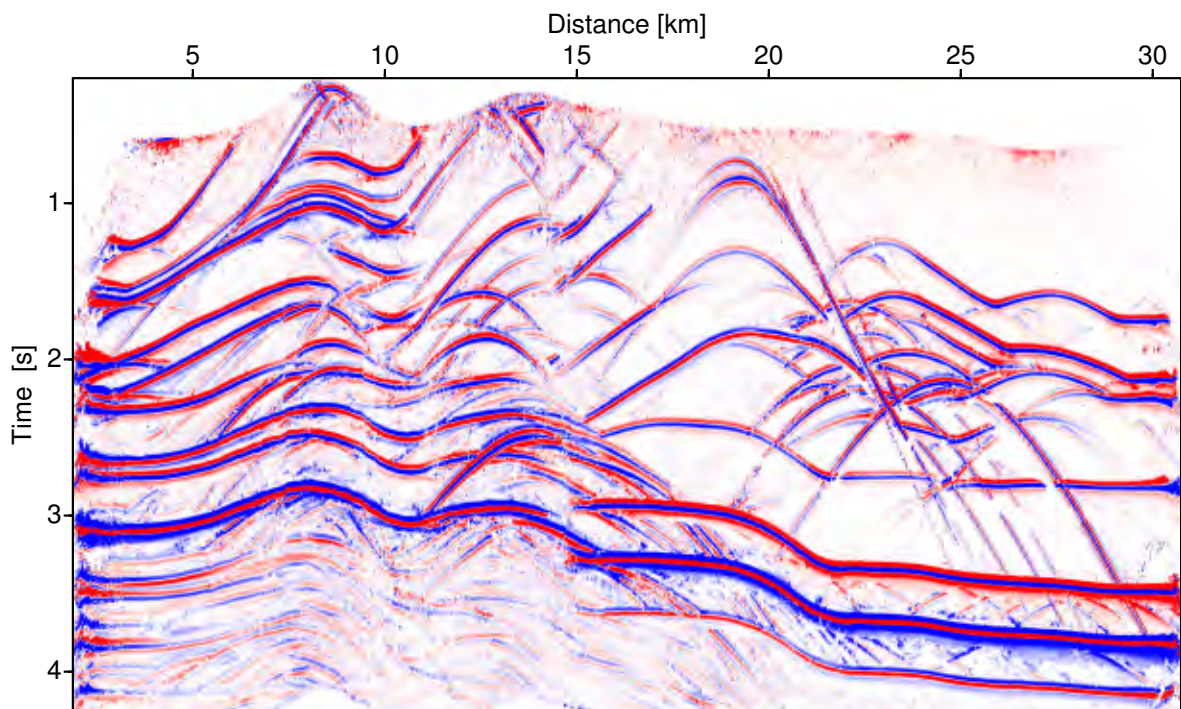
Figure 6.25: Result of optimized CRS stack, restricted to the projected first Fresnel zone, after residual static correction and redatuming. The redatuming procedure relates the achieved results to a fictitious horizontal measurement surface at $z = 1459$ m.
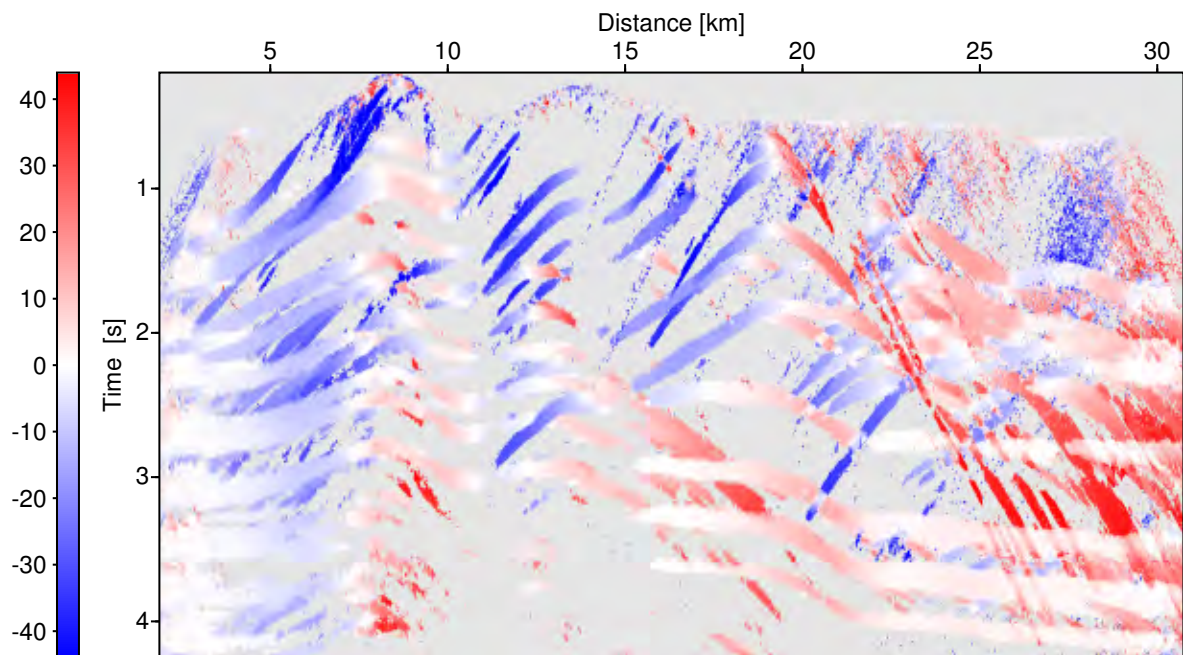
Figure 6.26: Emergence angle of the simulated ZO rays [deg] after residual static correction, related to a fictitious horizontal measurement surface at $z = 1459$ m. ZO samples with very low coherence value are masked out (gray), as they are not expected to be related to reliable attributes.
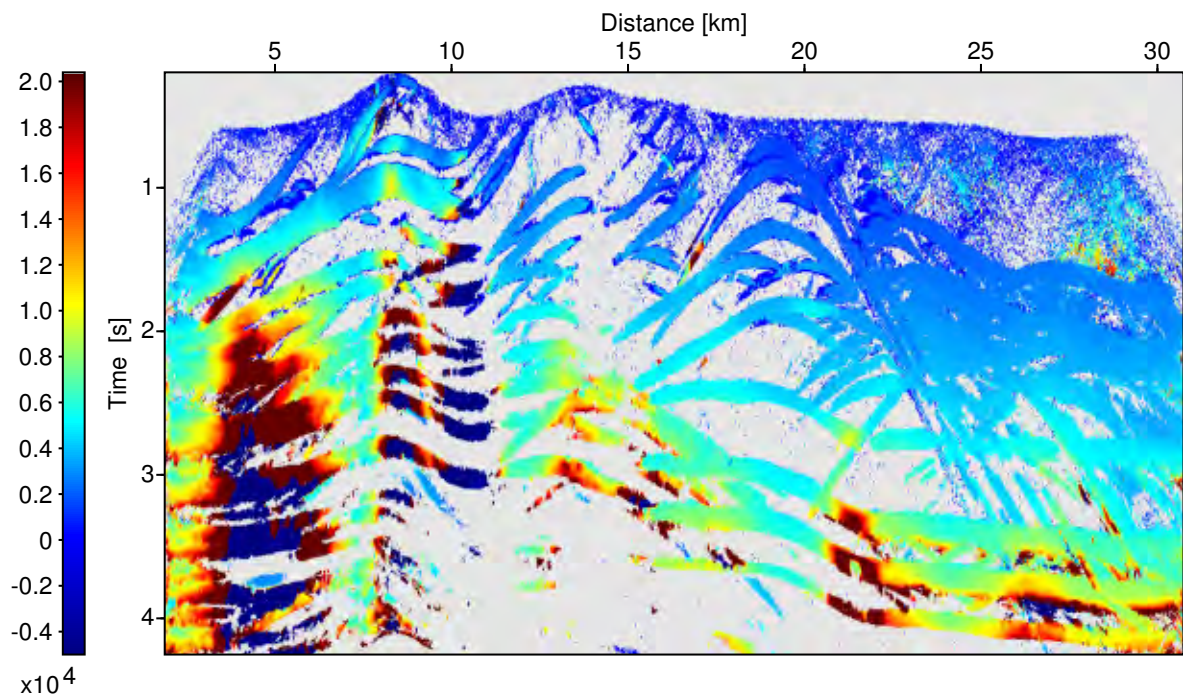
Figure 6.27: Radius of the Normal-Incidence-Point (NIP) wavefront [m] after residual static correction, related to a fictitious horizontal measurement surface at $z = 1459$ m. ZO samples with very low coherence value are masked out (gray), as they are not expected to be related to reliable attributes.

113
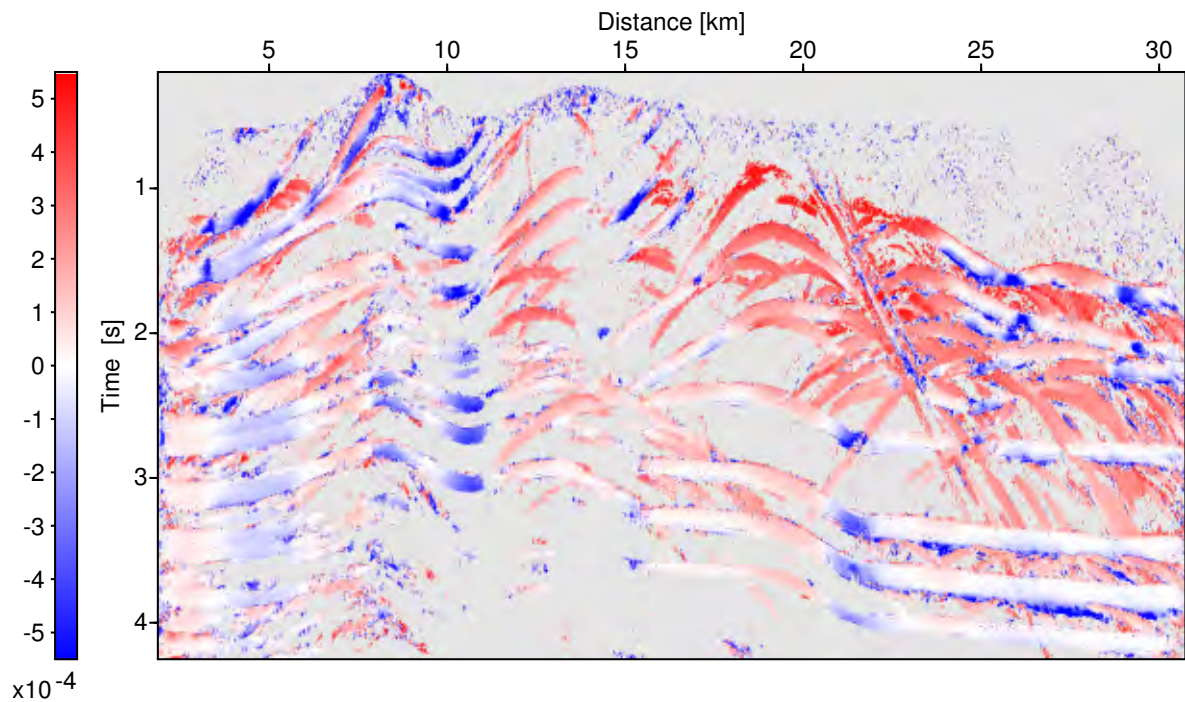
Figure 6.28: Curvature of the normal wave [1/m] after residual static correction, related to a fictitious horizontal measurement surface at $z = 1459$ m. ZO samples with very low coherence value are masked out (gray), as they are not expected to be related to reliable attributes.
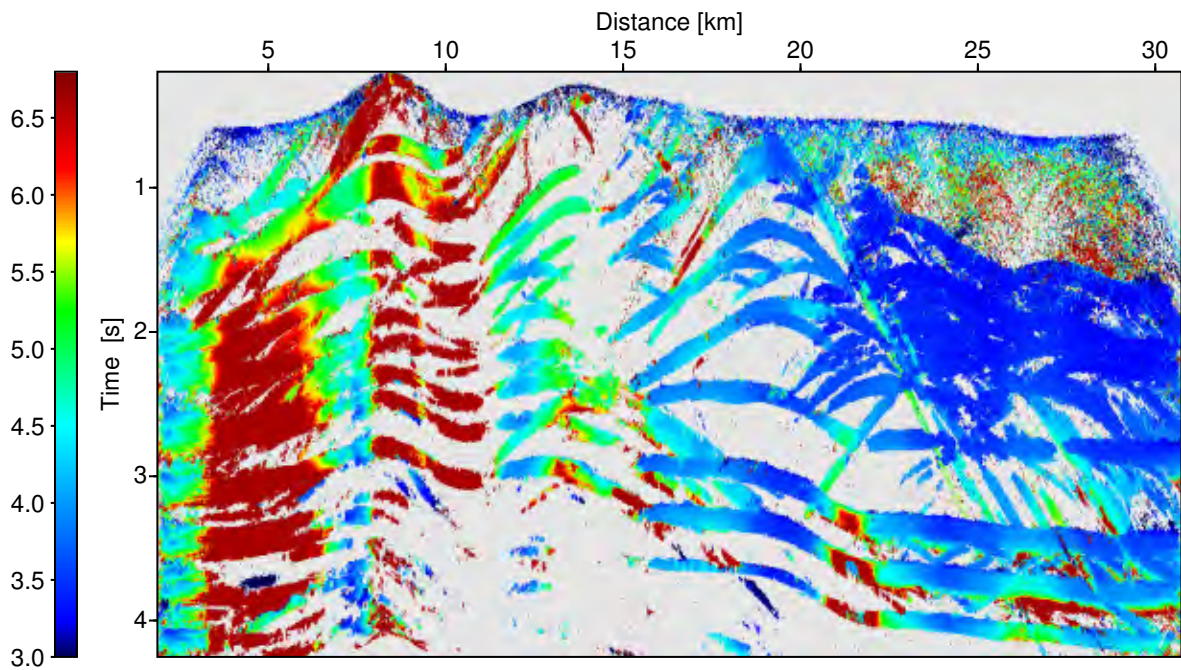
Figure 6.29: NMO velocity [km/s] after residual static correction calculated from optimized CRS attributes and related to a fictitious horizontal measurement surface at $z = 1459$ m. ZO samples with very low coherence value are masked out (gray), as they are not expected to be related to reliable attributes.

Chapter 7

Real data examples

In this chapter I will present two case studies based on real-data sets from North Brazil and the Arabian Peninsula. In both cases the complete CRS-stack-based imaging workflow was conducted including CRS stack for topography, residual static corrections, tomographic inversion and pre- and poststack depth migration.

The first data example was created in the framework of an ongoing research project conducted in collaboration with the Federal University of Pará (UFPA), Bélem, Brazil. The main issue of the presented work was to develop a new seismic reflection imaging workflow well suited for re-processing of existing seismic data with the aim to re-evaluate the exploration prospects. In this specific case, the seismic data was acquired under difficult conditions many years ago. Thus, the main problem encountered was the poor quality of the data, especially with respect to coverage and signal-to-noise-ratio. Due to the fact that the spatial CRS stacking operator fits the actual reflection events much better than conventional stacking operators and involves many neighboring CMP gathers into the stacking process, a strong improvement of the signal-to-noise ratio was expected. Furthermore, the large fold of the CRS operator provides a significantly increased statistical basis for residual static correction compared to conventional approaches, which also made this approach particularly suited for re-processing data such as the one at hand.

The second case study presented in this chapter is concerned with a challenging land data set from Saudi Arabia. This data set was selected and distributed to international research teams and contractors by the national Saudi Arabian oil-company, Saudi Aramco, with the purpose to test and further develop new methods to solve the specific problems of land data processing in the Middle East. These problems are mainly related to the near-surface geology of this region which often includes complexities as sand dunes, outcropping carbonates, caves, collapses, and a very deep water table. Below these structures, the rock strata becomes more uniform and regular. As a matter of fact, the presented data set suffers from rough top-surface topography, a strongly varying weathering layer, and a complex near-surface geology. Thus, it was important, besides the aforementioned benefits of CRS processing, that the topography could be directly considered for stack, residual static correction, and prestack depth migration.

7.1   Real data example A

The data used for this case study was acquired in the eighties of the last century by the national Brazilian oil-company, Petrobras, for petroleum exploration. The acquisition took place in the Brazilian part

of the Takutu basin: a Mesozoic intracontinental rift, oriented NE-SW, with approximately 300 km length and 40 km width, located at the border between Brazil and Guyana. Today, the data is used to re-evaluate the exploration prospects of this area. It is free for use on academic research and can be obtained from the ANP (Agência Nacional do Petróleo). Advanced data processing techniques are needed, since the near surface conditions and the complex geological structures that govern this region caused poor data quality and made conventional data processing very difficult to apply. The data set is provided in the form of non-processed field records, making a complete preprocessing workflow necessary.

7.1.1   Geology of the Takutu basin

Following the description of Eiras and Kinoshita (1990), the Takutu basin was developed in the central part of the Guyana shield. The rift is filled with sediments ranging from the Jurassic to the Quaternary. It is composed of two asymmetrical half-grabens: the SW part dips southeasterly and the NE part dips northwesterly. The structural scenario of the Takutu basin features horsts, grabens, anticlines, synclines, flower structures, and dip inversions (rollovers). Transcurrent faulting is considered to have reactivated local features that were developed in the rift stage (see Figure 7.1). The stratigraphic scenario of the Takutu basin is divided into four depositional sequences that reflect the geological evolution of the area. The first basal sequence is represented by the volcanic Apoteri formation and by the shaly Manari formation, both related to the pre-rift phase. The second sequence is represented by the evaporitic Pirara formation, and relates to the stage of maximum stretching in the rift phase. The third sequence is represented by the sands and conglomerates of the Takutu and Tucano formations, and is interpreted to correspond to the continuous decrease in stretching. The fourth sequence is represented by the lateritic and alluvium of the Boa Vista and North Savannas formations.

According to Eiras and Kinoshita (1990), the conclusions for the model of the Takutu basin were formally based on the interpretation of seismic data, seismic stratigraphy, surface geology, well data, geochronology, and geochemistry. Several structural styles were considered for the basin in focus and the most attractive were deltaic fan-shaped, compressional inversions, internal horst highs, and dip reversals. The conducted research project did not intent to trace new evidences for the structural scenario for the Takutu basin; this may follow with the course of the studies with more systematically processed data completing at least a full block of seismic lines for a proper geological interpretation.

7.1.2   Data acquisition and preprocessing

Among the processed lines, the selected line for this case study was the one numbered 204-239. It has the following survey information (see also Table 7.1.2): date of acquisition 1986; direction NW-SE; length 31.5 km; 631 shot points; 4 ms time sampling interval; 50 m spacing of shot points and stations; explosive charges of 0.9 kg at 2 m depth distributed as L-3x2/25 m. The acquisition geometry changed along the line, but in most parts split-spread acquisition was performed. There were shots missing and many traces had to be canceled out due to malfunctioning receivers. The resulting CMP fold is depicted in Figure 7.2. Unfortunately, the data quality from CMP no. 800 on (distance 20 km to 31.5 km) is very poor so that hardly any continuous reflection event could be imaged during first tests. Consequently, the target area for this case study was limited to the range between 0-20 km.

The preprocessing was performed with the SU package[1]. It involved four main tasks:

---

[1]developed by the Colorado School of Mines (see, e. g., Cohen and Stockwell, 2000)
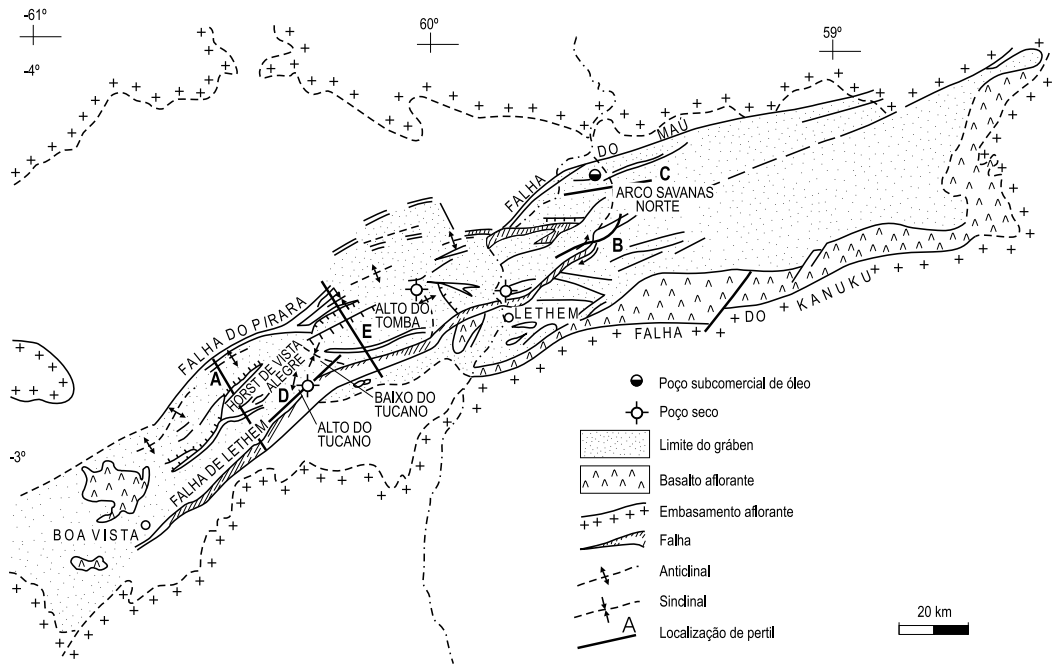
Figure 7.1: Structural map of the Takutu graben redrawn from Eiras and Kinoshita (1990) showing the direction of some seismic lines (A, D, E). The graben is about 300 km long and about 40 km wide, its direction is NE-SW.

	Number of shots	631
Shot and	Shot interval	50 m
receiver	Maximum number of receivers	96
geometry	Receiver interval	50 m
	Number of traces	54 128
Midpoint and	Number of CMP bins	1241
offset	Maximum CMP fold	62
geometry	Full offset range	-3850...2450 m
	Recording time	4 s
Recording	Sampling interval	4 ms
parameters	Dominant frequency	25 Hz
	Maximum frequency	50 Hz

Table 7.1: Information on the prestack data, obtained from the trace-headers.
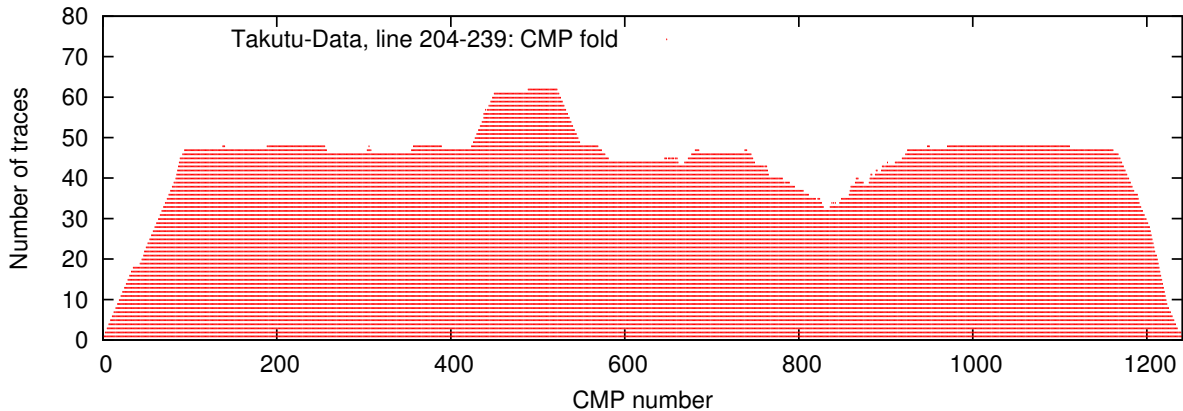
Figure 7.2: Number of traces contained in CMP gathers.

- *Geometry setting*: based on the original field records, the geometry information was assigned to the traces. The data set, as it was provided from the ANP, already contained field static corrections, relating the data to a planar reference level. Since the applied static correction times were not available, this correction could not be undone. However, even if it would have been possible to undo this correction it would probably not have made sense, because, even though, the topography itself can be handled by the CRS stack approach, the influence of a strongly variable near-surface geology cannot be removed by residual static corrections, only.
To restore the original source and receiver elevations inverse elevation statics (see Section 3.1) were applied. A constant replacement velocity of 2250 m/s was chosen, which should be close to the average near-surface velocity. For the dataset at hand the topography is only a minor problem. Nevertheless, restoring the original geometry helped to minimize the systematic error connected to the field static correction and, thus, to preserve the physical meaning of the attributes extracted by the CRS stack and later employed by the tomographic inversion.

- *Muting of bad traces*: after a first visual inspection of the data, several completely corrupted shot and receiver gathers were canceled out. Afterward, as a result of a closer analysis of the remaining shot gathers, many individual traces were zeroed out because of their high noise level caused by malfunctioning receivers and other unfavorable external influences.

- *f and f-k filtering*[2]: several band-pass filters with polygonal form were tested before a filter with corners 8-10-35-45 Hz was chosen. Subsequently, a f-k filter was used to attenuate surface waves (ground roll) and critically refracted waves.

- *Trace balancing and removal of spherical divergence*: trace balancing mainly by using automatic gain control (AGC) with a window size of 0.5 s was applied to correct for amplitude variations along the line caused, e. g., by the varying near-surface conditions.

No deconvolution was carried out on this data. Even though, a lot of time and effort was spent for the preprocessing a detailed discussing will here be omitted since the individual steps applied were rather basic and are well described in many text-books such as Yilmaz (2001) or Forel et al. (2005).

---

[2]Frequency-wavenumber filtering, also known as *dip filtering* since unwanted wave-types can often be discriminated by their dip in the f-k spectrum.
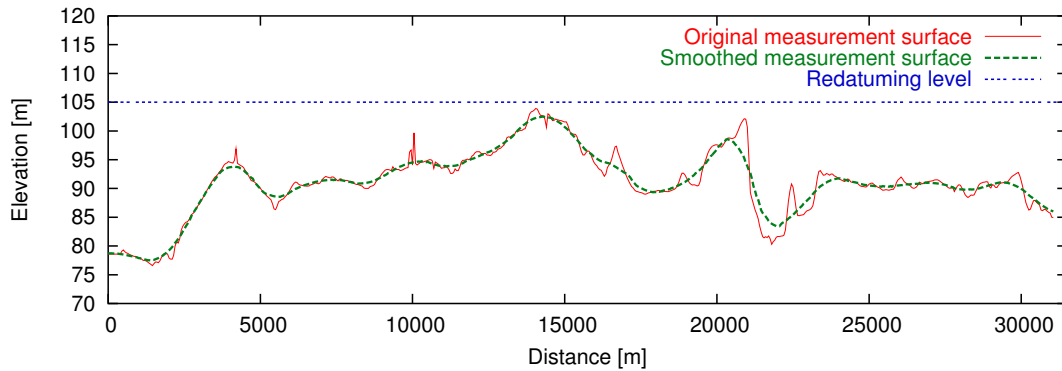
Figure 7.3: Comparison between original and smoothed measurement surface. The horizontal surface at $z = 105$ m was used as reference level for the redatuming.

7.1.3 CRS stack for topography

The first step of the conducted workflow was the application of the CRS stack for topography using a constant near-surface velocity of 2250 m/s equal to the replacement velocity used to restore the original topography. In detail, the following processing sequence was carried through:

- *Topography analysis.* The actual measurement surface was smoothed using a smoothing aperture of 2450 m equal to the size of the maximum offset aperture later considered by the CRS stack. This ensures that each point at the smoothed reference level can be well approximated by a parabola with its apex at the center of the respective stacking aperture (see Section 4.4.3). A comparison between the smoothed and the actual measurement surface is depicted in Figure 7.3. As can be seen, the differences in elevation between the actual measurement surface and its smoothed counterpart are very small.

- *Small scale static corrections.* For this data set the roughness of the topography does not pose a real problem. Only very little time shifts, ranging from -2 ms to 4 ms, had to be applied to the individual traces in order to relate the data to the smooth reference level. A constant replacement velocity of 2250 m/s was used to calculate the corrections.

- *Initial CRS stack.* A time dependent offset aperture was employed linearly increasing from 300 m at 0.3 s to 2450 m at 1.5 s. The maximum offset aperture contained in the data, i. e. -3850 m, is only reached at the last third of the line which lies outside the chosen target zone. Emergence angle values within the range of $\pm 80°$ were considered during the search. The NMO velocity was sought for within the range of 1500 to 7000 m/s. The midpoint aperture increased from 200 m at minimum traveltime to 800 m at maximum traveltime. For the plane-wave search only 30% of this aperture were used. For the sake of brevity initial CRS stack results are not displayed.

- *Event consistent smoothing.* For the parallelogram shaped smoothing window a spatial half-width of 75 m and a temporal half-width of 8 ms was chosen. The maximum angle deviation for samples to be accepted was two degree and a time-dependent coherence threshold linearly decreasing from 0.03 for minimum traveltime to 0.01 for maximum traveltime had to be ex-

119

ceeded. For each ZO sample smoothing was only applied if 80% of the samples within the surrounding window fulfilled these criteria.

- *Optimization.* Optimization was carried through for every sample of the ZO section. The resulting stack section is depicted in Figure 7.5. The size of the projected Fresnel zone calculated from the initial attributes was used to limit the search aperture. The final stacking aperture was limited by the projected Fresnel zone calculated from the optimized attributes.

- *Residual static correction.* Three iterations of residual static corrections were conducted. After each iteration the complete CRS stack process including automatic CMP stack and initial stack was applied to the updated, i. e. corrected, data set. The traveltime window used for the cross-correlations spread from 0.5 to 2 s. The maximum shift for an individual source or receiver location was limited to 60 ms per iteration. Source or receiver time shifts determined from cross correlation stacks with less than 500 contributing traces were not considered. The total residual static time shifts for the source and for the receiver locations are depicted in Figure 7.4. The stack section resulting from the final iteration of the CRS stack applied to the corrected prestack data is depicted in Figure 7.6.

- *Redatuming.* The horizontal redatuming level was chosen ten meters above the highest peak of the smoothed reference surface, i. e. at an elevation of 105 m. A redatuming velocity of 2250 m/s was used. The optimized stack section after redatuming is depicted in Figure 7.7. The coherence section after redatuming and the percentage increase of coherence before and after residual static correction are depicted in Figures 7.8 and 7.9. The attribute sections after redatuming and the associated NMO velocity section are depicted in Figures 7.10 to 7.13.

Discussion of the results. Unfortunately, it was not possible to obtain the original stack results for a comparison. Considering the low quality of the underlying prestack data, many reflections could be resolved by the presented approach. Particularly for traveltimes between 0.75 and 2 s the stack section shows a high resolution and signal-to-noise ratio so that some reflections can be traced along a distance of 10 km and more. Beyond 2 s only a few reflection events are visible. This might have two reasons: (a) the largest part of the seismic energy was already reflected by the reflectors above and (b) the wave impedance contrasts in the region below 2 s are too small to reflect enough of the remaining energy back to the subsurface. Comparing the stack result before and after the residual static correction, a significantly improved continuity of the reflections can be observed, e. g. at km 14 or in the difficult area between km 2 and km 6. The percentage increase of coherence depicted in Figure 7.9 further emphasizes this observation. Due to the fact that the difference in elevation between the planar redatuming level and the smoothly curved reference level is relatively small for this data set, the effect of the redatuming is hardly visible. Nevertheless, it provides a standardized input for the tomographic inversion which does not support input sections related to a floating datum. The NMO velocity section (see Figure 7.13) was calculated from the optimized values of β_0 and R_{NIP} after redatuming according to equation (C.3). In this case, the NMO-velocity differs from the actual stacking velocity used for the initial stack but corresponds to a horizontal measurement surface at $z = 105$ m (see Appendix C).

7.1.4 CRS-stack-based tomographic inversion

The second step of the conducted imaging workflow was to determine a smooth macrovelocity model via CRS-stack-based tomographic inversion. In detail, the following steps were involved:
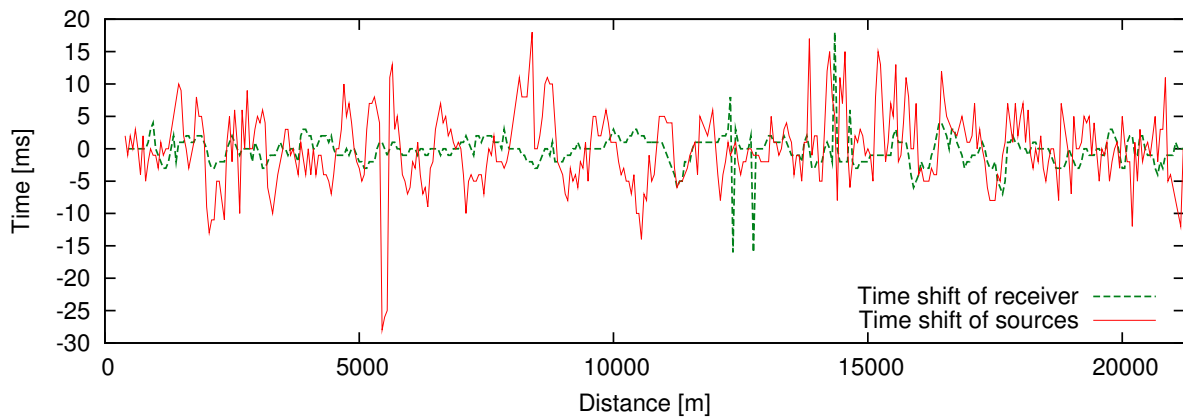
Figure 7.4: Accumulated static time shifts for the individual source and receiver locations after three iterations of residual static corrections.

- *Automatic picking within the redatumed stack results.* Input for the tomographic inversion process were 1538 samples of the redatumed stack section together with the associated values of emergence angle β_0 and NIP-wave radius R_{NIP}. The latter were picked using an automatic picking program which evaluates for every sample of the ZO section several criteria in order to define a valid pick location. For the presented data example the following criteria were used:

  - the coherence associated with the analyzed sample had to exceed a coherence threshold of 0.024.
  - the coherence of the nearest neighboring samples had to exceed 95% of this coherence threshold.
  - all samples within a user defined window centered around the analyzed pick location with a spatial half-width of 50 m and a temporal half-width of 25 ms had to exceed 90% of this coherence threshold.
  - the maximum emergence angle deviation between the sample in the center and the samples within the surrounding window must not exceed an angle threshold of 1.5°.
  - the amplitude of the stack envelope at the central sample had to be at least 25% higher than the mean amplitude inside a surrounding time window of 0.3 s length.

  Of course, this automatic picking process cannot be expected to work perfectly. For instance, multiple reflections or coherent noise cannot be distinguished from the searched-for reflection events. Thus, the resulting picks had to be checked and further edited before they were used for the tomographic inversion. The resulting pick locations are displayed in Figure 7.14.

- *Tomographic inversion.* Starting from a gradient model, the tomographic inversion ended after 18 iterations when no further model improvement could be achieved. The final macrovelocity model, depicted in Figure 7.15, consists of 221 B-spline nodes. In horizontal direction 21 node points with 1000 m spacing and in vertical direction 11 node points with 500 m spacing were used. A smaller grid was tested by did not lead to better results. The redatuming level at a depth of 105 m constitutes the upper border of the model.

Discussion of the results. Basically, the obtained macrovelocity model, depicted in Figure 7.15, represents a laterally variable gradient model. On the left hand side the velocities from 2 km depth

121

on increase slower than on the right hand side of the model, where interval velocities of 8.5 km/s are reached at the bottom. However, it has to be considered that, in general, the reliability of the inverted velocities decreases with depth and that in this particular case, the model is only linearly extrapolated from a depth of 4 km on where the deepest picks are located.

7.1.5   Kirchhoff pre- and poststack depth migration

As a final step of the conducted imaging workflow, a depth domain image of the subsurface structure was obtained by both, Kirchhoff pre- and poststack depth migration, using the program Uni3D, developed at Karlsruhe University.

- *Calculation of diffraction traveltime tables.* The necessary Green's function tables (GFTs) were calculated in the smooth macrovelocity model, depicted in Figure 7.15, by means of a program, developed at Karlsruhe, University that employs the so-called *fast marching eikonal solver* contained in the SEPlib package, provided by the Stanford Exploration Project. The GFT for the poststack depth migration was related to the planar reference level since the redatumed stack section was to be migrated. Contrary to this, the actual measurement surface had to be considered for the GFT used by the prestack depth migration.

- *Pre- and poststack depth migration.* The prestack migration was performed directly from topography using the residual-static-corrected prestack data, whereas the poststack depth migration was applied to the redatumed CRS stack section depicted in Figure 7.7. In both cases, a depth dependent operator aperture was used with a minimum value of 1000 m at the top of the migration target zone and a maximum value of 2000 m at the bottom. Linear interpolation of the operator aperture was applied in between[3]. For the output, a horizontal grid-size of 25 m and a vertical grid-size of 10 m was chosen in order to avoid image aliasing and steps in the image of the dipping reflectors, particularly at the left hand side of the target zone. The poststack depth migration result is depicted in Figure 7.18.
  In order to obtain the prestack depth migrated image shown in Figure 7.17, the prestack data was sorted in common offset sections which were then migrated separately. Afterwards, they were merged again to a migrated prestack data set, which was then resorted to so-called common image gathers (CIGs). Before these CIGs were finally stacked in offset direction, an offset- and depth-dependent mute was applied to avoid the stacking of stretched wavelets and, hence, a blurred (or completely destroyed) image. Some of these CIGs are depicted in Figure 7.16 together with the stacked prestack depth migration result, where the locations of the CIGs are each identified by vertical lines. The mute function, which starts at 250 m offset at the top of the model and linearly increases the offset range up to 2450 m at 2 km depth can easily be observed.

Discussion of the results. Based on the prestack depth migration results the quality of the macrovelocity model was evaluated. It can be observed that, even though no velocity update was performed, most of the events in the CIGs are flat. Some of the strongly curved events might correspond to multiple reflections. From the fact that most of the reflection events have virtually no moveout for increasing offset, a good consistency of the macrovelocity model and the underlying prestack data

---

[3]Choosing a time dependent operator aperture both minimizes the computation time and reduces the aliasing without loosing information or applying rigorous anti-aliasing filters that decrease the frequency content of the data and, thus, the possible resolution in the output domain.

can be concluded. The prestack depth migration result as well as the poststack depth migration result show many structural details; in particular, faults, vertical offsets of reflectors, deflection of reflectors, and fracturing are directly observable in the sections. Comparing both sections leads to the following observations: on the one hand, the prestack depth migration seems to provide a higher lateral resolution, even though a part of this impression might be caused by the lower signal-to-noise ratio. Furthermore, the prestack depth migration resolves some structures for which the CRS stack and as a consequence also the poststack depth migration failed (see, e. g., shallow reflectors at km 14). The latter is quite unusual but sometimes caused by the deficiencies of the initial search which does not employ the full potential of the spatial stacking operator by using one-parameter searches, only. On the other hand, the poststack depth migration results exhibits a generally higher signal-to-noise ratio and there are regions, especially in the deeper part of the target area, where some structures could be better resolved. The latter is typical for difficult areas in which the signal-to-noise ratio is quite low and the obtained macrovelocity model is not fully consistent to the data, so that the prestack migration operator fails in summing up enough coherent energy. Consequently, the poststack depth migration result provides valuable complementary information and both migrated sections should finally be used for the structural interpretation.
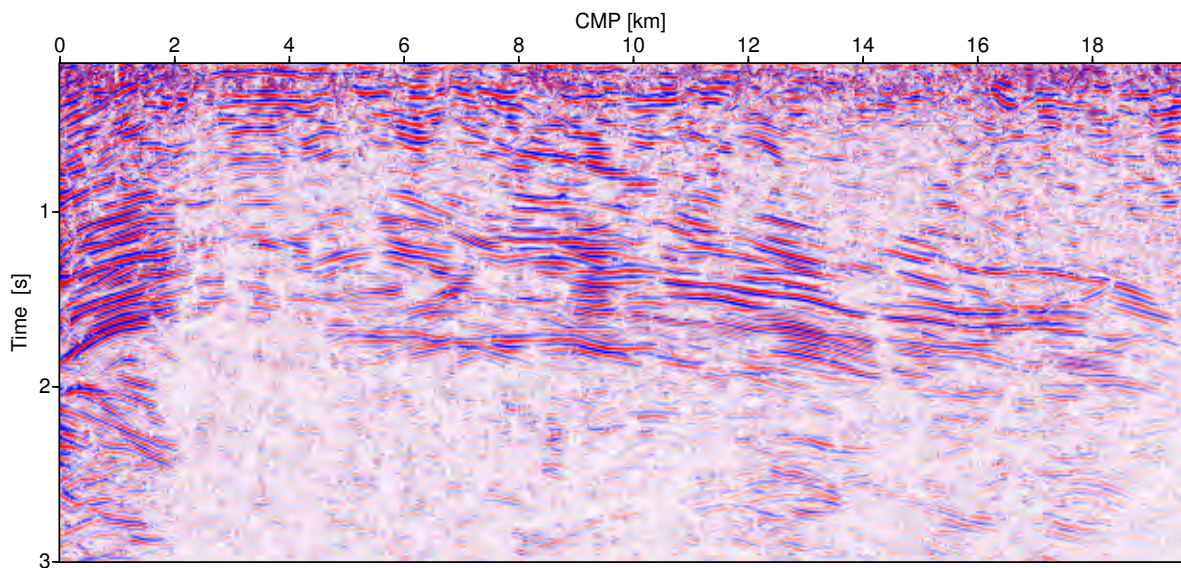
Figure 7.5: Result of the optimized CRS stack restricted to the projected first Fresnel zone. The simulated ZO traveltimes are related to the smoothed reference level.
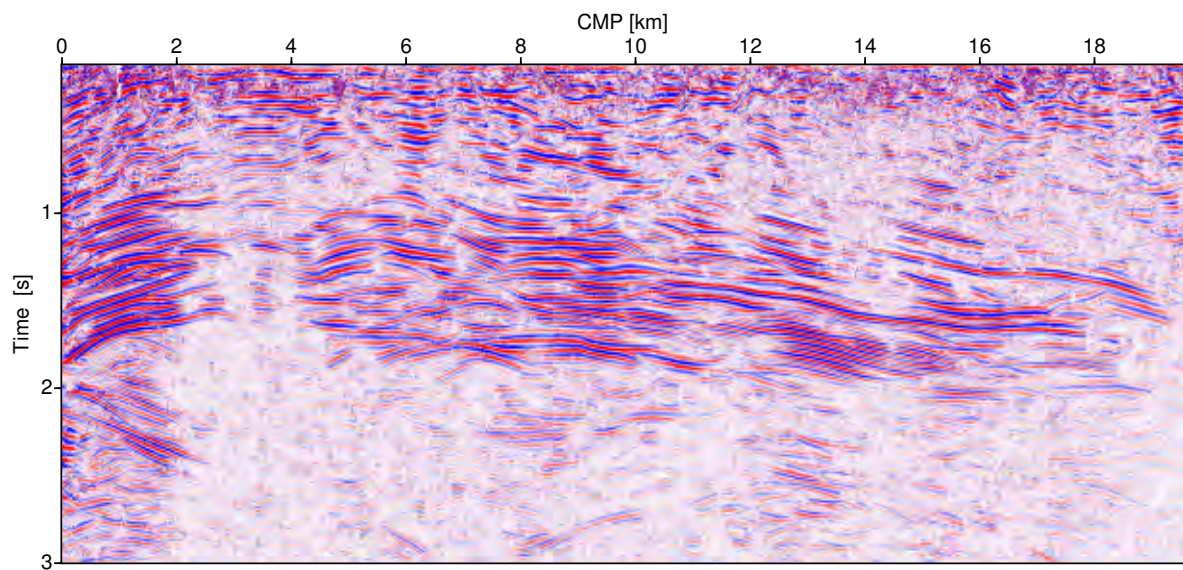
Figure 7.6: Result of the optimized CRS stack restricted to the projected first Fresnel zone after five iterations of residual static correction.
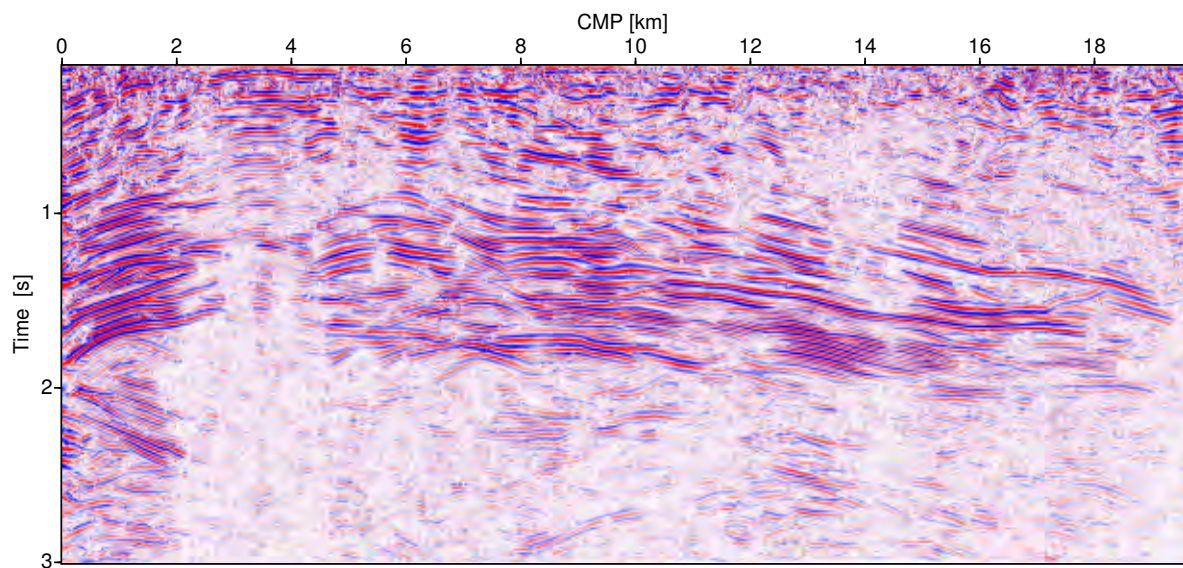
Figure 7.7: Result of the optimized CRS stack restricted to the projected first Fresnel zone after residual static correction and redatuming. The redatuming procedure relates the achieved results to a fictitious horizontal measurement surface at $z = 105$ m.
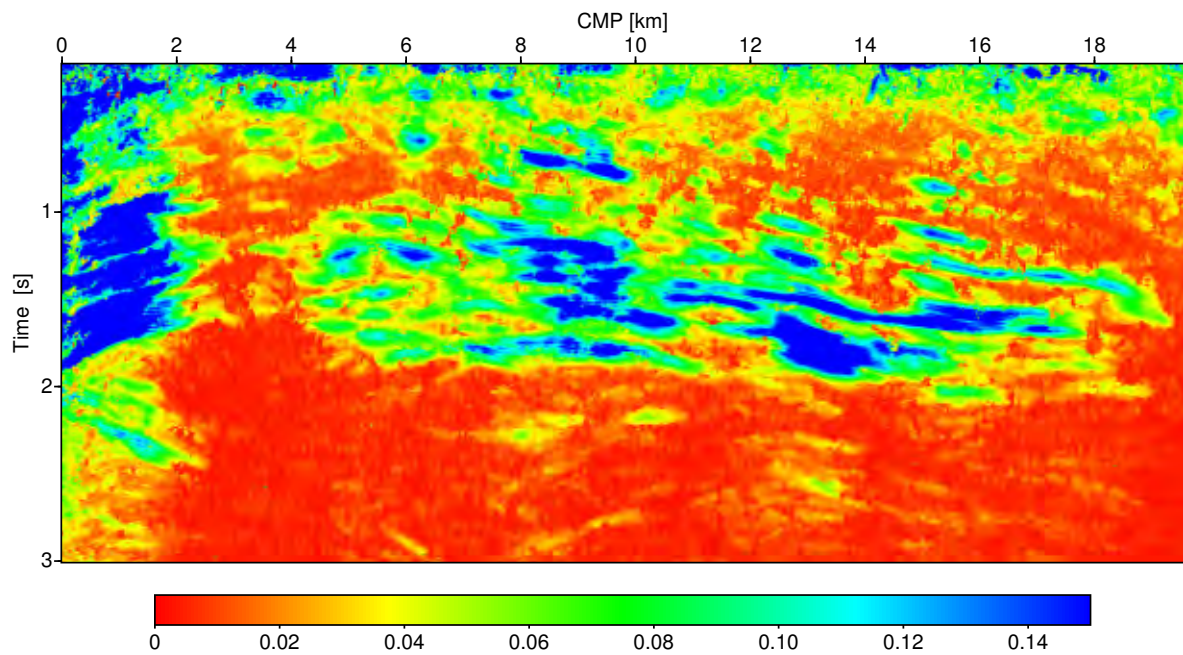
Figure 7.8: Coherence, associated with the optimized CRS stack after residual static correction, related to a fictitious horizontal measurement surface at $z = 105$ m.
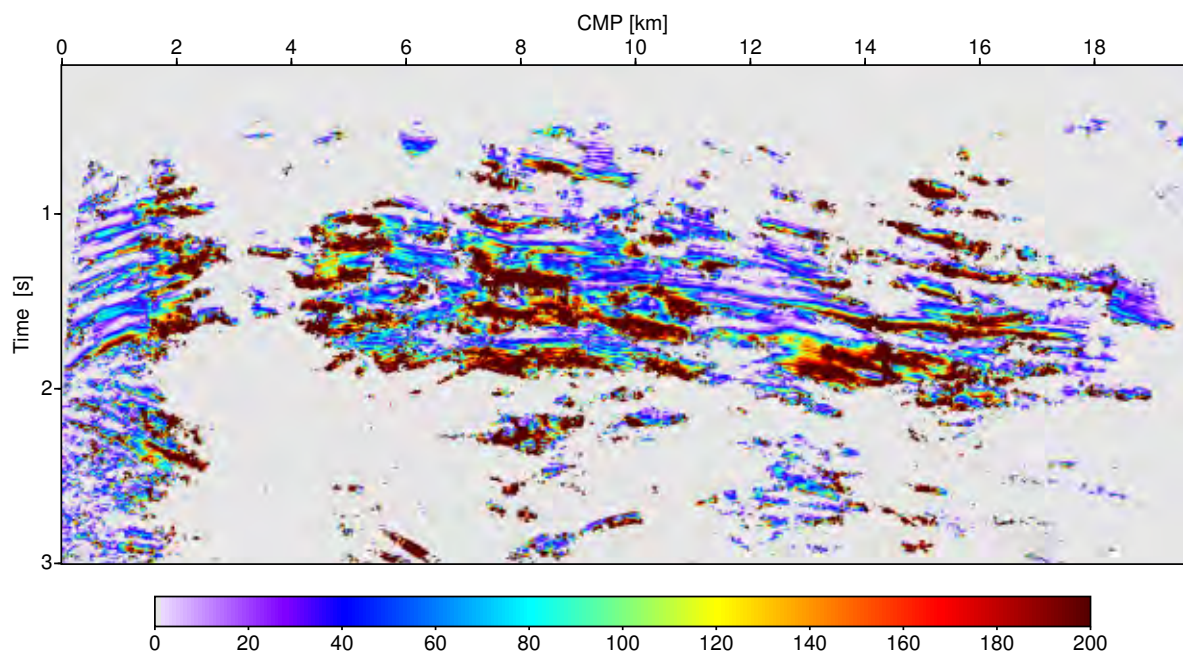
Figure 7.9: Percentage increase of coherence between optimized CRS stack before and after residual static correction, related to a fictitious horizontal measurement surface at $z = 105$ m. Samples with very low coherence value are masked out (gray), as they are not expected to be related to real reflection events.
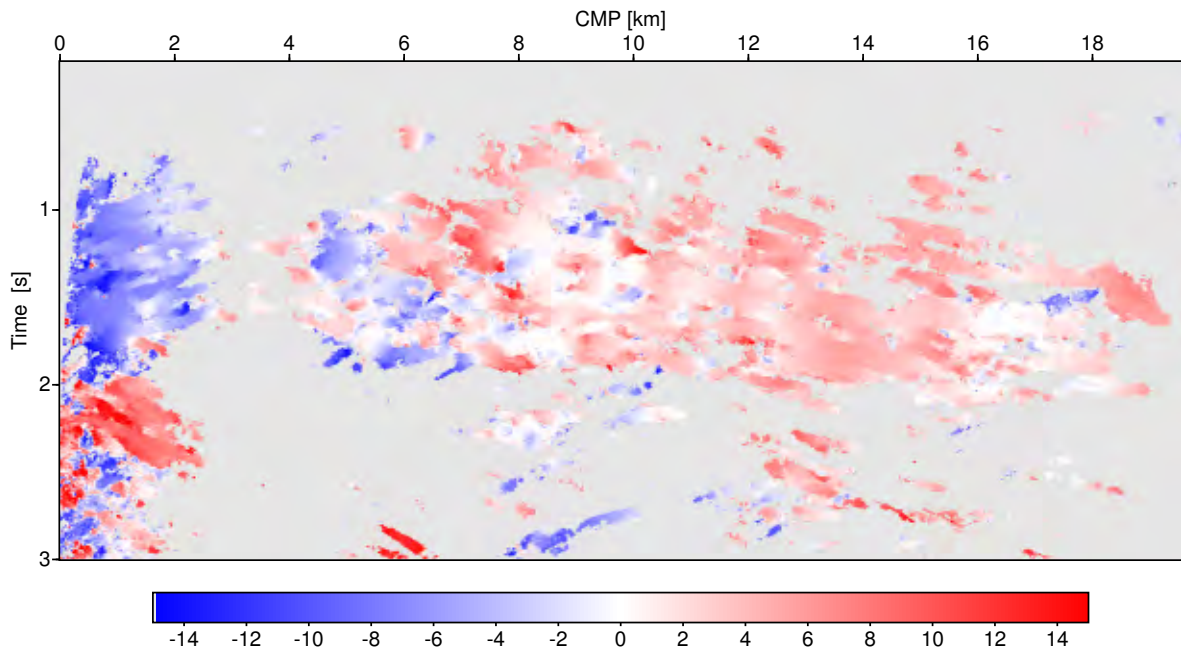
Figure 7.10: Emergence angle of the simulated ZO rays [deg] after residual static correction, related to a fictitious horizontal measurement surface at $z = 105$ m. ZO samples with very low coherence value are masked out (gray), as they are not expected to be related to reliable attributes.
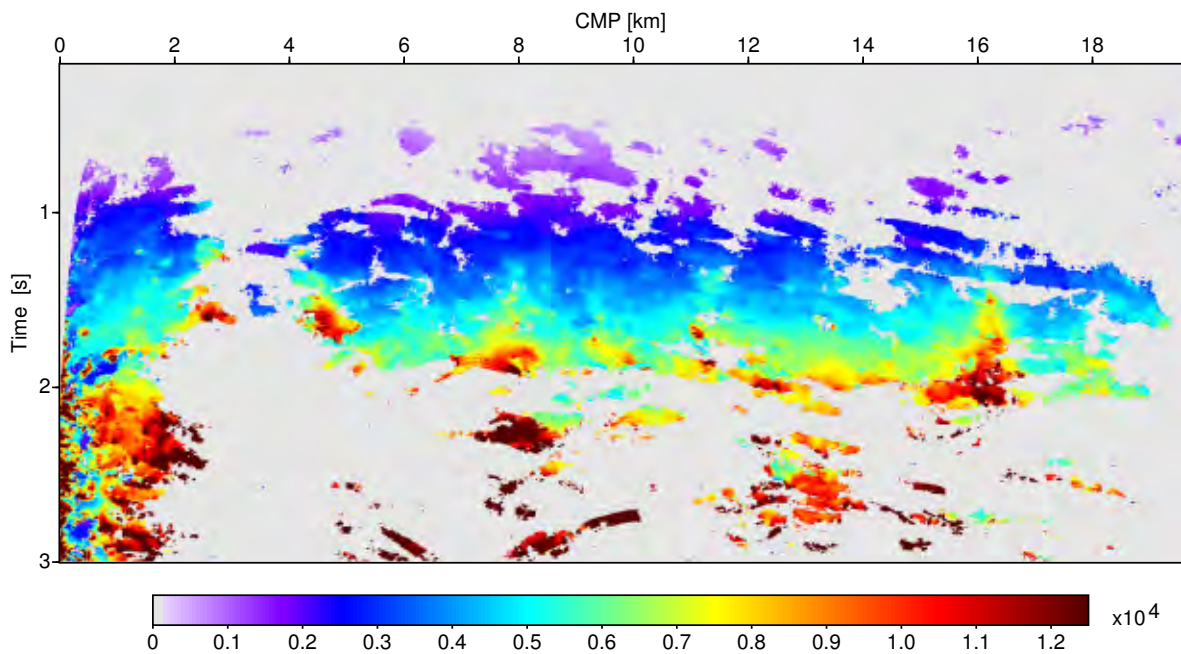
Figure 7.11: Radius of the Normal-Incidence-Point (NIP) wavefront [m] after residual static correction, related to a fictitious horizontal measurement surface at $z = 105$ m. ZO samples with very low coherence value are masked out (gray), as they are not expected to be related to reliable attributes.
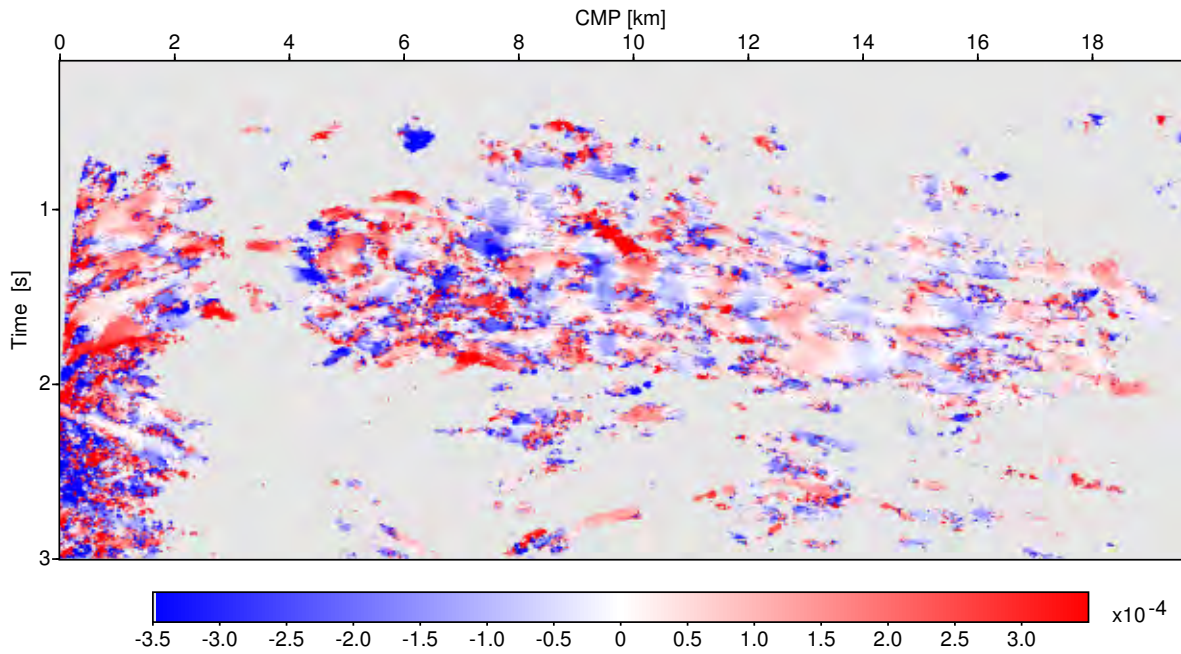
Figure 7.12: Curvature of the normal wave [1/m] after residual static correction, related to a fictitious horizontal measurement surface at $z = 105$ m. ZO samples with very low coherence value are masked out (gray), as they are not expected to be related to reliable attributes.
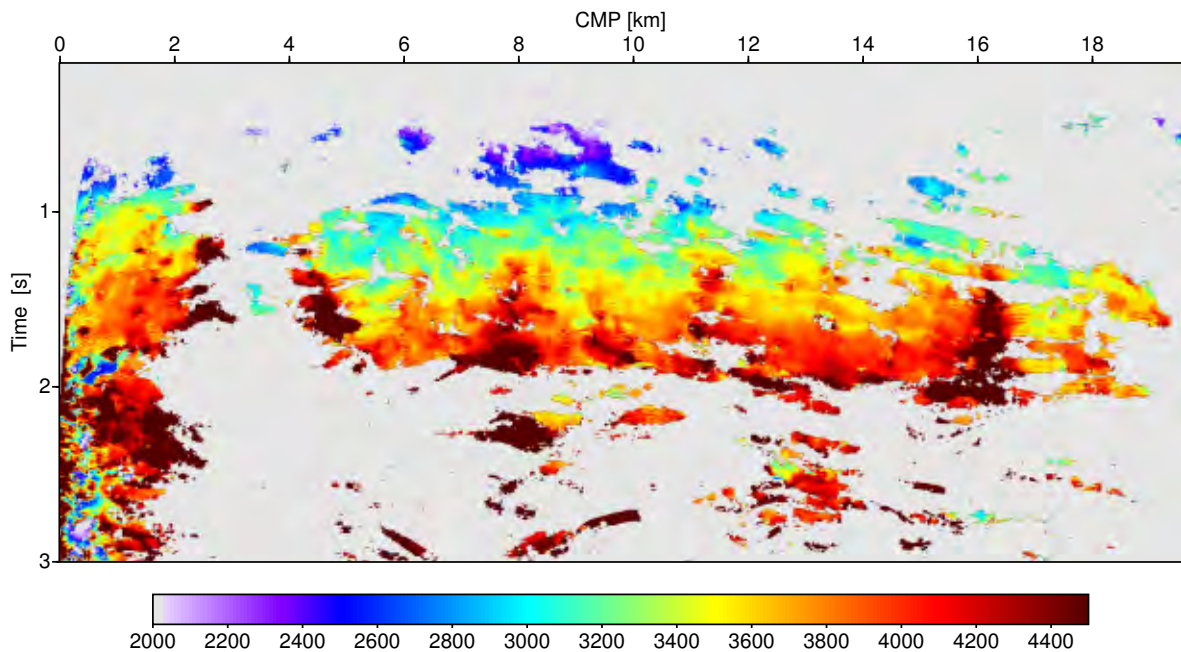
Figure 7.13: NMO velocity [m/s] calculated from optimized CRS attributes after residual static correction, related to a fictitious horizontal measurement surface at $z = 105$ m. ZO samples with very low coherence value are masked out (gray), as they are not expected to be related to reliable attributes.
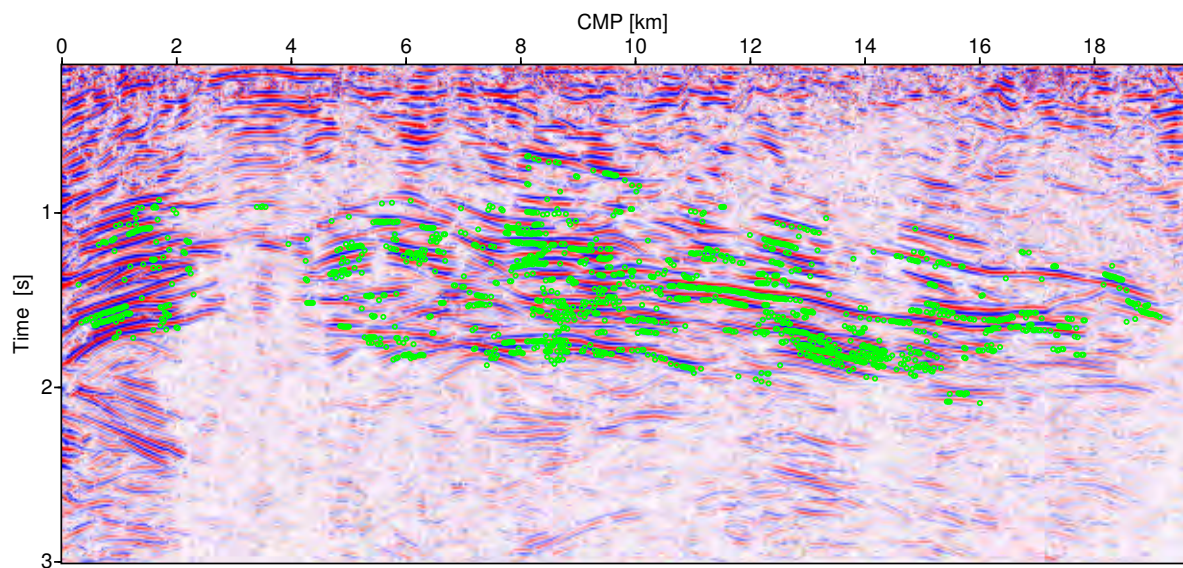
Figure 7.14: Green circles indicate the position of the redatumed ZO samples from which traveltime, midpoint position, emergence angle, and NIP-wave radius were extracted to serve as input for the tomographic inversion.
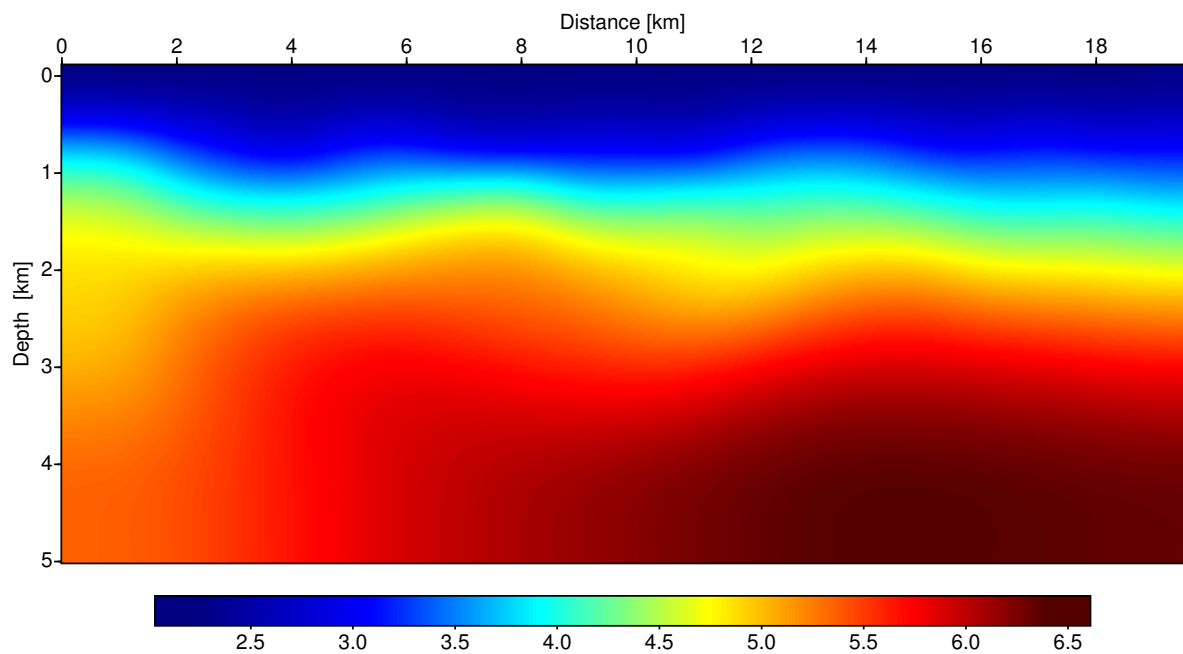
Figure 7.15: Smooth macrovelocity model [km/s] obtained by tomographic inversion.
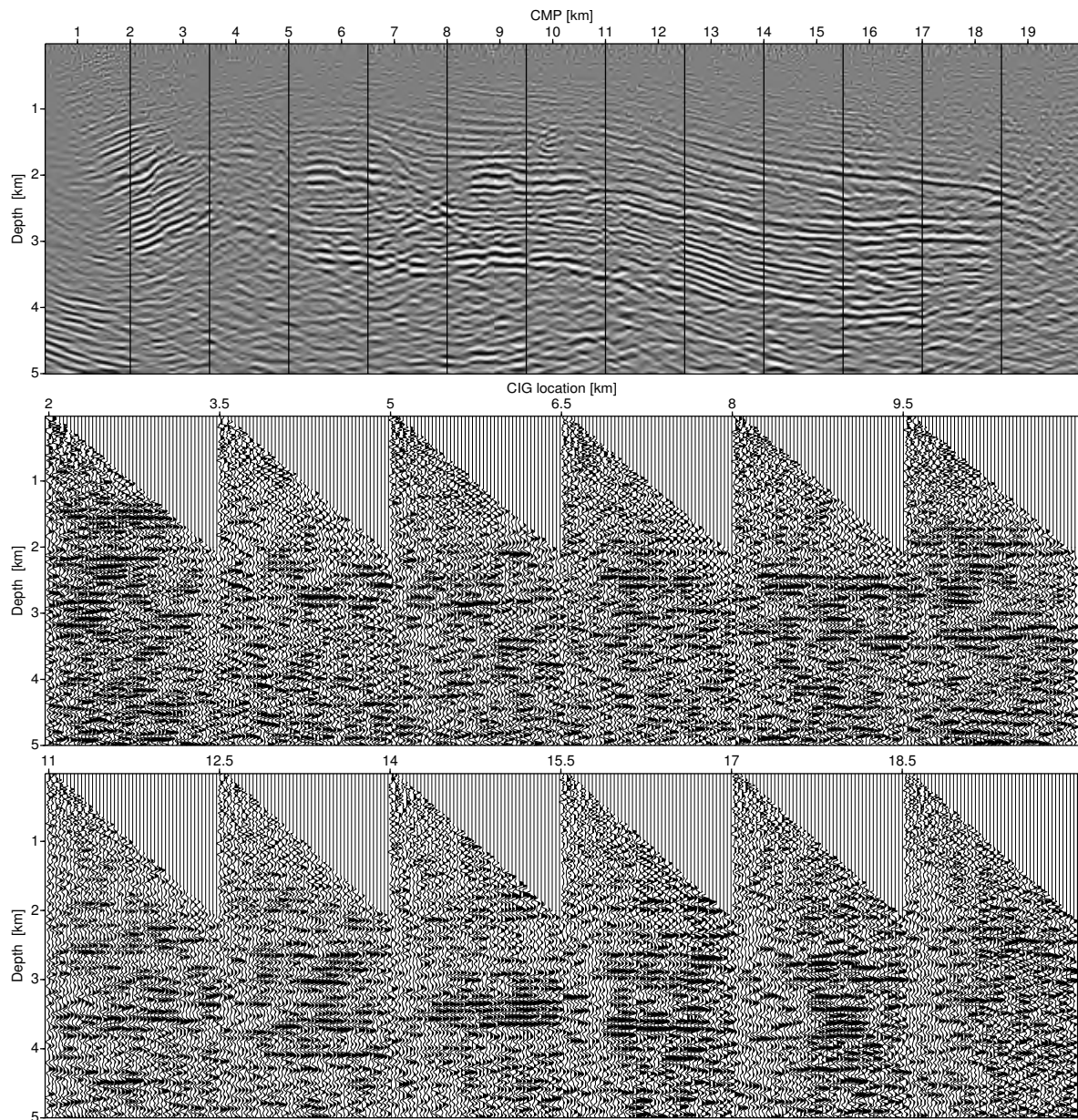
Figure 7.16: Some common-image gathers extracted from the prestack depth migration result before stacking over all offsets. For convenience, the result after stacking in offset direction is also displayed, where the locations of the CIGs are each identified by vertical lines. The mute function starts at 250 m offset at the top of the model and linearly increases up to 2500 m at 2 km depth.
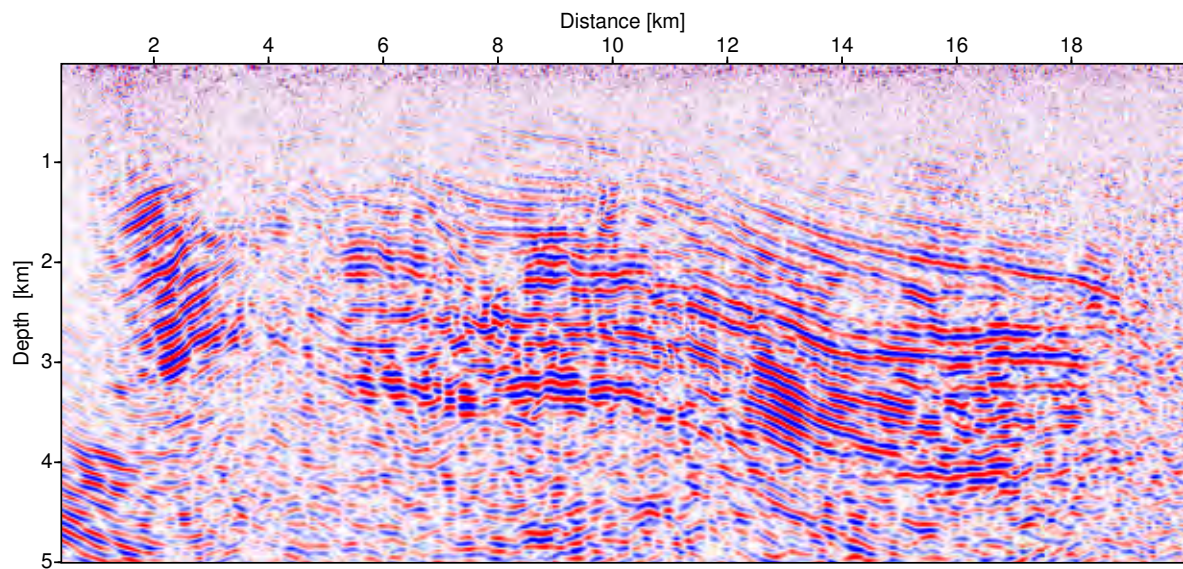
Figure 7.17: Result of the prestack depth migration applied to the prestack data after residual static correction. The smooth macrovelocity model, depicted in Figure 7.15, was used to generate the necessary diffraction traveltime tables.
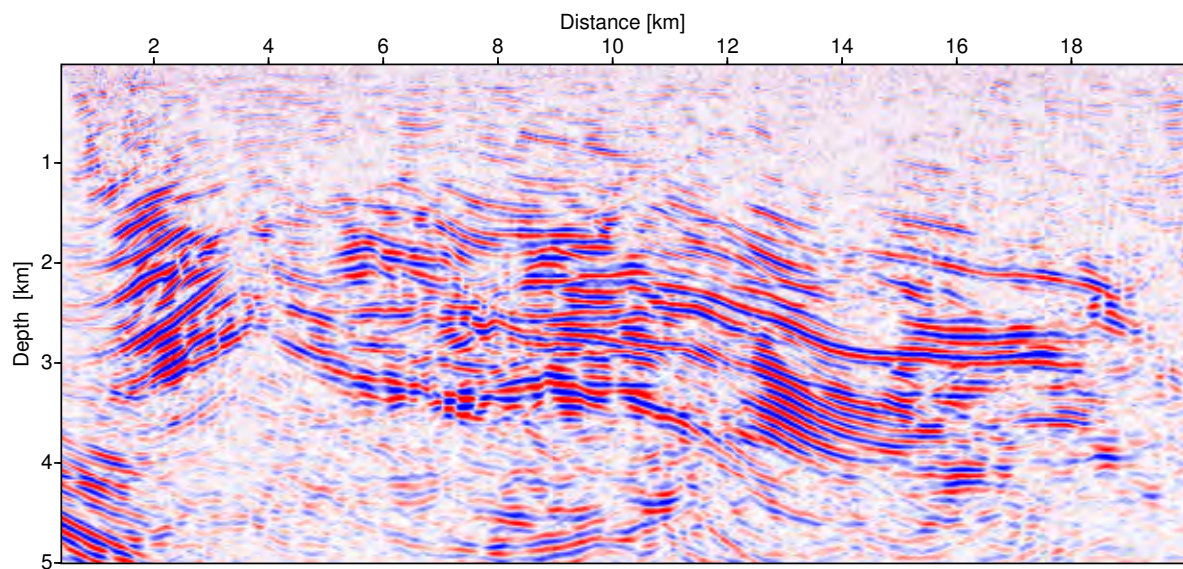
Figure 7.18: Result of the poststack depth migration applied to the optimized CRS stack section after residual static correction and redatuming, depicted in Figure 7.7. The smooth macrovelocity model, depicted in Figure 7.15, was used to generate the necessary diffraction traveltime tables.

7.2 Real data example B
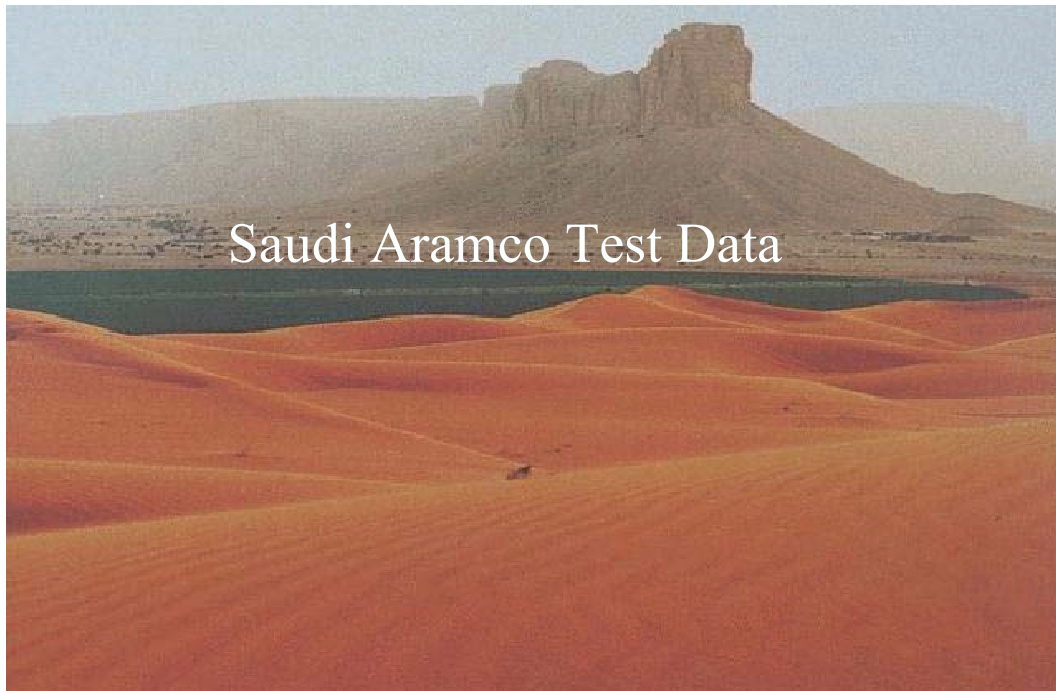
In the deserts of the Middle East, where most of the worlds oil and gas reserves are located, the measurement surface and the first few hundred meters below are often very complex and pose severe problems to seismic data processing. This final case study will be concerned with these near-surface problems considering the seismic processing of a challenging land data set from the Arabian Peninsula. The data was selected by the national Saudi Arabian oil company Saudi Aramco and distributed to a number of international research teams as a result of a workshop held in Manama, Bahrain, in 2004. On this workshop, scientists from oil companies, contractors, and academia agreed on the scarce general awareness about near-surface challenges to seismic imaging and decided to release a test data set, featuring typical near-surface problems. This data set served as a catalyst and benchmark for new technologies, similar as the Marmousi and the EAGE-SEG Salt Models had favored the progress of prestack depth migration. One year later, the EAGE research committee organized a workshop, held on the 67th annual EAGE Conference in Madrid, 2005, on which first results were presented, including preliminary versions of those results discussed in this section (see Koglin et al., 2005; Heilmann et al., 2005). In November 2006, a special issue of Geophysical Prospecting was published containing a collection of the work done so far, where also two papers presenting results discussed in the following can be found (Koglin et al., 2006; Heilmann et al., 2006).

7.2.1 Data acquisition and preprocessing

The seismic test line considered here is about 42 km long with a symmetrical split-spread geometry. Both, shot and receiver intervals are 30 m. The source-to-receiver offsets range from 15 m to 3600 m. According to the description of Bridle et al. (2006), "four vibrators were used to record four sweeps stacked vertically, with a listening time of 12 s. The recording instrument was a DFS-7 system, with

	Number of shots	1279
Shot and receiver geometry	Shot interval	30 m
	Maximum number of receivers	240
	Receiver interval	30 m
	Number of traces	306960
Midpoint and offset geometry	Number of CMP bins	2840
	Maximum CMP fold	120
	Full offset range	-3602...3607 m
Recording parameters	Recording time	2 s
	Sampling interval	4 ms
	Dominant frequency	30 Hz
	Maximum frequency	65 Hz

Table 7.2: Information on the prestack data, obtained from the trace-headers.

240 traces recorded per shot at a 4 ms sample rate and a 90 Hz high-cut antialias filter. The sweep and recording length are 120 ms and 5120 ms, respectively. The source pattern is a 4 x 6 parallelogram array: the offset of the pattern center is 15 m in the in-line direction and 56 m in the cross-line direction. The receiver array is composed of 52 receivers, in a rectangular pattern with dimensions 44 x 27.5 m. The maximum intrapattern relief is 3 m. The selected area has some widely varying near-surface challenges for seismic processing. The topography ranges from Quaternary gravel plains to hard carbonate outcrops of the Yamama and Sulaiy formations. In the central part of the line, some very thick Quaternary loose sand occurs, with gravel at the foot of an 80 m high cliff, made up of hard and fast carbonate of the Yamama formation. Additionally, other fast carbonates of the Sulaiy formation are characterized by karsting that is filled in with Quaternary sands. There are eight upholes varying in depth from 100 to 200 m, four of which are located along the line. The seismic velocity changes along the section indicate that the subsurface is far from uniform". Main parts of survey information taken from the header of the prestack data after preprocessing are compiled in Table 7.2.1.

The data is affected by complex near-surface geology and rugged topography (see Figure 7.19). Even though the latter can be directly addressed by the CRS stack process, the complex near-surface geology caused by sand dunes, carbonate outcrops, wadis and sabkahs (low-lying saline flats) made static correction absolutely necessary. This was shown by first tests using the raw prestack data as it was provided by Saudi Aramco. Later on, I fortunately obtained preprocessed data from our sponsor TEEC[4], where the influence of the complex near-surface geology, particularly of the strongly varying weathering layer, had been removed in a great measure by means of refraction statics, relating the data to a horizontal reference level at $z = 500$ m. All in all, the preprocessing performed involved following tasks:

- *Preprocessing by TEEC*: the initial signal processing, performed by TEEC, included: (a) Radon removal of steep dipping noise, (b) compensation for spherical divergence using automatic gain control with a gate size of 500 ms, (c) single-trace spike deconvolution with an operator length

---

[4]Trappe Erdöl Erdgas Consultant, Isernhagen, Germany.
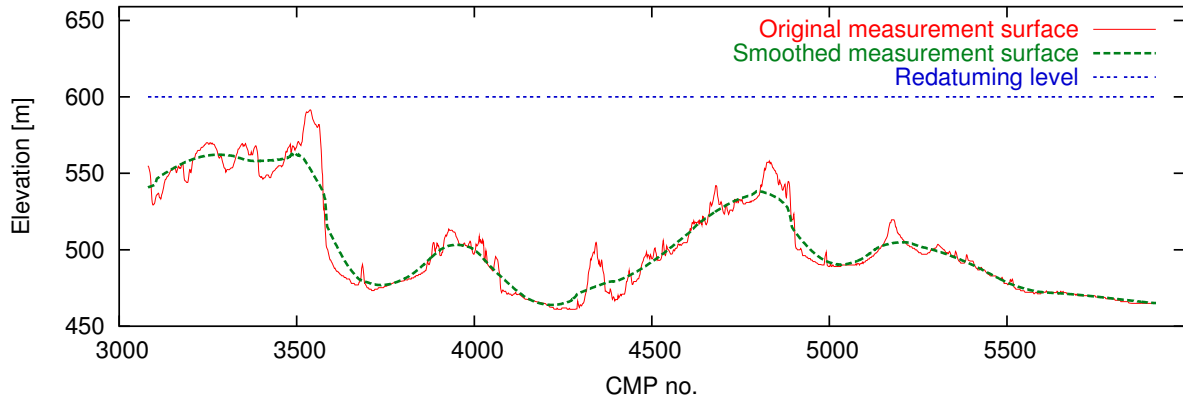
Figure 7.19: Comparison between original and smoothed measurement surface. The horizontal surface at $z = 600$ m was used as reference level for the redatuming.

of 80 ms, and (d) Bandpass filter with corner frequencies 5-10-60-80 Hz. For a basic discussion of the a aforementioned preprocessing steps I refer to Yilmaz (2001) or Forel et al. (2005).

- *Refraction statics by TEEC*: in order to estimate the amount of near-surface velocity variation, an initial velocity model was calculated from first-break picks. The first-break times obtained by manual picking entered into an industry-standard refraction statics tool. This refraction statics solution involved the construction of a near-surface velocity-depth model from refracted arrivals, which was then used to calculate the long-wavelength trend for the basic statics and, finally, to relate the prestack data to a horizontal datum at 500 m. For the weathering layer above the refractor, a constant velocity of 1000 m/s was assumed, since the near-offset traces did not allow velocity estimation for the very near surface from first-break picks and no other information was available. It has to be mentioned that the data at hand was provided by TEEC more than two years ago at an early state of the ongoing research. For a detailed discussion and current results of the processing workflow applied by TEEC, I would like to refer to Gierse et al. (2006) from where also parts of the description above were taken.

- *Inverse elevation statics*: to restore the original source and receiver elevations I applied inverse elevation statics with the constant replacement velocity of 3500 m/s, which is the average velocity above the horizontal datum at 500 m used for the refraction statics. The purpose of restoring the original geometry was to minimize the systematic error that elevation statics introduce to the prestack data by assuming that every ray emerges vertically and, thus, to preserve the physical meaning of the attributes to be extracted from the prestack data as far as possible.

The total static correction times, including refraction statics and inverse elevation statics, are depicted in Figure 7.20.

7.2.2 CRS stack for topography

As in the previous data examples, the first step of the conducted workflow was the application of the CRS stack for topography. I used a constant near-surface velocity $v_0 = 3500$ m/s since this
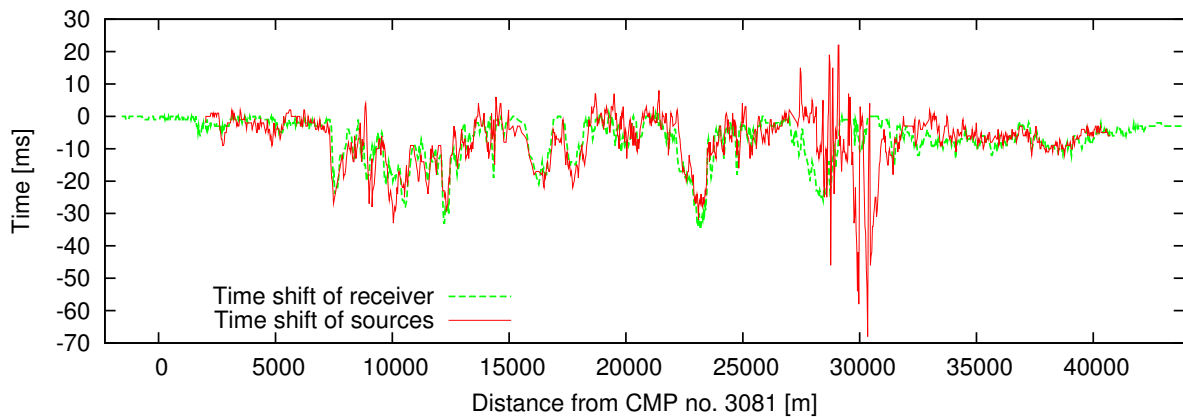
Figure 7.20: Static time shifts for the individual source and receiver locations resulting from refraction statics down to a horizontal level at $z = 500$ m and inverse elevation statics up to the actual topography with a replacement velocity of 3500 m/s.

velocity was chosen as replacement velocity to restore the original topography. In detail, the following processing sequence was carried through:

- *Topography analysis.* The actual measurement surface was smoothed using a smoothing aperture of 3600 m according to the size of the maximum offset aperture later considered by the CRS stack. This ensures that each point at the smoothed reference level can be well approximated by a parabola with apex at the center of the respective stacking aperture (see Section 4.4.3). A comparison between the smoothed and the actual measurement surface is depicted in Figure 7.19. The differences in elevation between the actual measurement surface and its smoothed counterpart reach up to 30 m.

- *Small scale static corrections.* To relate the data to the smooth reference level total static time shifts (source static + receiver static) ranging from -17.4 to 19 ms were necessary due to the roughness of the topography. The constant replacement velocity of 3500 m/s was used to calculate the corrections.

- *Initial CRS stack.* A time-dependent offset aperture was employed linearly increasing from 150 m at 0.1 s to 3600 m at 1.5 s. Since the target reflections are all quite flat, emergence angle values within the range of $\pm 50°$ were considered during the search. After some iterations of static correction, which removed most of the small scale undulations on the reflections, the search range of the emergence angle was further reduced to $\pm 30°$. The NMO velocity was sought for within the range of 2500 m/s to 7000 m/s. The midpoint aperture increased from 50 m at minimum traveltime to 800 m at maximum traveltime. For the plane-wave search only 40% of this aperture were used. The result of the initial CRS stack is displayed in Figure 7.22. Note that for data with high signal-to-noise ratio the stacking apertures, especially the midpoint aperture, might be chosen much smaller and, thus, a much higher lateral resolution can be obtained (see, e. g. Heilmann et al., 2004).

- *Event consistent smoothing.* A parallelogram shaped smoothing window having a spatial half-width of 60 m and a temporal half-width of 8 ms was employed. The maximum angle deviation for samples to be accepted was $2°$ and a time dependent coherence threshold linearly decreasing

from 0.025 for minimum traveltime to 0.015 for maximum traveltime had to be exceeded. For each ZO sample smoothing was only applied if 80% of the samples within the surrounding window fulfilled these criteria.

- *Optimization.* Optimization was carried through for every sample of the ZO section. The resulting stack section is depicted in Figure 7.23. The size of the projected Fresnel zone calculated from the initial attributes was used to limit the search aperture. The final stacking aperture was limited by the projected Fresnel zone calculated from the optimized attributes.

- *Residual static correction.* Twelve iterations of residual static corrections were conducted. Here, it has to be mentioned that the code for the residual static corrections was still under construction during the first iterations and different strategies how to iterate the residual static correction process were tested. Thus, far less iterations might have been necessary. For instance, the option to restack the corrected data without updating the attributes before starting a new iteration of residual static correction was tested. Also the option to omit the initial attribute search by only optimizing the previously obtained attributes now considering the corrected data was tested. Finally, I came to the conclusion that the strategy which is most time consuming on the first sight, namely to repeat after each iteration of residual static correction the complete CRS stack process including the initial attribute search, actually saves time since it provides an optimum result with a minimum number of iterations, whereas the other strategies might not converge to this result at all. The traveltime window used for the cross-correlations spread from 0.3 s to 1.4 s. The maximum shift for a certain source or receiver location was limited to 40 ms per iteration. Source or receiver time shifts determined from cross correlation stacks with less than 2000 contributing traces were not considered since the time shifts at the border of the line did not seem to be reliable. This discriminated about 2% of the obtained receiver statics. The average number of traces contributing to a correlation stack was about 17000 for the receivers and about 12000 for the sources. The total residual static time shifts for the source and for the receiver locations are depicted in Figure 7.21. An unwanted cycle-skip can be observed at distance 7700 m. The stack section and the coherence section resulting from the final iteration of the CRS stack applied to the corrected prestack data are depicted in Figure 7.24 and Figure 7.25. The percentage increase of coherence before and after residual static correction is depicted in Figure 7.26.

- *Redatuming.* The horizontal redatuming level was chosen ten meters above the highest peak of the smoothed reference surface, i. e. at an elevation of 600 m. A redatuming velocity of 3500 m/s was used. The optimized stack section after redatuming is depicted in Figure 7.27. The attribute sections after redatuming and the associated NMO velocity section are depicted in Figures 7.28 to 7.31.

Discussion of the results. Comparing the results of initial and optimized CRS stack (Figures 7.22 and 7.23), a significantly increased continuity of the reflection events can be observed. This further demonstrates that smoothing of the initial attributes followed by a local three parameter optimization is necessary to employ the full potential of the spatial CRS stack operator, particularly in case of complex near-surface conditions which lead to a strongly variable data quality along the line. However, for traveltimes smaller than 1 s there are still a number of gaps, interrupting the continuity of the reflection events, which are probably no feature of the subsurface structure itself but are caused by near-surface effects that were not resolved by the static corrections. Especially in the area between CMP no. 4900
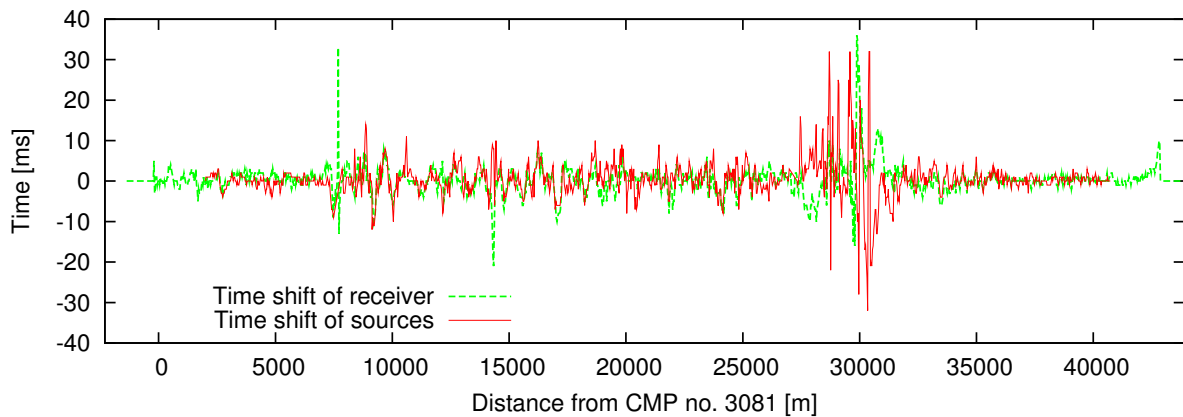
Figure 7.21: Accumulated static time shifts for the individual source and receiver locations after twelve iterations of residual static corrections.

and CMP no. 5150, the presented imaging approach failed completely due to an insufficient compensation of near-surface effects and the local distribution of sources and receivers which is strongly deviating from a straight line geometry in this region. Although the gap around CMP 5000 has not been closed completely, it has been considerably reduced by applying the residual static correction. The stack result after residual static correction (Figure 7.24) shows a strongly improved resolution and event continuity. Obviously, most of the small-scale undulations of the reflection events caused by remaining influences of the near-surface structure could be removed. The highly increased coherence of the data along the stacking operator (see Figure 7.26) further illustrates these observations. As a consequence of the improved coherence, also the associated attribute sections gained much in quality (see also Koglin et al., 2006) which was very helpful for the subsequent tomographic inversion.
Applying the redatuming procedure the acquisition footprint could be compensated to a large extent, as can be seen in Figure 7.27, particularly in the region below the step cliff at CMP 3600. The NMO velocity section (Figure 7.31) calculated from the optimized values of β_0 and R_{NIP} after redatuming according to equation (C.3) differs from the actual stacking velocity used for the initial stack but corresponds to a horizontal measurement surface at $z = 600$ m (see also Appendix C). Strongly increased NMO velocities can be observed below the *jebel* (mountain) on the left hand side of the wadi (CMP no. 3200 to CMP no. 3600).

7.2.3 CRS-stack-based tomographic inversion

The second step of the conducted imaging workflow was to determine a smooth macrovelocity model via CRS-stack-based tomographic inversion. In detail, the following steps were involved:

- *Automatic picking within the redatumed CRS stack results.* Input for the tomographic inversion process were 4133 samples of the redatumed CRS stack section together with their associated values of emergence angle β_0 and NIP-wave radius R_{NIP}. The latter were picked using an automatic picking program which evaluates for every sample of the ZO section several criteria in order to define a valid pick location. For the presented data example the following criteria were used:

  - the coherence associated with the analyzed sample had to exceed a coherence threshold of 0.045.

– the coherence of the neighboring samples had to exceed 90% of this coherence threshold.

– all samples within a used defined window centered around the analyzed pick location with a spatial half-width of 50 m and a temporal half-width of 25 ms had to exceed 80% of this coherence threshold.

– the maximum emergence angle deviation between the sample in the center and the samples within the surrounding window must not exceed an angle threshold of 1.5°.

– the amplitude of the stack envelope at the central sample had to be at least 50% higher than the mean amplitude of the stack envelope inside a surrounding time window of 0.6 s length.

Considering the large number of picks used for this data set the automatic picking process saved much time and effort. Nevertheless, the picks had to be thoroughly checked. For instance, multiple reflections or coherent noise cannot be distinguished from the searched-for reflection events by evaluating the above criteria, only. After a certain number of tests it was decided to skip all picks with traveltimes smaller than 0.75 s. The resulting pick locations are displayed in Figure 7.32.

• *Tomographic inversion.* Starting from a vertical gradient model, the tomographic inversion ended after 20 iterations when no further model improvement could be achieved. The final macrovelocity model, depicted in Figure 7.33, consists of 380 B-spline nodes. In vertical direction 10 node points with 500 m spacing and in the horizontal direction 38 node points with 1000 m spacing were used, skipping one node point at distance 17 km and 6 node points from km 27 to km 32, since no picks were located in these areas. Different grids were tested but did not lead to better results. The redatuming level at an elevation of 600 m constitutes the upper border of the model. The deepest picks that contributed to the tomographic inversion process were located at a depth of 3.3 km. Below that depth, the model is not directly constrained by the input data but mainly depends on the chosen regularization.

Discussion of the results. The macrovelocity model depicted in Figure 7.33 shows interval velocities ranging from 3500 m/s to 5000 m/s. The highest velocities are reached at the left hand side of the model for a traveltime of 1 s and a vertical zone of increased velocities can be observed at km 17.5. Both observations are quite consistent to the NMO velocities depicted in Figure 7.31. Excluding the right border of the model, a general trend to increased interval velocities for traveltimes around 1 s is significant. In first tests using also the picks for traveltimes smaller than 0.75 s this zone of increased velocities was even more pronounced and a strong velocity inversion in the area below could be observed. These features were assessed to be rather unlikely for the area under investigation and I decided to discriminate the shallow picks since they might be unreliable because of the strong influence that near-surface effects and static corrections might have to attributes extracted at small traveltimes. Doing this was not an easy decision since a macrovelocity model extracted from seismic data with the purpose to migrate the latter does not have to coincide with the geologically correct model of the interval velocities in the subsurface, even though both are in depth domain. If, e. g., static corrections or other influences cause artifically increased interval velocities in the data, then these velocities are needed for the migration. Unfortunately, the time-frame of this thesis did not allow a thorough analysis of the common image gathers resulting for both cases, which would have provided more objective evidence whether to keep the shallow picks or not.

7.2.4 Kirchhoff pre- and poststack depth migration

As a final step of the conducted imaging workflow, a depth domain image of the subsurface structure was obtained by both, Kirchhoff pre- and poststack depth migration using the program Uni3D, developed at Karlsruhe University.

- *Calculation of diffraction traveltime tables.* The necessary Green's function tables (GFTs) were calculated in the smooth macrovelocity model, depicted in Figure 7.33, by means of a program, developed at Karlsruhe, University that employs the so-called *fast marching eikonal solver* contained in the SEPLIB package, provided by the Stanford Exploration Project. The GFT for the poststack depth migration was related to the planar reference level since the redatumed stack section was to be migrated. Contrary to this, the actual measurement surface had to be considered for the GFT used by the prestack depth migration.

- *Pre- and poststack depth migration.* The prestack migration was performed directly from topography using the residual static corrected prestack data, whereas the poststack depth migration was applied to the redatumed CRS stack section depicted in Figure 7.27. In both cases, a depth dependent operator aperture was used with a minimum value of 1200 m at the top of the migration target zone and a maximum value of 1600 m at the bottom. Linear interpolation of the operator aperture was applied in between[5]. For the output, a horizontal grid-size of 15 m and a vertical grid-size of 10 m was chosen in order to avoid image aliasing and steps in the image of the dipping reflectors, particularly below the cliff at the left hand side of the wadi. The poststack depth migration result is depicted in Figure 7.34.
  In order to obtain the prestack depth migrated image shown in Figure 7.37, the prestack data was sorted in common offset sections which were then migrated separately. Afterwards, they were merged again to a migrated prestack data set, which was then resorted to so-called common image gathers (CIGs). Before these CIGs were finally stacked in offset direction, an offset- and depth-dependent mute was applied to avoid the stacking of stretched wavelets and, hence, a blurred (or completely destroyed) image. Some of these CIGs are depicted in Figure 7.35 together with the prestack depth migration result, after stacking in offset direction, where the locations of the CIGs are each identified by vertical lines. The mute function, which starts at 100 m offset at the top of the model and linearly increases the offset range up to 2650 m at 3.5 km depth can easily be observed. For comparison, the prestack depth migration result without residual static correction is depicted in Figure 7.36.

Discussion of the results. Based on the prestack depth migration results the quality of the macrovelocity model was evaluated. It can be observed that, even though no velocity update was performed, most of the events in the CIGs are flat, particularly in the relatively undisturbed areas at the borders of the survey. From the fact that most of the reflection events have virtually no moveout for increasing offset, a good overall consistency of the macrovelocity model and the underlying prestack data can be concluded. However, there are also some regions, e. g. at km 24, where an update of the velocity model, e. g. using the approach of Klüver (2006), would be advisable for a further improvement of the migration result.
The processing parameters for the CRS stack, particularly the apertures, were chosen to achieve an

---

[5]Choosing a time dependent operator aperture both minimizes the computation time and reduces the aliasing without loosing information or applying rigorous anti-aliasing filters that decrease the frequency content of the data and, thus, the possible resolution in the output domain.

maximum signal-to-noise ratio and stable attribute sections. As a consequence of this, the poststack depth migration result (Figure 7.34) is characterized by a high signal-to-noise ratio but might be too smooth in the eyes of an interpreter. Compared to this, the prestack depth migration result provides a significantly higher lateral resolution, even though a part of this impression might be caused by the lower signal-to-noise ratio. Both, the prestack depth migration as well as the poststack depth migration clearly imaged many continuous reflectors which can be traced across the complete section. Only in some regions which are still deteriorated by unresolved near-surface problems the reflectors are distorted or even completely interrupted. In the area from km 28 to km 31 the reflector images vanish almost completely, mostly encountering a certain pull-up at the borders of the gap. A structural interpretation aiming at identifying vertical offsets of reflectors, deflection of reflectors, fracturing, and faults has to be carried out carefully since, at least in some areas, the obtained images of the reflectors might still be influenced by features of the near-surface geology. Comparing the results of the prestack depth migration obtained for the data with and without residual static corrections (Figures 7.37 and 7.36), a significant improvement of the reflector continuity can be observed, e. g. in the area below the wadi between CMP no. 3600 and CMP no. 3900.
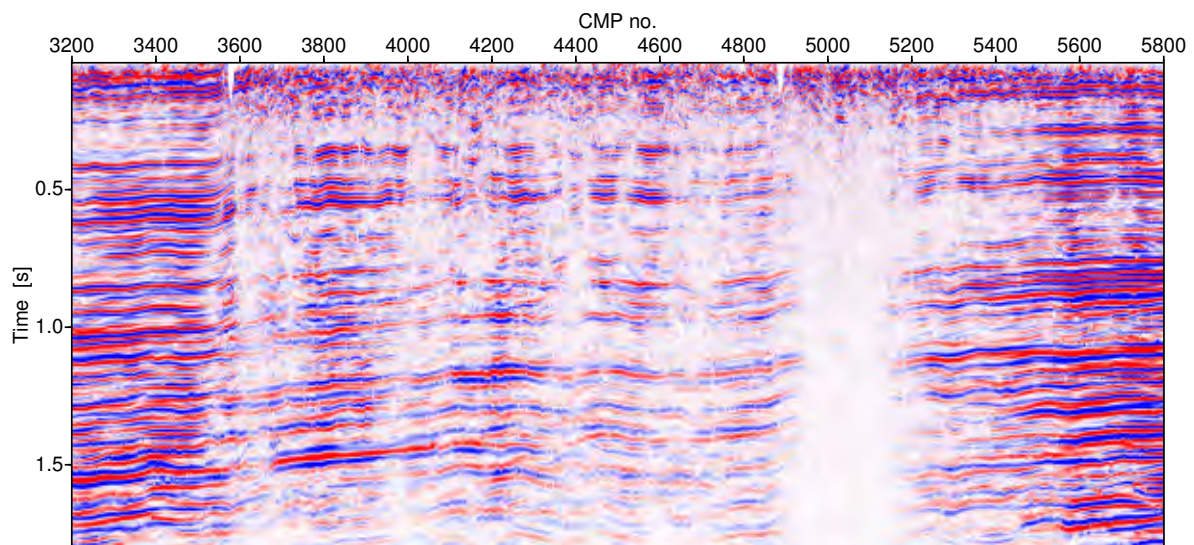
Figure 7.22: Result of the initial CRS stack restricted to the projected first Fresnel zone. The simulated ZO traveltimes are related to the smoothed reference level.
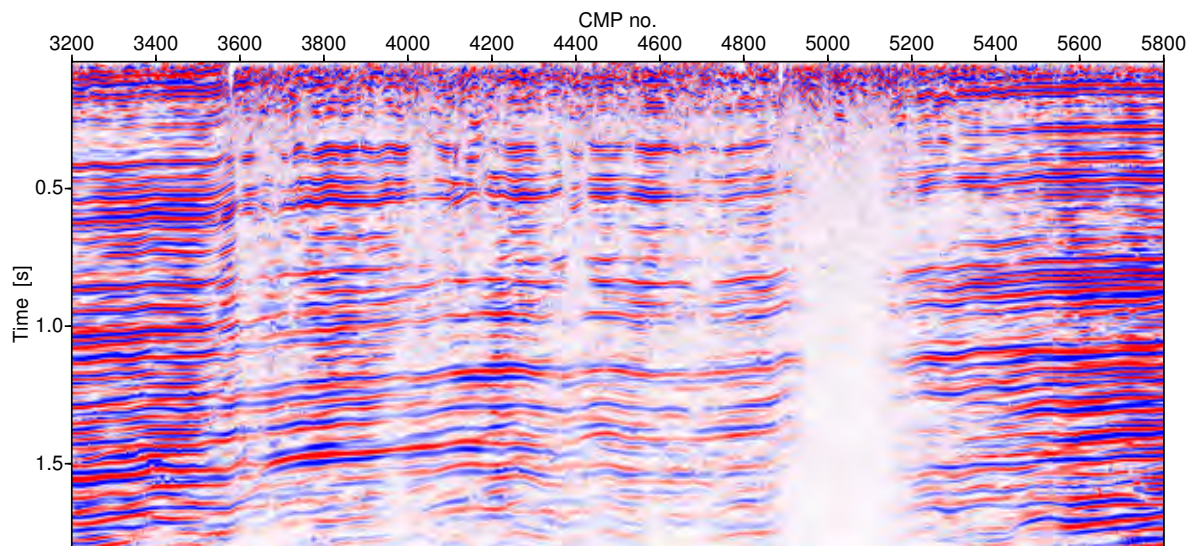
Figure 7.23: Result of the optimized CRS stack restricted to the projected first Fresnel zone. The simulated ZO traveltimes are related to the smoothed reference level.
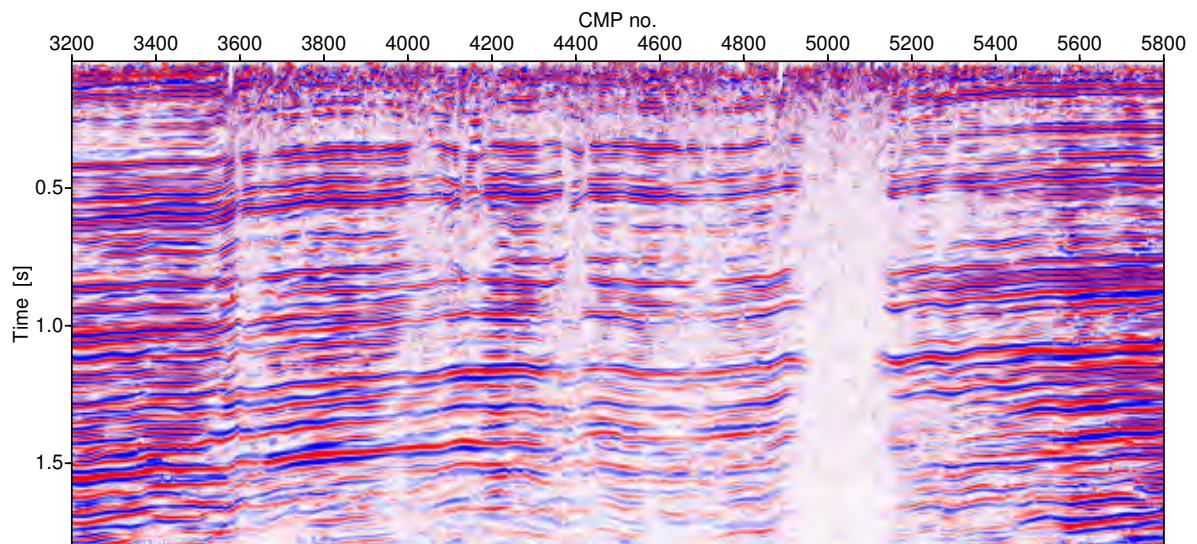
Figure 7.24: Result of the optimized CRS stack restricted to the projected first Fresnel zone after five iterations of residual static correction. The simulated ZO traveltimes are related to the smoothed reference level.
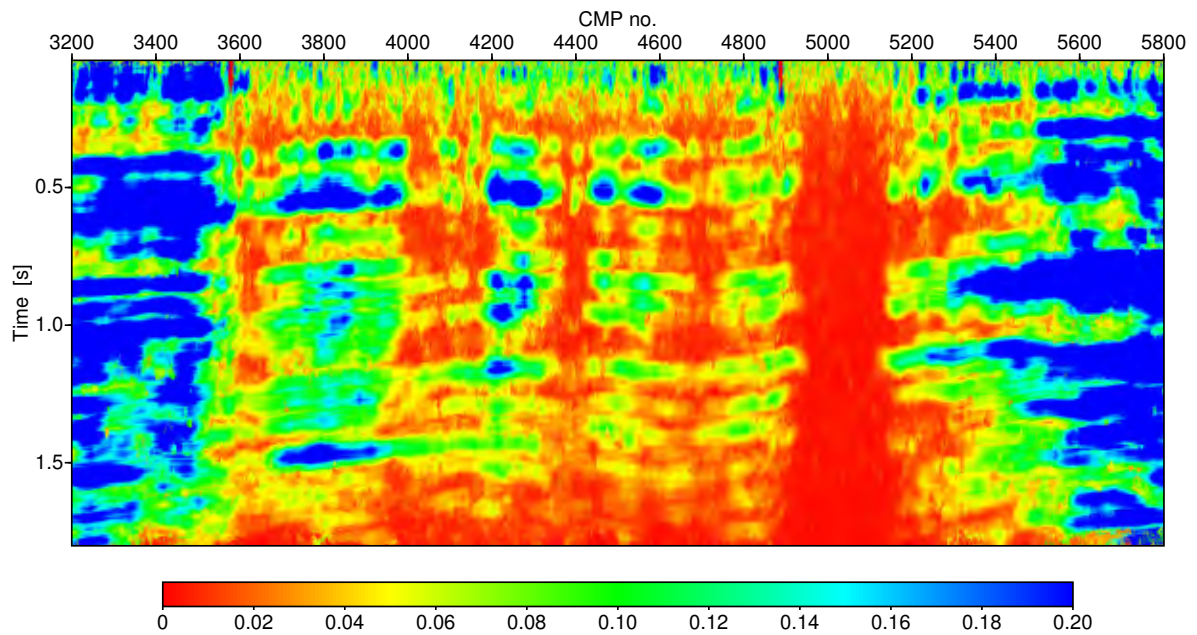
Figure 7.25: Coherence, associated with the optimized CRS stack after residual static correction. The simulated ZO traveltimes are related to the smoothed reference level.
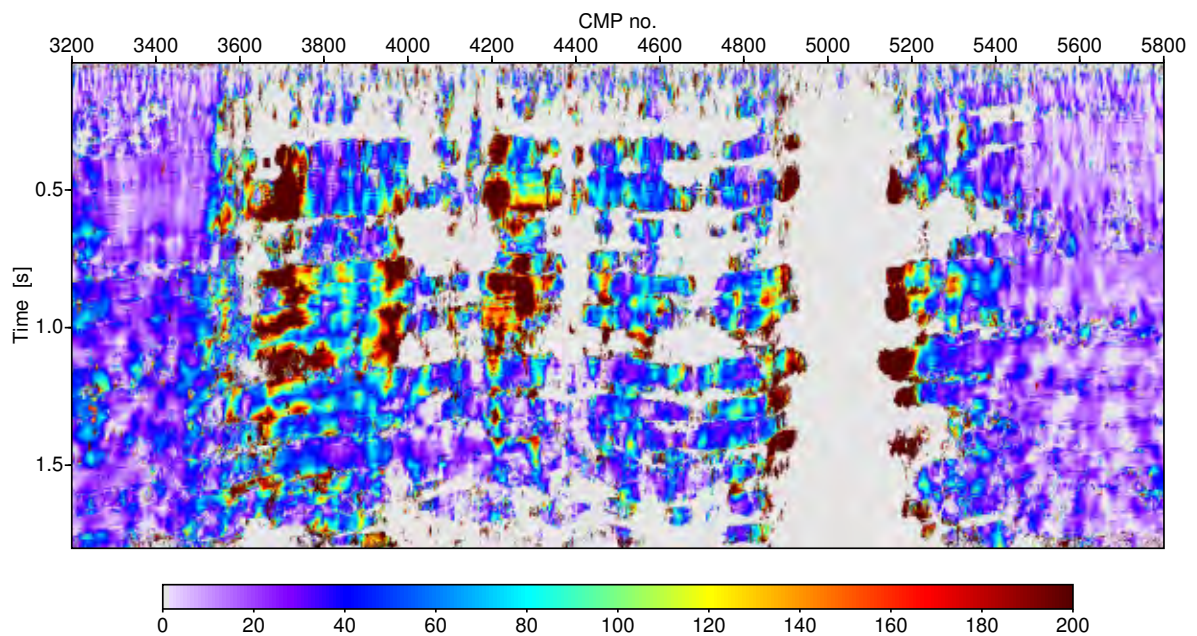
Figure 7.26: Percentage increase of coherence between optimized CRS stack before and after residual static correction. The simulated ZO traveltimes are related to the smoothed reference level. ZO samples with very low coherence value are masked out (gray), as they are not expected to be related to reliable attributes.
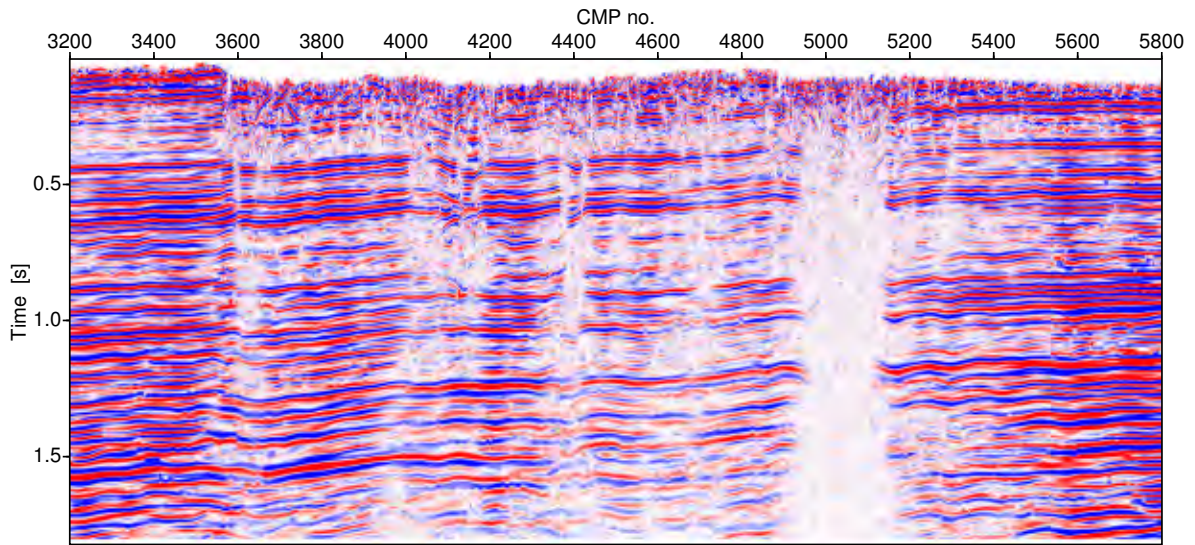
Figure 7.27: Result of the optimized CRS stack restricted to the projected first Fresnel zone after residual static correction and redatuming. The redatuming procedure relates the achieved results to a fictitious horizontal measurement surface at $z = 600$ m.
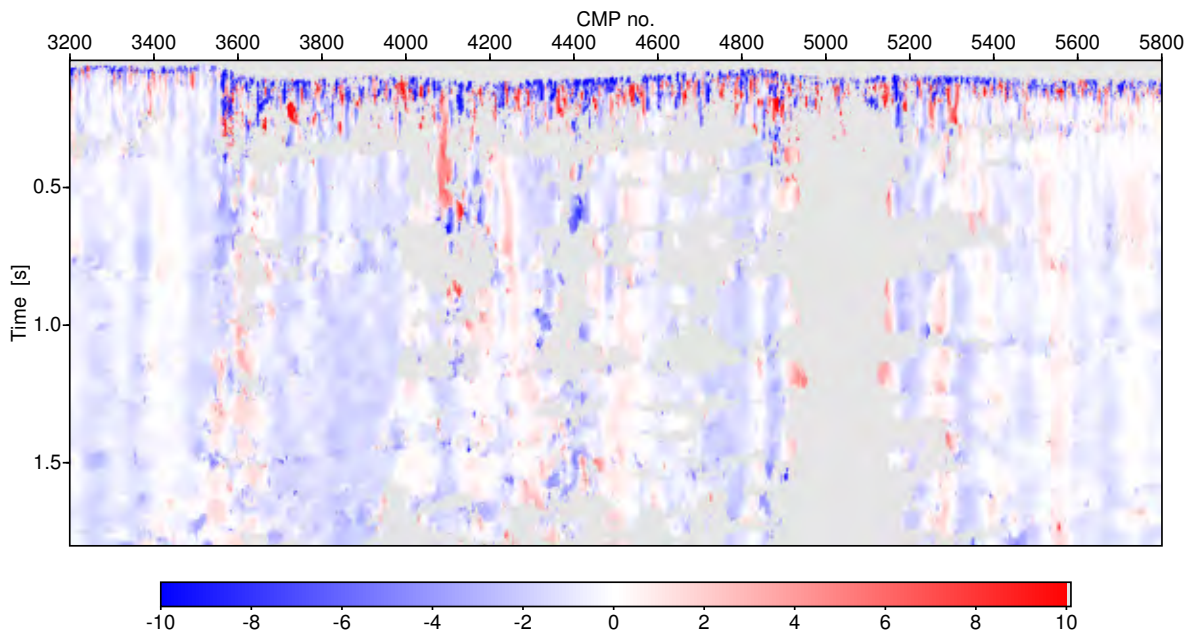
Figure 7.28: Emergence angle of the simulated ZO rays [deg] after residual static correction, related to a fictitious horizontal measurement surface at $z = 600$ m. ZO samples with very low coherence value are masked out (gray), as they are not expected to be related to reliable attributes.
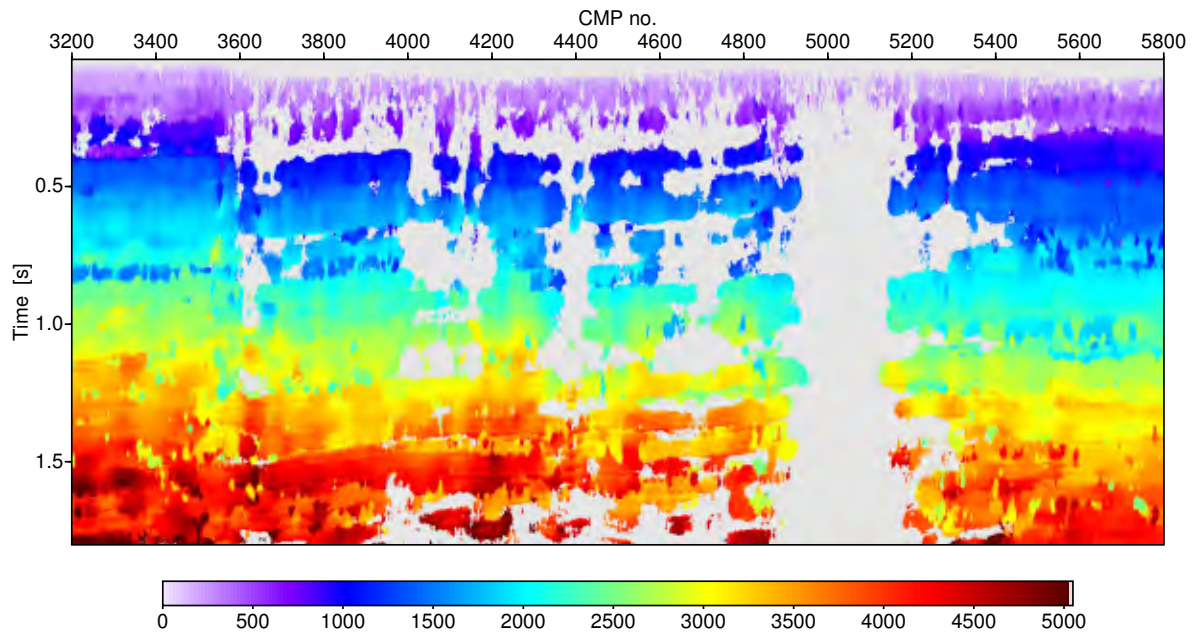
Figure 7.29: Radius of the Normal-Incidence-Point (NIP) wavefront [m] after residual static correction, related to a fictitious horizontal measurement surface at $z = 600$ m. ZO samples with very low coherence value are masked out (gray), as they are not expected to be related to reliable attributes.
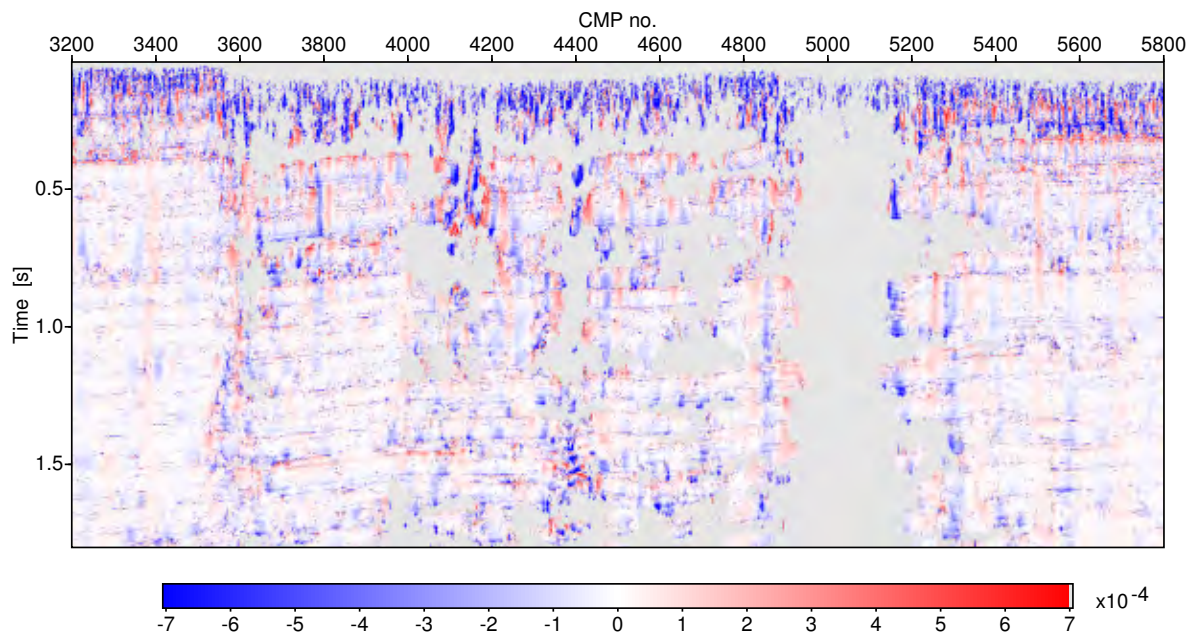
Figure 7.30: Curvature of the normal wave [1/m] after residual static correction, related to a fictitious horizontal measurement surface at $z = 600$ m. ZO samples with very low coherence value are masked out (gray), as they are not expected to be related to reliable attributes.
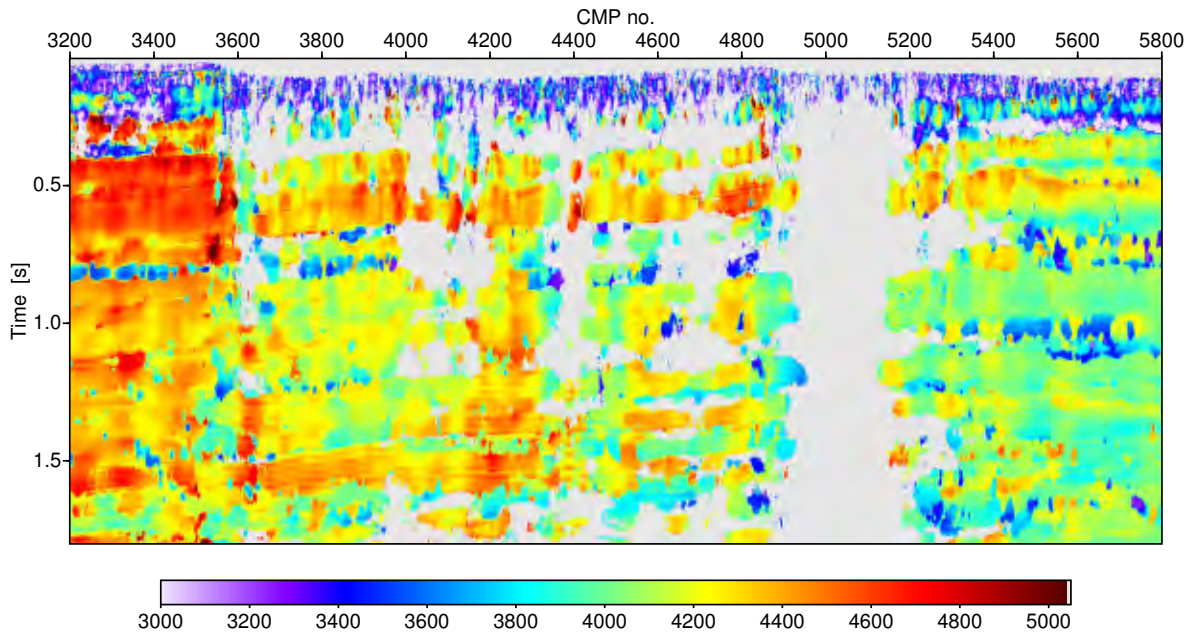
Figure 7.31: NMO velocity [m/s] calculated from optimized CRS attributes after residual static correction, related to a fictitious horizontal measurement surface at $z = 600$ m. ZO samples with very low coherence value are masked out (gray), as they are not expected to be related to reliable attributes.
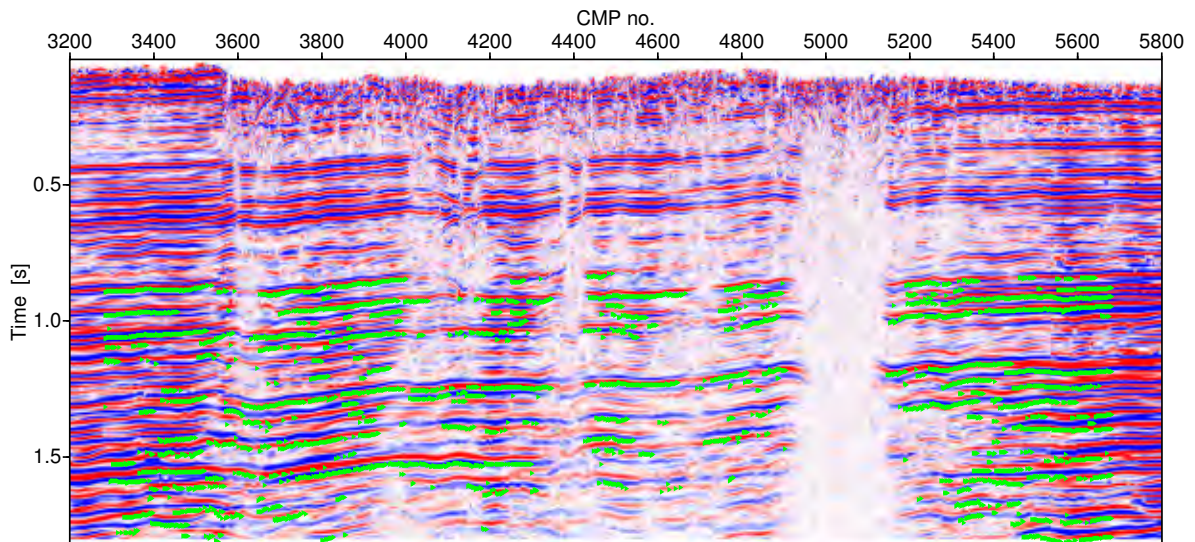
Figure 7.32: Green dots indicate the position of the redatumed ZO samples from which traveltime, midpoint position, emergence angle, and NIP-wave radius were extracted to serve as input for the tomographic inversion.
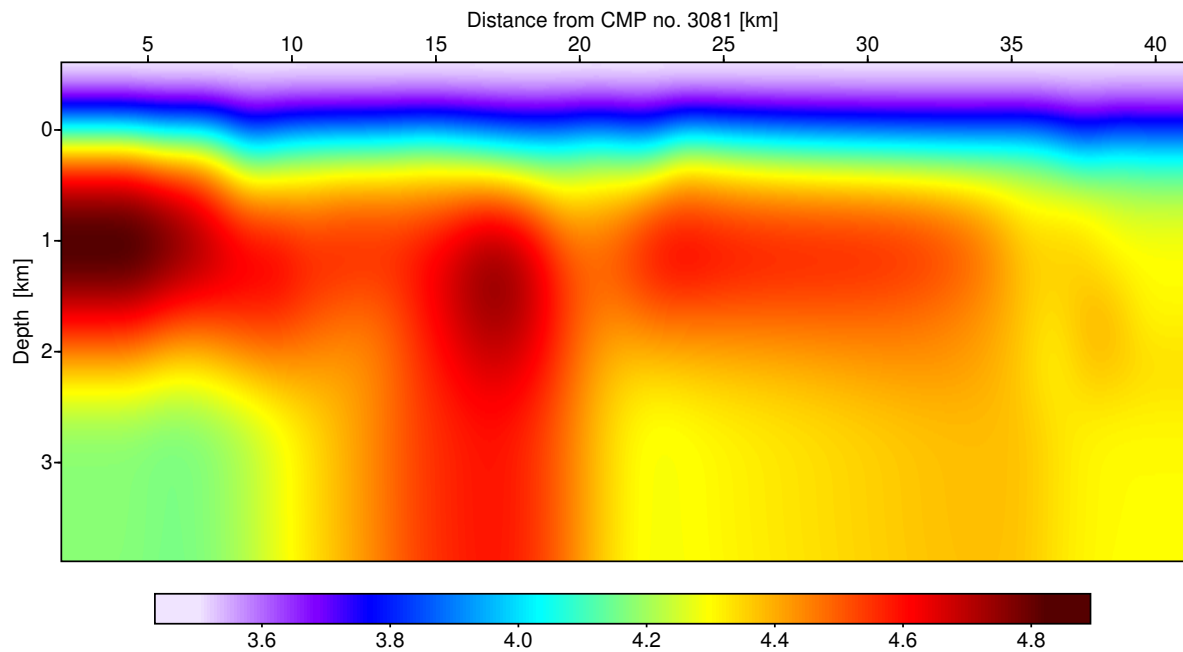
Figure 7.33: Smooth macrovelocity model [km/s] obtained by tomographic inversion.
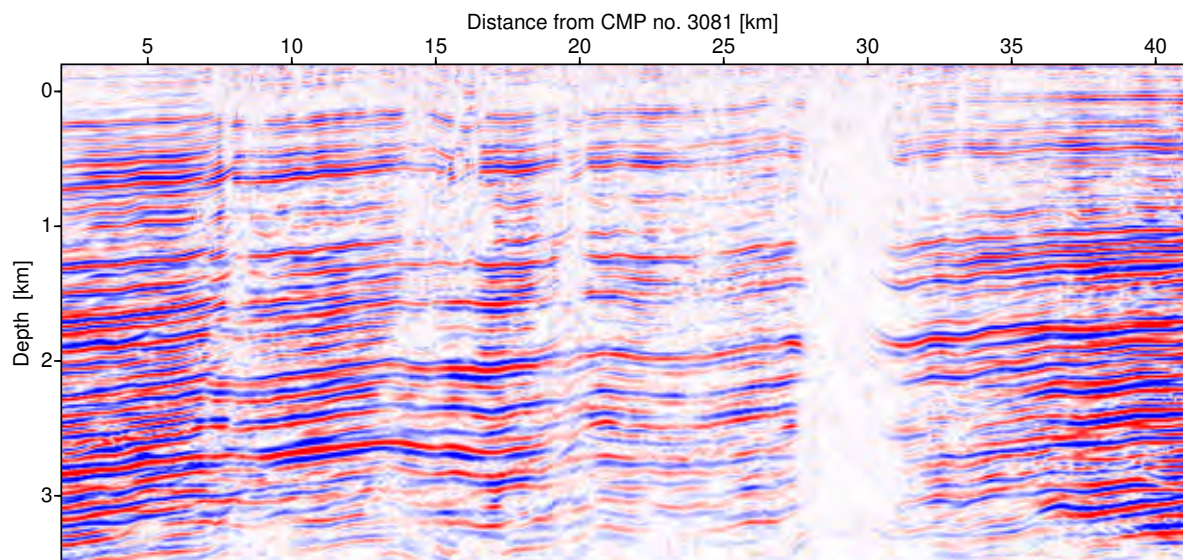
Figure 7.34: Result of the poststack depth migration applied to the optimized CRS stack section after residual static correction and redatuming depicted in Figure 7.27. The smooth macrovelocity model, depicted in Figure 7.33, was used to generate the necessary diffraction traveltime tables.
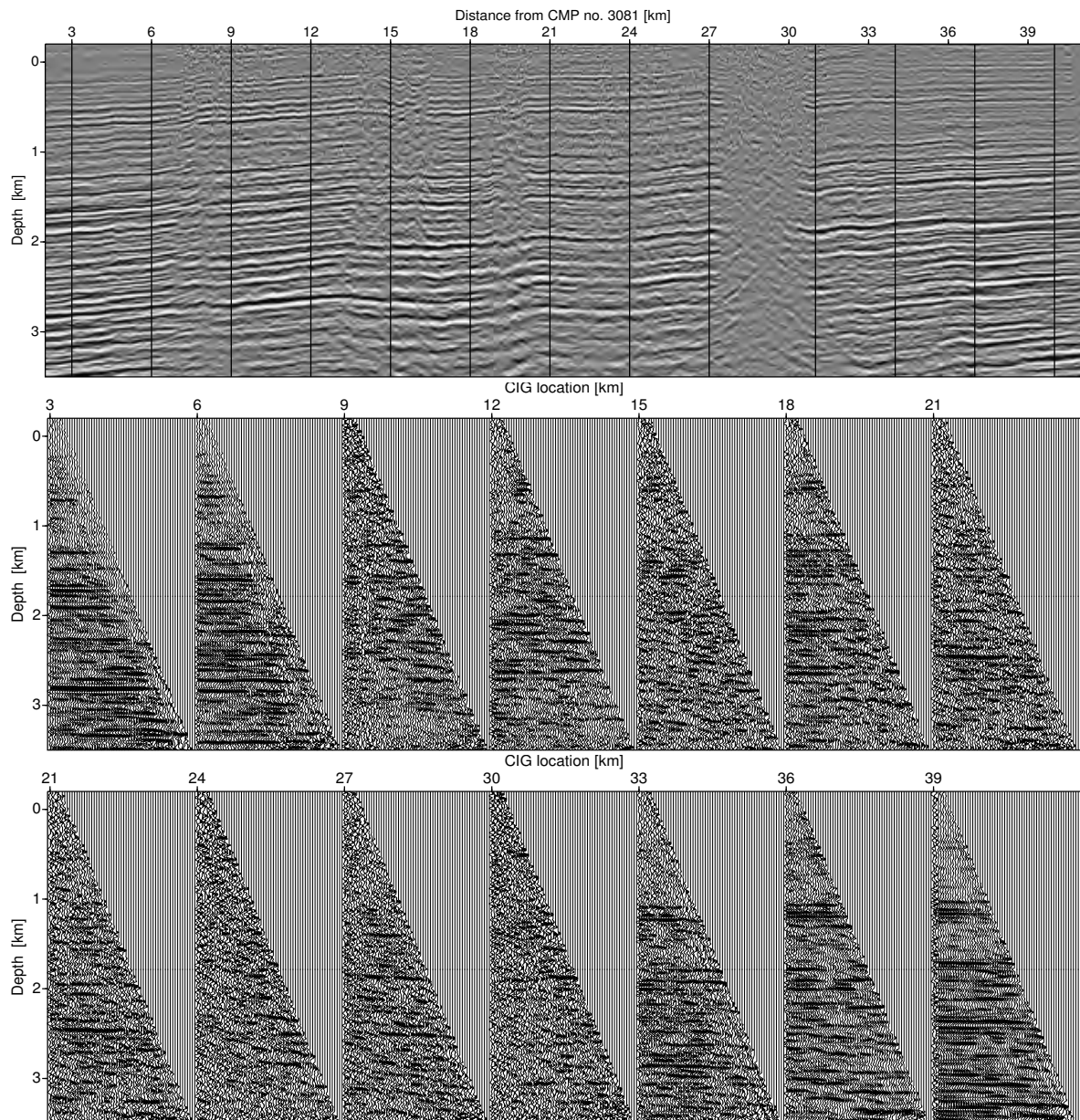
Figure 7.35: Some common-image gathers (CIGs) extracted from the prestack depth migration result before stacking over all offsets. For convenience, the result after stacking in offset direction is are also displayed, where the locations of the CIGs are each identified by vertical lines. The mute function starts at 100 m offset at the top of the model and linearly increases up to 2650 m at 3.5 km depth.
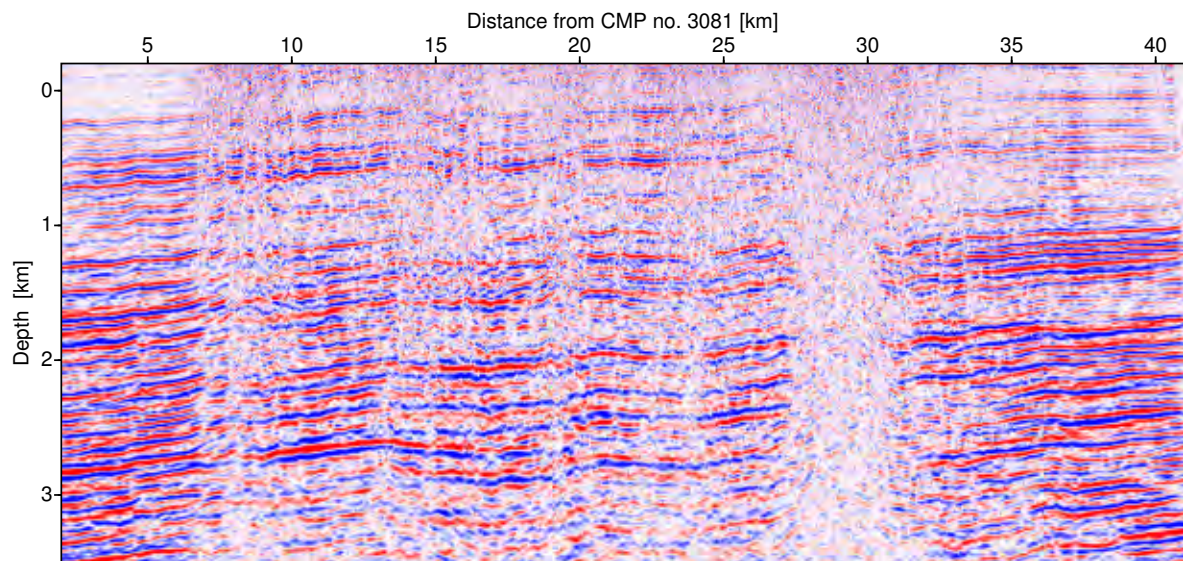
Figure 7.36: Result of the prestack depth migration applied to the prestack data without residual static correction. The smooth macrovelocity model, depicted in Figure 7.33, was used to generate the necessary diffraction traveltime tables.
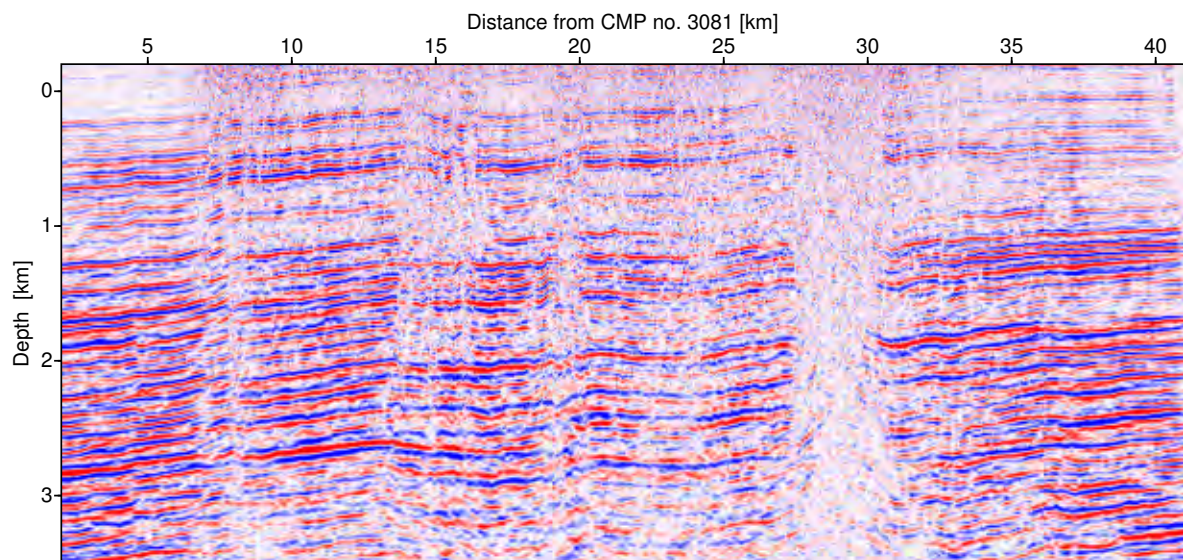
Figure 7.37: Result of the prestack depth migration applied to the prestack data after residual static correction. The smooth macrovelocity model, depicted in Figure 7.33, was used to generate the necessary diffraction traveltime tables.

Chapter 8

Conclusions and outlook

Today, the CRS stack method cannot be seen anymore as an isolated imaging process. It has evolved to be the fundamental process of an entire time-to-depth imaging workflow. Its modern data-oriented design makes the CRS stack method particularly suitable for complex land data processing. Therefore, I integrated topography handling and residual static corrections into this workflow and applied several synthetic tests with main emphasis on the near-surface challenges of land data processing involving the complexity of the time-to-depth imaging process. As a result, a consistent CRS-stack-based-imaging workflow for land data could be established. The latter was applied and further developed in two quite extensive case studies. In this thesis, theoretical and numerical aspects of this workflow as well as the obtained results were systematically analyzed and discussed, with main focus on the extended CRS stack method.

After a brief introduction on exploration seismics and seismic ray theory, special emphasis was put in the first part of this thesis on those theoretical aspects relevant for the development of the CRS stack for topography. Using the paraxial ray method, the two-point eikonal, a formula which approximately describes the traveltime difference between a central ray and rays in its paraxial vicinity, was obtained. Based on these results, stacking operators for arbitrary topography and for two important special cases, i. e. smoothly curved topography and planar topography, were derived. Finally, a redatuming method was introduced that utilizes the extracted CRS attributes to relate the CRS stack results from a floating datum to a fictitious horizontal reference level.

In the second part of this thesis, I discussed the practical implementation of the CRS stack, focusing on the extensions and changes required to support arbitrary topography. In this regard, the global multi-parameter optimization problem is the most challenging task: it has to be solved in an efficient manner, since the typically huge amount of data does not allow to test each plausible combination of the stacking parameters. For this purpose, I established a cascaded processing scheme, starting with the determination of initial attribute values by means of a global three-times-one parameter search. Since the complexity of the stacking operator for arbitrary topography does not allow such a pragmatic search strategy, a reduced stacking operator for smoothly curved topography is employed for the initial search. As a consequence, small static corrections are necessary to relate the prestack data to a fictitious smoothly curved reference datum. Furthermore, appropriate search ranges for the stacking parameters have to be defined. To reduce artifical fluctuations of the determined attribute values mainly caused by the split search, the initial attribute values enter into an event consistent smoothing process before they are optimized by a local three-parameter optimization which is considering the true source and receiver elevations. Finally, I discussed the implementation of a redatuming procedure

providing standardized results for interpretation and further processing by mapping both, stack and attribute sections, to a horizontal redatuming level. A very simple synthetic dataset was used to test and visualize important aspects of the presented processing scheme namely the pragmatic search strategy, the determination of a smoothly curved reference datum and its local dip and curvature, the estimation of appropriate search ranges, and the redatuming.

After this detailed discussion of the implementation of the CRS stack for topography, additional processing steps of the CRS-stack-based imaging workflow for land data were addressed, starting with the concept of CRS-stack-based residual static corrections which is of vital importance for land data processing. The determination of a smooth macrovelocity model by means of tomographic inversion is regarded as the most important application of the CRS attributes. As a result of the redatuming procedure topography has not to be considered in this processing step. Kirchhoff pre- and poststack depth migration using the previously determined macrovelocity model constitute the final steps of the presented workflow. The redatumed stack results serve as input for the poststack depth migration, whereas prestack depth migration is performed directly from topography using the prestack data after residual static correction. Thus, even prestack depth migration benefits from the CRS method.

Since most problems of seismic reflection imaging on land are quite complex and strongly depend on the specific nature of the target area, much effort was put into the practical application of the developed source code. For this purpose, two realistic synthetic data sets and two quite challenging real data sets were processed in order to test and further develop the presented imaging workflow. Both synthetic data sets were created by the oil industry and feature common problems of land data processing in a realistic manner. The first one resembles a situation often encountered in the arid areas of the Middle East. The rapidly changing source and receiver elevations made this dataset well suited to test the cascaded search and stacking scheme for topography and the redatuming procedure. To evaluate the obtained attribute values and ZO traveltimes tomographic inversion and poststack depth migration was applied, leading to results fully consistent with the underlying velocity model. The second synthetic data set represents a situation typical for the overthrust front of the Canadian Foothills. Processing these data the necessity of considering a laterally variable near-surface velocity got obvious. As a first step in this direction, I extended the CRS stack implementation to consider a laterally variable near-surface velocity which is assumed to be locally constant within the respective stacking aperture. First attempts to consider the actual near-surface velocity at each source and receiver location were made but not carried on since such detailed information on the near-surface velocities was not available for the real data sets at hand. Besides this, the residual static correction proved to be able to compensate the weakness of assuming a locally constant near-surface velocity to a large extent.

Finally, two case studies based on real data sets from North Brazil and the Arabian Peninsula were considered. The first case study resulted from an ongoing research project conducted in collaboration with the Federal University of Pará (UFPA), Bélem, Brazil. The main issue of this project, i. e. to develop a new seismic reflection imaging workflow well suited for the re-processing of existing seismic data, has been successfully addressed despite of the poor data quality. However, the experience with this data set also revealed that the split search strategy might fail in certain situations of low fold and poor signal-to-noise ratio. In such situations, a global three parameter optimization scheme is mandatory to use the full potential of the spatial traveltime approximation. In principle, the current computing power available in the hydrocarbon industry already allows for such an approach. However, this requires a highly parallelized code.

Most of the worlds oil and gas reserves are located in the deserts of the Middle East, where the measurement surface and the first few hundred meters below all too often pose severe problems to seismic data processing. The final case study is concerned with these near-surface problems consid-

ering a challenging land data set from the Arabian Peninsula. It was selected and distributed by Saudi Aramco to serve as a catalyst and benchmark for new methods to solve near-surface-related problems. Several research groups applied sophisticated imaging schemes to these data which allowed to compare the results of CRS-stack-based imaging with the results of other approaches (see *Geophys. Prosp.*, 54:663-777). In the course of this project it turned out that topography handling plus residual static correction was here not fully sufficient to compensate the deteriorating influence of the complex near-surface geology. To address this problem externally determined refractor statics had to be applied to the prestack data. To minimize the influence of these corrections on the CRS attributes inverse elevation statics with a constant replacement velocity were applied to reconstitute the original acquisition geometry. Future implementations of the CRS stack might consider a given macro-model of the near-surface velocities to directly account for large-scale inhomogeneities of the near-surface. The latter cannot be addressed by residual static corrections, but information for an iterative near-surface velocity model refinement might be obtained.

Appendix A

Notation and list of symbols

The variable names chosen to exemplify the used notation have no relation to physical parameters.

$\prod a$ Product symbol $\sum b$ Summation symbol

$$\vec{x} = \begin{pmatrix} x_1 \\ x_2 \\ x_3 \end{pmatrix} \quad \text{Vector}$$

$$\underline{X} = \begin{pmatrix} x_{11} & x_{12} & x_{13} \\ x_{21} & x_{22} & x_{23} \\ x_{31} & x_{32} & x_{33} \end{pmatrix} = \left(x_{ij} \right) \quad \begin{array}{l} 3 \times 3 \text{ Matrix} \\ (i, j = 1, 2, 3) \end{array}$$

$$\mathbf{X} = \begin{pmatrix} x_{11} & x_{12} \\ x_{21} & x_{22} \end{pmatrix} = \left(x_{ij} \right) \quad \begin{array}{l} 2 \times 2 \text{ Matrix} \\ (i, j = 1, 2) \end{array}$$

$$\underline{\underline{X}} = \begin{pmatrix} \mathbf{X_1} & \mathbf{X_2} \\ \mathbf{X_3} & \mathbf{X_4} \end{pmatrix} = \left(x_{ij} \right) \quad \begin{array}{l} 4 \times 4 \text{ Matrix} \\ (i, j = 1, 2, 3, 4) \end{array}$$

$$\vec{x}^T = (x_1, x_2, x_3) \quad \text{Transposed vector}$$

$$\underline{X}^T = \left(x_{ji} \right) \quad \text{Transposed matrix}$$

$$\vec{f} = \vec{f}(\vec{x}) = \begin{pmatrix} f_{x_1} \\ f_{x_2} \\ f_{x_3} \end{pmatrix} \quad \text{Vector field}$$

$$f = f(\vec{x}) \quad \text{Scalar field}$$

$$\vec{a} \times \vec{b} \quad \text{Vector product}$$

$$\vec{a} \cdot \vec{b} \quad \text{Scalar product}$$

$$\vec{\nabla} = \begin{pmatrix} \frac{\partial}{\partial x_1} \\ \frac{\partial}{\partial x_2} \\ \frac{\partial}{\partial x_3} \end{pmatrix} \quad \begin{array}{l} \text{Nabla operator} \\ \text{(Cartesian)} \end{array}$$

$$\vec{\nabla}_{\vec{f}} = \begin{pmatrix} \frac{\partial}{\partial f_{x_1}} \\ \frac{\partial}{\partial f_{x_2}} \\ \frac{\partial}{\partial f_{x_3}} \end{pmatrix} \quad \begin{array}{l} \text{Nabla operator} \\ \text{(different variable)} \end{array}$$

$$\frac{df(u(x))}{dx} = \frac{df}{du}\frac{du}{dx} \quad \begin{array}{l} \text{Full derivative} \\ \text{(chain rule)} \end{array}$$

$$\frac{\partial a}{\partial b} \quad \text{Partial derivative}$$

$$\vec{\nabla} \cdot \vec{f} = \frac{\partial f_{x_1}}{\partial x_1} + \frac{\partial f_{x_2}}{\partial x_2} + \frac{\partial f_{x_3}}{\partial x_3} \quad \text{Divergence}$$

$$\vec{\nabla} f = \begin{pmatrix} \frac{\partial f}{\partial x_1} \\ \frac{\partial f}{\partial x_2} \\ \frac{\partial f}{\partial x_3} \end{pmatrix} \quad \text{Gradient}$$

$$\vec{\nabla} \times \vec{f} = \begin{pmatrix} \frac{\partial f_{x_3}}{\partial x_2} - \frac{\partial f_{x_2}}{\partial x_3} \\ \frac{\partial f_{x_1}}{\partial x_3} - \frac{\partial f_{x_3}}{\partial x_1} \\ \frac{\partial f_{x_2}}{\partial x_1} - \frac{\partial f_{x_1}}{\partial x_2} \end{pmatrix} \quad \text{Curl}$$

$$\Delta = \left(\vec{\nabla} \cdot \vec{\nabla}\right) = \frac{\partial^2}{\partial x_1^2} + \frac{\partial^2}{\partial x_2^2} + \frac{\partial^2}{\partial x_3^2} \quad \begin{array}{l}\text{Laplace operator}\\\text{(Cartesian)}\end{array}$$

$$\mathcal{J} = \frac{1}{c} \det\left(\underline{\mathcal{J}}\right) = \frac{1}{c} \left| \frac{d(a_1, a_2, a_3)}{d(b_1, b_2, b_3)} \right| \quad \begin{array}{l}\text{Jacobian}\\\text{determinant}\end{array}$$

$$\underline{\mathcal{J}} = \frac{d(a_1, a_2, a_3)}{d(b_1, b_2, b_3)} = \begin{pmatrix} \frac{da_1}{db_1} & \frac{da_1}{db_2} & \frac{da_1}{db_3} \\ \frac{da_2}{db_1} & \frac{da_2}{db_2} & \frac{da_2}{db_3} \\ \frac{da_3}{db_1} & \frac{da_3}{db_2} & \frac{da_3}{db_3} \end{pmatrix} \quad \text{Jacobian matrix}$$

$$\mathbf{A}^{-1} = \frac{1}{\det(\mathbf{A})} \begin{pmatrix} a_{22} & -a_{12} \\ -a_{21} & a_{11} \end{pmatrix} \quad \text{with} \quad \det(\mathbf{A}) = a_{11}a_{22} - a_{12}a_{21} \quad \begin{array}{l}\text{Inverse matrix}\\(2 \times 2)\text{ case}\end{array}$$

$$\det(\underline{\mathbf{X}}) = x_{11}x_{22}x_{33} + x_{21}x_{32}x_{13} + x_{31}x_{12}x_{23} - x_{13}x_{22}x_{31} - x_{23}x_{32}x_{11} - x_{33}x_{12}x_{21} \quad \text{Determinant}$$

$$\vec{0} = (0, 0, 0)^T \quad \text{or} \quad \underline{\mathbf{0}} = \left(0_{ij}\right) \quad \begin{array}{l}\text{Zero vector}\\\text{or matrix}\end{array}$$

$$\underline{\mathcal{I}} = \left(\delta_{ij}\right) = \begin{pmatrix} 1 & 0 & 0 \\ 0 & 1 & 0 \\ 0 & 0 & 1 \end{pmatrix} \quad \text{Identity matrix}$$

A.1 List of abbreviations

The following list contains the abbreviations used in this thesis and their expanded writings:

2D	two-dimensional	GFT	Green's function table
3D	three-dimensional	LVL	low-velocity layer
CDP	common-depth-point	MZO	migration to zero-offset
CMP	common-midpoint	NIP	normal incidence point
CO	common-offset	CRS	common reflection surface
CR	common-receiver	P-wave	primary wave
CRP	common-reflection-point	S-wave	secondary wave
CRS	common-reflection-surface	RSC	residual static correction
CS	common-source or common-shot	S/N	signal-to-noise
ZO	zero offset	FD	finite-difference
NMO	normal moveout	DMO	dip moveout
CIG	common image gather	AGC	automatic gain control

Appendix B

The projected Fresnel zone

If one compares the dominant wavelength of a typical seismic wavelet ($\lambda \approx 30 - 70 \, m$) with the scale of the subsurface structures to be imaged, i.e. tens of meters, it is obvious that the actual frequency content of seismic reflection data is too low to justify the concept of mathematical rays with infinitesimal volume. In fact, seismic wave propagation is affected by a finite subsurface volume around the considered ray. That part of this volume which is responsible for the major contribution is known as the *first Fresnel volume* (see, e.g. Červený, 2001). Its size depends on the frequency content of the data which, in turn, limits the maximum achievable resolution. In order to express the latter in terms of reflector properties the *first interface Fresnel zone* is defined as the intersection of the first Fresnel volume with a reflector. In Kravtsov and Orlov (1990) one finds the following definition for the first interface Fresnel zone (see also Figure B.1) around a reflection point X_P: a reflection point X_R in the vicinity of X_P lies inside the first interface Fresnel zone if the associated diffraction traveltime t_D from the source down to X_R and back to the receiver satisfies the relation

$$| t_D (X_R) - t_R (X_P) | \leq \frac{T}{2} \, , \tag{B.1}$$

where t_R denotes the reflection traveltime along the central ray and T the period of a mono-frequent source signal. For transient wavelets, $T/2$ has to be replaced by some measure of the effective wavelet length.

The most suitable property to define an optimum stacking aperture is the so-called *first projected Fresnel zone*, since it is directly related to the source and receiver positions at the measurement surface. For the sake of brevity, the term 'first' will be omitted in the following. It was demonstrated by Hubral et al. (1993b) how the projected Fresnel zone for ZO rays can be estimated from properties of the central ray, only. This was later generalized by Schleicher et al. (1997) to arbitrary acquisition geometries.

For the source and receiver locations $(\mathbf{x}'_S, \mathbf{x}'_G)$ inside of the projected Fresnel zone associated with a source at $\mathbf{x}_S$ and receiver at $\mathbf{x}_G$ a similar relation as for the interface Fresnel zone can be set up:

$$\left| t_D \left(\mathbf{x}'_S, \mathbf{x}'_G \right) - t_R \left(\mathbf{x}_S, \mathbf{x}_G \right) \right| \leq \frac{T}{2} \, . \tag{B.2}$$

A relation to estimate the size of the projected Fresnel zone using the determined kinematic wavefield attributes can be easily found by comparing the approximate diffraction and reflection traveltimes

155
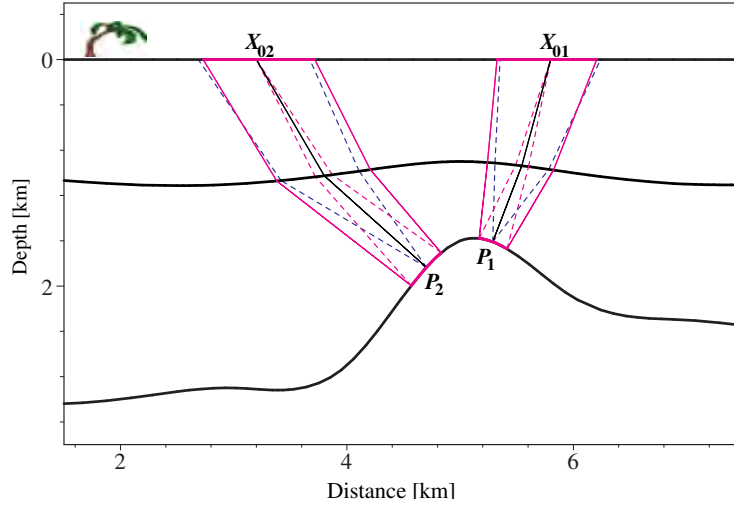
Figure B.1: The first Fresnel zones of two ZO rays, the associated interface Fresnel zones, and the projected Fresnel zones at the surface are depicted in magenta. A dominant frequency of 30 Hz was assumed. Solid lines represent normal ZO rays, dashed lines are diffracted rays. The normal rays yielding the borders of the projected first Fresnel zones (magenta segments of the acquisition line) are shown as solid magenta lines. The projected Fresnel zones at the surface define the optimum midpoint aperture for stacking at X_{01} and X_{02}, respectively. Figure according to Mann (2002).

according to equation (B.2). For the sake of simplicity the parabolic traveltime expression for a smoothly curved reference surface (3.20) is used to substitute t_R and t_D in equation (B.1), where we have to set $K_N := K_{NIP}$ to obtain the diffraction traveltime:

$$\frac{T}{2} = \left| \frac{\cos^2(\beta_0 + \alpha_0)(m_x - m_{x_0})^2}{v_0 \cos \alpha_0} (K_N - K_{NIP}) \right| . \tag{B.3}$$

The later should also be valid, in good approximation, for a rough measurement surface for which the diffraction traveltime and thus also the projected Fresnel zone cannot be described in terms of $m_x - m_{x_0}$, only, but depends on $m_z - m_{z_0}$, too. Please note that equation (B.3) contains no offset-dependent terms[1]. As a consequence, it is not possible to estimate the size of the projected Fresnel zone for arbitrary acquisition geometries, in case the paraxial diffraction and reflection traveltimes are expressed in terms of properties of a normal central ray.

However, solving equation (B.3) for $m_x - m_{x_0}$ yields an approximation of the width W_F of the projected Fresnel zone for the ZO configuration (see Figure B.1) which is given by

$$\frac{W_F}{2} = \left| m_x - m_{x_0} \right| = \frac{\cos \alpha_0}{\cos(\beta_0 + \alpha_0)} \sqrt{\frac{v_0 T}{2 \left| K_N - K_{NIP} \right|}} , \tag{B.4}$$

and which is well suited to define an optimum midpoint aperture for the CRS stack.

---

[1]According to the NIP wave theorem (Hubral, 1983), the reflection traveltimes in the CMP gather are up to second order in t equal to the diffraction traveltimes that correspond to a diffractor at the normal incidence point (NIP) of the associated normal ray. For central rays with finite offset this relation does, in general, not hold according to the so-called CDP wave theorem, a generalization of the NIP wave theorem introduced by Schleicher (1993).

Appendix C

NMO velocity for non-planar surfaces

Throughout this thesis, the NMO velocity is defined as the velocity that specifies those hyperbolas in the CMP gather that yield the highest coherence and, thus, the best stacking result. This definition is quite common within the context of the CRS stack method. According to this definition, the terms NMO velocity and *stacking velocity* can be used synonymously. Note, that this definition of the NMO velocity differs a little bit from the classical definition as that velocity which is best to reduce the quasi-hyperbolic traveltimes in the CMP gather to a horizontal line. A slightly different expression for the NMO velocity is obtained if a parabolic second order traveltime approximation is considered instead of the hyperbolic one. E. g., the parabolic NMO velocity does not depend on τ_0. For the sake of simplicity the parabolic traveltime formulas will be neglected in the following. Nevertheless, similar considerations would also hold in this case.

If data acquisition was carried out on an arbitrarily curved measurement surface and no elevation statics were applied to relate the data to a planar reference level, the definition of a CMP gather has to be modified as an ensemble of traces signified by the same x-coordinate of the midpoint[1], i. e. $\Delta m_x = 0$. This is necessary, since for a realistic acquisition geometry on a rough measurement surface hardly two traces share exactly the same midpoint $\vec{m}(m_x, m_z)$.

C.1 NMO velocity for smoothly curved topography

Inserting the condition $m_x = 0$ into the CRS traveltime formula for a smoothly curved measurement surface (3.21) yields the hyperbolic second order description of the traveltimes within a CMP gather for this specific case, which reads

$$\tau_{\text{hyp}}^2(h_x) = \tau_0 + \frac{2\,\tau_0\,h_x^2}{v_0\,\cos^2\alpha_0}\,\left(K_{\text{NIP}}\,\cos^2(\beta_0 + \alpha_0) - K_0\,\cos(\beta_0 + \alpha_0)\right)\,. \tag{C.1}$$

In analogy to the NMO velocity defined for a planar measurement surface (Shah and Levin, 1973), the NMO velocity for a smoothly curved measurement surface can be introduced by rewriting equation

---

[1]Chira et al. (2001) introduced the term odd-dislocation (OD) gather to denote the case of $\Delta m_x = 0$ more precisely.

(C.1) in the following way:

$$\tau^2(h_x) \quad = \quad \tau_0^2 + \frac{4h_x^2}{v_{\text{NMO}}^2} \text{, with} \tag{C.2a}$$

$$v_{\text{NMO,SC}}^2 \quad = \quad \frac{2v_0 \cos^2 \alpha_0}{\tau_0 \left(K_{\text{NIP}} \, \cos^2(\beta_0 + \alpha_0) - K_0 \, \cos(\beta_0 + \alpha_0) \right)} \; . \tag{C.2b}$$

Please note: Even for a planar measurement surface with constant near-surface velocity, v_{NMO} becomes imaginary in case $K_{\text{NIP}} < 0$. However, imaginary values of v_{NMO} are much more likely for a curved measurement surface as can be observed from equation (C.2b).

Inserting $\alpha_0 = 0$ and $K_0 = 0$ in equation (C.2b) results in the NMO velocity for a horizontal[2] measurement surface

$$v_{\text{NMO,H}}^2 = \frac{2v_0}{\tau_0 \, K_{\text{NIP}} \cos^2 \beta_0} \; . \tag{C.3}$$

According to its definition, $K_{\text{NIP}}(X_0)$ does not depend on whether obtained for a horizontal or for a smoothly curved measurement surface through X_0. By contrast, the NMO velocity values which would be measured in these two experiments differ, because the NMO velocity is not a local wavefront attribute like K_{NIP}, K_{N}, and β_0 but a stacking parameter that depends on the acquisition geometry of the CMP gather.

Solving equation (C.3) for K_{NIP} and inserting into equation (C.2b) yields the relationship between the NMO velocity $v_{\text{NMO,SC}}$ obtained for a smoothly curved measurement surface and its corresponding value $v_{\text{NMO,H}}$ that would be measured on a fictitious horizontal surface through X_0

$$v_{\text{NMO,SC}}^2 = \frac{2v_0 \cos^2 \alpha_0}{\tau_0 \left(\frac{2v_0 \cos^2(\beta_0 + \alpha_0)}{\tau_0 v_{\text{NMO,H}}^2 \cos^2 \beta_0} - K_0 \, \cos(\beta_0 + \alpha_0) \right)} \; . \tag{C.4}$$

Here, $v_{\text{NMO,H}}$ can be seen as the NMO velocity that would be obtained after applying a perfect elevation static correction to the pre-stack data.

C.2 NMO velocity for arbitrary topography

If we look at the traveltimes within a CMP gather for arbitrary top-surface velocity (3.11) with $m_x = 0$

$$\begin{aligned}
\tau_{\text{hyp}}^2(\Delta \vec{m}, \vec{h}) \quad = \quad & \left(\tau_0 - \frac{2}{v_0} \, (\Delta m_z \cos \beta_0) \right)^2 \\
& - \frac{2 \, \tau_0 \, K_{\text{N}}}{v_0} \, (\Delta m_z \sin \beta_0)^2 \\
& + \frac{2 \, \tau_0 \, K_{\text{NIP}}}{v_0} \, (h_x \cos \beta_0 - h_z \sin \beta_0)^2 \; ,
\end{aligned} \tag{C.5}$$

it is obvious that a NMO velocity cannot be defined in analogy to the cases of planar or smoothly curved topography. Here the traveltimes in the CMP gather depend on each of the three wavefront attributes independently so that the latter cannot be combined to a single stacking velocity.

---

[2]Here and throughout this thesis the term "horizontal" shall always include flatness.

C.3 Zero-dip NMO velocity

For a planar measurement surface it is possible to separate the influence of the overburden from the influence of the take off angle β_0, within equation (C.2b) by introducing the zero-dip NMO velocity,

$$v_{\text{NMO,ZD}}^2 = \frac{2v_0}{\tau_0 K_{\text{NIP}}} = v_{\text{NMO,H}}^2 \cos^2 \beta_0 \, , \tag{C.6}$$

and rewriting equation (C.2a) in the following way:

$$\tau^2(h_x) = \tau_0^2 + \frac{4h_x^2 \cos^2(\beta_0 + \alpha_0)}{\cos^2 \alpha_0 \, v_{\text{NMO,ZD}}^2} \tag{C.7a}$$

$$= \tau_0^2 + \frac{4h_x^2}{\cos^2 \alpha_0 \, v_{\text{NMO,ZD}}^2} - \frac{4h_x^2 \sin^2(\beta_0 + \alpha_0)}{\cos^2 \alpha_0 \, v_{\text{NMO,ZD}}^2} \, . \tag{C.7b}$$

The last term, which depends on the reflector dip, can be removed in a velocity independent way by applying the so-called Gardener Dip Moveout (DMO) procedure described in Gardener et al. (1990). Afterwards, the zero-dip NMO velocity can be determined in the conventional way. In the early days of reflection seismics all reflecting layers were assumed to be horizontal. Thus it was the zero-dip NMO velocity, which appeared in the first moveout formulas.

Solving the left side of equation (C.6) for K_{NIP} and inserting into equation (C.2b) leads to the useful relation between the zero-dip NMO velocity which would be obtained on a fictitious planar measurement surface through X_0, and the NMO velocity, obtained on a smoothly curved measurement surface, described by K_0, α_0. It reads

$$v_{\text{NMO}}^2 = \frac{2v_0 \cos^2 \alpha_0}{\tau_0 \left(\frac{2v_0 \cos^2(\beta_0 + \alpha_0)}{\tau_0 v_{\text{NMO,ZD}}^2} - K_0 \, \cos(\beta_0 + \alpha_0) \right)} \, . \tag{C.8a}$$

Vice versa

$$v_{\text{NMO,ZD}}^2 = \frac{2v_{\text{NMO}}^2 \, v_0 \, \cos^2(\beta_0 + \alpha_0)}{v_{\text{NMO}}^2 K_0 \, \cos(\beta_0 + \alpha_0)\tau_0 + 2v_0 \cos^2 \alpha_0} \, . \tag{C.8b}$$

C.4 RMS velocity

The RMS velocity constitutes the average wave propagation velocity above a certain reflector within a medium composed of homogeneous layers separated by parallel and planar interfaces. According to Dix (1955), it can be calculated from the interval velocities and associated interval traveltimes:

$$v_{\text{RMS,i}}^2 = \frac{v_1^2 \Delta t_1 + v_2^2 \Delta t_2 + ... + v_i^2 \Delta t_i}{t_{0,i}} \qquad i = 1, \ldots, N \, , \tag{C.9}$$

where v_i denotes the velocity of the ith layer, $t_{0,i}$ the two way traveltime of the central ray reflected at layer i and $\Delta t_i = t_{0,i} - t_{0,i-1}$ the two way traveltime within the ith layer. Vice versa, the interval velocity of the ith layer can be computed using the formula

$$v_i = \left[\frac{v_{\text{RMS,i}}^2 \, t_{0,i} - v_{\text{RMS,i-1}}^2 \, t_{0,i-1}}{t_{0,i} - t_{0,i-1}} \right]^{1/2} \, . \tag{C.10}$$

For a medium composed of homogeneous layers separated by parallel and planar interfaces and for offsets which are small compared to depth, the zero-dip NMO velocity approximatively coincides with the RMS velocity along the ZO ray. In this case, the relation between the RMS and the actual measured NMO velocity reads

$$v_{\mathrm{NMO,SC}}^2 = \frac{2v_0 \cos^2 \alpha_0}{\tau_0 \left(\frac{2v_0 \cos^2(\beta_0+\alpha_0)}{\tau_0 \, v_{\mathrm{RMS}}^2} - K_0 \, \cos(\beta_0 + \alpha_0) \right)} \ , \qquad (C.11a)$$

and, vice versa

$$v_{\mathrm{RMS}}^2 = \frac{2v_{\mathrm{NMO}}^2 \, v_0 \, \cos^2(\beta_0 + \alpha_0)}{v_{\mathrm{NMO}}^2 K_0 \, \cos(\beta_0 + \alpha_0)\,\tau_0 + 2v_0 \cos^2 \alpha_0} \ . \qquad (C.11b)$$

Appendix D

Used hard- and software

The presented CRS stack implementation was installed and applied on various platforms with different operating systems, e. g., SuSE Linux, Fedora Core, and Solaris. Most of the results shown in this thesis were processed on a PC with two 1.8 GHz AMD Opteron 244 processors, 4 GB RAM, and the operating system SuSE Linux 9.2.

The underlying CRS stack implementation for planar topography (Mann, 2002) as well as all extentions for land data processing are entirely written in C++ (Stroustrup, 1997) and require the standard libraries as well as the Standard Template Library (STL). The integrated development environment KDevelop was used for the programming together with the version control system CVS and the documentation system Doxygen. The code was compiled with the GNU project C++ compiler gcc version 3.3.1 (SuSE Linux) and optimization level 3. Processing parameters can be passed to the implementation via the command line and optional parameter files. The input and output routines were designed to achieve a wide compatibility with the Seismic Un*x format (see, e. g. Cohen and Stockwell, 2000).

Additional data processing and most of the data visualization, on screen as well as in PostScript format, was performed with various utilities of the Seismic Un*x package release 3.9. This freely available package uses a data format that is very similar to the industry standard SEG-Y and allows to handle irregular acquisition geometries. Further information about Seismic Un*x can be found in Stockwell (1997) and Stockwell (1999).

Green's function tables were computed using the so-called *fast marching eikonal solver* contained in the SEPLIB package, provided by the Stanford Exploration Project. The pre- and poststack depth migrations based on these GFTs were performed with Uni3D, a true-amplitude migration and demigration software developed at the Geophysical Institute, University of Karlsruhe.

For data visualization and computer algebra the mathematical program package Matlab (The MathWorks) was used. Furthermore, CorelDraw (Corel Corporation) and the freely available programs gnuplot and xfig were utilized to create some of the figures.

The thesis itself was written with the integrated LaTeX (Lamport, 1986) environment Kile. The document preparation system LaTeX is a macro package for the typesetting system TeX (Knuth, 1991).

List of Figures

List of Tables

References

Aki, K. and Richards, P. G. (1980). *Quantitative Seismology – Theory and Methods*, volume 1. W. H. Freeman & Co.

Al-Ali, M. and Verschuur, D. J. (2006). An Integrated Method for Resolving the Seismic Complex Near Surface Problem. *Geophys. Prosp.*, 54.

Alkhalifah, T. and Bagaini, C. (2006). Straight-rays redatuming: A fast and robust alternative to wave-equation-based datuming. *Geophysics*, 71(3):37–46.

Andretta, M., Birgin, E. G., and Martínez, J. M. (2005). Practical active-set Euclidian trust-region method with spectral projected gradients for bound-constrained minimization. *Optimization*, 54(3):305–325.

Babich, V. (1956). Ray method of the computation of the intensity of wave fronts (in Russian). *Doklady Akad. Nauk SSSR*, 110:355–357.

Ben-Menachem, I. and Beydoun, W. B. (1985). Range of validity of seismic ray and beam methods in general inhomogeneous media: General theory. *Geophys. J. Royal Astron. Soc.*, 82:207–234.

Bergler, S. (2001). Common-Reflection-Surface stack for common offset – theory and application. Master's thesis, Karlsruhe University.

Bergler, S. (2004). *On the determination and use of kinematic wavefield attributes for 3D seismic imaging*. Logos Verlag, Berlin.

Berkhout, A. J. and Verschuur, D. J. (2001). Seismic imaging beyond depth migration. *Geophysics*, 66(06):1895–1912.

Billette, F. and Lambaré, G. (1998). Velocity macro-model estimation from seismic reflection data by stereotomography. *Geophys. J. Intern.*, 135:671–690.

Birgin, E. G., Biloti, M., Tygel, M., and Santos, L. T. (1999a). Nonmonotone Spectral Projected Gradient Methods on Convex Sets. *SIAM Journal on Optimization*, 10(4):1196–1211.

Birgin, E. G., Biloti, R., Tygel, M., and Santos, L. T. (1999b). Restricted Optimization: A Clue to Fast and Accurate Implementation of the Common Reflection Surface Method. *J. Appl. Geophys., Special Issue on Model-Independent Imaging*, 42(3-4):142–155.

Bishop, T., Bube, K., Cutler, R., Langan, R., Love, P., Resnick, J., Shuey, R., Spindler, D., and Wyld, H. (1985). Tomographic determination of velocity and depth in laterally varying media. *Geophysics*, 50(1):903–923.

References

Bleistein, N. (1984). *Mathematical Methods for Wave Phenomena*. Academic Press Inc., New York.

Bleistein, N. (1999). Hagedoorn told us how to do Kirchhoff migration and inversion. *The Leading Edge*, 18:918–927.

Boelsen, T. and Mann, J. (2005). 2D CO CRS stack for OBS and VSP data and arbitrary top-surface topography. In *Extended abstracts, 67th Conf.* Eur. Assn. Geosci. Eng. Session P181.

Bortfeld, R. (1989). Geometrical ray theory: Rays and traveltimes in seismic systems (second-order approximations of the traveltimes). *Geophysics*, 54:342–349.

Bridle, R., Barsoukov, N., Al-Homaili, M., Ley, R., and Al-Mustafa, A. (2006). Comparing state-of the art near-surface models of a seismic test line from Saudi Arabia. *Geophys. Prosp.*, 54:667–680.

Brown, R. (2002). Historical Tidbit. Who was Irvine Perrine? *Timelines, Jan. Issue, Geophys. Soc. Tulsa*.

Červený, V. (2001). *Seismic ray theory*. Cambridge University Press, Cambridge.

Červený, V. and Hron, F. (1980). The ray series method and dynamic ray-tracing system for three-dimensional inhomogeneous media. *Bull. Seis. Soc. Am.*, 70:47–77.

Chira, P., Tygel, M., Zhang, Y., and Hubral, P. (2001). Analytic CRS stack formula for a 2D curved measurement surface and finite-offset reflections. *J. Seis. Expl.*, 10(1-3):245–262.

Claerbout, J. F. (1985). *Imaging the earth's interior*. Blackwell Scientific Publications.

Cohen, J. K. and Stockwell, J. J. W. (2000). Seismic Un*x Release 34: a free package for seismic research and processing. Center for Wave Phenomena, Colorado School of Mines. *Geophysical Journal International*, 125:431–442.

Cox, M. J. G. (1999). *Static Corrections for Seismic Reflection Surveys*. Soc. Expl. Geophys., Tulsa.

Dahl-Jensen, T. (1989). Static correction on crystalline rocks. *Geophys. Prosp.*, 37(5):467–478.

de Bazelaire, E. (1988). Normal moveout revisited: Inhomogeneous media and curved interfaces. *Geophysics*, 53(2):143–157.

de Bazelaire, E. and Viallix, J. R. (1994). Normal moveout in focus. In *Extended Abstracts, 54th Mtg. Eur. Assoc. Expl. Geophys.*, pages 174–175.

de Boor, C. (1978). *A practical guide to splines*. Springer-Verlag, Berlin.

Deregowski, S. M. (1986). What is DMO? *First Break*, 4(7):7–24.

Deregowski, S. M. (1990). Common-offset migrations and velocity analysis. *First Break*, 8(6):224–234.

Dix, C. H. (1955). Seismic velocities from surface measurements. *Geophysics*, 20(1):68–86.

Duveneck, E. (2004). *Tomographic determination of seismic velocity models with kinematic wavefield attributes*. Logos Verlag, Berlin.

Duveneck, E. and Hubral, P. (2002). Tomographic velocity model inversion using kinematic wavefield attributes. In *Expanded Abstracts*. 72nd Ann. Internat. Mtg., Soc. Expl. Geophys. Session IT 2.3.

Eiras, J. F. and Kinoshita, E. M. (1990). Geology and petroleum perspectives of the Takutu Basin. *In: Raja Gabaglia, G. P. and Milani, E. J. Origin and Evolution of Sedimentary Basins. (In Portuguese)*, pages 97–220.

Farra, V. and Madariaga, R. (1987). Seismic waveform modeling in heterogeneous media by ray perturbation theory. *J. Geophys. Res.*, 92(B3):2697–2712.

Flueh, E. R., Klaeschen, D., and Bialas, J. (2002). Options for multi-component seismic data acquisition in deep water. *First Break*, 20(12):764–769.

Forel, D., Benz, T., and Pennington, W. D. (2005). *Seismic Data Processing with Seismic Un*x*. Soc. Expl. Geophys., Tulsa.

Garabito, G. and Paschoal, W. (2003). 2D-CRS stack: A comparison between the extended and global search strategies. *Annual WIT report*, pages 15–25. http://www.wit-consortium.de.

Gardener, G., Wang, S., Pan, N., and Zhang, Z. (1990). Dip moveout and prestack imaging. In *Extended Abstracts, 18th Ann. Offshore Tech. Conf.*, pages 75–84.

Gazdag, J. (1978). Wave-equation migration by phase shift. *Geophysics*, 43:49–76.

Gelchinsky, B., Berkovitch, A., and Keydar, S. (1997). *Multifocusing homeomorphic imaging: Parts I und II*. Special Course on Homeomorphic Imaging. Wave Inversion Technology Consortium, Geophysical Institute, Karlsruhe University.

Gierse, G., Pruessmann, J., and Coman, R. (2006). CRS strategies for solving severe static and imaging issues in seismic data from Saudi Arabia. *Geophys. Prosp.*, 54:709–719.

Gill, P. E., Murray, W., and Wright, M. H. (1981). *Practical Optimization*. Academic Press, London and New York.

Gray, S. and Marfurt, K. (1995). Migration from Topography: Improving the Near-Surface Image. *Can. J. Expl. Geophys.*, 31:18–24.

Gray, S. H. (2005). Gaussian beam migration of common-shot records. *Geophysics*, 70(4):S71–S77.

Gurevich, B., Keydar, S., and Landa, E. (2001). Multifocusing imaging over an irregular topography. *Geophysics*, 67(2):639–643.

Hagedoorn, J. (1954). A process of seismic reflection interpretation. *Geophys. Prosp.*, 2:85–127.

Hale, D. (1991). *Dip Moveout Processing, Course Notes Series, Vol. 4*. Soc. Expl. Geophys., Tulsa.

Heilmann, Z. (2002). The Common-Reflection-Surface Stack under Consideration of the Acquisition Surface Topography and of the Near-Surface Velocity Gradient. Master's thesis, Karlsruhe University. http://www.wit-consortium.de.

Heilmann, Z., Mann, J., Duveneck, E., and Hertweck, T. (2004). CRS-Stack-Based Seismic Reflection Imaging – A Real Data Example. In *Expanded Abstracts*. 66th Conf., Europ. Assn. Geosci. Eng. Session P211.

References

Heilmann, Z., Mann, J., and Koglin, I. (2006). CRS-stack-based seismic imaging considering top-surface topography. *Geophys. Prosp.*, 54:681–695.

Heilmann, Z., von Steht, M., Koglin, I., Klüver, T., and Jäger, C. (2005). CRS-stack-based seismic imaging considering top-surface topography. In *Workshop on advances and challenges in near surface seismic, Extended abstracts, 67th Conf.* Eur. Assn. Geosci. Eng. Session W6-03.

Hertweck, T. (2004). *True-amplitude Kirchhoff migration: analytical and geometrical considerations*. Logos Verlag, Berlin.

Hertweck, T., Jäger, C., Mann, J., and Duveneck, E. (2003). An integrated data-driven approach to seismic reflection imaging. In *Extended Abstracts*. 65th Conf., Europ. Assn. Geosci. Eng. Session P004.

Hertweck, T., Mann, J., and Klüver, T. (2005). Event-consistent smoothing in the context of the CRS stack method. *J. Seis. Expl.*, 14(2-3):197–215.

Herzberger, M. (1958). *Modern Geometrical Optics*. Interscience, New York.

Himmelblau, D. M. (1972). *Applied Nonlinear Programming*. McGraw-Hill, New York.

Höcht, G. (1998). Common-Reflection-Surface stack. Master's thesis, Karlsruhe University.

Höcht, G. (2002). *Traveltime approximations for 2D and 3D media and kinematic wavefield attributes*. PhD thesis, Universität Karlsruhe. http://www.ubka.uni-karlsruhe.de/vvv/2002/physik/3/3.pdf.

Hubral, P. (1983). Computing true amplitude reflections in a laterally inhomogeneous earth. *Geophysics*, 48(8):1051–1062.

Hubral, P., editor (1999). *Special Issue on Macro-Model Independent Seismic Reflection Imaging*, volume 42(3,4) of *J. Appl. Geophy.*, Amsterdam. Elsevier.

Hubral, P. and Krey, T. (1980). *Interval velocities from seismic reflection traveltime measurements*. Soc. Expl. Geophys.

Hubral, P., Schleicher, J., and Tygel, M. (1992). Three-dimensional paraxial ray properties, Part I: Basic relations. *J. Seis. Expl.*, 1:265–279.

Hubral, P., Schleicher, J., and Tygel, M. (1993a). Three-dimensional primary zero-offset reflections. *Geophysics*, 58(5):692–702.

Hubral, P., Schleicher, J., and Tygel, M. (1996). A unified approach to 3-D seismic reflection imaging, Part I: Basic concepts. *Geophysics*, 61:742–758.

Hubral, P., Schleicher, J., Tygel, M., and Hanitzsch, C. (1993b). Determination of Fresnel zones from traveltime measurements. *Geophysics*, 58(5):703–712.

Hubral, P., Tygel, M., and Schleicher, J. (1995). Geometrical-spreading and ray-caustic decomposition of elementary seismic waves. *Geophysics*, 60:1195–1202.

Jäger, C. and Hertweck, T. (2002). Using Uni3D version v0.23: a manual. *Annual WIT report*, pages 143–150. http://www.wit-consortium.de.

172

Jäger, C., Hertweck, T., and Spinner, M. (2003). True-amplitude Kirchhoff migration from topography. In *Expanded Abstracts*. 73rd Ann. Internat. Mtg., Soc. Expl. Geophys. Session MIG 2.1.

Jäger, R. (1999). The Common-Reflection-Surface stack – theory and application. Master's thesis, Karlsruhe University.

Jeannot, J. P. and Faye, J. P. (1986). Prestack migration velocities from focusing depth analysis. In *Expanded abstracts, 56th Ann. Internat. Mtg., Soc. Expl. Geophys.*, pages 438–440.

Karal, F. and Keller, J. (1959). Elastic wave propagation in homogeneous and inhomogeneous media. *J. Acoust. Soc. Am.*, 31:694–705.

Kelamis, P. G., Erickson, K. E., Taner, T., Verschuur, D. J., and Berkhout, A. J. (2000). CFP-based redatuming: Synthetic and field data examples. In *Expanded Abstracts, 69th Ann. Internat. Mtg., Soc. Expl. Geophys.*, pages 509–512.

Kelly, K. R., Ward, R. W., Treitel, S., and Alford, R. M. (1976). Synthetic seismograms: A finite-difference approach. *Geophysics*, 41(1):2–27.

Kirkpatrick, S., Gelatt, C. D., J., and Vehhi, M. P. (1983). Optimization by simulated annealing. *Science*, 220:671–680.

Klüver, T. (2006). Velocity model building using migration to residual time. In *Expanded Abstracts, 76th Ann. Internat. Mtg., Soc. Expl. Geophys.*, pages 2022–2026. Soc. Expl. Geophys.

Klüver, T. and Mann, J. (2005). Smoothing and automated picking of kinematic wavefield attributes. In *Expanded abstracts, 75th Ann. Internat. Mtg., Soc. Expl. Geophys.*, pages 1894–1897.

Knuth, D. E. (1991). *Computers & typesetting, vol. A: the TEXbook*. Addison-Wesley, Reading.

Koglin, I. (2005). *Estimation of Residual Static Time Shifts by means of the CRS-based Residual Static Correction Approach*. Logos Verlag, Berlin.

Koglin, I. and Ewig, E. (2003). Residual Static Correction by Means of Kinematic Wavefield Attributes. In *Extended Abstracts, 65th Conf. and*, Session D18. Eur. Assn. Geosci. Eng.

Koglin, I., Heilmann, Z., and von Steht, M. (2005). CRS-stack-based residual static correction – a real data example. In *Workshop on advances and challenges in near surface seismic, Extended Abstracts, 67th Conf.* Eur. Assn. Geosci. Eng. Session W6-04.

Koglin, I., Mann, J., and Heilmann, Z. (2006). CRS-stack-based residual static correction. *Geophys. Prosp.*, 54:697–707.

Kravtsov, Y. A. and Orlov, Y. I. (1990). *Geometrical Optics of Inhomogeneous Media*. Springer Verlag, New York.

Lamport, L. (1986). *LaTeX A document preparation system*. Addison-Wesley, Reading.

Langenberg, K. L. (1986). *Applied Inverse Problems*. Fraunhofer-Institut für zerstörungsfreie Prüfverfahren, Kassel, Germany.

Levin, F. K. (1971). Apparent velocity from dipping interface reflections. *Geophysics*, 36:510–516.

References

Liu, Z. and Bleistein, N. (1995). Migration velocity analysis: theory and an iterative algorithm. *Geophysics*, 60(1):142–153.

MacKay, S. and Abma, R. (1992). Imaging and velocity estimation with depth-focusing analysis. *Geophysics*, 57(12):1608–1622.

Mann, J. (2002). *Extensions and Applications of the Common-Reflection-Surface Stack Method*. Logos Verlag, Berlin.

Mann, J. and Duveneck, E. (2004). Event-consistent smoothing in generalized high-density velocity analysis. In *Expanded Abstracts*, pages 2176–2179. 74th Ann. Internat. Mtg., Soc. Expl. Geophys. ST1.1.

Mann, J., Duveneck, E., Bergler, S., and Hubral, P. (2004). *The Common-Reflection-Surface (CRS) stack – a data-driven space-time adaptive seismic reflection imaging procedure*, chapter VIII.4. Applications of Space-Time Adaptive Processing. The Institution of Electrical Engineers (IEE).

Mann, J., Duveneck, E., Hertweck, T., and Jäger, C. (2003). A seismic reflection imaging workflow based on the Common-Reflection-Surface stack. *J. Seis. Expl.*, 12:283–295.

Mann, J. and Höcht, G. (2003). Pulse stretch effects in the context of data-driven imaging methods. In *Extended Abstracts*. 65th Conf. , Europ. Assoc. Geosci. Eng. Session P007.

Mayne, W. H. (1962). Common reflection point horizontal data stacking techniques. *Geophysics*, 27(6):927–938.

Müller, T. (1999). *The Common Reflection Surface Stack Method – Seismic imaging without explicit knowledge of the velocity model*. Der Andere Verlag, Bad Iburg.

Müller, T., Jäger, R., and Höcht, G. (1998). Common reflection surface stacking method – imaging with an unknown velocity model. In *Expanded Abstracts, 68th Ann. Internat. Mtg., Soc. Expl. Geophys.*, pages 1764–1767.

Neidell, N. S. and Taner, M. T. (1971). Semblance and other coherency measures for multichannel data. *Geophysics*, 36(3):482–497.

Nelder, J. A. and Mead, R. (1965). A simplex method for function minimization. *Computer Journal*, 7:308–313.

Normark, E. (1993). Residual statics estimation by stack-power maximation in the frequency domain. *Geophys. Prosp.*, 41(5):551–563.

Paige, C. C. and Saunders, M. A. (1982a). Algorithm 583 – LSQR: sparse linear equations and least squares problems. *ACM Trans. Math. Softw.*, 8(2):195–209.

Paige, C. C. and Saunders, M. A. (1982b). LSQR: an algorithm for sparse linear equations and sparse least squares. *ACM Trans. Math. Softw.*, 8(1):43–71.

Popov, M. M. (2002). *Ray Theory and Gaussian Beam Method for Geophysicists*. Universidade Federal da Bahia, Salvador.

Press, W. H., Teukolsky, S. A., Vetterling, W. T., and Flannery, B. P. (1992). *Numerical recipes in C; the art of scientific computing*. Cambridge University Press, Cambridge, 2nd edition.

Profeta, M., Moscoso, J., and Koremblit, M. (1995). Minimum field static corrections. *The Leading Edge*, 14(6):684–687.

Robinson, E. A. and Treitel, S. (1980). *Geophysical signal analysis*. Prentice-Hall, Inc.

Ronen, J. and Claerbout, J. F. (1985). Surface-consistent residual statics estimation by stack-power maximization. *Geophysics*, 50(12):2759–2767.

Rothman, H. (1985). Nonlinear inversion, statistical mechanics, and residual statics estimation. *Geophysics*, 50(12):2784–2796.

Rothman, H. (1986). Automatic estimation of large statics corrections. *Geophysics*, 51(2):332–346.

Salvatierra, M., Yano, F., Santos, L. T., Martinez, J. M., Andreani, R., and Tygel, M. (2003). A global optimization algorithm applied to the CRS problem. *Annual WIT report*, pages 26–31. http://www.wit-consortium.de.

Schleicher, J. (1993). *Bestimmung von Reflexionskoeffizienten aus Reflexionsseismogrammen*. PhD thesis, Universität Karlsruhe.

Schleicher, J., Hubral, P., Tygel, M., and Jaya, M. S. (1997). Minimum apertures and Fresnel zones in migration and demigration. *Geophysics*, 62(01):183–194.

Schneider, W. (1978). Integral Formulation for Migration in Two and Three Dimensions. *Geophysics*, 43:49–76.

Shah, P. M. and Levin, F. K. (1973). Gross properties of time-distance curves. *Geophysics*, 38(4):643–656.

Sheriff, R. E. (2002). *Encyclopedic Dictionary of Applied Geophysics*. Soc. Expl. Geophys., Tulsa. Fourth Edition.

Spinner, M. (2006). 3D CRS-based limited aperture Kirchhoff time migration. In *Expanded Abstracts, 76th Ann. Internat. Mtg., Soc. Expl. Geophys.*, pages 2569–2573.

Stockwell, Jr., J. W. (1997). Free software in education: a case study of CWP/SU: Seismic Un*x. *The Leading Edge*, 16(7):1045–1049.

Stockwell, Jr., J. W. (1999). The CWP/SU: Seismic Un*x package. *Computers and Geosciences*, 25(4):415–419.

Stoffa, P. L., Fokkema, J. T., de Luna Freire, R. M., and Kessinger, W. P. (1990). Split-step Fourier migration. *Geophysics*, 55(04):410–421.

Stolt, R. H. (1978). Migration by Fourier transform. *Geophysics*, 43(1):23–48.

Strang, G. and Fix, G. (1973). *An analysis of the finite element method*. Prentice Hall.

Stroustrup, B. (1997). *The C++ Programming Language*. Addison-Wesley, 3rd edition.

Taner, T., Koehler, F., and Alhilalik, A. (1974). Estimation and correction of near-surface time anomalies. *Geophysics*, 39(4):441–463.

References

Tygel, M., Schleicher, J., and Hubral, P. (1996). A unified approach to 3-D seismic reflection imaging, Part II: Theory. *Geophysics*, 61:759–775.

Ursin, B. (1982). Quadratic wavefront and traveltime approximations in inhomogeneous layered media with curved interfaces. *Geophysics*, 47(7):1012–1021.

Vesnaver, A. (2004). The near-surface information gap for time and depth imaging. *Geophys. Prosp.*, 52(06):653–661.

Vesnaver, A., Bridle, R., Henry, B., Ley, R., Rowe, R., and Wyllie, A. (2006). Geostatistical integration of near-surface geophysical data. *Geophys. Prosp.*, 54:763–777.

Vieth, K.-U. (2001). *Kinematic wavefield attributes in seismic imaging*. PhD thesis, Karlsruhe University.

Wyllie, M., Gregory, A., and Gardner, G. (1956). Elastic wave velocities in heterogeneous and porous media. *Geophysics*, 21(1):41–70.

Yang, K., Wang, H., and Ma, Z. (1999). Wave equation datuming from irregular surfaces using finite difference scheme. In *Expanded Abstracts, 70th Ann. Internat. Mtg., Soc. Expl. Geophys.*, pages 1465–1468.

Yilmaz, Ö. (1987). *Seismic data Processing*. Soc. of Expl. Geophys., Tulsa.

Yilmaz, Ö. (2001). *Seismic Data Analysis*. Soc. Expl. Geophys., Tulsa.

Zhang, Y. (2003). *Common-Reflection-Surface Stack and the Handling of Top Surface Topography*. Logos Verlag, Berlin.

Zhang, Y., Bergler, S., and Hubral, P. (2001). Common-Reflection-Surface (CRS) stack for common offset. *Geophys. Prosp.*, 49(6):709–718.

Danksagung / Acknowledgements

Bei allen, die durch ihre Unterstützung zum Entstehen dieser Arbeit beigetragen haben, möchte ich mich hiermit herzlich bedanken.

Allen voran möchte ich an dieser Stelle Herrn **Prof. Dr. Peter Hubral** nennen, der diese Arbeit betreut und durch vielfältige Unterstützung ermöglicht hat. Während der Jahre die ich seiner Arbeitsgruppe angehörte vermochte er stets mittels großer fachlicher wie auch menschlicher Kompetenz eine Arbeitsatmosphäre zu schaffen in der jeder Einzelne sich frei seinen Interessen und Fähigkeiten entsprechend entwickeln konnte. Nicht zuletzt durch sein unermüdliches Engagement für das WIT Konsortium ermöglichte er mir den Besuch zahlreicher nationaler wie auch internationaler Tagungen wovon ich in vielerlei Hinsicht profitieren konnte.

Prof. Dr. Dirk Gajewski danke ich für die Übernahme des Korreferat – und für sein Verständnis bezüglich der etwas langwierigen Fertigstellung dieser Dissertation.

Dr. Jürgen Mann gilt mein besonderer Dank für die langjährige fachliche Betreuung die er mir zuteil werden ließ. Einen Großteil meiner Kenntnisse sowohl die Verarbeitung seismischer Daten als auch die Anfertigung wissenschaftlicher Texte und Präsentationen betreffend verdanke ich ihm. Seine wissenschaftliche Objektivität und uneigennützige Hilfsbereitschaft prägte meines Empfindens nach stets das kollegiale Verhältnis in unserer Arbeitsgruppe. Seinen gründlichen Korrekturen ist manche Verbesserung der vorliegenden Arbeit zu verdanken.

Dr. Erik Duveneck, **Dr. Christoph Jäger** und **Dr. Thomas Hertweck** möchte ich für ihre Mithilfe im sogenannten "Hotrock Projekt" danken, durch welches die Finanzierung des ersten Jahres meiner Doktorandenzeit sichergestellt werden konnte. An dieser Stelle auch ein herzliches Dankeschön an **Dr. Horst Kreuter**, **Prof. Dr. Norman Harthill** und **Dr. Christian Hecht** von der Hot-Rock Verwaltungs- und Engineering GmbH, Karlsruhe, an **Dr. Johannes Gottlieb** von der Montanes GmbH, Karlsruhe, und an **Dr. Rüdiger Misiek** und **Christoph Witte** von der Deutschen Montan Technologie GmbH (DMT), Essen.

Dr. Ingo Koglin hat mich durch mein gesamtes Studium der Geophysik stets als Freund und zuverlässiger Kollege begleitet, hierfür möchte ich ihm an dieser Stelle danken. Besonders in Zeiten in denen sich unsere Tätigkeitsfelder stark überlappten, so zum Beispiel bei der Verarbeitung des Saudi Aramco Testdatensatzes und der damit verbundenen Weiterentwicklung und Zusammenführung unserer Software, war es mir immer ein Vergnügen mit Ingo zusammenzuarbeiten.

Markus von Steht dessen Diplomarbeit ich betreuen durfte gilt mein besonderer Dank. Seinem Teamgeist, Engagement und Einfallsreichtum ist so manches Ergebnis dieser schönen und fruchtbaren Zeit zu verdanken.

Natürlich dürfen an dieser Stelle auch **Miriam Spinner**, **Alex Müller** und **Tilman Klüver** nicht unerwähnt bleiben denen ich für ihre freundliche Hilfe bei kleinen und größeren Problemen, für eine

178

Lebenslauf

Persönliche Daten

Name:	Björn Zeno Heilmann
Geburtsdatum:	17. Februar 1972
Nationalität:	deutsch
Geburtsort:	Pforzheim

Schulausbildung

1978 - 1982	Grundschule Bretten
1982 - 1991	Gymnasium Bretten
17.05.1991	Allgemeine Hochschulreife

Zivildienst

10/1991 - 04/1993	Lebenshilfe Karlsruhe e.V.

Hochschulausbildung

1993 - 1995	Studium der Geographie an der Ruprecht-Karls-Universität Heidelberg
1995 - 2002	Studium der Geophysik an der Universität Karlsruhe (TH)
29.08.2002	Diplom
seit 01.11 2002	Doktorand an der Fakultät für Physik der Universität Karlsruhe (TH)